AIX-MARSEILLE UNIVERSITY
FACULTY OF SCIENCES OF LUMINY
DOCTORAL SCHOOL OF LIFE AND HEALTH SCIENCES
DEVELOPMENTAL BIOLOGY INSTITUTE OF MARSEILLE

Thesis presented for the degree of Doctor of Philosophy

Discipline : Developmental Biology
Speciality : Tissue Mechanics

Pruthvi CHAVADIMANE SHIVAKUMAR

Mechanical basis of cell shapes and cell arrangements during retinal morphogenesis in *Drosophila*

Presented on 30/11/2017 to the jury composed of :

Katja RÖPER	Reviewer
Alexandre J. KABLA	Reviewer
Sylvie HÉNON	Examiner
Pierre-François LENNE	Thesis supervisor

Acknowledgements

First and foremost, I would like to sincerely thank Pierre-François for giving me the opportunity to work in his lab. He has supported me in every possible way and guided me throughout my PhD. I am grateful for the time he has taken to mentor me during my PhD. His help has been always available in spite of his busy schedule.

I would like to sincerely thank the jury members of my PhD thesis: Dr. Alexandre J. Kabla and Dr. Katja Röper from Cambridge University, and Prof. Sylvie Hénon from Paris Diderot University, for agreeing to judge my PhD thesis and to participate in my PhD viva.

I would like to sincerely thank all the present and past members of Team Lenne. In particular, I would like to thank Eunice: I couldn't have asked for a better collaborator than her, who has also taught me several experimental techniques in biology. I have had many discussions with Raphael who has always shared his ideas generously. Claire was always available to help, especially with ablation experiments. I would like to thank Remy for all his help with imaging and Pierre R. for providing feedback on my thesis. I would like to thank Monika, Anais, Pierre M., Pritha, Ali, Wei, Olivier, Edith, Crystal for making my stay in France a wonderful experience.

I would like to sincerely thank all the members of Team Lecuit, headed by Thomas Lecuit. Our joint-group meetings were helpful with many great ideas and feedback from Thomas. I would also like to thank Ankita, Girish, Steve, Sabine, Alain, Amrutha, Qiyan, Benoit, Jules, Claudio, Jean-marc from Team Lecuit and Benoit, Chris, Veronika from Team Le Bivic.

I would also like to sincerely thank Carla, Magali and Mélina for taking care of numerous administrative tasks during my PhD.

I would like to thank my family and friends back in India for their love and support. My parents and my sister have constantly encouraged me to pursue my dreams and I could not have completed my PhD without their encouragement. *I dedicate this thesis to you*.

Contents

Foreword

Tissues and organs are sculpted by changes in cell shape, rearrangements of cells, cell division and cell deaths. Cells achieve the required change or arrangement with the help of forces generated within them or external forces present in their environment. The active forces result from actomyosin contractility. A single cell tends to round up due to actomyosin contractility that acts to oppose the internal hydrostatic pressure in the cell, when it is isolated from the tissue (Stewart et al., 2011). Whereas, a cell on a substrate spreads out like a water droplet with varying levels of adhesion (for example adhesion through integrins) depending on the substrate stiffness [Figure 0.1a] (Discher et al., 2005; Georges & Janmey, 2005). Cell morphology depends on the actomyosin contractility that changes its property to adapt to the substrate stiffness [Figure 0.1a]. Here, actomyosin contractility and adhesion by integrins shape the isolated cell.

Adherens junction [Figure 0.1b] is the position at the epithelial cell contact that is enriched in adhesion molecules and is associated with actomyosin network inside the adhering cells [Figure 0.1c] (Tepass & Harris, 2007; Yagi & Takeichi, 2000). The shape of the epithelial cell is determined to a great extent by these components at the AJs. The physical properties of these two components are quite opposite in nature (Maître & Heisenberg, 2011). At the cell contact, contractile actomyosin reduces the surface of contact between cells, whereas adhesion (say, by E-cadherin) increases the contact surface. Intriguingly, E-cadherin molecules depend on β-catenin, α-catenin and actin network in the adhering cells (Bershadsky, 2004; Jamora & Fuchs, 2002). Hence the successful adhesion depends, not only on the interaction between adhesion molecules, but also on the interaction with actin and actin organization (Yamada & Nelson, 2007). The opposing yet interdependent forces generate an interfacial tension at the cell contact and define the cell shapes (see also review by Lecuit & Lenne, 2007).

Drosophila retina has been a frequently used model over the last three decades to study tissue patterning, cell type specification, axon target selection etc. (Peláez et al., 2015;

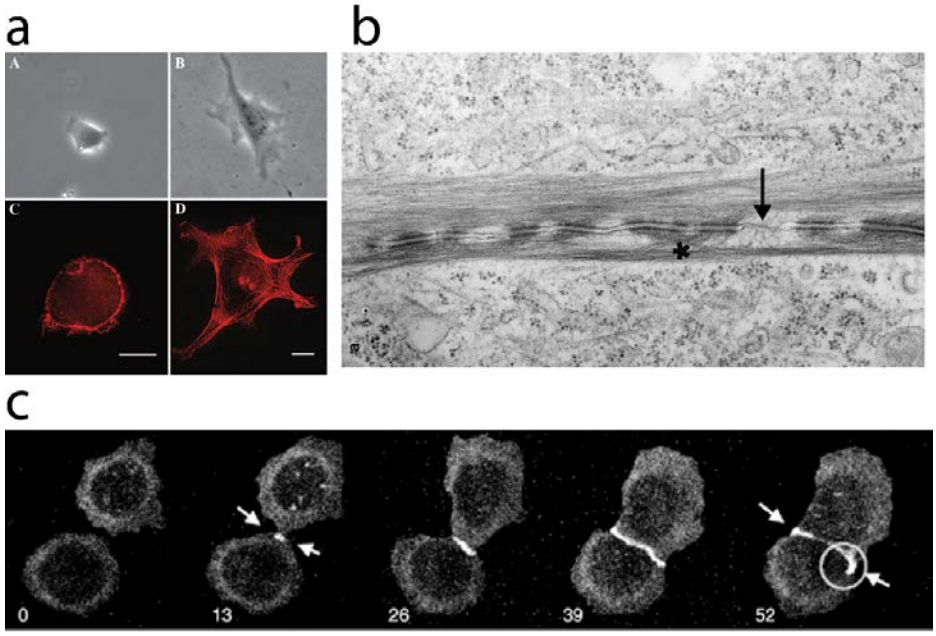

Figure 0.1: Actomyosin, Adherens junction (AJ) and cell contact formation

a) Morphology (top) and actin (bottom) organization in fibroblast, on soft (left) and hard (right) substrates *(image: Georges & Janmey, 2005).* b) Transmission electron microscopy image of keratinocytes cell contact showing AJ and desmosomes. c) Time lapse images of the cell contact formation of MDCK cells (bottom left: time in minutes) *(Image: modified from Jamora & Fuchs, 2002).*

Rusconi, Hays, & Cagan, 2000; Yonekura et al., 2007). AJs of *Drosophila* retina are well characterized in the context of cell shapes. *Drosophila* retina expresses all three classical cadherins: E-cadherin (Ecad), N-cadherin (Ncad) and N-cadherin2 (Ncad2). Ecad and Ncad protein distribution is known (Hayashi & Carthew, 2004; Yonekura et al., 2007), but the protein distribution of Ncad2 is not yet known. An inspiring work by Hayashi and Carthew (Hayashi & Carthew, 2004) reported that the differential expression of Ncad and Ecad controls the cone cell shape. They show through experiments that cone cells minimize their surface area like soap bubbles [Figure 0.2a, b].

By considering the whole ommatidium in the picture, Käfer et al. (Käfer et al., 2007) try to model the shape of the ommatidium to understand the extent to which cells can be compared to inanimate objects like soap bubbles. In contrast to bubbles, cells with adhesion molecules—like cone cells with Ecad and Ncad—tend to increase the contact surface area,

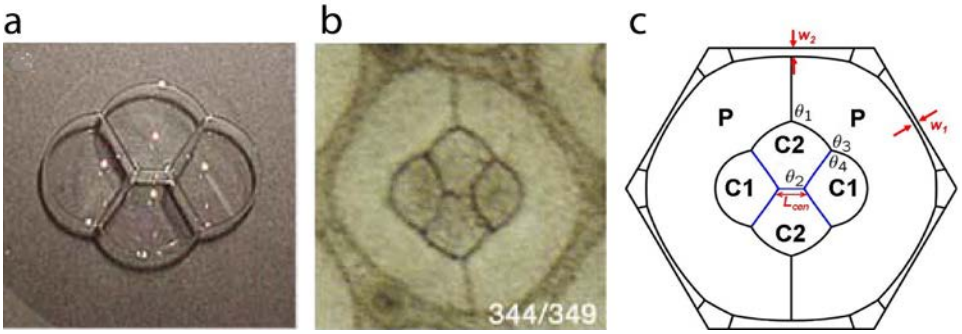

Figure 0.2: Ommatidium structure and resemblance to soap bubbles

a, b) An image of four soap bubbles and an ommatidium highlighting the resemblance of cone cells and soap bubbles (*image: modified from Hayashi & Carthew, 2004*). c) The simulated structure of an ommatidium using a Surface Evolver model with the differential adhesion as the key biological ingredients (*image: Hilgenfeldt et al., 2008)*.

whereas surface tension in soap bubbles decreases the contact surface area. Käfer et al. using a cellular potts model (Käfer et al., 2007) and Hilgenfeldt et al. (Hilgenfeldt et al., 2008) using a Surface Evolver model put forth the idea that in addition to the property of cadherins, they have to invoke the role of actomyosin contractility as a cell elasticity term [Figure 0.2c]. Hence the interfacial tension of cell contact is maintained by the activity of actomyosin and cadherins.

Based on these studies we asked the question: how far is the interfacial tension regulated by actomyosin and cadherins? The recent study by Maître et al. (Maitre et al., 2012) showed that the shape of cell doublets from different germ layers of zebrafish largely depends on the Myosin-II (MyoII) generated cortical tension, rather than E-cadherin adhesion. How does the interfacial tension influence the cell shapes *in vivo*, and how do the cadherins and MyoII generate the interfacial tension? From our experiments and simulations, we find that Ncad has a differential role that greatly influences cone cell shapes and cone cell arrangements through MyoII. We show that cell shapes depend little on cadherin bonds *per se,* and mainly on MyoII contractility. The description and discussion of these findings along with the methods we employed is the main aim of this thesis.

The research presented in this thesis is based on joint work between Eunice H. Chan (a former postdoc in the team) and I. Eunice took the biological approach to problems, for example genetic perturbations of different proteins and live imaging, whereas I took a more physical and computational approach involving mechanical measurements and simulations. Along with the aim to understand cone cell shapes, I was also interested in understanding the T1-like transition among cone cells during retinal morphogenesis. The approaches to solve this are discussed in this thesis, but it is still an open question.

At the beginning of my project, Eunice had already looked at MyoII with both Sqh::Ch and Zip::YFP, and she had observed that certain Ncad mutants do not undergo T1 transition. We argued that there could be a change in local mechanical forces that are acting against this transition. As a confirmation we did observe a higher level of MyoII at the cell interfaces of these Ncad mutant cells (this is discussed in Chapter 3, Results). We later noticed that wildtype cone cell contacts and Ncad mutant cone cell contacts did not have two levels of MyoII (we expected two levels on the basis of the presence or the absence of Ncad at the contact), but three levels. This led to further investigations on Ncad, MyoII, and ablation experiments with a simple mechanical model to explain cone cell shapes.

This thesis is divided into five chapters. In the first chapter a broad overview of the biological components (Ncad, MyoII etc.) under study, the current knowledge in the field of cell shapes and various methods used to study them is given. The second chapter covers the methods used to address the problem: laser ablation and Surface Evolver simulations. The third chapter covers the results. The fourth chapter concludes the thesis with discussions and perspectives.

The material covered in the second chapter (Section 2.1) has been published as a book chapter in the book '*Drosophila* methods and protocols' (Shivakumar & Lenne, 2015) and the material covered in the third chapter (Section 3.1) comprises of our recently published article in eLife (Chan et al., 2017).

Chapter 1: Introduction

1.1 Tissue morphogenesis

Animal development starts from a single cell into an adult. A series of events takes this single cell into a complex arrangement composed of millions of cells arranged in many different ways to form rudimentary organs; this process is generally termed as morphogenesis. Morphogenesis is a word derived from the Greek words *morphê* meaning shape and *genesis* means creation. It can be translated as 'generation of forms'. The study of morphogenesis comprises of a broad range of questions: from how a group of cells undergo differentiation and rearrangement giving rise to a fully functional mature heart, to the formation of a particular shape of a cell by the coordination and arrangement of cellular components inside the cell.

In spite of the diversity of forms in the animal kingdom, the basic stages of early development are similar. The single cell zygote formed by the fusion of an egg and a sperm, undergoes a series of divisions. This leads to a single layered cluster of cells. Through a process called gastrulation, this single layer further gives rise to three germ layers, namely endoderm, mesoderm and ectoderm. Each of these germ layers later forms organs and tissues. This initial process of development is similar in both vertebrates and invertebrates, this similarity includes embryonic morphology and cellular behavior, conservation of many signaling pathways etc. For example, the hedgehog gene in the *Drosophila* that creates a banded pattern in embryo for a proper cell differentiation is found in mice and humans. Any defects in this pathway can lead to cancer. Studies in model organisms such as *C. elegans*, *Drosophila* and Zebrafish have given and are still providing a great deal of information on the role of genetics as well as the role of mechanical forces in developmental biology.

During tissue morphogenesis, cells can divide; cells can be detached from the tissue; cells can be fused, compressed or stretched by the neighboring cells and tissues. The cells are prone to changes in their shapes during these processes [Figure 1.1]. For instance, a morphogenetic process that occurs during gastrulation of *Drosophila* embryo is the ventral furrow formation. The ventral furrow internalizes the mesodermal precursor cells into the

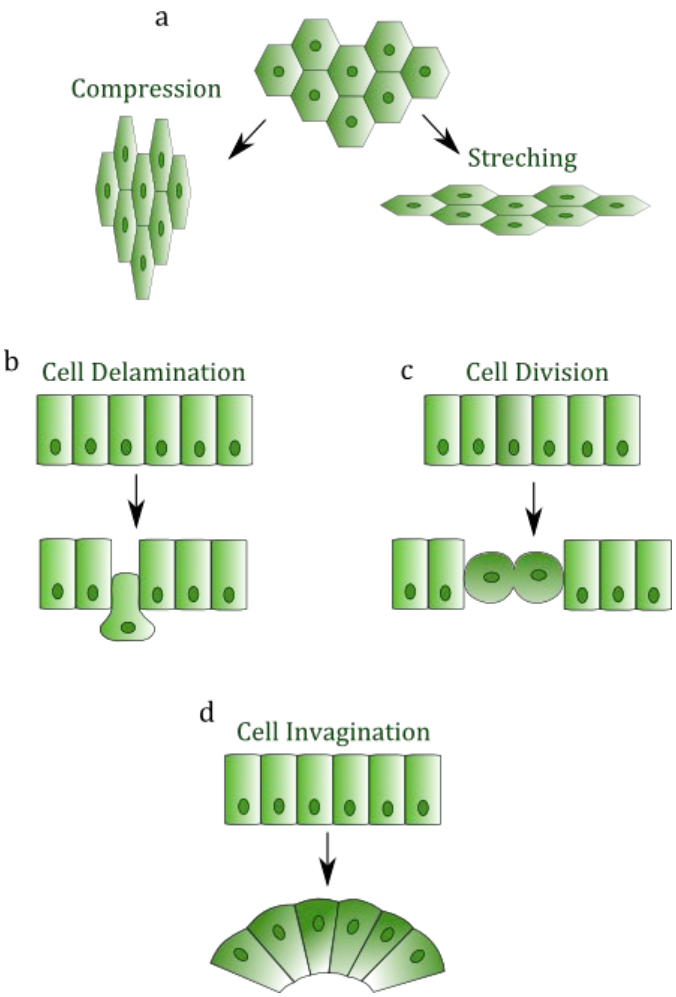

Figure 1.1: Cartoon depicting different morphogenetic processes

a) Shortening or elongation of the tissue by cell compression and stretching (top view). b) Cell number reduction through cell delamination. c) Cell proliferation through cell division d) Bending and folding of the tissue through cell invagination. (b-d side views).

embryo. The internalized cells will become the mesoderm. This process is associated with changes in cell shape. The columnar cells change their shape to trapezoidal in a single layer of epithelium (Sweeton et al., 1991) [Figure 1.2a]. Here cell shape change is a way to achieve the invagination.

Certain cells have a fixed shape, for example, Erythrocytes which maintain a biconcave shape

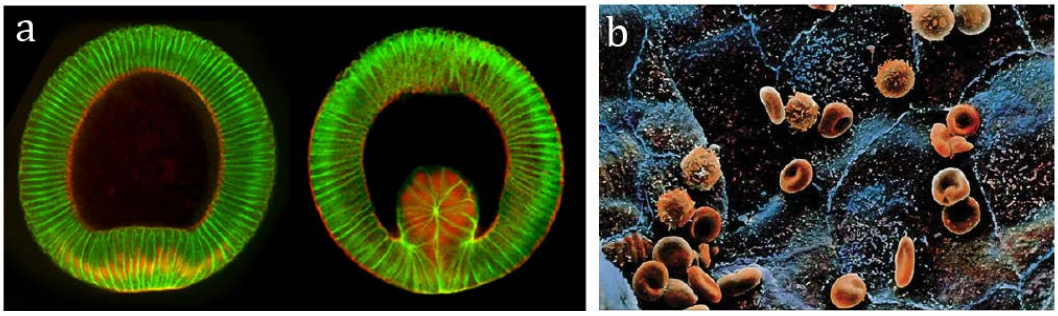

Figure 1.2: Cell shape changes and cell shape observed in development

a) Ventral furrow formation in Drosophila. Apical constriction by Myosin-II (in red, nucleus are also marked in red) drives cell shape change that internalizes the tissue leading to mesoderm invagination (*image: from http://www.hhmi.org, by Eric Wieschaus*). b) The biconcave shaped human red blood cells (*image: Encyclopedia Britannica*).

throughout their lifetime. Erythrocytes— *erythros* means red and *-cyte* means cell in Greek— commonly called red blood cells, are the vertebrate cellular component of blood that carry oxygen from lungs to the tissues [Figure 1.2b]. These cells lack a nucleus and are composed of hemoglobin — an iron rich protein that binds to oxygen. Their characteristic cell shape is crucial, as it allows oxygen exchange over the largest possible area. The deviation from the biconcave shape can lead to diseases in humans: oval-shaped cells cause pernicious anemia and crescent-shaped cells cause sickle cell anemia. In this case particular shape of a red blood cell is the desired outcome during the cell formation.

In this thesis, we address how two subcellular structures—non-muscle Myosin-II and adhesion protein N-cadherin— co-ordinate themselves, giving rise to different cell shapes. This chapter broadly covers the background for the thesis and the current understanding in subcellular structures, their physical properties and the methods used to observe and study them.

1.1.1 Cell shapes: a general view

When one thinks of cells, 'blob' like structures come to mind, in fact that is how we have studied them in our elementary school and that is how they look in cell cultures; for example

HeLa cells. But in living organisms, if we take ourselves as an example, human body has numerous cells with varied and intricate shapes [Figure 1.3a]. In the book "Mechanics of the Cell", the author David Boal suggests that the essay "Form follows function" published by the architect Louis Sullivan, holds true not just for buildings but also for living cells (Boal, 2012). The architect coined this phrase with the principle in mind that the shape of an object or a building must be based on its primary function. Cells in tissues seem to follow the same principle. The best example is nerve cells, they have a branched shape and a network like arrangement for better transmission of nerve signals and relay of information from brain to sensory organs, and back. The simple epithelial tissues, whose basic role is to act as a protection layer for the underlying organ or body, have various shapes according to where they are located and the specificity of the role they play [Figure 1.3b]. It is not a surprise that they are named according to their shape, we have for example, columnar or cuboidal epithelial tissues.

Cells in tissues come in various shapes and sizes but with a common architectural background. They have diverse shapes but the same basic structural elements such as a fluid like sheet with filamentous network underneath, with the cells connected to one another by adhesion proteins. The filamentous structure maintains the shape of cells by modulating itself depending on the surrounding environment and function of the cells (Chen et al., 1997; Keller, 2006). Some cells must be flexible and prone to large deformation (e.g. red blood cells), whereas some have to be rigid, capable of bearing external forces (e.g. plant cells). Some cells in tissues have to be intact, maintaining the same position and shape over time (e.g. neurons in brain), whereas some actively change shape moving past other cells in the tissues (e.g. macrophages).

Cells change shape, size and arrangement, sometimes attaching and sometimes detaching themselves from tissues over the course of the development of an organism (Kim et al., 2015; Levayer et al., 2016). Addressing the question of what dictates the whole geometry of the cell is quite complicated given the wide range of cell shapes. But looking at the cells in two-dimensions, two components have a great impact on their shape; actomyosin cortex and cadherin adhesion (Lecuit & Lenne, 2007).

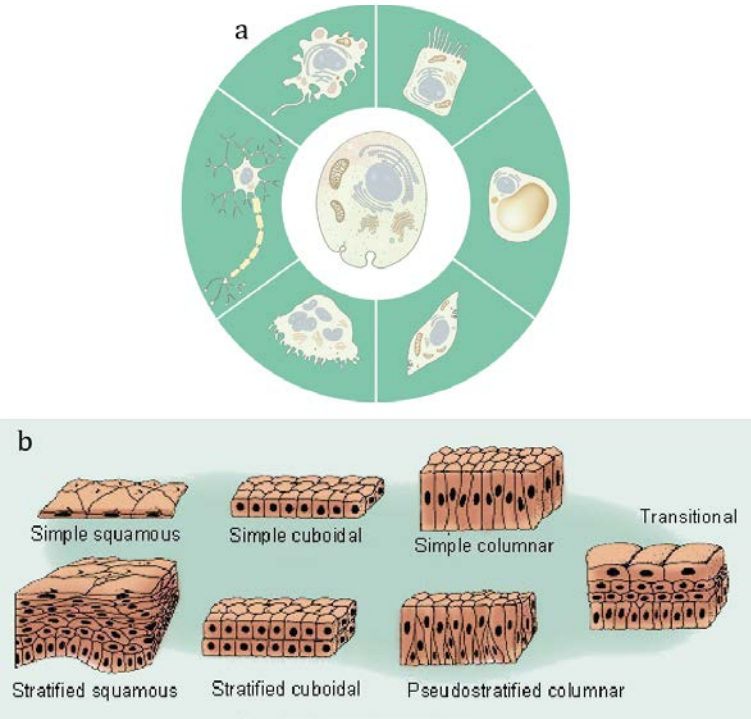

Figure 1.3: Diversity in cell shapes

a) Different cell shapes observed in human body: (from left clockwise) neuron, macrophage, intestine epithelial cell, adipocyte, muscle cell and osteoclast (*image: modified from MBInfo contributors. Compartmentalization in cells).* b) Different epithelial cells with different cell shapes (from top left clockwise) simple squamous, simple cuboidal, simple columnar, transitional, stratified squamous, stratified cuboidal, pseudostratified columnar epithelial tissues (*image: modified from Wikipedia-epithelial tissues)*.

As a simple example let us consider two spherical cells, when they are in contact, the cadherins provide adhesion. The property of cadherins is such that they tend to increase the cell contact (de Vries et al., 2004), but cells have actomyosin cortex underneath the plasma membrane whose tensile force decreases the contact between cells (Rauzi, Lenne, & Lecuit, 2010) [Figure 1.4a]. Depending on the contact tension generated as a result of these two conflicting forces, the cell contact will have a shorter junction or a longer junction (Maître & Heisenberg, 2011). This changes the overall shape of cells which can be noted by the differences in the contact angle, along with the length of cell contact. A tensed junction will have a more acute angle with a shorter junction, and a relaxed junction will have a more

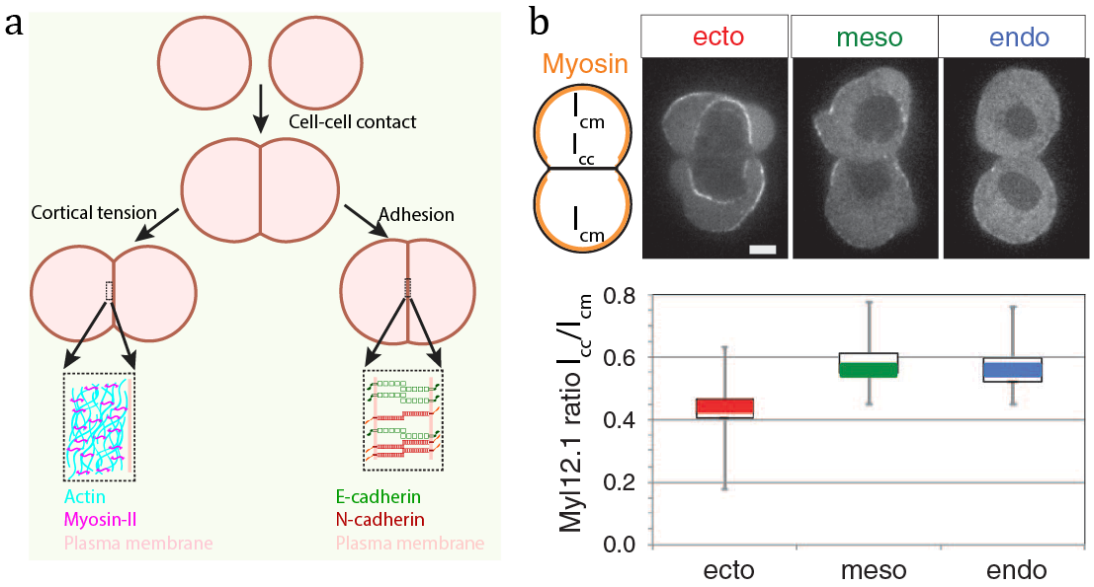

Figure 1.4: Shape of two cells in contact

a) Cartoon of two separate cells forming cell contact by adhesion. At the cell contact when the cortical tension due to actomyosin [zoomed out inset] dominates, cells have shorter contact with larger acute angle of contact (left). When the adhesion by cadherins (zoomed out inset) dominates, cells have longer contact with larger obtuse angle of contact (right). b) The doublets from *zebrafish* ectoderm, mesoderm and endoderm cells with graph showing the Myosin-II intensity ratio. Ectoderm cells have longer cell contact with lower value for the Myosin-II intensity ratio, suggesting that Myosin-II concentration determines the doublets shape (*image: adapted from Maître et al, 2012*).

obtuse angle with a longer junction. In the doublet experiments by Maître et al. (Maître et al., 2012) on ectoderm, mesoderm and endoderm cells from *Zebrafish* embryo, they have shown that Myosin-II generated tension has a major effect on the shapes of the doublet as compared to the adhesion by cadherins [Figure 1.4b]. It is unknown as to how the cell shapes in 2D, *in vivo*, are maintained by cadherins and Myosin-II.

1.1.2 Myosin-II

Cells can change shape autonomously with the help of their contractile actomyosin networks. The actomyosin network, as the name suggests, is composed of actin filaments and Myosin-II motors. The actin network is a highly organized structure that is linked with the plasma membrane (Clark, Dierkes, & Paluch, 2013). It is composed of actin monomers, which

assemble and dis-assemble to form actin filaments (Pollard & Cooper, 2009). These actin filaments form branched or unbranched networks with the help of cross-linker proteins like Arp2/3 and Formin (Pollard, 2007). This network is highly dynamic, it is elastic at a timescale shorter than the actin filaments turnover time. Upon applying force, it resists the deformation and restores its initial configuration once the force is released. It is viscous on a timescale on which the actin network is undergoing remodeling. Upon applying a slow stress, it flows like a fluid and takes a new form once the force is released. Hence the actin network is viscoelastic in nature (Bray & White, 1988; Forgacs et al., 1998; Salbreux, Charras, & Paluch, 2012).

Actomyosin network is active in the sense that, Myosin-II motors exert forces on the actin filaments, creating active tension in the system. Myosin-II motors have been shown to reduce the viscosity by sliding on actin filaments (Le Goff et al., 2002). In softer actin networks, Myosin-II motors have been shown to increase the network stiffness, by pulling on actin filaments (Koenderink et al., 2009). Actomyosin at the cell cortex generates, transmits and endures the forces by modulating itself spatially and temporally. Its precise control of stiffness maintains the cell shape and generates cell shape changes.

Myosin-II (non-muscle myosin) is a hexamer of two heavy chains, two essential light chains and two regulatory light chains. The heavy chains bind to the actin [Figure 1.5a]. In *Drosophila,* myosin heavy chain is encoded by Zipper (zip), essential light chain is encoded by myosin light chain cytoplasmic (Mlc-c) and the regulatory light chain is encoded by spaghetti squash (Sqh). The phosphorylation of the regulatory light chain activates Myosin-II (MyoII) (Betapudi, 2014). Tail-to-tail association of MyoII hexamers generate force by pulling on actin filaments [Figure 1.5b]. Sliding of MyoII on actin requires energy and is provided by hydrolysis of ATP. The major role of MyoII is the generation of tension, but the tension itself can promote the recruitment of MyoII and the stabilization of junctions in *Drosophila* embryos. Tension plays the role of a positive feedback component (Fernandez-Gonzalez et al., 2009). Three non-muscle MyoII (A, B and C) are present in vertebrates, whereas only one MyoII is found in *Drosophila* and *C. elegans.*

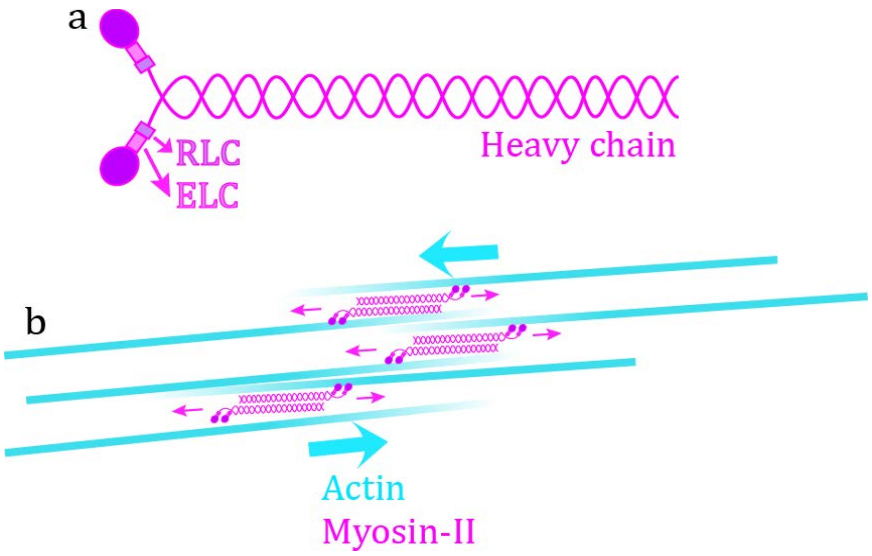

Figure 1.5: Myosin-II, and Myosin-II generated tension

a) Single Myosin-II hexamer in open conformation containing two regulatory light chain (RLC), two essential light chain (ELC) and two heavy chains. b) Myosin-II motors (in magenta) on actin filaments (in cyan), the Myosin-II motors pull on the actin filaments generating active tension in the actin filaments.

Actomyosin regulates numerous morphogenetic processes. Along with hydrostatic pressure, actomyosin cortex drives cell rounding during mitotic division (Stewart et al., 2011). During cytokinesis, MyoII forms contractile ring which pinches the dividing cell at the center and aids in the formation of a new contact (Guillot & Lecuit, 2013; Uehara et al., 2010). MyoII is involved in the fundamental part of morphogenesis, such as tissue separation, where two populations of cell types are physically separated by a MyoII boundary, for example the compartment boundary of wing disc (Major & Irvine, 2006). An actomyosin boundary is formed at the interface between normal and aberrant cells that induces elimination by apoptosis or formation of a cyst (Bielmeier et al., 2016). MyoII generated contractility provides a force to fold the wing disc by an angle of 90^{o} during the metamorphosis of *Drosophila* wing (Aldaz, Escudero, & Freeman, 2013). *Drosophila* tracheal tube formation is initiated by MyoII driven invagination of a group of cells (Brodu & Casanova, 2006). Salivary gland formation in *Drosophila* is driven by MyoII contractile cable around Placode cells (Röper, 2012).

To overcome tissue crowding, live-cell delamination occurs in *Drosophila* notum through junctional and apical MyoII accumulation (Marinari et al., 2012). In eye imaginal disc, morphogenetic furrow is characterized by MyoII apical constriction of cells, followed by photoreceptor cluster formation. MyoII has a distinct expression pattern around the clusters as they mature and reduction in MyoII leads to cluster defects (Escudero, Bischoff, & Freeman, 2007). In a neuroblast, ingression is a process in which a single cell moves inside the *Drosophila* embryo and undergoes division to form neurons. The ingression process is driven by MyoII (Simões et al., 2017).

The amount of MyoII motors present is important because it gives an idea about the force generated in the system or the anisotropy in the forces. During mesoderm invagination, apical constriction of cells is mediated by apical accumulation of MyoII (Martin, Kaschube, & Wieschaus, 2009). In *C.elegans*, the asymmetric cell division of two daughter cells is formed by unbalanced MyoII driven cortex contraction in the dividing cells (Mayer et al., 2010). In *Drosophila* germ band elongation, the T1 transition is mediated by asymmetric localization of MyoII (Bertet, Sulak, & Lecuit, 2004) providing anisotropic force (Rauzi et al., 2008). Actomyosin contractions at the poles of dividing cells cause cell shape instabilities, which sometimes affect cell division (Sedzinski et al., 2011). Hence MyoII is a crucial component in any cellular process, and a good candidate for cell shape studies.

1.1.3 Cadherins: E-cadherin and N-cadherin

Cells are polarized, which means that there is an intrinsic asymmetry in the structure and organization of cellular components. Epithelial cells have apical-basal polarity, that facilitates the differential distribution of cytoskeleton components, protein complexes etc. The membrane facing the lumen or free surface is referred to as apical membrane and the membrane that is away from the lumen is the basal membrane. The epithelial tissue forms a continuous sheet of cells through cell-cell adhesion. Cells make contact through different types of junctions, namely tight junctions (TJ), adherens junctions (AJ) and desmosomes (Des). In vertebrates, at lateral cell-cell contacts, tight junction (TJ) is located more apically followed by adherens junction and desmosome [Figure 1.6a]. Invertebrates do not have a

tight junction and desmosome, they have an adherens junction and a septate junction (SJ) [Figure 1.6a']. Hence AJs are observed in all multicellular animals as an adhesion complex. In both *Drosophila* and vertebrates, studies have shown that cadherins are the main components of the adherens junctions. They are transmembrane proteins with three parts: an extracellular part, a transmembrane part and a cytoplasmic part.

The extracellular part generally has repeated units of extracellular domains (ECs), each of the EC domains is composed of approximately 110 amino acid sequences. The EC domain is involved in the adhesion process. The cytoplasmic part binds to p120-catenin and β-catenin. P120-catenin is required for the stabilization of the cadherins at the cell membrane; cadherins are internalized through endocytosis in absence of p120-catenin (Davis, Ireton, & Reynolds, 2003), and β-catenin connects the cadherins to actomyosin network through α-catenin [Figures 1.6b, c]. Cells lacking the cytoplasmic parts cannot make a successful cell-cell contact (Nagafuchi & Takeichi, 1988). The subgroup of cadherins superfamily, with this conserved binding capability to p120-catenin and β-catenin, is classified as classical cadherins, irrespective of their EC domain organization. The other subgroups of cadherins superfamily are desmosomal cadherins, protocadherin, fat & dachsous cadherin, etc.

Taken together, AJs can be viewed as the cell junctional structures maintained by classical cadherin and catenin complexes together with the actomyosin network. Classical cadherins are responsible for adhesion in AJs. The similarity between the vertebrates and D*rosophila* classical cadherins is that they have conserved the cytoplasmic part but they differ in the extracellular part.

Vertebrate classical cadherins were first discovered as Ca^{2+}-dependent, homophilic adhesion molecules. Removal of Ca^{2+} from the cells in cell culture leads to the disruption of adhesion (Volk & Geiger, 1986). These cadherins consist of five EC domains in their extracellular region. There are approximately twenty mammalian classical cadherins, with all of them having five EC domains [Figure 1.6b]. They are further classified into type I and type II cadherins. The type I cadherins include E-cadherin, N-cadherin, R-cadherin, P-cadherin etc., and they have a major role in the maintenance of AJs. They were named after the tissues where they were first found: epithelial, neural, retinal and placental tissues. Their presence

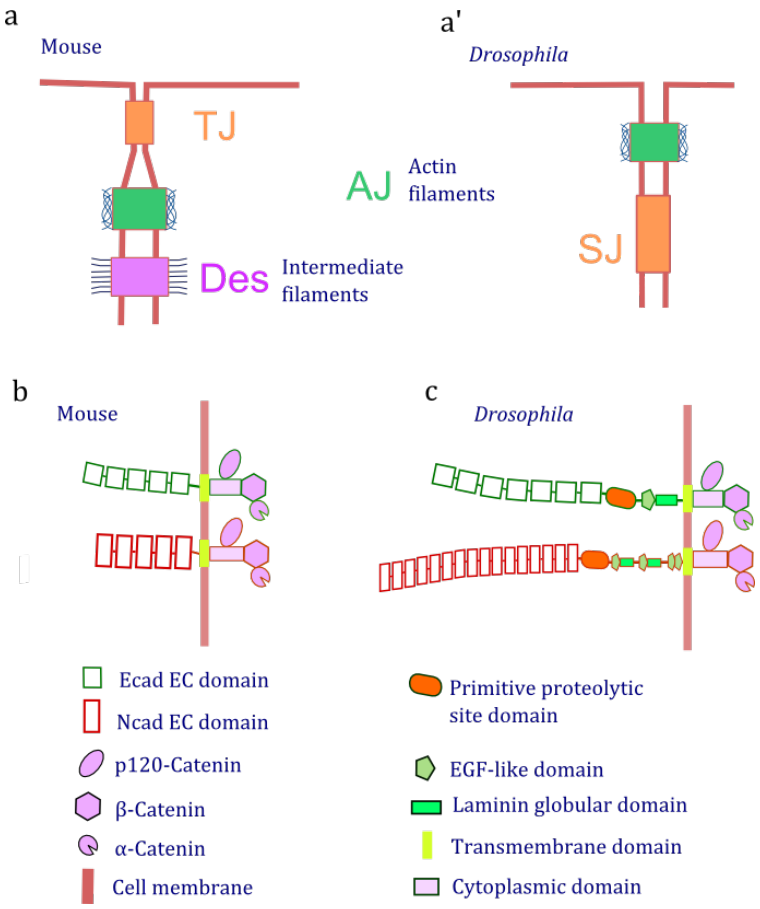

Figure 1.6: Vertebrate and invertebrate cell-cell contacts

a-a') Junctional components found in mouse and Drosophila epithelial cells; tight junction (TJ), adherens junction (AJ), desmosome (Des), septate junction (SJ). b) Structure of E-cadherin (in green) and N-cadherin (in red) in a mouse with catenin complexes. c) Structure of *D*E-cadherin (in green) and *D*N-cadherin (in red) in *Drosophila* with catenin complexes and other components. Both vertebrate and invertebrate classical cadherins have three different domains, extracellular domain (EC), and transmembrane domain in the plasma membrane (in light pink), and the cytoplasmic domain that binds to catenin complexes (*image: adapted from Oda and Takeichi, 2011).*

is not necessarily restricted to any particular tissue or organ. The type II cadherins include cadherin-5, -6, -7, etc. There is likely to be some difference in the functions between these subclasses, for example, it has been shown that the force required to separate cells with type

I cadherin (E-cadherin) mediated adhesion is much higher than the type II (cadherin-7) mediated adhesion (Chu et al., 2006). Also, cells expressing type I cadherin (N-cadherin) are less motile than cells transected with type II (cadherin-7) (Dufour et al., 1999).

*D*E-cadherin is the first invertebrate classical cadherin discovered in *Drosophila*, its extracellular domain is different in comparison to its vertebrate counterpart. Vertebrate E-cadherin has five EC domains, whereas *D*E-cadherin has seven EC domains [Figures 1.6b, c]. The other difference is that they have a primitive classical cadherin proteolytic site domain (PCPS), an EGF- like domain (EGF) and a laminin globular domain (LmG) in between their EC domain and transmembrane domain (Oda & Tsukita, 1999) [Figure 1.6c]. For the formation of epithelial AJs, *D*E-cadherin is absolutely necessary. Mutations in DE-cadherin lead to failure in cell arrangement during embryogenesis and oogenesis (Wang et al., 2004).

Drosophila has two other genes that encode two more classical cadherins, they are *D*N-cadherin and CadN2. *D*N-cadherin is much bigger than *DE*-cadherin, as it contains sixteen EC domains, a PCPA, four EGF-like domains and two LmGs [Figure 1.6c]. *D*N-cadherin is expressed in mesodermal and neural tissues, and is essential for neural development and synaptic connection, similar to vertebrate N-cadherin. Mutation in *D*N-cadherin is embryonic lethal or causes defects in axon patterning and growth cones in adults (Yagi & Takeichi, 2000). CadN2 has only six EC domains and it seems that it is not involved in adhesion (Yonekura et al., 2007).

C. elegans has two classical cadherins derived from a single gene, HMR-1A and HMR-1B. HMR-1A has two EC domains whereas HMR-1B has fourteen EC domains. HMR-1A is comparable to *Drosophila* E-cadherin as it is required for early morphogenetic processes (example: ventral epithelial closure), but embryos are able to develop through gastrulation (Broadbent & Pettitt, 2002). HMR-1B is comparable to *Drosophila* N-cadherin in structure and function, as it is required for the motor neuron axon growth. From now on in this thesis there is no distinct naming for *Drosophila* or vertebrate cadherins; they are simply referred to as Ecad/Ncad.

Extracellular domain of Ecad has been shown to form two types of interactions to create

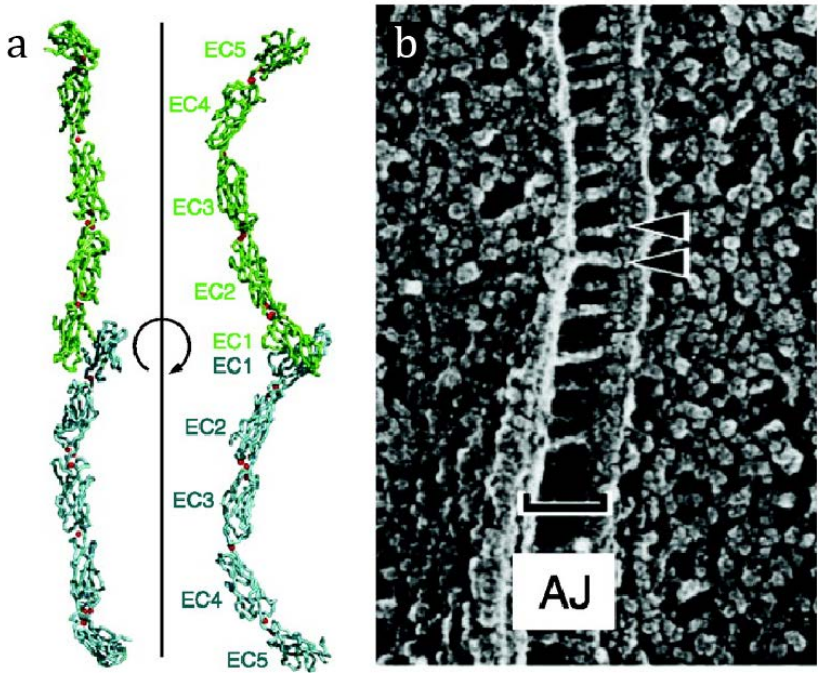

Figure 1.7: Cadherins interaction at cell contact

a) Crystal structures of C-cadherin with *trans*-interaction *(Shapiro et al., 2007).* b) Electron microscopy image of an intestinal adherens junction, arrows point at the sparsely placed rodlike structures in the extracellular space *(Hirokawa & Heuser, 1981)* (*image: taken from Hirano & Takeichi, 2012)*.

adhesion. *Trans*-interaction involves Ecad molecules from neighboring cells interacting [Figure 1.7a], and *cis*-interaction involves Ecad molecules from the same cell interacting (Harrison et al., 2010, 2011). These *trans*- and *cis*-adhesion bonds together form clusters resulting in a stronger adhesion. The unbinding force of a single adhesion bond (VE-cadherin) using atomic force microscopy has been shown to be weaker but upon increasing the contact time, VE-cadherin has been shown to form complexes that increase the binding strength (Baumgartner et al., 2000).

Cadherins generally make homophilic interactions in a concentration dependent manner, for example, cells with Ecad preferentially make links to cells with Ecad, also cells with high Ecad form adhesion with cells having high Ecad against cells with low Ecad level (Friedlander et al., 1989; Steinberg, And, & Takeichit, 1994). This is the basis for many sorting processes, in

Drosophila egg chamber the oocyte is positioned depending on the Ecad levels in Nurse cells and Border cells (Godt & Tepass, 1998). In cell culture, the mouse Ncad expressing cells sort out from the mouse Ecad expressing cells (Shan et al., 2000). These suggest that cadherin bonds depend on cadherin type and cadherin concentration, which is to say that they make homotypic contacts.

There are instances where Ecad and Ncad interact to form heterotypic contacts. For example, cultured cells containing L-CAM (Ecad) and A-CAM (Ncad) form epithelial sheets with cell

contacts between A-CAM and L-CAM on solid substrate (Volk, Cohen, & Geiger, 1987). Whereas in *Drosophila* eye, cone cells which generally express both Ecad and Ncad detach themselves from surrounding primary pigment cells when they lack Ecad (Hayashi & Carthew, 2004). This shows that there is no heterotypic contact between these two cadherins in this model.

In *Drosophila*, Ecad is expressed early in all adherens junctions, later it is downregulated and replaced with Ncad in newly formed mesoderm and neural tissues. This switch of cadherins is necessary for transition of immobile epithelial cells to migrating mesenchymal cells, for example in neural tube formation in chick embryo (Pla et al., 2001). However, there are cases in which Ecad is involved in cell movement. In *Drosophila* oocyte, initially both Ecad and Ncad are expressed, as the border cell movement initiates, Ncad disappears (Tanentzapf et al., 2000) and removal of Ecad from border cells blocks its movement (Niewiadomska, Godt, & Tepass, 1999). During retinal morphogenesis in eye imaginal disc, both Ecad and Ncad are expressed at the cell contacts between photoreceptors. These photoreceptor clusters undergo rotation, here Ecad is a positive regulator of rotation, loss of Ecad leads to under-rotation of clusters (Mirkovic & Mlodzik, 2006). These conflicting and varied results show that the role of the cadherins depends on the tissue and organism in which they are being expressed, and also the conditions in which the studies are done—*in vivo or in vitro*.

Ncad is a very good example of the versatile role of cadherins. Ncad was discovered for the first time in chick neural retina, and their primary function is in axonal growth and to aid in synapse formation. It has been shown that in squamous epithelium, Ncad changes the cell morphology and epithelial to mesenchymal tissue transition, along with replacement of Ecad

at the cell contacts (Islam et al., 1996). In human breast epithelial tissue, Ncad induces cell motility without change in Ecad expression and cell morphology (Nieman et al., 1999), showing that there is a direct role of Ncad in cell motility. This property is quite different from adhesion, suggesting that Ncad does not just act as an adhesion protein. Here, it has been shown that the extracellular part of Ncad is responsible for the invasive nature of cancerous cells, in particular the 69-amino acid in the EC domain. An antibody recognizing this amino acid inhibited the cell motility behavior without affecting the cell morphology, suggesting that these two phenomena are independent of each other. Invasive property of Ncad and adhesive property of Ncad are two separate features (Kim et al., 2000) (see also review by Derycke & Bracke, 2004). Similarly, during *Drosophila* eye development the extracellular part of Ncad is essential for the photoreceptor R7 target selection and the cytoplasmic part of Ncad is essential to maintain the growth cone morphology (Yonekura, Xu, Ting, & Lee, 2007).

Ncads are mainly studied in the context of cancer due to the upregulation of Ncad along with the downregulation of Ecad during metastasis. There are instances in mouse osteosarcoma, where Ncad suppresses the cell motility (Kashima et al., 2003) (see also review by Derycke & Bracke, 2004). Taken together, these studies show that it is possible that Ncad does not behave in the same way in all tissues. These studies also point out that the obvious focus is on its infamous role in metastasis, but not much on its native adhesion nature, especially *in vivo*.

1.1.4 Interplay between Actomyosin and Cadherins

At the adherens junction, the extracellular part of the cadherins makes Ca^{2+}-dependent adhesion. The cytoplasmic part of the cadherins inside the cells are connected to actomyosin cytoskeleton through cytoplasmic binding partners such as α-catenin, β-catenin and p120 catenin [Figure 1.8a]. This complex is commonly referred to as the cadherin-catenin complex and it plays a role in mechano-transduction. Disruption of actomyosin integrity by drugs or genetic perturbation affects cell adhesion in cell cultures (Niessen, Leckband, & Yap, 2011). The cells that lack the catenin complex display poor adhesion, and their presence provides

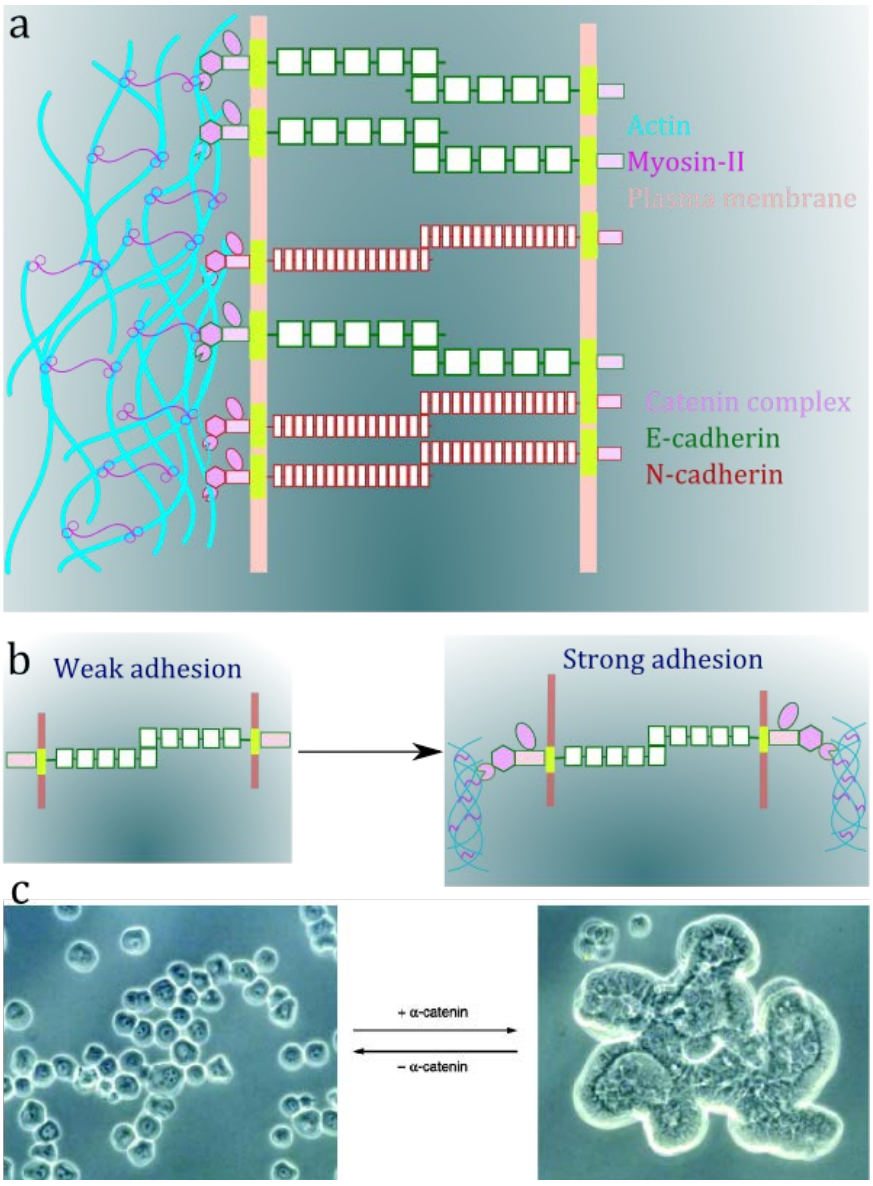

Figure 1.8: Cadherin linked with actomyosin via catenin complex

a) E-cadherin (in green) and N-cadherin (in red) undergo homophilic interaction with the neighboring cell cadherin molecules, and internally through catenin complexes (β-cat, α-cat and p120, in pink)—together called cadherin-catenin complex—binds to actomyosin (Myosin-II in magenta and actin in cyan) in the cell cytoplasm, cell plasma membrane is in beige. b) Schematics of strengthening of adhesion bond through catenin complexes that link cadherins to actomyosin. c) Images of lung carcinoma PC9 cells that normally lack α-catenin show weak adhesion (left) and when α-catenin is introduced, show strong adhesion between cells the changes that overall architecture of a group of cells.

strong adhesion between cells [Figure 1.8b, c] (Hirano & Takeichi, 2012).

MyoII has been shown to be crucial for Ecad localization at cell contacts of cell cultures. Activation of MyoII requires Ecad hemophilic adhesion (Shewan et al., 2005) in cultured cells transfected with human Ecad. These cells fail to concentrate Ecad at cell contacts and form adhesive bonds when treated with blebbistatin (an inhibitor of MyoII). Cell doublets suspended in non-adhesive microwell showed anisotropy of Ecad recruitment correlating with the MyoII gradient at the cell contact. This anisotropy in contractility produces deformation of the doublet (Engl et al., 2014). These results show that there is a close relationship between Ecad and MyoII.

Cadherins and actomyosin coordinate in many processes of morphogenesis. During ventral furrow formation in *Drosophila* gastrulation, pulsatile actomyosin network moves the Ecad adherens junction from subapical to apical. As the apical constriction proceeds, the MyoII clusters pull the Ecad junction inward transiently (Martin, Kaschube, & Wieschaus, 2009). Actomyosin provides stability and acts as a scaffolding for Ecad adhesion, Ecad lacking cytoplasmic part cannot form adhesion (Takeichi, 1991), suggesting that there is a direct interaction between the two. During cell division, Ecad anchored to the cytokinetic actomyosin ring, pulls it towards the apical plane, and detaches just before the new contact is formed between daughter cells (Guillot & Lecuit, 2013). Adhesion tension and actomyosin generated tension are thought to maintain the packing of epithelial cells in *Drosophila* wing disc (Farhadifar et al., 2007).

Cadherin-FRET sensor measurements in MDCK cells has shown that, at a cell-cell contact, Ecad is under actomyosin generated tension, which increases when cells are stretched (Borghi et al., 2012). Similar results are observed *in vivo*, the border cell movement in *Drosophila* ovary depends on differential expression of Ecad between nurse cell, border cell and pole cell. The Ecad at the leading border cells have low FRET as compared to their rear counterparts (Cai et al., 2014). Ecad recruits reinforcements in a force dependent way; upon stretching, α-catenin opens up, providing a binding site for vinculin, and vinculin further connects to actomyosin (Yao et al., 2014). There is mechanical coupling between Ecad and actomyosin to maintain the epithelial integrity.

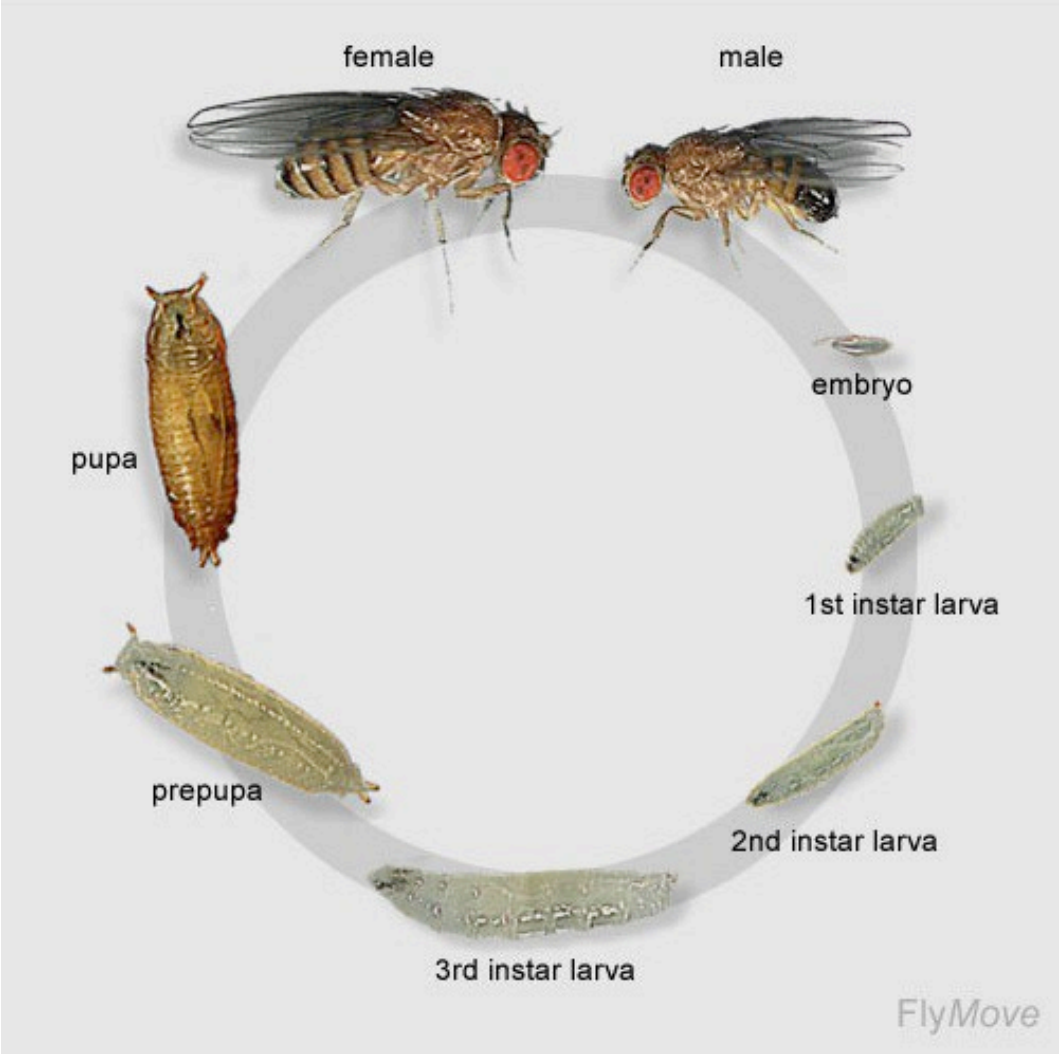

Figure 1.9: Life cycle of *Drosophila melanogaster*

Female *Drosophila* lays around 40 eggs at a time, the embryos undergo morphogenesis and form larvae that hatch into first instar larvae 12-15 hours after egg laying. They then undergo two molts into second instar and third instar larvae. After the larvae have grown in size, they stop moving (prepupa) and form puparium. Later they undergo metamorphosis into adult flies *(image: from FlyMove: http://flymove.uni-muenster.de/Homepage.html).*

In *C.elegans,* the single celled zygote that lacks any intercellular adhesion has cadherin clusters. These non-junctional cadherin clusters are associated with cortical actin and are involved in retrograde flow of actomyosin cortex. It has been shown that non-junctional cadherin negatively regulates MyoII at the cortex (Padmanabhan, Ong, & Zaidel-Bar, 2017).

Increase in non-junctional cadherin affects the first division of the zygote. This study reveals the adhesion-independent role of cadherins and its association with actomyosin.

Even though there is a close coupling between cadherin and actomyosin, their local property is quite opposite of each other. At the contact between cells, cadherins increase the contact length and are thought to produce negative cell contact tension whereas actomyosin decreases the contact length, and produces positive tension at the cell contact. This quite opposing yet connected linkage makes them interesting. There are many instances where one has an impact on the other, but it is still poorly understood.

1.2 Model organism: *Drosophila melanogaster*

Drosophila melanogaster, or commonly called fruit fly, was used by Thomas Hunt Morgan more than a century ago, and this started the era of genetics (Kenney & Borisy, 2009; Morgan, 1910). *Drosophila* is not just used in the study of genetics, but also in other studies such as memory and learning, mechanisms of diseases and mechanical forces in biology. They are fast breeding, easy to handle, cost effective and have a vast community of users, which has made them an efficient model organism in biology. Every life stage of *Drosophila,* from egg to embryo to adult fly is used in the process of scientific research [Figure 1.9].

Development of the fly is temperature dependent, it takes over 50days at 12°C, 19 days at 18°C and 8.5 days at the ideal temperature 25°C. At 25°C, the egg hatches at 12-15 hours after egg laying (AEL). Larvae develops for about four days undergoing two molts, once at 24 hours after hatching into second instar, and again at 48 hours after hatching into third instar. During this time they feed and grow in size. Later the larva forms puparium (the outer cuticle that forms during pupal stage), undergoes metamorphosis, and the adult fly ecloses four days after puparium formation (APF) [Figure 1.9].

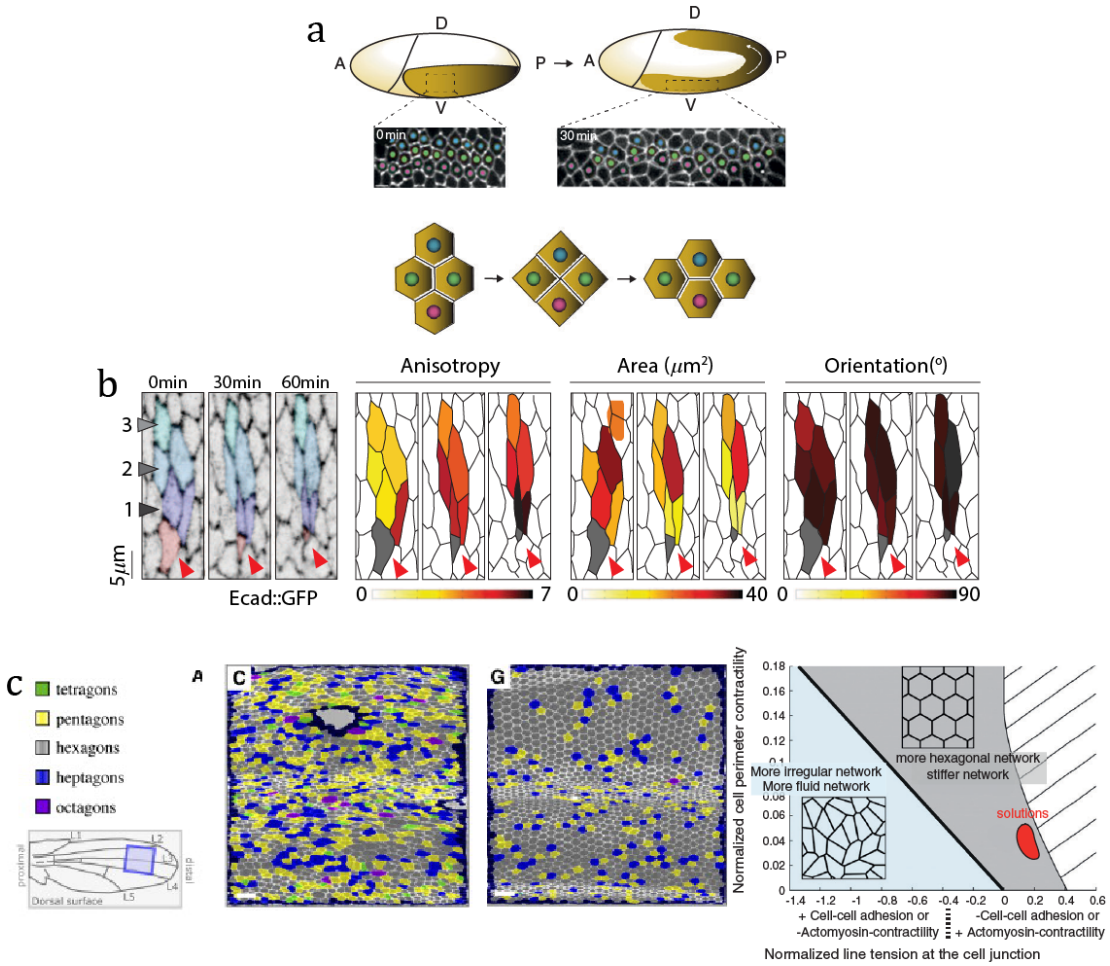

Figure 1.10: Cell shape changes during *Drosophila* morphogenetic processes

a) During germ band elongation in *Drosophila* gastrulation, the tissue elongates by T1 transition. Green cells lose contact by the shrinkage of a vertical junction to form a four-way vertex and the new junction forms between blue and red cells (*image: Rauzi and Lenne, 2011).* b) Passive cell shape change in *Drosophila* leg disc epithelium by cell apoptosis. Apoptotic cell (marked by red arrow) pulls the neighboring cells, which change their shape (anisotropy, area and orientation) and this process generates folds in the tissue (*image: modified from Monier et al., 2015)*. c) Cells in wing disc epithelium (at the pupal stage) change their shape by themselves from disordered to ordered hexagonal cells. The graph shows the dependence of the shape of the cell packing on actomyosin and cell-cell adhesion (image*: modified from Classen et al., 2005; Farhadifar et al., 2007*).

1.2.1 Examples of cell shape changes during *Drosophila* morphogenetic processes

Many studies have shown the role of mechanical forces in embryogenesis, morphogenesis and tissue patterning (Lecuit, Lenne, & Munro, 2011; Munjal & Lecuit, 2014; Rauzi & Lenne,

2011). It is now well accepted in the field of developmental biology that mechanical forces generated by living cells are as important as genetic and chemical signals for the development of an organism. Many examples of *in vivo* studies on the role of physical forces in the development of *Drosophila* can be found in the literature (Hutson et al., 2003; Kiehart et al., 2000; Rauzi et al., 2008). A few studies on cell shape and cell shape changes that are generated by actomyosin contractility and adhesion in *Drosophila* epithelium are discussed below.

Cell intercalation (or T1 transition) is one of the processes that drives tissue elongation. This is a cell rearrangement process during which cells exchange neighbors resulting in an extension of tissue. Germ band extension in *Drosophila* embryo is one of the examples of intercalating cells. Intercalating cells remodel their junction by shrinking the vertical junction, forming a four-way vertex and extending in the horizontal direction, thus creating a new junction [Figure 1.10a]. It has been shown that during this process, MyoII is enriched in the vertical junction and it is necessary for junction remodeling (Bertet, Sulak, & Lecuit, 2004). This MyoII enriched junction generates tension anisotropy which is revealed by laser ablation experiments (Rauzi, Verant, Lecuit, & Lenne, 2008). Ecad distribution is complementary to MyoII distribution and it is maintained by Ecad endocytosis (Levayer, Pelissier-Monier, & Lecuit, 2011). Endocytosis of Ecad at the vertical junctions fluctuate from 'left' and 'right' vertical junctions. These polarized, fluctuating Ecad complexes set medial actomyosin pulling forces on the junctions (Levayer & Lecuit, 2013).

Cell shape changes can be passive, an active process that changes the neighboring cells shapes to create tissue folding is apoptosis (Monier et al., 2015). Apoptosis is the controlled cell death that occurs in multicellular organisms. In *Drosophila* leg epithelium morphogenesis, apoptosis induces tissue tension increase that pulls the neighboring cell, creating folds. Monier et al., showed that dying cells accumulate Ecad below their apical surfaces that coincide with the fold. This Ecad accumulation is generated by apico-basal MyoII cable. The neighboring cells are pulled as a result, and elongate in the direction of the fold, thus decreasing their apical area [Figure 1.10b]. This generates a ring of stretched cells in the tissue where apoptosis takes place.

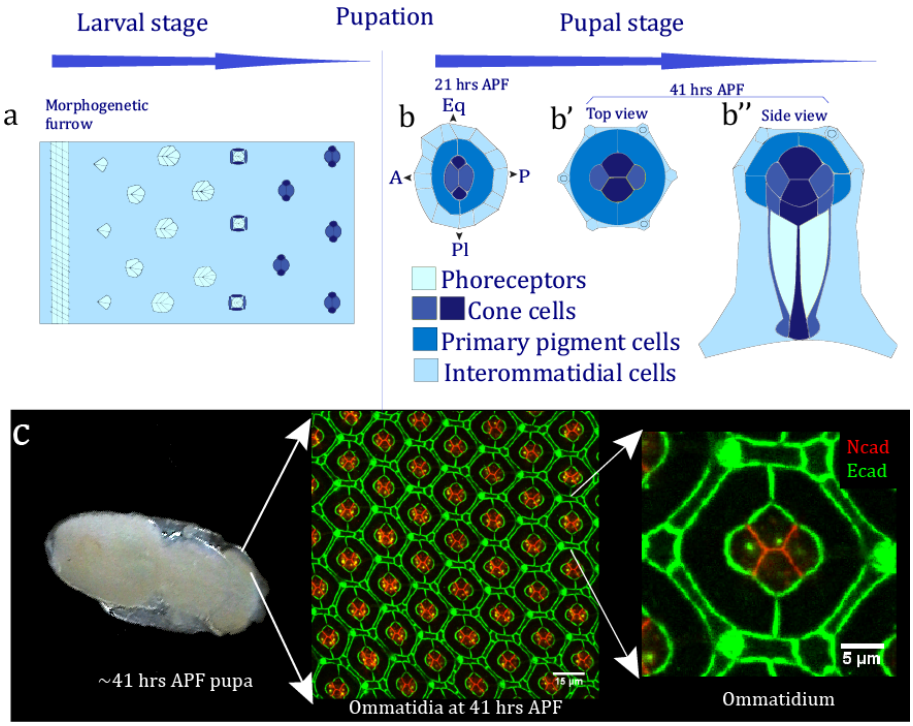

Figure 1.11: Retinal morphogenesis

a) Cartoon of a part of an eye imaginal disc with morphogenetic furrow and photoreceptor cluster formation b-b'') Cartoons of ommatidium structure during pupal stage, at 21 hours APF (b) the anterior (A) and posterior (P) cone cells are in contact, 41hours APF- top view (b') the polar (Pl) and equatorial (Eq) cells are in contact, side view (b'') cone cells form the floor and roof of the photoreceptors. c) A pupa around 41 hrs APF with its puparium removed *(image: http://www.devbio.net)*, image of ommatidia at 41 hrs APF (scale bar 15 µm) with zoomed-in image of an ommatidium (scale bar 5µm).

Drosophila wing disc epithelium is the model system that is often used to study tissue growth, cell packing and geometry. Cells in the wing disc arrange themselves from a disordered state to ordered hexagonal cells shortly before the hair formation [Figure 1.10c] (Classen et al., 2005). Farhadifar et al. enquired as to how the cell-generated physical forces influence cell packing geometry in the wing disc of third instar larvae. They showed that the wing disc with a stable and stationary cell configuration is maintained by junctional level forces from actomyosin generated contractility and adhesion by cadherins, as well as cell level forces such as elasticity by treating actomyosin as an elastic ring. With the help of laser ablation and *in silico* predictions, they were able to obtain different regimes of cell packing

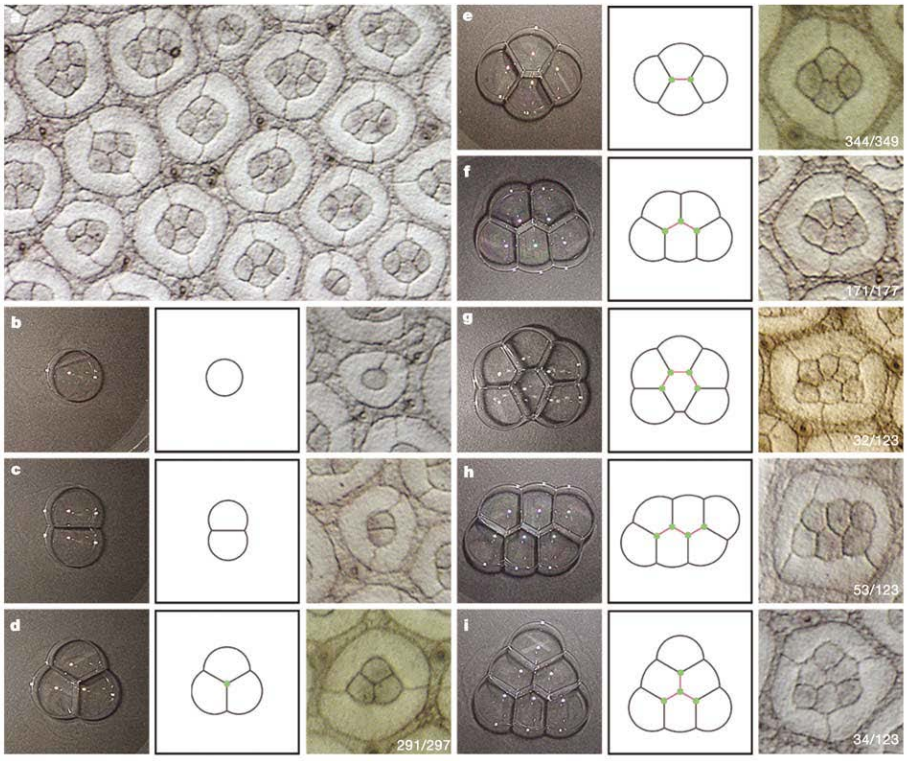

Figure 1.12: Cone cell arrangements matching the soap bubble arrangements

Rough eye (ROI) mutants with less or more number of cone cells than in the wildtype. Cone cell shapes and arrangements precisely correlate with shapes and arrangements of soap bubbles, for six soap bubbles three arrangements are possible and all these arrangements are observed among cone cells (the last three comparisons) *(image: Hayashi & Carthew, 2004).*

(either fluid like or stiffer elastic) depending on which force dominates (adhesion by cadherins or actomyosin contractility) [Figure 1.10c] (Farhadifar et al., 2007).

1.2.2 Ommatidia: a model system to study cell shape

The *Drosophila* compound eye is composed of a lattice like structure, with repetitive units called ommatidia. There are around 800 ommatidia in a single eye. Each ommatidium has eight photoreceptor cells, four cone cells (CCs) and two primary pigment cells. The inter ommatidial cells (IOCs) are shared between neighboring ommatidia. There are six secondary

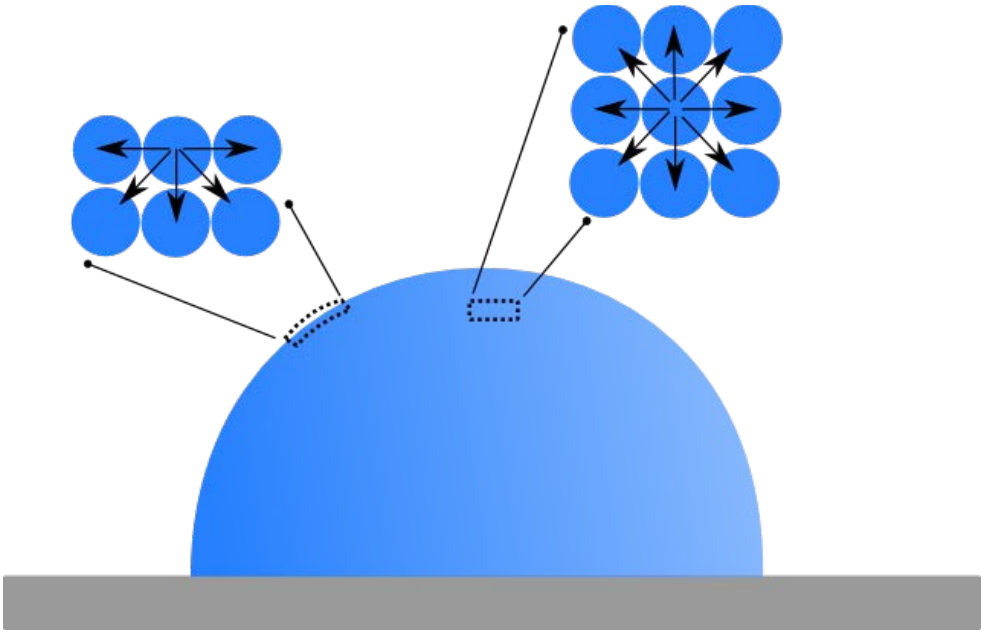

Figure 1.13: Cartoon explaining surface tension

A water molecule on the surface of a water droplet has unbalanced forces whereas a water molecule inside the droplet has balanced forces with net force equal to zero.

pigment cells, three tertiary pigment cells and three mechanosensory hair cells called bristles. An ommatidium has a complex structure, four cone cells form the floor and roof of eight precisely arranged photoreceptors. Two donut-shaped primary pigment cells encapsulate the cone cells [Figure 1.11b', b''].

A subset of cells during larval stage of the fly proliferates to form eye imaginal disc. At the third larval instar, a strip of cells in the eye disc driven by signaling cascade undergoes apical constriction, which is referred to as the morphogenetic furrow. The apical constriction in the morphogenetic furrow is facilitated by MyoII that moves anteriorly. As it progresses, it leaves behind a differentiated cluster of cells which are future ommatidial cells [Figure 1.11a]. These clusters undergo further cell differentiation, cell shape change, cell rearrangement and cell apoptosis during pupal stage that give rise to an adult eye.

At 25^0C, if the beginning of the pupation time is taken as the zeroth hour, by 41 hours after puparium formation, all the cells will have almost reached their final shape. One noticeable, highly consistent, orchestrated cell arrangement is T1 like transition of cone cells; the initial

anterior and posterior cone cell contact shortens and makes equatorial and polar cone cell contact [Figure 1.11b, b']. The mechanism behind this arrangement is unclear.

In spite of its complex structure and developmental process, the ommatidium of retinal epithelium is an ideal system to study cell shapes. An important feature is the existence of differential expression of cadherins at the cell contacts, *viz.,* Ecad and Ncad (Hayashi & Carthew, 2004). These cadherins do not form heterophilic adhesion, Ncad does not interact with Ecad and *vice-versa*. Different cell shapes are observed depending on which cone cell and how many cone cells lack Ncad. These changes in shape can be visualized in the adherens junction plane, making it a simple system to study in two dimensions.

Hayashi and Carthew showed that the shape and arrangement of cone cells resemble the shape and arrangement of four soap bubbles. They studied the shape of *Rough eye* (Roi) mutants, this mutation lead to the formation of an abnormal number of cone cells. They found that Roi mutants also have a striking resemblance to soap bubbles [Figure 1.12]. Six soap bubbles have three possible configurations and all of these configurations were observed in cone cells. This led to the speculation that cone cells minimize their surface area, similar to soap bubbles.

Cells are not as simple as soap bubbles; two soap films fuse to form a single film at the contact, whereas at the contact between cells, they are separated by their plasma membrane and adhere to each other through adhesion proteins. These adhesion proteins are linked to actomyosin inside the cell cytoplasm through cross linkers. Nonetheless, many studies have exploited the idea of the surface energy minimization in physical models to explain the ommatidium shape, with differential adhesion as a biological ingredient (Hilgenfeldt, Erisken, & Carthew, 2008; Käfer et al., 2007). It has been shown that a simple soap bubble like model does not mimic the ommatidium shape, it requires contribution from actomyosin to reproduce the shape (Käfer et al., 2007). Taken together, these studies show that Ecad is necessary to maintain the tissue integrity, Ncad is crucial for maintaining the cone cell shape and the role of MyoII cannot be neglected. The questions that are unanswered are: how is the MyoII localized and how does it affect the cone cell shapes? Which are the key regulators of cone cell shapes? Is there any crosstalk between these components?

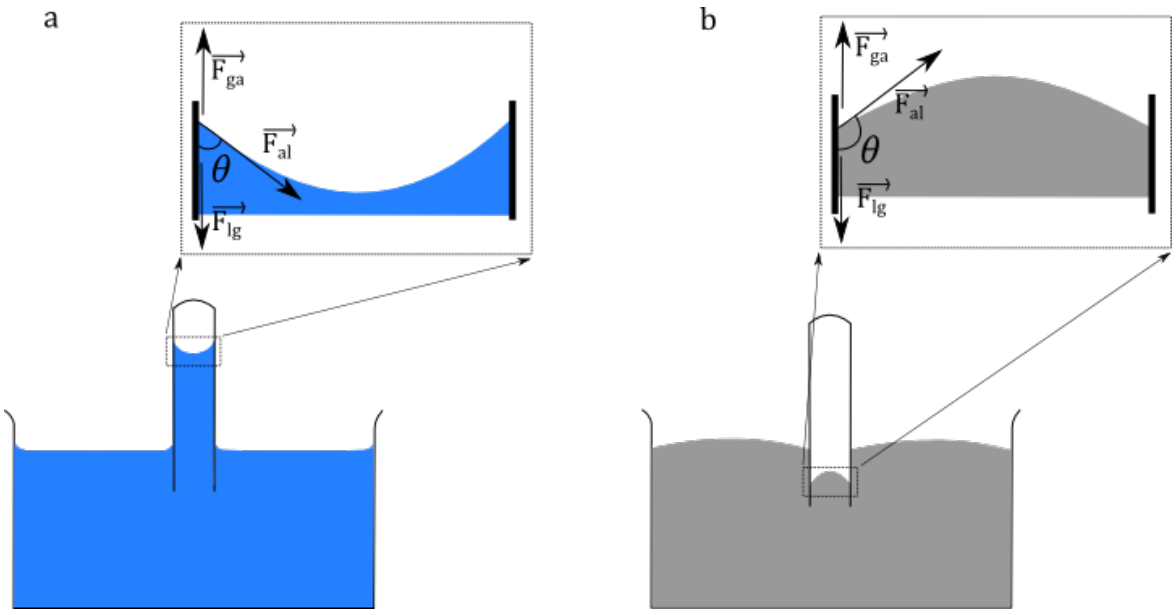

Figure 1.14: Cartoon showing different shapes of meniscus in capillary action

a) Shape of the water meniscus in a capillary tube. There is a higher adhesion between the water molecules and the tube, the force balance between this adhesion and the surface tension of water gives the concave shape for the meniscus. b) Shape of the mercury meniscus. The lower adhesion between the mercury and the tube, and surface tension of mercury produce a convex meniscus. The contact angle formed by the liquid depends on the forces, Fal, the force acting along the interface of air and liquid, Flg, the force acting along the interface of liquid and glass, Fga, the force acting along the interface of glass and air, and is given by cosθ= Fga- Flg / Fal.

1.3 Concepts of physics in cell shapes

1.3.1 Surface tension

The molecules in a liquid have strong intermolecular attractive forces. A molecule within the bulk of the liquid material experiences attractive forces in all directions from its neighboring molecules. So the net force acting on the molecule is zero. However, a molecule on the liquid surface experiences attractive forces only from the neighboring molecules which are below it and on its side. This imbalance in the intermolecular forces results in a net downward force. This force at the surface is termed as surface tension [Figure 1.13].

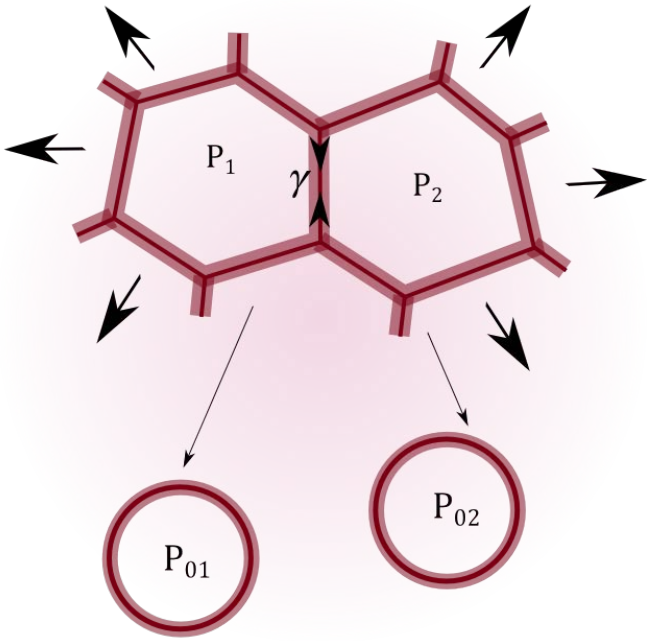

Figure 1.15: Perimeter elasticity of an elastic network

Cartoon depicting two structures under pulling stress with perimeters P_1 and P_2 and their relaxed target perimeters P_{01} and P_{02} respectively. The tension γ of the contact between these two structures depends on the deformation of each perimeter under stress.

For a given liquid, surface tension is a constant, but smaller the surface area, lower its potential energy. Hence surface tension acts to minimize the area of the liquid. A sphere is the smallest possible surface for a given volume. It is the reason for the spherical shape of a dewdrop, or a single soap bubble in air. In a soap bubble spherical shape results from the surface tension of the water, and surfactants reduce the surface tension of water and help in forming a thin layer of water. The same phenomenon occurs in mammalian lungs facilitating efficient exchange of gas with blood. Certain cells in our lungs secrete a pulmonary surfactant that reduces the surface tension of alveoli, the tiny air sacs in lungs and this allows the alveoli to expand easily.

We can see the action of two forces changing the shape of a surface by looking at capillary action. Here, a surface (referred to as the meniscus) is created by the action of adhesion and

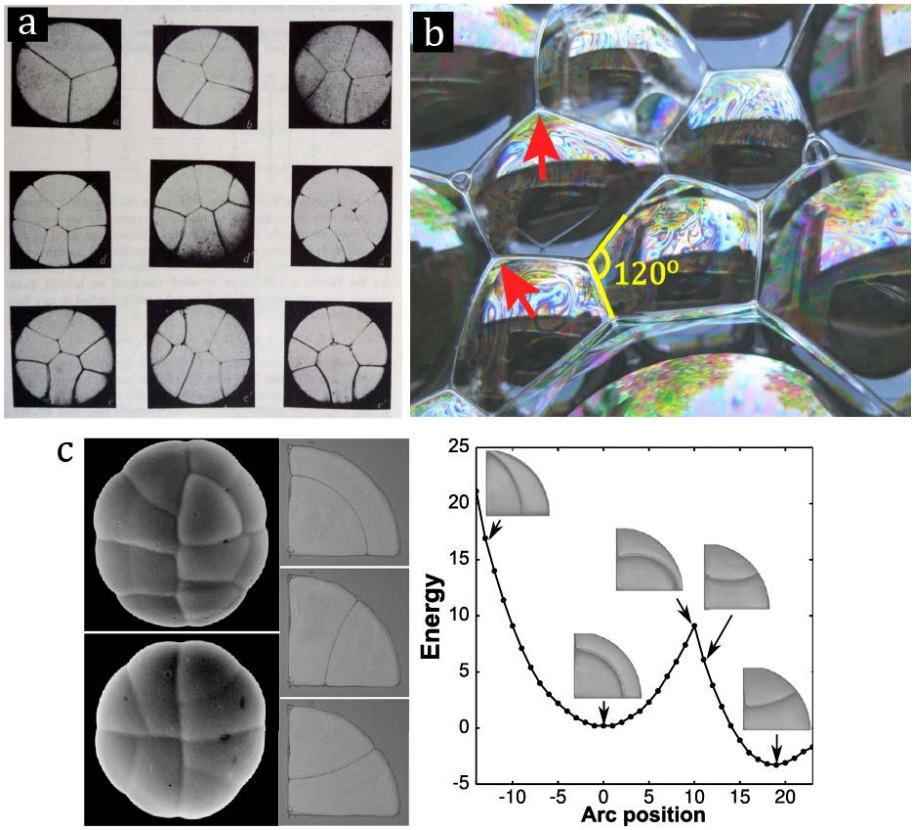

Figure 1.16: Soap bubbles and their analogies used in biology

a) The experiment of D'arcy Thompson, soap bubbles in petri dish: the shape of three and seven bubbles in a constrained (here circular) environment. He compared these to the shape of cells in various early embryos (*image: from 'On growth and form', D'arcy Thompson, 1917*). b) Structure of soap bubbles with three-way vertex (red arrows) and angle of contact 120° (*image: modified from atomics website by Reinhard Nitze*). c) Glandular trichomes of *Dionaea muscipula* (on the left), three configurations of soap bubbles in a quadrangle (center), the energy plot for different arc (cell contact) position, with energy minima (*image: Besson & Dumais, 2011*).

surface tension. Adhesion of liquid to the wall of the tube will exert an upward force on the liquid, whereas the surface tension tries to hold the surface intact. This results in a concave meniscus [Figure 1.14a]. If the adhesion between the liquid and wall of the tube is weaker—like in mercury—then the resulting meniscus is convex as shown in Figure 1.14b**.**

1.3.2 Elasticity

Elasticity is the property of a material to deform upon application of a force, and to go back to its original form when the force is removed. The restoring force is directly proportional to the physical change in the material (length, area, perimeter etc.) from its original value, and this is defined in Hooke's law. A piano wire is more elastic than a rubber band, as it goes back to its original length more precisely than a rubber band, even though it is harder to stretch than a rubber band. In rubbers and other polymers, elasticity is due to the stretching of polymers whereas in piano strings and other metals the atomic lattice changes shape and size when the force is applied. Hence there is a wide range of elastic materials with different elastic behaviors.

A spring is a very common example of an elastic object, Hooke's law for a spring is

$$F = -k(x - x_0) \tag{1.1}$$

where k is the spring constant, x_0 is the original length of the spring, x is the length of the spring under the applied force, and F is the restoring force in the spring (which is equal to the applied force). The energy stored in the spring (E) due to the deformation is nothing but the work done during the deformation and is given by

$$E = \int_{x_0}^{x} -k(x - x_0) = \frac{1}{2}k(x - x_0)^2 \tag{1.2}$$

Consider two connected elastic structures with perimeter P1 and P2, in a deformed network with the same elastic constant (say, k) as shown in Figure 1.15. When there is no deformation, their preferred perimeters are P_{01} and P_{02}. Then the potential energy of the system is given by

$$E = \frac{1}{2}k(P_1 - P_{01})^2 + \frac{1}{2}k(P_2 - P_{02})^2 \tag{1.3}$$

The tension (γ) generated at the contact between these two structures due to deformation will be

$$\gamma = k(\Delta P_1 + \Delta P_2) \tag{1.4}$$

This tension depends on the amount of deformation, $\Delta P_1 = P_1 - P_{01}$ and $\Delta P_2 = P_2 - P_{02}$

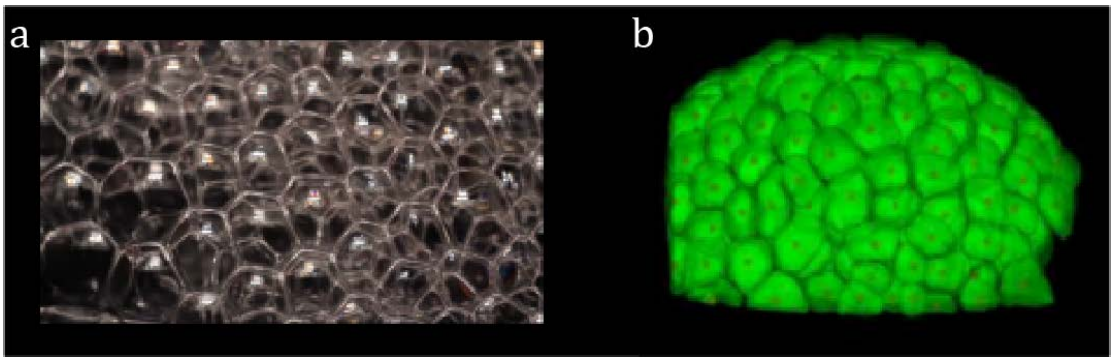

Figure 1.17: Comparison of soap bubbles to cells

The structure of soap bubbles strikingly resembles the pattern of cells in the growing *zebrafish* embryo (*image: Megason Lab*).

1.3.3 Soap bubbles and their analogy to cells and tissues

This is the centenary year of D'arcy Wentworth Thompson's masterwork '*On growth and form*' (published in 1917), which was a stepping stone in mathematical and physical approaches to developmental biology (Thompson, 1917). He put forth the idea—which was ahead of its time—that physical forces play an important role in shaping the organisms. He used mathematical analysis to explain the form of organisms. He made the first comparison between a group of cells and soap bubbles, by blowing bubbles on a petri dish and comparing them to the first few cell divisions during the embryonic development of many organisms [Figure 1.16a]. His argument for this analogy is that cells, like soap bubbles, minimize their energy by surface area minimization under different constraints.

Before Thompson, the botanist Leo Errera used a similar argument for cell division in plant cells, this is known as Errera's rule. Errera's rule states that the new cell wall that forms between two daughter cells behaves like a soap film. This means that, under a given constraint, the new wall takes the configuration with the least possible area. This development pattern was further explained in detail by Thompson. Besson and Demais manipulated the soap film boundary of two soap bubbles trapped in a quadrant. They found

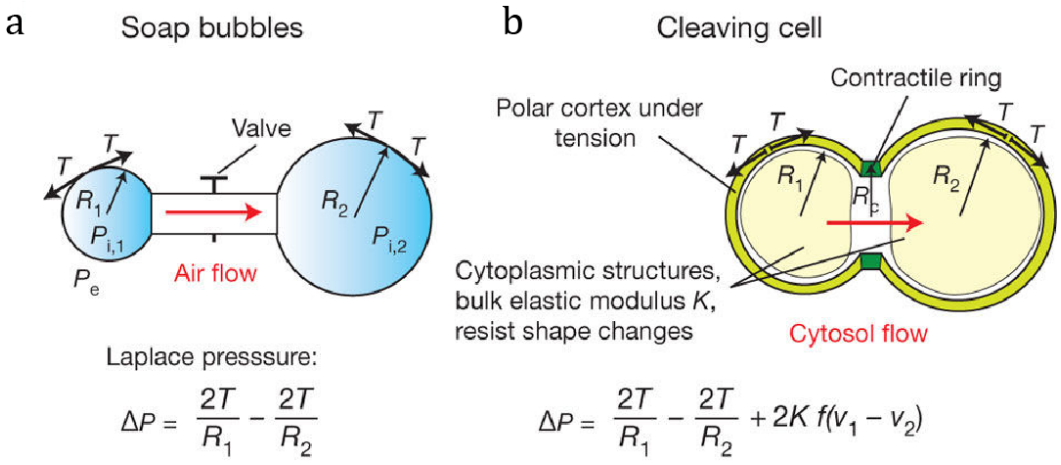

Figure 1.18: Cartoon of connected soap bubble model and dividing cell

a) The two connected soap bubbles with surface tension T, radii R_1 and R_2, internal pressures $P_{i,1}$, $P_{i,2}$ and external pressure P_e. b) Cartoon of a dividing cell with cleavage furrow radius R_c, cortex tension T, the elastic response of the cell K f (V_1-V_2), the pressure difference between poles ΔP (*Image: from Sedzinski et al., 2011).*

that the constrained bubbles always take one of a few configurations which are their local energy minima. These are the exact configurations observed in cells of trichomes—a structure on the leaves of a Venus flytrap [Figure 1.16c] (Besson & Dumais, 2011).

Joseph Plateau first came up with a mathematical explanation to describe the structure of soap bubbles. A single soap bubble in air has a perfectly spherical shape, since a sphere is the smallest area that encompasses a given volume. This shape is determined by the surface tension in the soap film. In soap bubbles, energy minimization is achieved through surface area minimization. As a consequence of this, in 2D with three or more soap bubbles or in foams, the contact is always formed by three soap bubbles with an angle of 120° between two adjacent faces [Figure 1.16b]. Four soap bubbles meeting and forming a four-way vertex is not observed because such an arrangement is energetically unstable.

The structure of epithelial tissues indeed looks like the structure of bubbles [Figure 1.17]. As explained in the Section 1.2.2 cells are more complex than soap bubbles and it is a simplification to compare them both. Nonetheless, this simplified approach can be used as a starting point to understand the complex biological structure.

1.4 Physical approaches to tissue morphogenesis

1.4.1 Models to study biological systems

Models are used to get the simple abstract picture of complex biological systems; they are used to make predictions which can later be tested experimentally; they are used to make different hypotheses or to test simple hypotheses which are too complex or time consuming for experiments; they are used to clarify whether any experimental observation is significant or not. Mechanics being one of the key regulators in tissue morphogenesis, models come in handy to study tissue or cellular processes. Models are used extensively to study epithelial morphogenesis as a minimal approach to understand the system of interest.

There is always feedback between the models and the experiments; from preliminary experimental observations one develops a minimal physical model, which in turn gives hypotheses that can be tested with the experiments and then the experimental results are used to improvise and explain the processes in the model. As an example, Sedzinski et al. (Sedzinski et al., 2011) show that there is contractile actomyosin cortex present at the poles of the dividing cells, they produce resistive forces that counteract the furrow ingression speed. Their aim was to understand how these forces at the poles affect overall cell shape and achieve division without shape instabilities. They develop a minimal model of two connected soap bubbles that mimic the dividing cells [Figure 1.18]. This simple model predicted that the fluctuation above a certain critical value in surface tension or volume leads to cell shape instability. They tested this prediction experimentally through laser ablation and drug treatment. However their experiments on cortex perturbations showed shape oscillations, which was not predicted by the model. They implemented this as an effect of cortex turnover in the redefined model.

The vertex model is the most extensively used model in epithelial morphogenesis (Farhadifar et al., 2007; Fletcher et al., 2014; Spahn & Reuter, 2013). Cell neighbor exchange and cell arrangements are the key components in epithelial morphogenesis, in the vertex model these cellular processes can be incorporated. This ability makes the vertex model very robust and easy to compare with the biological processes. Most vertex models in 2D either represent the adherens plane or the cross section of epithelial tissue. Lately, many

researchers are also using 3D vertex models considering the lateral and basal planes (Bielmeier et al., 2016), but this is redundant unless changes are observed in those planes. Vertex models give the energy minimized state of cell shape and arrangements of cells in tissues at a given time, but not how cells or tissues develop over time. The time of simulations in search of minimal energy cannot be compared to the time of developmental processes.

In this thesis, a type of vertex model called Surface Evolver model is used to study cell shapes of ommatidia. In the Surface Evolver model, cells are defined by vertices, edges and faces either in 2D or in 3D. We choose to define only the apical surface of the ommatidium where cadherins and MyoII (adherens plane) are present. This reduces the complexities in the model as cells in the ommatidium vary in lengths, and any changes in cell shape can be visualized in the apical plane (see also Figure 1.11b''). Surface Evolver has been used in other studies also, in germ band elongation to show how coordinated T1 transition and neighbor exchange of cells elongate the tissue resulting in a directional movement (Rauzi et al., 2008), and in the study of ommatidium shape with differential adhesion as input from experiments (Hilgenfeldt et al., 2008). The biological ingredient in our Surface Evolver model is the interfacial tension that is experimentally measured and incorporated in the model. This is discussed further in the following chapters.

1.4.2 Forces in tissues and various techniques to measure them

Cells in epithelium have the ability to experience forces and exert forces in their natural environment: for example cells lining the airways in the lung, and the macrophages exploring the tissues and organs. During tissue morphogenesis cells are pushed, pulled and sometimes even thrown out of the tissues. How much, where in the tissue and when during development cells generate these forces or sense these forces are always an important question. There are many techniques to address these problems, a few are invasive methods—manipulations using light or magnetic fields, and a few are non-invasive methods—measurements using image analysis.

Atomic force microscopy (AFM) is a widely used method to measure the material properties of cells like the contractility of a cell cortex (Krieg et al., 2008) or the internal turgor pressure

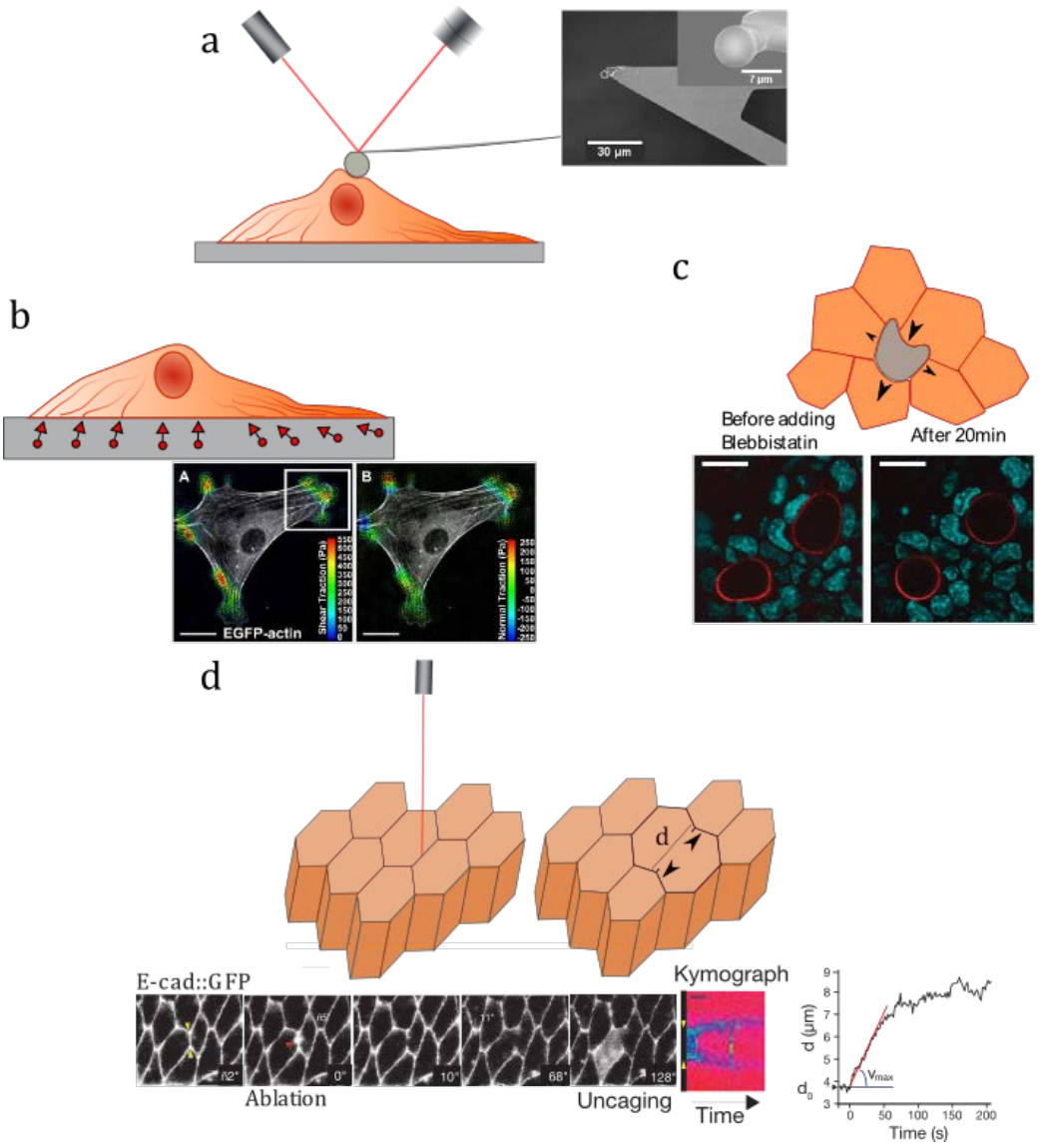

Figure 1.19: Cartoons of different mechanical force measurement techniques

a) Schematics: Atomic force microscopy (AFM) with cantilever scanning the cell surface, image: SEM image of an AFM cantilever with a microbead *(Suarez et al., 2013).* b) Schematics: traction force microscopy with fluorescent beads embedded in the substrate and arrows on the beads pointing towards the direction of the pulling force, Experiment: Shear and vertical traction stress vectors generated by mouse embryo fibroblasts (*Legant et al., 2013*). c) A deformed fluorescent oil droplet between the cells, arrows show the direction and magnitude of the force exerted by cells on the droplet, Experiment: Microdroplets (red) in mammary epithelial cell aggregates (DNA in cyan) before and after blebbistatin (*Campàs et al., 2013*). d) Schematics: laser ablation experiment before and after ablation, d is the opening distance between the vertices of ablated cell contact, experiment: ablation of a cell contact in *Drosophila* embryo, Kymograph shows the time evolution of ablated junction with the graph of distance verses time (slope of the linear part of the curve gives the initial velocity that is proportional to the junction tension) (*Rauzi et al., 2008*).

of plant cells (Beauzamy, Nakayama, & Boudaoud, 2014). In AFM, the materials under study are pushed or indented to read the response [Figure 1.19a]. Micropipette aspiration works in the opposite way, the cells are pulled to study the response. The surface tension is calculated by measuring the radii of the cell and pulled portion of the cell along with the aspiration pressure (Maître et al., 2012). Using micropipette aspiration, it has been shown that the surface tension due to the actomyosin controls the progenitor cell doublet shape, over cell adhesion.

Traction force microscopy is a technique in which cells are seeded on or in the artificial gels that mimic the extracellular matrix, embedded with fluorescent microbeads [Figure 1.19b]. The traction exerted by the cells result in bead movements, these movements are calibrated to stresses (Legant et al., 2010). Here the forces measured are *in vitro* and it is unclear whether cells exert and experience the same forces *in vivo*. As an improvement to this technique, Zhou et al. micro-surgically separated *Xenopus* embryo and embedded these explants in agarose gel. As the tissue exerts a force, the gel deforms. By measuring this deformation, mechanical stresses during convergent extension of *Xenopus* gastrulation were studied (Zhou et al., 2015). This method provides tissue level forces, but from an explant. Similar *in vivo* cell scale measurements are performed by injecting fluorescent oil droplets coated with ligands that can bind to cell-surface receptors. Cells exert forces on the droplet resulting in a change in the shape of the droplet [Figure 1.19c]. This change in shape is further used to quantify the forces around cells (Campàs et al., 2013).

The two methods that make use of light to measure the cell scale or tissue scale forces are laser ablation and optical tweezers. In laser ablation, micro-scale cuts on cell junctions (Rauzi, Verant, Lecuit, & Lenne, 2008) or tissues (Bonnet et al., 2012) are made using Near-IR or UV lasers to measure the junction tension and stress anisotropy in the tissue [Figure 1.19d]. In optical tweezers, either a bead or a cell junction is optically trapped with laser and a stress is applied to measure the strain and hence tissue properties (Bambardekar et al., 2015). Like optical tweezers, another method to apply a force on bead is by a magnetic field, this method is called magnetic tweezers (Fernández-Sánchez et al., 2015).

A force sensor that is integrated inside the tissue to measure force is the Förster Resonance

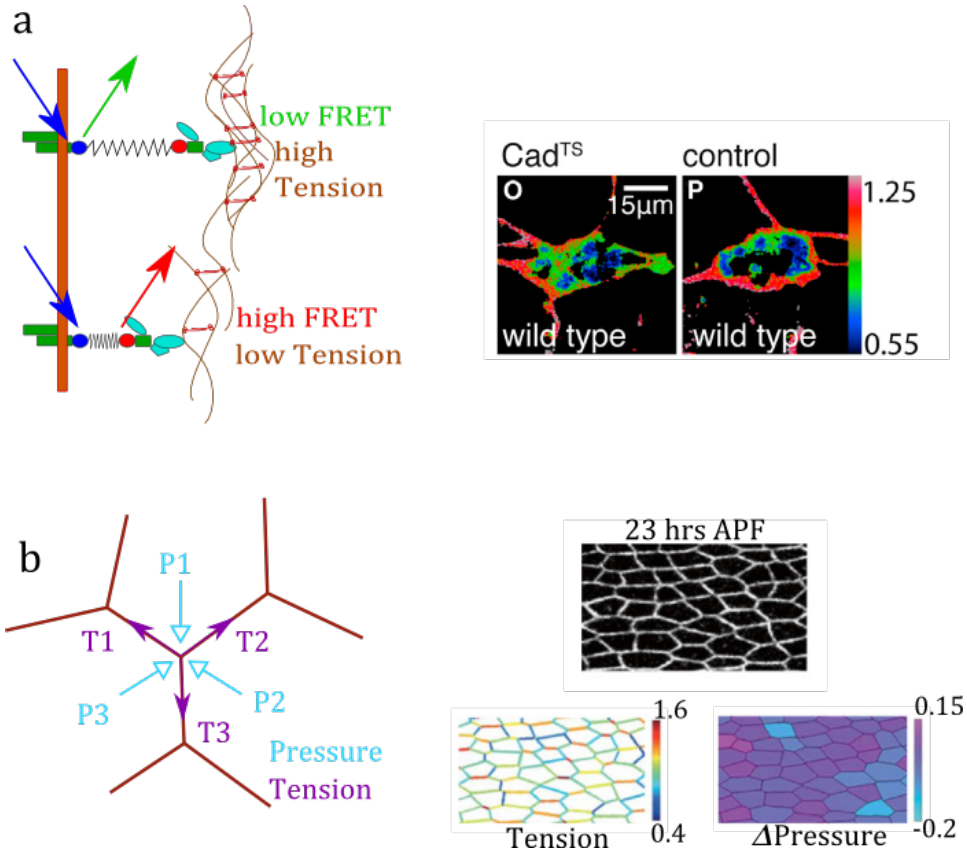

Figure 1.20 : Non-invasive force measurement techniques

a) Schematics of FRET measurement technique, with tension sensor attached to cadherin molecule, a high FRET signal implies a low tension and a low FRET implies a high tension on the molecule. Experiment FRET images of border cell with Ecad tension sensor (Cad^{TS}) and control (*Cai et al., 2014*). b) Schematics of cell contacts, the force inference image analysis method gives cell contact tensions and cell pressures based on the cell shapes from the image by solving the force balance equations. T1, T2, T3 and P1, P2, P3 are the inferred tensions and pressures. Experiment: an input image used to estimate the forces (*Drosophila* pupal wing at 23 hrs APF) and the output inferred tensions and pressures *(Ishihara & Sugimura, 2012)*.

Energy Transfer (FRET) sensor [Figure 19a]. It is a visual method in which a force can be measured at molecular levels. Using this, it has been shown that the tension on Ecad generated by actomyosin in dividing and non-dividing epithelial cells is the same as in *Xenopus* embryos (Herbomel et al., 2017). A method which does not require any kind of manipulation or disruption of cells or tissues in order to measure forces is the force-

inference method. It is the estimation of the cell contact tensions and cell pressures with the help of experimental images, by solving the force balance equations [Figure 19b] (Sugimura & Ishihara, 2013).

Each of the force measurement techniques has its pros and cons; the appropriate method has to be chosen depending on the biological question. In the review by Sugimura, Lenne and Graner (Sugimura, Lenne, & Graner, 2016), they outlined the details of each methods, their applications and limitation. We have used the laser ablation technique to measure the cell contact tension, this is explained in detailed in Section 2.1.

1.5 Rationale and objectives of this thesis

It is known that the motor protein, MyoII, is the driving force for the cell shape changes and cell arrangements during *Drosophila* apical constriction in mesoderm invagination and germ band elongation (Martin, Kaschube, & Wieschaus, 2009; Rauzi et al., 2008) [Figure 1.21a]. It has been shown that the mesoderm and endoderm progenitor cells adhere more to substrates coated with Ecad than ectoderm cells, suggesting that these cells have different adhesive properties. Additionally, these progenitor cells displayed different levels of cell cortex tension, and blebbistatin treatment reduced their cortex tension to the same level (Krieg et al., 2008). Using cell doublets in vitro and pipette aspiration, Maitre et al. have shown that MyoII has very large impact on the shape of cell doublets from different germ layers of developing *Zebrafish* embryo and that adhesion has a minor impact (Maitre et al., 2012) [Figure 1.21b].

However, in *Drosophila* eye the shape of cone cells seems to greatly depend on an adhesion protein, Ncad. Cone cells shape vary significantly in different Ncad mutant cells compared to wildtype cells. Based on the striking resemblance of cone cells topology to soap bubble topology both in wildtype and altered number of cone cells, the impression is that Ncad adhesion minimizes the surface area of cone cells, similar to soap bubbles. Ecad is universally expressed in all cells and, hence it is essential for maintaining tissue integrity. Any cell lacking Ecad, detaches from its neighbors at the AJ plane (Hayashi & Carthew, 2004) [Figure

1.22a]. *In silico* models predicted that a contribution from actomyosin contractility is as important as adhesion by cadherins, and among cone cells Ncad adhesion has to be higher than Ecad adhesion (Hilgenfeldt, Erisken, & Carthew, 2008; Käfer, Hayashi, Marée, Carthew, & Graner, 2007) [Figure 1.22b].

Collectively, the specific questions that are yet be answered are the following;

1) The protein distribution of Ecad and Ncad in wildtype and Ncad mutant cone cell is known, but what is the protein distribution of MyoII in them?

2) Is the drastic change in shape of cone cells due to the absence of Ncad adhesion alone, or due to the change in Ecad or MyoII contractility?

3) Do adhesion molecules have an impact on MyoII or *vice versa*? Is there any interplay between them as they are interconnected via β-catenin and α-catenin?

4) What is the interfacial tension of different cell contacts and can it be used as a readout of cell shapes?

5) How much is the influence of cadherins and MyoII on the interfacial tension *in vivo*?

We investigated all the above mentioned questions in an *in vivo* model *Drosophila* retina with the help of fly genetics, confocal imaging, mechanical measurements and computer simulations. We employed fly genetics for the perturbation of different proteins, (for example, generating Ncad mutants in mosaic condition), confocal imaging to study the protein distribution and their concentration measurements, laser ablation technique, to perform mechanical measurements (for example to measure cell contact interfacial tension) and a simple physical model based on the principle of energy minimization (using Surface Evolver) to explain the cone cell shapes *in silico*.

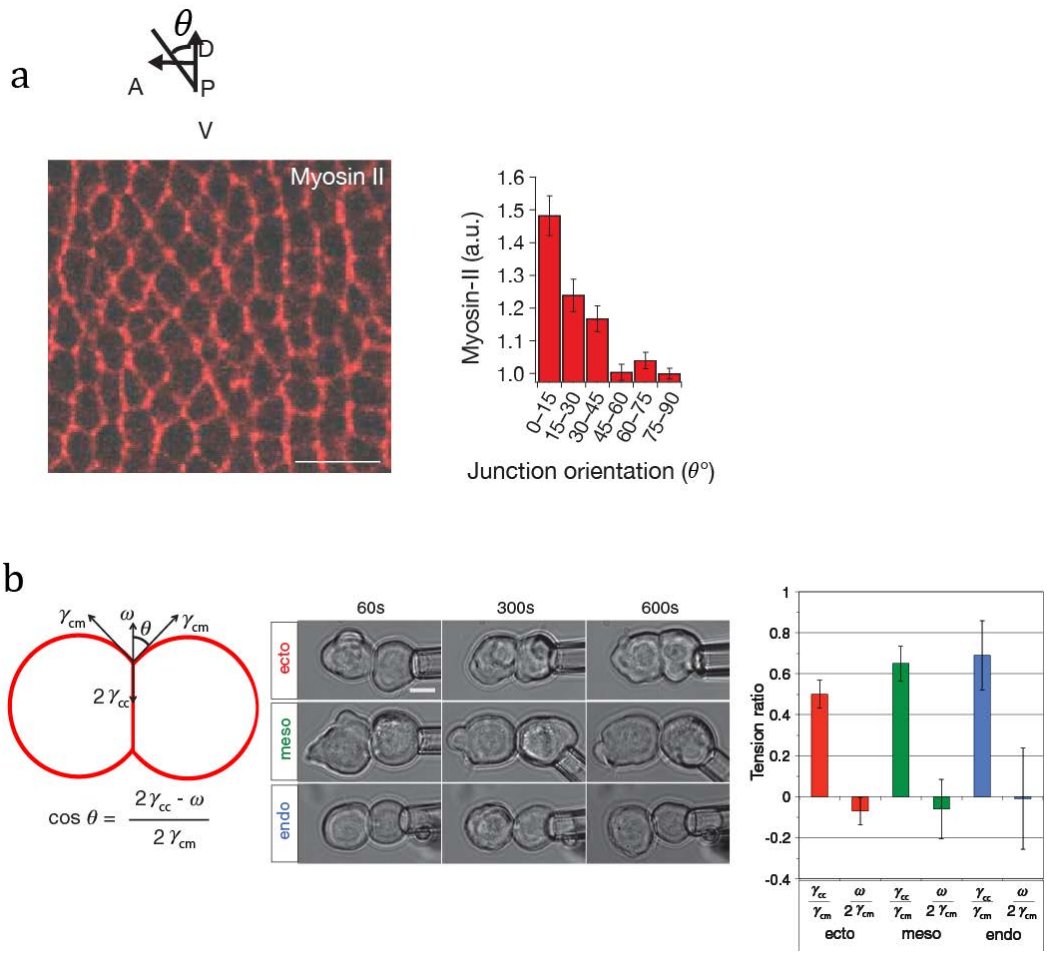

Figure 1.21: MyoII driven cell shape changes

a) The enrichment of MyoII in the shrinking vertical junction during germband elongation in *Drosophila* embryo, and the relative MyoII concentration at different junction orientations *(image: modified from Rauzi et al., 2008).* b) Schematics of different forces acting on the cell doublet and their relation to the contact angle (θ) of the doublet, the contact formation of ectoderm (ecto), mesoderm (meso) and endoderm (endo) doublets and the graph of tension ratios (ratio of cortex tension to the cell- medium tension, γ_{cc} /γ_{cm} and ratio of cortex tension to the cell- medium tension, $\omega/2\gamma_{cm}$) for ecto, endo and mesoderm doublets *(image: modified from Maître et al., 2012)*.

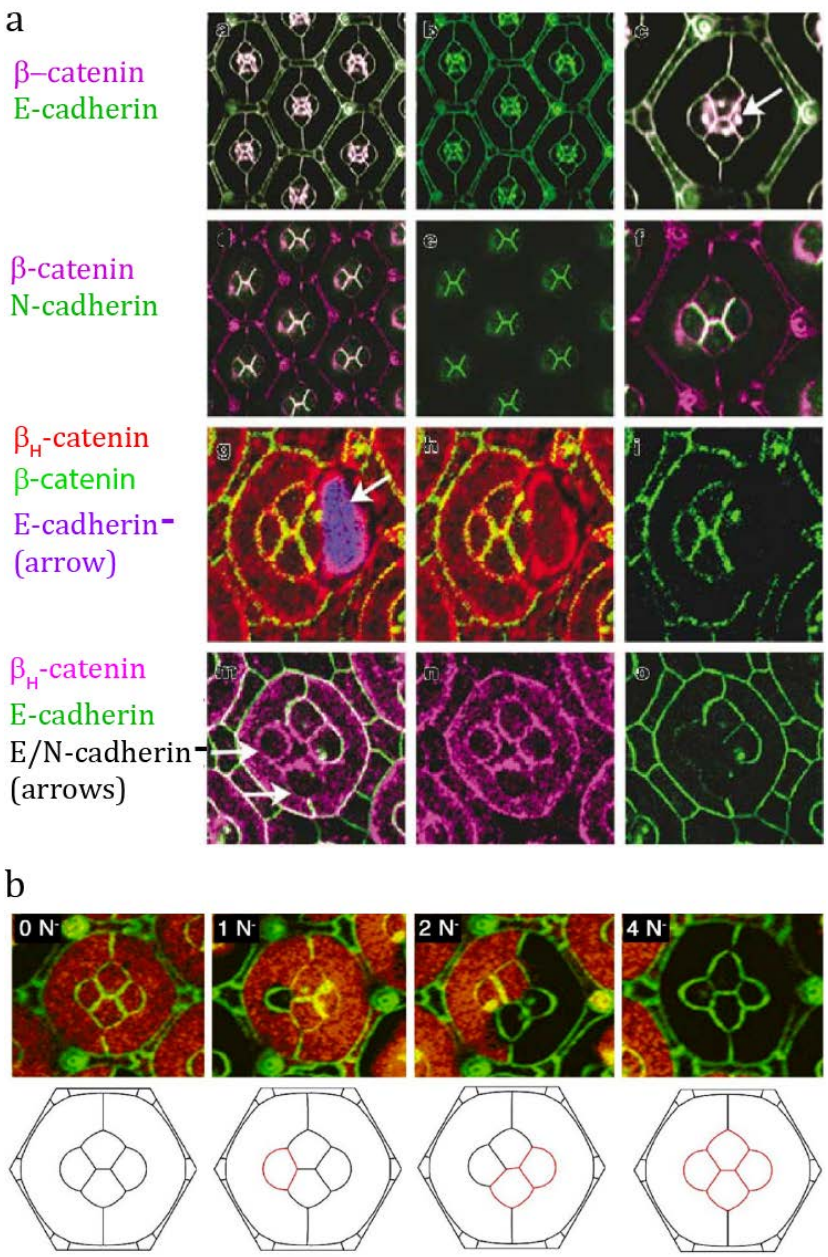

Figure 1.22: Cadherin driven cell shape changes

a) Localization of Ecad and Ncad in ommatidia. Ecad mutant leads to apical detachment of cell (in purple), Ecad/Ncad double mutant leads to apical detachment of cone cells (white arrows) *(image: modified from Hayashi and Carthew, 2004)*. b) Comparison of experimental images to the simulated images of wildtype and different Ncad mutant cone cells (cone cells not marked in red) *(image: modified from Hilgenfeldt et al., 2008)*.

Chapter2: Methods

This chapter covers the methods that we have used to study retinal morphogenesis. One of the first goals of our research was to perform mechanical measurements in the retina to relate interfacial tensions to distribution of adhesion and MyoII molecules. The Section 2.1 method: laser ablation detailing the laser ablation approach was published as a protocol in '*Drosophila*: methods and protocols' (Shivakumar & Lenne, 2016). To model the cell shapes we have adapted and implemented previously-developed Surface Evolver simulations (Hilgenfeldt et al., 2008; Brakke, 1992).

2.1 Laser ablation

Laser ablation to probe the epithelial mechanics in *Drosophila*

Pruthvi C. Shivakumar and Pierre-François Lenne

Aix-Marseille Université, CNRS, Institut de Biologie du Développement de Marseille, IBDM UMR7288, 13009 Marseille, France
Corresponding author: pierre-francois.lenne@univ-amu.fr

Summary:
Laser ablation is nowadays widespread technique to probe tissue mechanics during development. Here we describe the set-up of one such ablation system and ablation experiments performed on the embryo and pupa of *Drosophila*. We describe in detail the process of sample preparation, how to disrupt single cell junctions and perform linear or circular cuts at the tissue scale, and how to analyze the data to determine relevant mechanical parameters.

Keyword: Tissue mechanics, Force measurements, Epithelia, Morphogenesis
Running Head: Laser ablation in *Drosophila*

2.1.1 Introduction

During the development of an animal, cells change their shape and position to give rise to a large variety of tissue morphologies (Heisenberg & Bellaïche, 2013). To understand how mechanical forces shape tissues in *Drosophila*, laser ablation has proven a versatile approach from the subcellular scale to the tissue scale (Farhadifar et al., 2007; Hutson & Tokutake, 2003; Rauzi et al., 2008). Pulsed laser, in particularly the near-infrared (NIR) femtosecond (fs) lasers can ablate multiple cells or subcellular structures such as cytoskeletal filaments, thereby revealing the forces they convey (Rauzi & Lenne, 2011). In subcellular ablation and cell junction ablation, a tightly focused laser is targeted on the cellular structure of interest; the cut produces a force imbalance. By this sudden imbalance between severed and non-severed structures, ablation creates a change in cellular geometry. For instance, severing of actin-myosin networks at epithelial junctions in *Drosophila* results in the movement of cell vertices (tricellular junctions). The initial velocity of vertices after ablation is a proxy to tension of the severed actin-myosin network or cell-cell junction. Comparison between tensions along different junctions can reveal anisotropy of stresses. At the tissue scale, laser ablation can sever several cells. The initial velocity of wound margin after ablation measures the stress-to-viscosity ratio in the direction of the velocity within the tissue (Bonnet et al., 2012; Bosveld & Nodal, 2012). Here we present a laser ablation setup and its application to cellular and tissue level ablation in the *Drosophila* embryo and pupa.

2.1.2 Materials

Safety Measures

1. Use adapted light-protecting goggles (typically with optical density 7 at 1,030 nm wavelength).
2. Build the setup in a dedicated room with controlled access.
3. Wear a lab coat to protect the skin and do not wear any jewels to avoid light reflection.

Laser Specification

1. Yb::YAG solid state laser (T-Pulse, Amplitude systems, Pessac, FRANCE) with 1W average power, 1030 nm wavelength with spectral width 7nm, 50 MHz, 160 femtosecond (fs). Femtosecond lasers at different near infrared wavelengths can also be used.

Optical path

1. A mechanical shutter with opening/closing time scale of one millisecond.
2. A polarizer to vary the power of the laser, one $\lambda/2$ waveplate for 1030 nm wavelength.
3. IR-coated mirrors to change the direction of the path of the laser.
4. A dual axis galvanometer optical scanners.
5. A telescope containing two lenses with IR coating.
6. Periscope to change the path of the laser perpendicular to the current one.
7. A dichroic mirror for IR light reflection and visible light transmission.
8. An inverted microscope with high numerical aperture and a high magnification IR corrected objective lens.
9. A commercial spinning disc coupled to microscope with fast imaging.
10. An optical bench with mirror holders and screws.

Imaging and ablation software

1. A spinning disc microscope (PerkinElmer) with objective 100X (NA 1.40, oil immersion, PlanApoVC, Nikon) for imaging.
2. Homemade Qt software to control opto-mechanical components, such as shutter and voltage control of galvanometer mirrors (via National Instruments card). This will produce different cuts, such as a point, line, or a circle.
3. Image processing software, such as Fiji/ImageJ, to analyze data.

Samples for the experiment

1. To locate the laser point: 0.17 mm cover slip, fluorescent marker pen.

2. For the biological sample: 0.17 mm cover slip, bleach, heptane glue, halocarbon oil and embryos (of preferable stage), glass slide, Blu-tack/Patafix (a reusable pressure-sensitive adhesive), two sided gum tape, 0.17 mm coverslip, paper pieces (approximately 0.2mm) and the Pupae (of preferable time point, after puparium formation (APF)).

2.1.3 Methods

All the experiments are carried out at room temperature (22^{o}C).

Safety methods

1. Wear IR protective goggles to avoid eye damage.
2. Wear a lab coat to protect the skin and avoid wearing any jewelry.
3. Make sure that the optical bench is not at eye level.
4. Use the IR visor and IR fluorescent paper to visualize the laser beam.

Setting-up the laser dissection optical path (*see* NOTE 1)

1. Place the laser and microscope on the optical bench in such a way that the laser beam is deflected 90^{o} twice along its path to reach the microscope (see Fig. 1).
2. Place the shutter just in front of the laser whose diameter is larger than of the laser beam diameter (*see* **NOTE 2**).
3. After the shutter, place $\lambda/2$ waveplate before the polarization prism; they have to be as close as possible to the laser. While setting up, first place the prism on a manual rotator, with maximum transmission and then position the $\lambda/2$ waveplate in front of it (*see* **NOTE 3**). Both of these act as a variable laser beam attenuator (*see* **NOTE 4**).
4. Use two mirrors to change the path of the laser by 90^{o} (see mirror 1 and 2 in Fig. 1). These two mirrors should be mounted on holders with two degrees of freedom and aligned in such a way that the laser path is directed towards the mirror galvanometer.

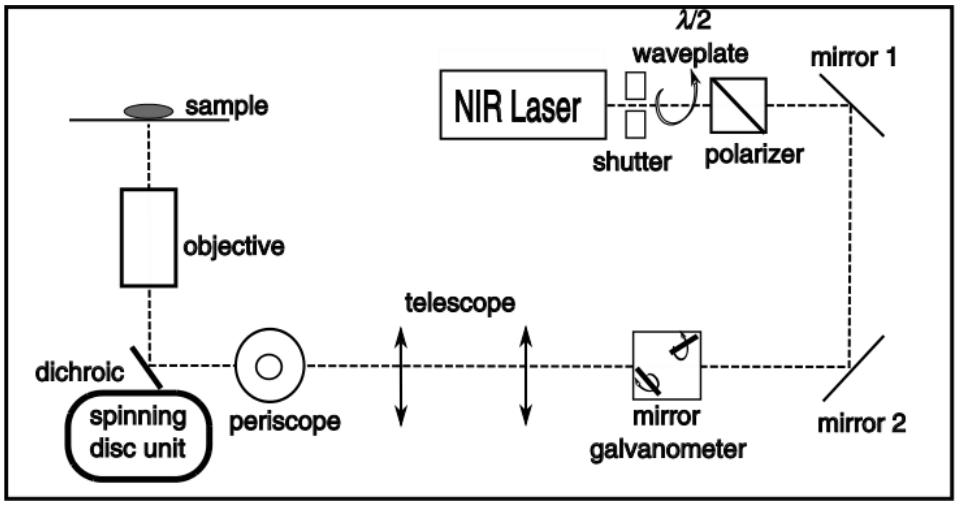

Figure 2.1: Schematics of the laser ablation setup

This view combines both top view (from NIR laser to telescope) and side view (from periscope to sample.

5. Place the dual-axis mirror galvanometer on the laser path (*see* **NOTE 5**). And the galvanometer mirrors have to be optically conjugated with the back aperture of the objective (*see* **NOTE 6**).
6. Place the telescope after the mirror galvanometer to expand the laser beam to match diameter of the back aperture of the objective (*see* **NOTE 7**). The telescope has to be perfectly aligned with the laser beam (*see* **NOTE 8**).
7. Put two irises in front of the telescope to help align the laser beam by tilting the two mirrors. Use the two mirrors to align the beam to the center of two lenses (*see* **NOTE 9**).
8. Use a periscope with two mirrors to lift the laser beam towards the microscope entry port (*see* **NOTE 10**).
9. Mount the dichroic mirror under the back aperture of the objective at ~ 45^{o} angle so that the laser beam is directed from the periscope to the objective (*see* **NOTE 11**).

<u>Laser point alignment on the screen and calibration of the laser cut</u>

1. Place the coverslip coated with fluorescent ink in the sample holder of the microscope. Proper alignment with the shutter open and no input to the

galvanometer mirrors will show a laser point on the imaging software screen (*see* **NOTE 12**).

2. This laser spot is used for the point cut. Get the correspondence between the voltages fed to the galvanometer mirrors and the laser spot position on the imaging software screen (*see* **NOTE 13**).
3. The input parameters must be calibrated in the program for other cuts (i.e. circle or line) to specify the preferred length of the line or diameter of the circle in the image. In our program, the signals sent to the galvanometer mirrors are sinusoidal, and variation in the amplitude and phase difference of these two sinusoidal signals gives different cuts. For example, two signals with equal amplitude but with a 90^{o} phase difference gives a circle cut (*see* **NOTE 14**).
4. The calibration will vary depending on the magnification of the objective lens used in the setup (*see* **NOTE 15**).

<u>Sample preparation</u>

1. Biological sample preparation: Embryo
   1.1. To perform ablation experiments during embryo gastrulation, collect *Drosophila* embryos after 4 hours of egg-laying, then bleach and wash with water. Depending on the stage of interest, collect the eggs after the appropriate amount of time at the preferred temperature.
   1.2. Place the embryos on a plate of agar gel, using a brush align them.
   1.3. Spread some heptane glue on the cover slip. Gently press the cover slip on the embryos so they stick to the glue.
   1.4. Put a few drops of halocarbon oil over the embryos so they stay hydrated and survive over long time periods (Cavey & Lecuit, 2008).

2. Biological sample preparation: Pupa
   2.1. Collect zero hour pupae and keep them at 25^{o}C until preferred ablation stage (i.e. 28 hours after puparium formation (APF) for retina ablations described here) (*see* **NOTE 16**).

2.2. Place two-sided gum tape (approx. 30X mm) on the glass side. Attach a small piece of paper (approx. 30X mm) on the tape as a headrest for the pupa and to raise the eye slightly.

2.3. Place the pupa sideways on the gum tape so the head is on the paper (*see* **NOTE 17**).

2.4. For imaging and ablation experiments, gently remove the puparium from the pupa head with forceps without damaging the pupa (*see* **NOTE 18**).

2.5. Once the puparium is removed, apply adhesive (e.g. blu-tack/patafix) to the four corners of the gum tape to mount the cover slip over the pupa.

2.6. Place a tiny drop of oil (e.g. Voltalef oil) on the coverslip, and gently place the coverslip on the adhesive in such a way that the oil drop is on the pupa eye (*see* **NOTE 19**).

2.7. Gently press the coverslip on the adhesive carefully without damaging the pupa. This process slightly flattens the curved eye structure, which enables a large portion of the tissue to be in focus under the microscope.

<u>Laser dissection</u>

1. Embryo ablation

1.1. Use *Drosophila* embryos expressing either fluorescently tagged Myosin-II (Sqh::GFP) to mark the myosin network or E-cadherin::GFP to mark the adherens junctions.

1.2. Set the average power of the ablation laser to be 250mW at the back aperture of the objective, and the duration of the exposure to be 50-100ms (*see* **NOTE 20**).

1.3. Use a spinning disc confocal microscope set to the following parameters: exposure time of 250ms, laser power at 10% (maximum 20% for GFP), and a recording rate of 1 frame per second or higher (*see* **NOTE 21**).

1.4. Apply the same procedure for a cell junction cut in the embryo, although the ablation laser power may vary slightly.

2. Pupal eye ablation

2.1. Use the *Drosophila* pupae with the β-catenin tagged with GFP to label the membranes (adherens junction plane) (*see* **NOTE 22**).

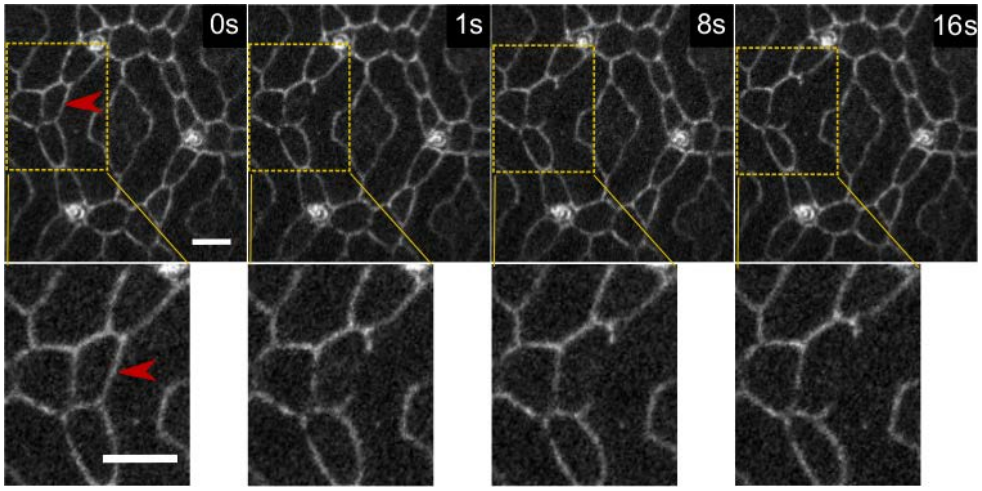

Figure 2.2: A junction cut ablation experiment in a 28 hrs APF *Drosophila* pupal eye

The pupae express E-cadherin tagged with GFP (Ecad::GFP) to visualize the cell junctions, and the site of ablation is identified by the red arrow. The bottom panel are the zoomed inset of the area within yellow rectangle for each time point. Scale bar 4μm.

2.2. Place the targeted cell junction within the focal plane and align the laser point on the junction.

2.3. For 28 hours APF pupae, the average laser power must be 380mW at the back aperture of the objective and the duration of the exposure within 50-200ms.

2.4. Use a spinning disc confocal microscope set to the following parameters: exposure time of 250ms, power at 10%, and a recording rate of 1 frame per second (*see* **NOTE 23**).

2.5. Apply the same procedure for tissue level ablation in the eye, varying the duration of exposure depending on the radius of the circular ablation.

Analysis

1. Open the recorded ablation images in Fiji/ImageJ and measure the opening distance between vertices of the ablated junction as they, move apart over the time. Plot the vertex-to-vertex distance over time. The initial velocity of the vertices just after the ablation is determined by the ratio of the remaining force in the non-severed structure

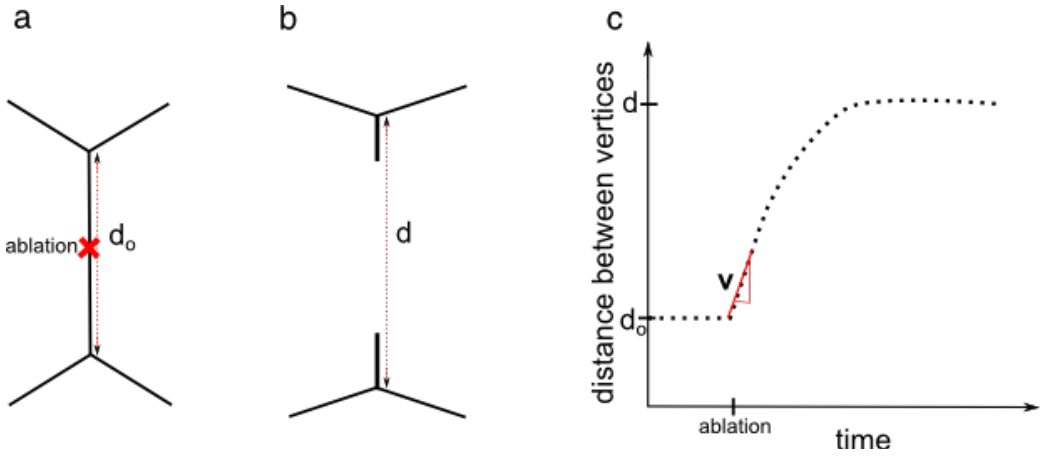

Figure 2.3: Schematics of a junctional cut

a) Cell junction before ablation with the junction length d_0 and b) After ablation with the two vertices opening length d. c) A graph of distance between two vertices over time with a linear fit (in red), slope of this linear fit measures the initial velocity.

over the friction coefficient; this ratio is proportional to the tension of the severed junction just prior the ablation (*see* **NOTE 24**).

2. Circular ablation of a tensed tissue results in the contraction of the tissue inside the circle. The tissue retracts with an elliptic shape if stresses are anisotropic (*see* **NOTE 25**). Fit the shape outline over time and measure the minor and major axes. The initial velocity of retraction in one axis is equal to the stress-to-viscosity ratio along that axis. The ratio of velocities of the two axes gives the anisotropy of stress (*see* **NOTE 26**).

2.1.4 Notes

1. Here we describe the design of a home-built setup. Alternatively two-photon microscopes, which use NIR-fs lasers are also suitable for these types of experiments. UV pulsed-lasers have also been used successfully (Kiehart et al., 2000).

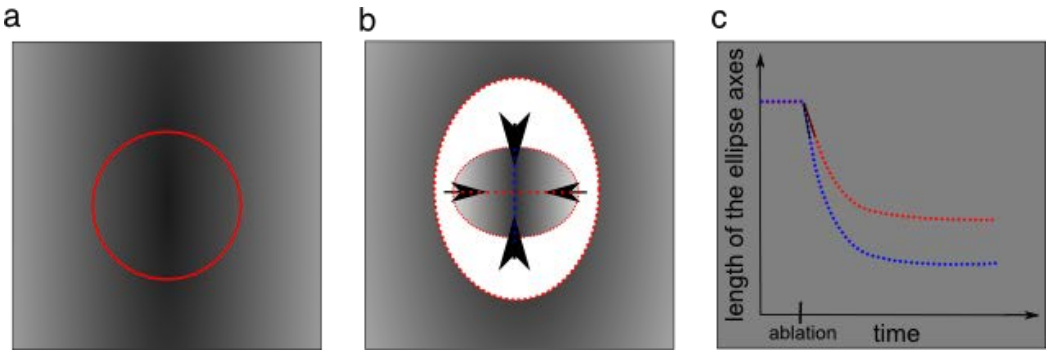

Figure 2.4: Schematics of a circular cut

a) Schematics of circular cut in a tissue before ablation with circle to be cut in red and b) after ablation with fitted ellipse to measure the minor and major axes (blue and red perpendicular lines). c) A graph of minor (blue) and major (red) axes lengths versus time with a linear fit for both the curves, with slope measuring the linear velocity.

2. Most mechanical shutters function like an iris, so, when it is fully closed there is still a small aperture. Therefore, place the shutter in such a way that, when the shutter is closed it should completely block the laser beam, and when it is open it fully transmits the laser beam.
3. The efficiency of a $\lambda/2$ waveplate is normally <100%, so if the polarization prism is not oriented along the laser beam polarization, the maximum transmission of the attenuator will be reduced. Therefore place the power meter after the prism and adjust it to get the maximum power for optimal orientation.
4. Light reflected by the attenuator should be sent to a beam trap (a black metal chamber for light absorption).
5. The galvanometer mirrors are used to obtain different cuts (point, line or circle). In our setup the ablating laser spot moves to produce cuts of different shapes; alternatively, one can move the stage of the sample holder (with a software to control the movement in order to obtain different cuts) instead of the laser.
6. The galvanometer mirrors must be conjugated with the back aperture of the objective, otherwise when the mirrors move, laser beam goes out of the aperture and laser beam will be lost.

7. The focal length of two lenses should be such that |f1/f2| gives the preferred beam expanding factor. If the back aperture of the objective is 8mm and the beam diameter is 1mm, then the expanding factor is 8. So one can use f1=240mm, f2=-30mm. The distances between two lenses should be |f1|-|f2|. The focal lengths below 20-30mm degrade the integrity of the laser beam, so it is better not to use lenses below this value. The lens with the smaller focal length must be placed first. Use a plano-convex lens and position the convex part of the lens facing outwards.
8. To focus the laser beam in the same plane as the imaging laser beam and to compensate the chromatic aberration of the microscope objective, the telescope lenses must be adjusted to produce a small divergence of the beam. An easy way is to observe the laser spot on the imaging software screen as one adjusts the telescope lenses in order to obtain a bright and focused spot.
9. For the laser beam alignment on telescope lenses, use the mirror which reflects the laser beam first to align the laser beam on first lens of the telescope and second mirror to align the beam on the second lens. Continue doing this till the laser beam is properly aligned.
10. Accurately select the size of the two mirrors that are placed after the telescope and mounted on the periscope and the size of the dichroic mirror. The minor axis should be at least as long as the diameter of the back aperture of the objective used and the major axis should be at least twice as long.
11. Inverted microscopes are suitable for laser ablation setups because they can have accessible space below the back aperture of the objective lens.
12. If the laser beam is aligned properly, then the high intensity laser spot is observed on the imaging software screen. If not, slightly adjust the periscope mirrors to get the correct spot position, which corresponds to maximum intensity. Moving one periscope mirror forms a line on the screen, while moving the other periscope mirror forms a line perpendicular to the previous one. The point of intersection of these two is the correct laser spot.
13. Extract the coordinates of the resulting ablation shape using the imaging software. This is then used to center/position the sample for the ablation experiments or use

the corresponding voltage values (previously calibrated) to move the laser spot on the preferred ablation position.

14. The resultant parameters obtained can later be used to get the cuts of desired units (normally in μm) for length or diameter.
15. Calibration varies for different objectives. For example, in our ablation system with a 100X objective, the two sinusoidal signals of 0.3V amplitudes and a 90^{o} phase difference sent to the galvanometer mirrors correspond to a circle with a 14μm diameter.
16. An easy way to recognize a zero hour pupa is that, it looks like a pupa in shape but still has the light whitish color of a larva.
17. Placing the pupa sideways is crucial because, we need to have access to one of the eyes. To avoid confusion always use the same eye, consistently analyzing either the right or left eye only.
18. A trick to remove the puparium: there is, a cap like structure near the head, and it is easier to remove this cap first so the puparium can be peeled off easily.
19. Using an oil drop helps to locate the eye under the microscope.
20. The ablation laser parameter sometimes varies from sample to sample, so if this happens, slightly change the laser power (20-30mW). This applies to all samples, pupae or embryos.
21. When imaging over long periods of time, sometimes it might be necessary to correct *Z*-drift while recording, otherwise analyzing the cuts will be a problem. This applies to all samples, pupae or embryos.
22. Markers other than β-catenin::GFP can be used to label cell junctions, such as E-cadherin::GFP. However, since the E-cadherin signal is low in some junctions, β-catenin is preferable.
23. The recording time can be lowered below 250ms but imaging laser exposure time must be changed accordingly. Quality of imaging is essential as the first few time points after ablation are used to extract recoil velocities by linear fitting. It is important to keep the number of points and the recording time interval the same to be able to compare tension at different junctions.

24. Ablation of a cell-cell junction leads to force imbalance as the tension of the targeted junction is abolished. The recoil velocity *v* just after ablation is determined by the ratio of the tension *T* of the targeted junction just prior to ablation and the friction forces, which resist the movement of vertices:

    $\nu = T(t=0+)/\mu$, where ν is the initial velocity, T is the junction tension and μ denotes the friction coefficient. The relaxation time, τ, is obtained by fitting an exponential to the curve and is determined by the ratio of friction over elastic modulus.

25. In a tissue level cut, many cell-cell contacts are ablated at once, for a single cell junction cut, the tension of the ablated junction is given by the initial velocity of vertices and the friction coefficient,

$$T = \nu\mu$$

    Applying the same argument over many cell-cell contacts leads to

$$\sigma \sim \eta\nu/L$$

$$\nu \sim L\sigma/\eta$$

    where L is the diameter of the ablation circle (used before cutting). The σ/η value for each axis gives stress-to-viscosity ratio in that direction and the ratio of σ/η values for the both the axes provides the anisotropy of stress in the tissue.

    The relaxation time, τ , for both the axes can be calculated by fitting an exponential curve.

26. One can measure the σ/η by doing line cuts; however the advantage of a circular cut is that it is possible to get the stress-to-viscosity ratio and stress anisotropy from a single experiment. This also makes the comparison easy.

2.2 Surface Evolver Simulation

Mechanics plays a significant role in epithelial morphogenesis, with cell adhesions and actomyosin contractility being the key regulators. With the advances in imaging like confocal microscopy, super-resolution microscopy, and mechanical measurements like optical tweezers, laser ablation the role of mechanics is now better understood. Models provide a complimentary tool along with these studies. Vertex models are commonly used in the area of epithelial morphogenesis (Fletcher et al., 2014). In these models, either the cross-section of epithelial sheets, or their apical plane is considered. Cells are treated as polygons made up of vertices connected by edges (Farhadifar et al., 2007). Such a two dimensional model is the minimal approach, there are also three dimensional vertex models with vertices and edges for lateral and basal surfaces (Bielmeier et al., 2016). The edges can shrink or elongate, the vertices can move, and the cells can undergo neighbor exchange. Some vertex models are force based (Weliky & Oster, 1990) and some are energy based (here forces emerge due to energy minimization) (Farhadifar et al., 2007; Landsberg et al., 2009). In this chapter, an energy based vertex model is implemented in an interactive program called Surface Evolver. We discuss a physical model to describe cone cell shapes and arrangements in retinal epithelium.

2.2.1 Surface Evolver- introduction

Surface Evolver is a freely available software to study surfaces that are shaped mainly by surface tension and other energies like gravitational energy and elastic energy. It is a suitable program to study soap bubbles and foams. An initial configuration is defined by the user in a datafile and the Evolver takes the defined surface towards its minimal energy configuration through the gradient descent method (Brakke, 1992). The surfaces can be one-dimensional ‘string models’ or two-dimensional ‘soapfilm models’. Along with surface tension (in the string model default values 1, the user can modify the values), the energy can be gravitational energy, elastic energy or user-defined quantities that can be expressed in terms of an integral

over the surface. The quantities are dimensionless, but one can use any physical units provided they are consistent.

The epithelial sheets are defined in a datafile with the vertices, edges connecting the vertices, and faces containing the edges. Each face is like a cell whose area can be either fixed or changing, depending on the problem of interest. In our simulations we fixed the area of the cells. In the experiments, the area can change with the amount of MyoII in the cell which can be attributed to the apical cell elasticity. In the simulations, variation in the area can be accounted for through an area elasticity term. This term sets the value of the cell area and is not important for the shape or arrangement of cells (Hilgenfeldt et al., 2008). Fixing the area reduces the number of free parameters and simplifies the problem. In Surface Evolver, each fixed quantity has a Lagrange multiplier—the rate of change of energy w.r.t. the constraint target value—associated with it. For the volume (or here, the area) the Lagrange multiplier is the pressure. The user can obtain the value of the pressure at any iteration step. Several constraints can be imposed on the vertices or edges, for example a particular vertex or edge can be fixed. One of the main features of vertex models is cell intercalation or T1 transition (Fletcher et al., 2014). As the surface minimizes its energy, if the length of any edge is below the threshold value (a value not normally observed in tissues) then it is allowed to intercalate. Surface Evolver offers the possibility to implement T1 transitions, creating a new vertex if necessary. Evolver reduces the energy by iteration, while obeying the constraints if any.

2.2.2 Experimental background and previous models

As explained in Section 1.2.2, at the level of the adherens junction, each ommatidium has four cone cells *viz.,* Equatorial (Eq), Polar (Pl), Anterior (A) and Posterior (P) and two primary pigment cells. The ommatidium also has six secondary pigment cells, three tertiary pigment cells, and three bristles shared with neighboring ommatidia [see also Figure 1.11]. Cone cells express both Ecad and Ncad, and all other cells express only Ecad**.** There is no interaction between Ecad and Ncad, hence Ncad is present only at the cone cell contacts.

Hayashi and Carthew (Hayashi & Carthew, 2004) suggested that cone cells might be minimizing their surface area, like soap-bubbles, because of the striking similarity in their arrangement and shapes. They also showed that Ncad maintains the wildtype cone cell shape, as Ncad mutants significantly changed their shape compared to the wildtype. The hypothesis of surface minimization was tested by Käfer et al. and Hilgenfeldt et al. (Hilgenfeldt et al., 2008; Käfer et al., 2007), by developing a physical model to explain the ommatidium shape based on experimentally obtained images. In both studies the energy function used is similar, but the modeling method is different. Käfer et al. used the cellular potts model, whereas Hilgenfeldt et al. used Surface Evolver. We know from studies of Käfer et al. that it is not possible to simulate the ommatidium shape using a simple soap-bubble like model. In a soap-bubble like model the energy, E, is related to the surface tension and area elasticity as follows.

$$E = \sum_{interfaces} \gamma_{ij} P_{ij} + \lambda_A \sum_{cells,i} \left(A_{ij} - A_{0ij}\right)^2 \qquad (2.1)$$

here P_{ij} is the length of the cell contact shared by cell i and cell j, A is the actual area of the cell, A_0 is the preferred area and λ_A is the area modulus of elasticity. With this energy function Käfer et al. had to increase the adhesion between Equatorial (top) and Polar (down) cone cells, which is not the case in experiments. Hence they came up with a model called variable tension model, in which energy function is as follows.

$$E = -\sum_{interfaces} J_{ij} P_{ij} + \lambda_P \sum_{cells,i} \left(P_{ij} - P_{0ij}\right)^2 + \lambda_A \sum_{cells,i} \left(A_{ij} - A_{0ij}\right)^2 \qquad (2.2)$$

Here $J<0$ is the adhesion term, so it is represented as negative line tension and $J=0$ means no adhesion for that contact. The new energy term, $\lambda_P \sum_{cells,i} \left(P_{ij} - P_{0ij}\right)^2$, maintains a positive interfacial tension, with P is the actual perimeter of the cell, P_0 is the preferred perimeter of the cell and λ_P is the perimeter modulus (perimeter elastic constant). In Hilgenfeldt et al. they have neglected the energy term, $\lambda_A \sum_{cells,i} \left(A_{ij} - A_{0ij}\right)^2$, as it does not influence the cell shapes but only the size of the cells; it also reduces the number of free parameters. They simulated the shape of several mutant ommatidia: Ncad mutants, *Rough eye* (Roi) mutants,

Ecad overexpression. Their computational work shows the importance of the role played by actomyosin network; however experimental proofs are needed.

2.2.3 Motivation and inputs used from the experiments

In the wildtype and Ncad mutant, when we looked at MyoII depending on the cadherins expressed in the cells (should not be confused with the cadherins observed at the junction), we observed three levels of MyoII at the junction. For example, let us consider two cells, cell 1 and cell 2 making contact. Then we found;

1) The lowest level of MyoII at the contact, when both cell 1 and cell 2 expressed both the Cadherins (both Ecad and Ncad adhesion at this contact)

2) Intermediate level of MyoII when both cell 1 and cell 2 expressed Ecad alone (only Ecad adhesion at this contact)

3) The highest level of MyoII when cell 1 expressed Ecad and cell 2 expressed Ecad as well as Ncad (there, note that here is only Ecad adhesion at this contact).

Laser ablations at these contacts revealed three levels of interfacial tensions corresponding to the three levels of MyoII**.** In the previous models, the free parameters were adjusted to compare to the wildtype ommatidium. We wanted to inject the experimental inputs into the model and mimic the wildtype along with the Ncad mutant cone cells. Along with the junction cuts, we measured the target perimeter of the cone cell (only equatorial and polar cone cells). Primary pigment cells at 41hrs APF are difficult to separate.

2.2.4 Mathematical formulation

In our model, adhesion is no longer an input parameter, since we measured the interfacial tension of each contact. We assumed that adhesion by cadherins, which tries to increase the

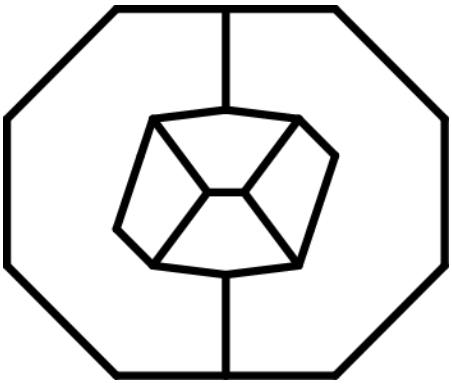

Figure 2.5: Initial configuration

Initial configuration containing six cells used in Surface Evolver to minimize the energy function.

contact between two cells, and cortical tension by MyoII, which tries to decrease the contact between two cells, result in a net tension which we call local tension γ_{loc}. MyoII has another contribution in the form of perimeter elasticity, which is the energy corresponding to the change in the cell perimeter (of cell i) from its preferred (target) perimeter, $P_{0i,}$ to the actual perimeter, $P_{i,}$ and K is the elastic constant. Thus we minimize the energy E given by,

$$E = \sum_{contact,ij} \gamma_{locij} l_{ij} + \sum_{cells,i} \frac{K}{2} \frac{(P_i - P_{0i})^2}{P_{0i}} \qquad (2.3)$$

where the length of cell contact *ij* between cell i and j.

2.2.5 Datafile

We minimize the energy function defined in equation (2.3) using Surface Evolver software starting from an unrealistic configuration (initial configuration) as shown in the [Figure 2.1]. Since we are interested in the cone cell shape and arrangements rather than the whole ommatidium itself and (also for the sake of simplicity), we have neglected the cells surrounding primary pigment cells (secondary pigment cells, tertiary pigment cells and bristles). Hence the initial configuration is composed of six cells. The first term in the energy

function, the energy contribution from local tension, can be set for each junction type. In Surface Evolver its default value is 1 and can be changed for each junction. The perimeter elasticity term in the energy function is programmed by method instance.

The interfacial tension is the energy change corresponding to the change in length, in other words the derivative of the energy function, *E,* in equation (2.3) with respect to the length l_{ij}. This derivative gives the interfacial tension of that contact (γ_{ij}),

$$\gamma_{ij} = \gamma_{loc,ij} + K\frac{\Delta P}{P_{0i}} + K\frac{\Delta P}{P_{0j}} \tag{2.4}$$

Thus the interfacial tension γ depends on the local tension and change in perimeter of cell *i* and change perimeter of cell *j*. We assume the change in perimeter $\Delta P/P_0$ is same for each cell. Hence,

$$\gamma \approx \gamma_{loc} + 2K\frac{\Delta P}{P_0} \tag{2.5}$$

From ablation experiments we have the interfacial tension γ and three interfacial junction terms for three types of cell contacts.

1) Cone cell – cone cell contact with the least tension

2) Primary pigment cells contact with the intermediate tension

3) Contact between cone cell and primary pigment cell with the highest tension

As mentioned in Section 2.1, the cuts do not give the absolute values of the junction tension, but the relative values. Hence they are normalized to the cone cell –cone cell contact with the least tension. Rewriting the equation (2.5),

$$\gamma \approx \gamma_{loc} + \gamma_{el} \tag{2.6}$$

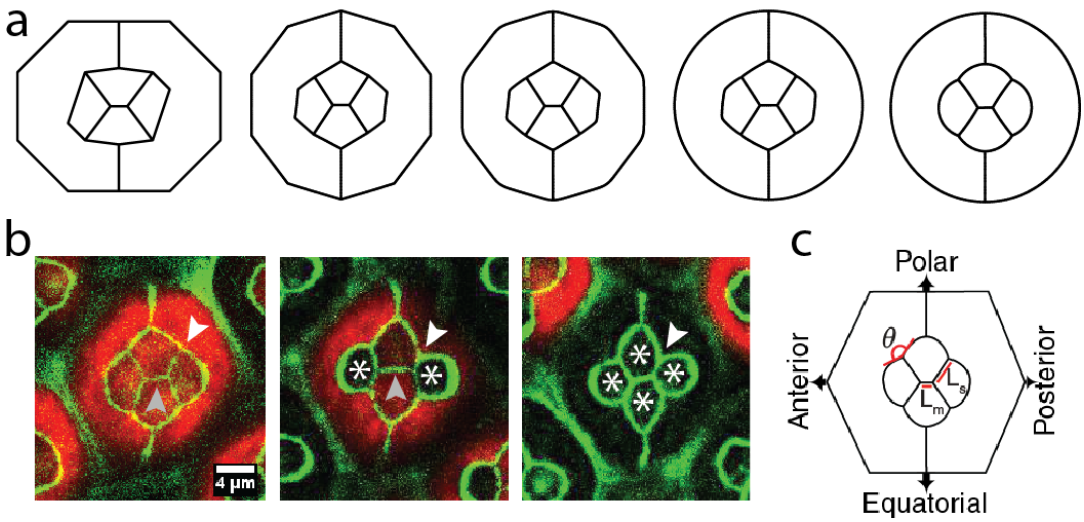

Figure 2.6: Simulation and fit parameters

a) A few examples of shape of six cells configuration at different iteration steps evolving towards minimal energy configuration b) Wildtype and Ncad mutants highlighting the change in angles (white arrows) and length of middle junction (grey arrows) in comparison to one another. Ncad mutant cells are marked by white asterisks. c) Schematics fit parameters measured in experiments and simulations with two axes polarity anterior (A)/posterior(P) and equatorial (Eq)/polar(Pl), contact angle between cone cell and primary pigment cell (θ), ratio of contact length shared by A/P and Eq/Pl cell (Ls) to contact length shared by Eq and Pl cells (Lm) (right).

where $\gamma_{el} = 2K\frac{\Delta P}{P_0}$ is the contribution to the tension from the perimeter elasticity. We measure γ_{el} from circle ablation and found $\frac{\Delta P}{P_0} = 8\%$ so $\gamma_{el} = 1.6K$.

For contact between cone cells

$$1 \approx \gamma_{loc} + 1.6K \tag{2.7}$$

For contact between primary pigment cells

$$1.3 \approx \gamma_{loc} + 1.6K \tag{2.8}$$

For contact between cone cell and primary pigment cell

$$2.04 \approx \gamma_{loc} + 1.6K \tag{2.9}$$

The interfacial tensions measured using ablation are 1, 1.3 and 2.04 after normalization. The only free parameter left is *K.* Writing the equation 2.6 in terms of local tension we get,

$$\gamma_{loc} \approx \gamma - 1.6K \tag{2.10}$$

We ran simulations for different values of *K*, ranging from 0.1 to 6 for both wildtype and Ncad mutant Ommatidia [an e.g. Figure 2.2a]. In simulations for Ncad mutants, the values of γ_{loc} for the respective junction are changed accordingly. For example, when all cone cells are Ncad mutants, then all the junctions have same value of γ_{loc}.

We fit the different simulated ommatidium shapes of wildtype and Ncad mutants to the experimentally observed shape using two fitting parameters. The fitting parameters are the angle and a length ratio [Figure 2.2c]. We choose these two descriptors because when one compares the wildtype cone cell shapes to the different Ncad mutants, they change significantly (compare the middle horizontal junction in wildtype and Ncad mutants in Figure 2.2b).

The Tables 2.1 and 2.2 give the mean value obtained from the experiments, we calculated the sum of residuals for the measured angles and ratios for wildtype and four different Ncad mutants. We use the weighted least square method to obtain cone cell shapes in simulation that match the experimentally observed shapes for the five configurations. In MyoII perturbed conditions, we measure the apical area (A)**.** We change the fixed areas accordingly in our simulation and the target perimeter was set by $P_0 = 2\sqrt{A\pi}$**.**

We observe that two Ncad mutants [Figure 2.3a] have vertical middle junction in contrast to the wildtype which has horizontal middle junction. We compare the minimized energy for different junction lengths, for both vertical and horizontal middle junctions. To obtain different junction lengths, we fixed those junctions in the simulations as shown in Figure 2.2b and noted the corresponding energy. Figure 2.2c shows the energy landscape for an ommatidium with equatorial cone cell lacking Ncad.

Angle (°)	Wildtype	Anterior cone cell Ncad mutant	Anterior and posterior	Adjacent cone cells Ncad mutant	All cone cells Ncad mutant
experiment	147.7±9 (n=210)	99.2±15 (n=9)	93.7±11 (n=8)	104.2±11 (n=28)	93.5±12 (n=64)
simulation	150.7	87.2	95.9	76.0	89.6

Table 2.1: Angle measurement

The angle (°) measured for wildtype and different Ncad mutant ommatidia in experiments and simulation

Ratio (Lm/Ls)	wildtype	Anterior cone cell Ncad mutant	Anterior and posterior	Adjacent cone cells Ncad mutant	All cone cells Ncad mutant
experiment	0.6±0.1 (n=43)	1.6±0.4 (n=9)	1.8±0.4 (n=8)	1.6±0.7 (n=28)	1.1±0.3 (n=15)
simulation	0.4	1.4	2.0	0.4	0.6

Table 2.2: Length ratio (Lm/Ls) measurement

The length ratio (Lm/Ls) measured for wildtype and different Ncad mutant ommatidia in experiments and simulation.

In results and corresponding supplementary materials, Section 3.1, the biological basis and the experiments are explained in detail.

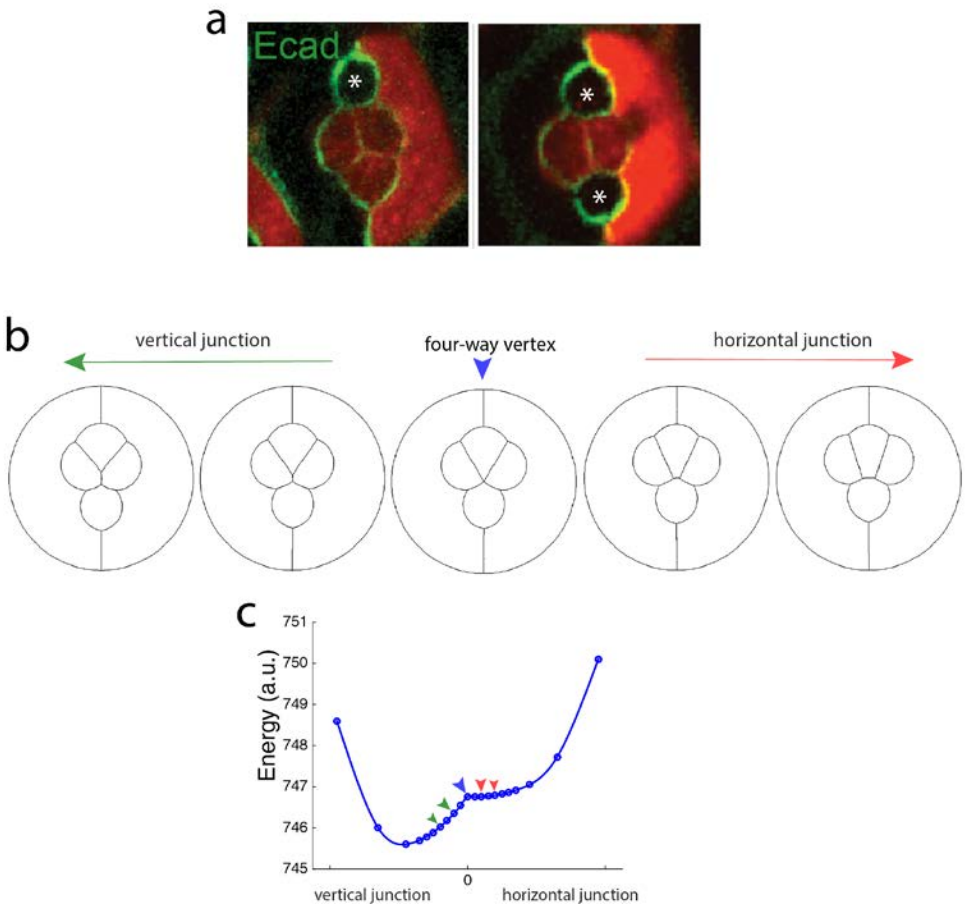

Figure 2.7: Eq/Pl Ncad mutants and energy landscape

a) Eq and Eq/Pl Ncad mutant cone cells. Ncad mutant cells are marked by white asterisks. b) Simulations with middle junctions fixed at different lengths in both vertical and horizontal configurations, including four-way vertex configuration to note and compare the energy. c) The energy (in a.u.) plotted for different junction lengths at different configurations (the arrows in green, blue and red correspond to the respective simulated ommatidia in b).

Chapter 3: Results

Section 3.1 of this chapter covers the results of our observations and concentration measurements of MyoII, Ecad and Ncad (tagged version of Ncad with the help of CRISPR) in *Drosophila* retina at 41 hrs APF and based on the observations of MyoII, measurements of interfacial tension using the laser ablation technique (discussed in Section 2.1). This chapter also includes the results from simulations using Surface Evolver (based on the energy minimization principle). We conclude this section by combining our concentration measurements and interfacial tension measurements, to obtain the relative contributions of MyoII cortical tension, Ecad adhesion and Ncad adhesion to the tension of cell contact. Section 3.2 includes the experiments aimed at understanding the neighbor exchange among cone cells which occurs during retinal morphogenesis. All of our hypotheses were tested using the laser ablation technique and so far they yield no positive result. Section 3.3 covers the experiments of Ecad overexpression in pupal wing disc, based on the results obtained on the Ncad mis-expression in wing disc.

3.1 Patterned cortical tension mediated by N-cadherin controls cell geometric order in the *Drosophila* eye

Adhesion molecules hold cells together, but also couple cell membranes to a contractile actomyosin network, which limits the expansion of the cell contacts. The role of adhesion molecules and actomyosin contractility in tissue morphogenesis is well established, but their importance and co-ordination in achieving cell shapes and cell arrangements remain unclear. We use the *Drosophila* eye as a model system to tackle this question in this section.

This section is composed of an article that has been published in the journal eLife. As mentioned in '*Foreword*' of this thesis, it is a joint work between myself and Eunice Chan. My contributions to this project include: quantification of all the images and data, performing laser ablation experiment, developing the physical model and performing the simulations.

eLIFE elifesciences.org

RESEARCH ARTICLE

Patterned cortical tension mediated by N-cadherin controls cell geometric order in the *Drosophila* eye

Eunice HoYee Chan*†, Pruthvi Chavadimane Shivakumar†, Raphaël Clément, Edith Laugier, Pierre-François Lenne*

Aix Marseille Univ, CNRS, IBDM, Marseille, France

Abstract Adhesion molecules hold cells together but also couple cell membranes to a contractile actomyosin network, which limits the expansion of cell contacts. Despite their fundamental role in tissue morphogenesis and tissue homeostasis, how adhesion molecules control cell shapes and cell patterns in tissues remains unclear. Here we address this question in vivo using the *Drosophila* eye. We show that cone cell shapes depend little on adhesion bonds and mostly on contractile forces. However, N-cadherin has an indirect control on cell shape. At homotypic contacts, junctional N-cadherin bonds downregulate Myosin-II contractility. At heterotypic contacts with E-cadherin, unbound N-cadherin induces an asymmetric accumulation of Myosin-II, which leads to a highly contractile cell interface. Such differential regulation of contractility is essential for morphogenesis as loss of N-cadherin disrupts cell rearrangements. Our results establish a quantitative link between adhesion and contractility and reveal an unprecedented role of N-cadherin on cell shapes and cell arrangements.

DOI: 10.7554/eLife.22796.001

***For correspondence:** ho-yee.chan@univ-amu.fr (EHoYC); pierre-francois.lenne@univ-amu.fr (P-FL)

†These authors contributed equally to this work

Competing interests: The authors declare that no competing interests exist.

Funding: See page 23

Received: 29 October 2016
Accepted: 08 May 2017
Published: 24 May 2017

Reviewing editor: Frank Jülicher, Max Planck Institute for the Physics of Complex Systems, Germany

Introduction

Cells acquire different shapes and arrangements to form tissues, depending on their functions and microenvironment. During tissue morphogenesis, cells actively form and remodel their cell contacts, generating forces to drive various morphogenetic events (***Lecuit and Lenne, 2007***). In epithelia, cell division (***Herszterg et al., 2013***; ***Guillot and Lecuit, 2013***; ***Founounou et al., 2013***), cell intercalation (***Bertet et al., 2004***; ***Blankenship et al., 2006***) and cell delamination (***Marinari et al., 2012***) are basic mechanisms of morphogenesis, which all involve gain or loss of cell contacts (***Heisenberg and Bellaïche, 2013***). Two systems contribute to changes in cell contacts: Cadherin complexes and actomyosin networks (***Harris, 2012***; ***Baum and Georgiou, 2011***).

At the level of a single cell contact, formation of cadherin-cadherin bonds favors contact expansion. Actomyosin contractility acts antagonistically by reducing cell contact size (***Lecuit and Lenne, 2007***; ***Winklbauer, 2015***). There is numerous evidence in vivo that shows actomyosin-generated tension regulates cell shape (***Rauzi et al., 2008***; ***Martin et al., 2009***). In vitro, contact size is mainly determined by actomyosin contractility but not cadherin engagement (***Maître et al., 2012***). However, in *Drosophila* retina, N-cadherin mutants show drastic alteration of contact size and cell shape (***Hayashi and Carthew, 2004***), which suggests that cadherin-associated adhesion cannot be discounted. Even though the forces produced by cadherins and actomyosin networks act antagonistically, both systems are interconnected as cadherins are associated with intracellular actomyosin networks via catenins and other actin-binding proteins (***Priya et al., 2013***; ***Röper, 2015***).

Due to the intrinsic links between cadherin-dependent adhesion and actomyosin contractility, it is challenging to address whether and how cadherin adhesion regulates cell shape. What is the direct contribution of cadherin-cadherin bonds to cell shape? Do cadherins influence cell shape through

actomyosin contractility? To address these questions, we investigated the origin of cell shapes in vivo in the highly organized *Drosophila* retina, which features differential expression of cadherin molecules and is amenable to quantification of cell shapes and mechanical measurements. In particular, the *Drosophila* retina is an ideal system to study heterotypic contacts, and their differences with homotypic contacts.

Drosophila retina is composed of approximately 750 facets called ommatidia (**Cagan and Ready, 1989**; **Tepass and Harris, 2007**), each of which includes four cone cells (C) embedded in two primary pigment cells (P), along with other cell types shared by neighboring ommatidia (**Figure 1A,B**). The pattern of cone cells arrangement is strikingly similar to that of soap bubbles (**Hayashi and Carthew, 2004**). While this visual resemblance suggests that cells might minimize their surface of contact, both contractility and adhesion have to be considered for cell shape and cell arrangements (**Lecuit and Lenne, 2007**), as indicated by physical models (**Käfer et al., 2007**; **Hilgenfeldt et al., 2008**). Two classical Type I cadherins, E-cadherin (Ecad) and N-cadherin (Ncad) are expressed in the retina and specific expression of N-cadherin solely in cone cells governs the cone cell shape and arrangements (**Hayashi and Carthew, 2004**). In silico predictions based on energy minimization reproduce well the cone cell shapes but have limited experimental support (**Käfer et al., 2007**; **Hilgenfeldt et al., 2008**). In particular, the contributions of Ncad-mediated actomyosin contractility, as well as the interfacial tension in cone cell shape control, have not been explored.

Ncad is involved in numerous morphogenetic processes including cell migration, neural tube formation, and axon guidance (**Derycke and Bracke, 2004**; **Hirano and Takeichi, 2012**; **Lee et al., 2001**). To date, the direct implication of Ncad and actomyosin complexes on cell sorting and patterning during development is unclear. Ncad depletion in *Xenopus* neural plate leads to the loss of activated form of myosin light chain (**Nandadasa et al., 2009**). Actin cytoskeleton remodelling in *Drosophila* glial cells is tightly regulated by Ncad levels (**Kumar et al., 2015**). In cell culture, a dynamic interaction was reported between Ncad and actomyosin complexes in myocytes (**Comunale et al., 2007**; **Ladoux et al., 2010**; **Shih and Yamada, 2012**; **Chopra et al., 2011**), neurons (**Bard et al., 2008**; **Luccardini et al., 2013**; **Garcia et al., 2015**; **Okamura et al., 2004**; **Chazeau et al., 2015**) and fibroblasts (**Ouyang et al., 2013**).

Here we combine mechanical measurements, quantitative microscopy and modelling to revisit the role of Ncad in cell shapes and cell arrangement. We show that Ncad bonds contribute two fold less than Myosin-II (MyoII) to interfacial tension, but that Ncad also affects localization and levels of MyoII, and thus cell shapes. We reveal that heterotypic interfaces between Ncad-expressing and non-Ncad-expressing cells accumulate MyoII more than homotypic interfaces, thereby stabilizing specific cell configurations. Our results emphasize the interplay between cadherins and actomyosin networks, which determines cell shape and cell arrangements during morphogenesis.

Results

Cadherins and Myosin-II distribution in pupal retinas

To visualize the patterns of cadherins in ommatidia, we analyzed their expression in Ncad::GFP (**Figure 1C**) and Ecad::GFP knock-in retinas (**Figure 1D**) (*See Material and methods for details*). As previously reported (**Hayashi and Carthew, 2004**), Ncad is localized at cone cell-cone cell contacts (C|C), where it forms homophilic complexes (**Figure 1C**, *white arrowhead*). Ncad is also found at low level at the junctions between cone cell and primary pigment cell (C|P) (**Figure 1C**, *cyan arrowhead* and **Figure 1—figure supplement 1A**). At C|P contacts, Ncad cannot form trans-homophilic bonds but cis-homophilic bonds, as it is expressed in cone cells but not in primary pigment cells. In addition, Ncad-Ecad trans-heterotypic bonds appear to be absent, as *Ecad* mutant cone cell loses contact from the neighbouring Ecad expressing primary pigment cell (**Hayashi and Carthew, 2004**). Ecad is present in all cell contacts albeit at different levels. Ecad concentration is lower at C|C relative to C|P and at primary pigment cell and primary pigment cell contacts (P|P) (**Figure 1D**). To visualize the pattern of MyoII, we imaged Myosin heavy chain (Zip)::YFP knock-in retinas (**Figure 1E**), and Myosin light chain (Sqh)::GFP flies driven by *Sqh* promotor in *Sqh* mutant background (**Figure 1—figure supplement 1B**). We also stained Zip::YFP or Sqh::GFP retinas with Phospho-Myosin-II light chain antibodies which labels active MyoII to check how well they correlate with each other (**Figure 1—figure supplement 1C,D**). As reported earlier (**Warner and Longmore, 2009**;

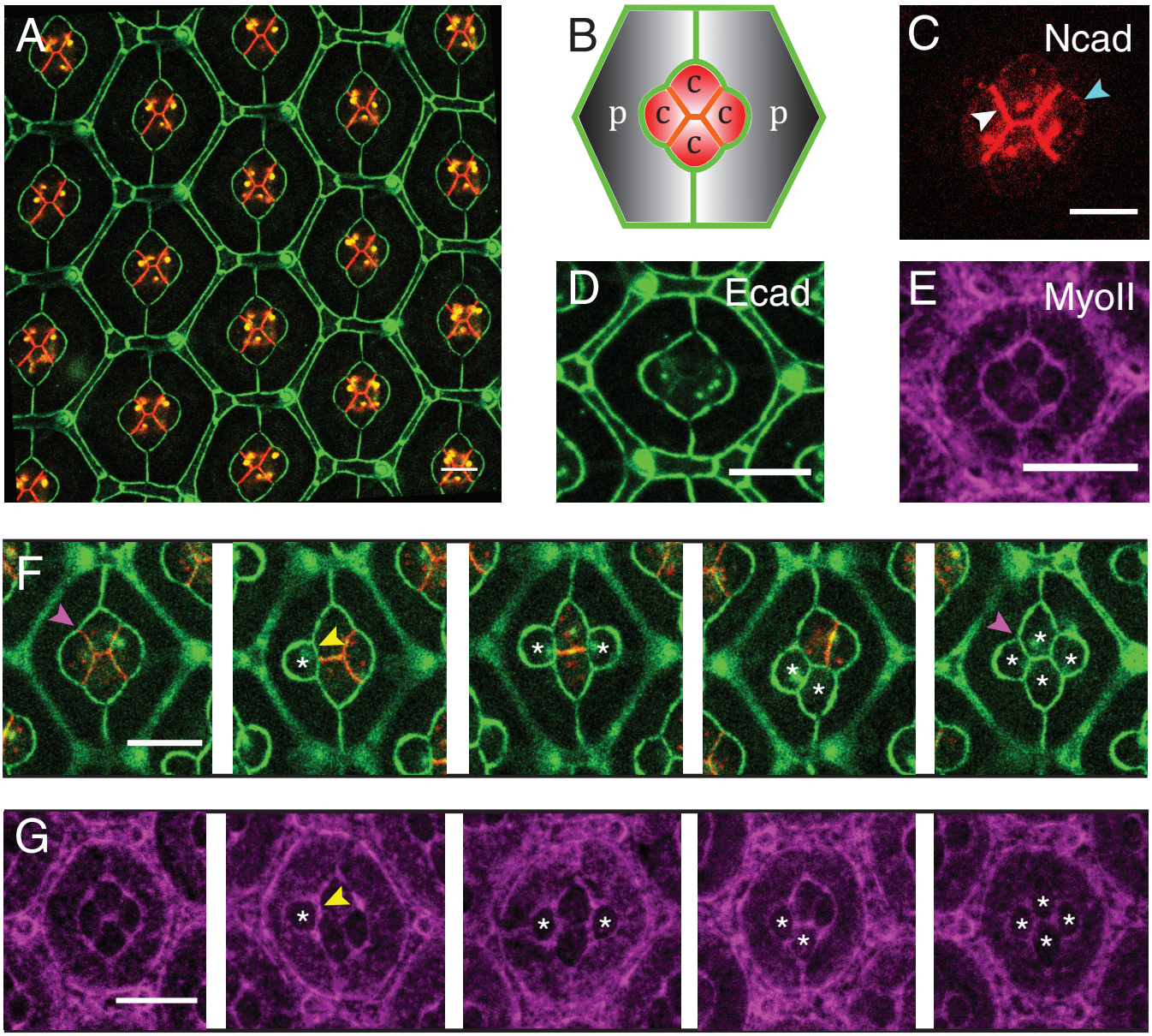

Figure 1. Patterns of *Drosophila* eye with the distributions of cadherins and Myosin-II (MyoII) in wildtype and $Ncad^{M19}$ mosaic ommatidia. (**A**) Image of pupal retina at 41 hr after puparium formation (APF) consisting of repeating lattice structure called ommatidia labeled with Ecad::GFP (green) and Ncad::mKate2 (red). (**B**) A schematic of the most apical view of an ommatidium, which contains four cone cells (**C**) and two primary pigment cells (P), and the localization of cadherins (Ecad in green and Ncad in red). (**C–E**) An individual ommatidium with Ncad::GFP in red (**C**), Ecad::GFP in green (**D**), Zip::YFP in magenta (**E**). (**F–G**) Wildtype and $Ncad^{M19}$ mosaic ommatidia labelled with Ecad::GFP (green), Ncad (red) and Zip::YFP (magenta). $Ncad^{M19}$ cone cells are marked by white asterisks. Magenta arrowheads in (**F**) shows the angle change in full $Ncad^{M19}$ cone cells compared to wildtype. White arrowhead indicates the C|C contact with homophilic complexes and cyan arrowhead indicates the C|P contact in (**C**). Yellow arrowheads indicate one of the contacts at the interface between wildtype and $Ncad^{M19}$ cells to highlight the absence of Ncad adhesion in (**F**) and significant increase in MyoII levels in (**G**). Scale bar, 10 μm.

DOI: 10.7554/eLife.22796.002

The following source data and figure supplements are available for figure 1:

Figure supplement 1. Ncad and MyoII levels using different reporters (Myosin-II light chain, Myosin-II heavy chain and Phospho-myosin-II light chain).

DOI: 10.7554/eLife.22796.003

Figure supplement 1—source data 1. Dataset for ***Figure 1- supplement figure 1A***.

DOI: 10.7554/eLife.22796.004

Yashiro et al., 2014; *Deng et al., 2015*), Phospho-Myosin-II light chain antibodies show a punctate distribution, but overall the three markers indicate that MyoII is enriched at cell contacts and is also present as apical mesh at a lower concentration.

Loss of N-cadherin not only affects cone cell shape but also Myosin-II levels

To assess the impact of Ncad on cone cell shapes, we performed mosaic analysis to generate Ncad loss of function ($Ncad^{M19}$) clones in pupal retinas. *Ncad* mutation in one or multiple cone cells results in significant cell shape changes (*Figure 1F*), as reported earlier (*Hayashi and Carthew, 2004*). Shape variations are dependent on the numbers and combinations of wildtype and $Ncad^{M19}$ cone cells in the mosaic ommatidia (*Figure 1F*). In a full $Ncad^{M19}$ ommatidium, the four cone cells acquire a cruciform shape rather than the normal diamond shape (last and first image respectively in *Figure 1F*). Reduction in cell contact length (*Figure 1F, yellow arrowhead*) and change in angles (*compare first and the last image of Figure 1F, magenta arrowhead*) suggests that adhesion by homophilic bonding of Ncad causes a significant expansion of contacts between cone cells. Apart from the cell shape changes, there are variations in MyoII levels at mosaic $Ncad^{M19}$ ommatidium. For instance, at wildtype and $Ncad^{M19}$ cone cell contact, there is a significant increase in MyoII level (*Figure 1G, yellow arrowhead*). So, the loss of *Ncad* induces change in MyoII concentrations, suggesting a possible contribution of MyoII contractility in shaping cone cell patterns (*Figure 1G*).

Differential Myosin-II levels and interfacial tension

To explore the role of contractile forces in cone cell shapes, we determined the distribution of MyoII, a proxy for contractility, and measured interfacial tension acting at cell contacts in wildtype and $Ncad^{M19}$ mosaic ommatidia.

We used Zip::YFP fluorescence intensity as a readout of MyoII concentration. We observed different levels of MyoII at cell contacts, depending on whether (i) the two cells, for example cell 1 and cell 2 in contact express both Ecad and Ncad (1(E,N)|2(E,N)), (ii) the two cells in contact express only Ecad (1(E)|2(E)), (iii) one of the two cells in contact expresses only Ecad and another expresses both Ecad and Ncad (1(E)|2(E,N)) (*Figure 1G*, yellow arrowhead and *Figure 1F,G*).

In wildtype ommatidia, MyoII level was found 2.2-fold higher at the contact between cone cell and primary pigment cell, C(E,N)|P(E), than at C(E,N)|C(E,N) contacts. MyoII at contacts between primary pigment cells, P(E)|P(E), was found 1.8-fold higher than at C(E,N)|C(E,N) contacts (*Figure 2A–C*, *Supplementary file 1* - table 1). A same trend in MyoII concentration is also observed when using Sqh::GFP as marker (*Figure 2—figure supplement 1A–C*, *Supplementary file 1* -table 1). Interestingly, in $Ncad^{M19}$ mosaic ommatidium comprised of two $Ncad^{M19}$ cone cells, we again observed three distinct levels of MyoII depending on the genotype of the two cone cells in contact (WT and WT (C(E,N)|C(E,N)), WT and $Ncad^{M19}$ (C(E,N)|C(E)), $Ncad^{M19}$ and $Ncad^{M19}$ (C(E)|C(E))) (*Figure 2D–F* and *Figure 2—figure supplement 1D–H*, *Supplementary file 1* -table 1). These data revealed a simple gradation in MyoII concentration c_{Myo}, similar to the wildtype at C(E,N)|C(E,N), P(E)|P(E) and C(E,N)|P(E) contacts: c_{Myo}(C(E,N)|C(E,N))=1, c_{Myo}(C(E)|C(E))=1.6, and c_{Myo}(C(E,N)|C(E))=2.3 (in arbitrary units). Our data indicates that differences in MyoII concentrations at contact are dependent on Ncad expression in the cells.

Apart from MyoII, we also observed differences in Ecad levels when comparing C(E,N)|C(E,N), C(E)|C(E), C(E,N)|C(E) contacts (*Figure 2—figure supplement 1F,G,H*, *Supplementary file 1* -table 2), raising the possibility that the changes in MyoII levels might be a consequence of Ecad homotypic interactions. However, MyoII levels are uncorrelated with Ecad levels, ruling out this possibility (*Figure 2—figure supplement 1G and H*).

MyoII level anti-correlates with cell contact length (*Figure 2—figure supplement 1G,H*), which is consistent with the idea that MyoII regulates length. One can argue that the knowledge of MyoII distribution is not sufficient to characterize contractility and that F-actin distribution and organization might also be an important determinant (*Reymann et al., 2012*). Thus, we stained for F-actin using phalloidin and found that F-actin is mostly apical and junctional like MyoII, but its distribution does not strictly correlate with that of MyoII; homotypic C(E,N)|C(E,N) contacts show higher F-actin level than C(E,N)|P(E), C(E,N)|C(E), P(E)|P(E) and C(E)|C(E) contacts (*Figure 2—figure supplement 2A–C*).

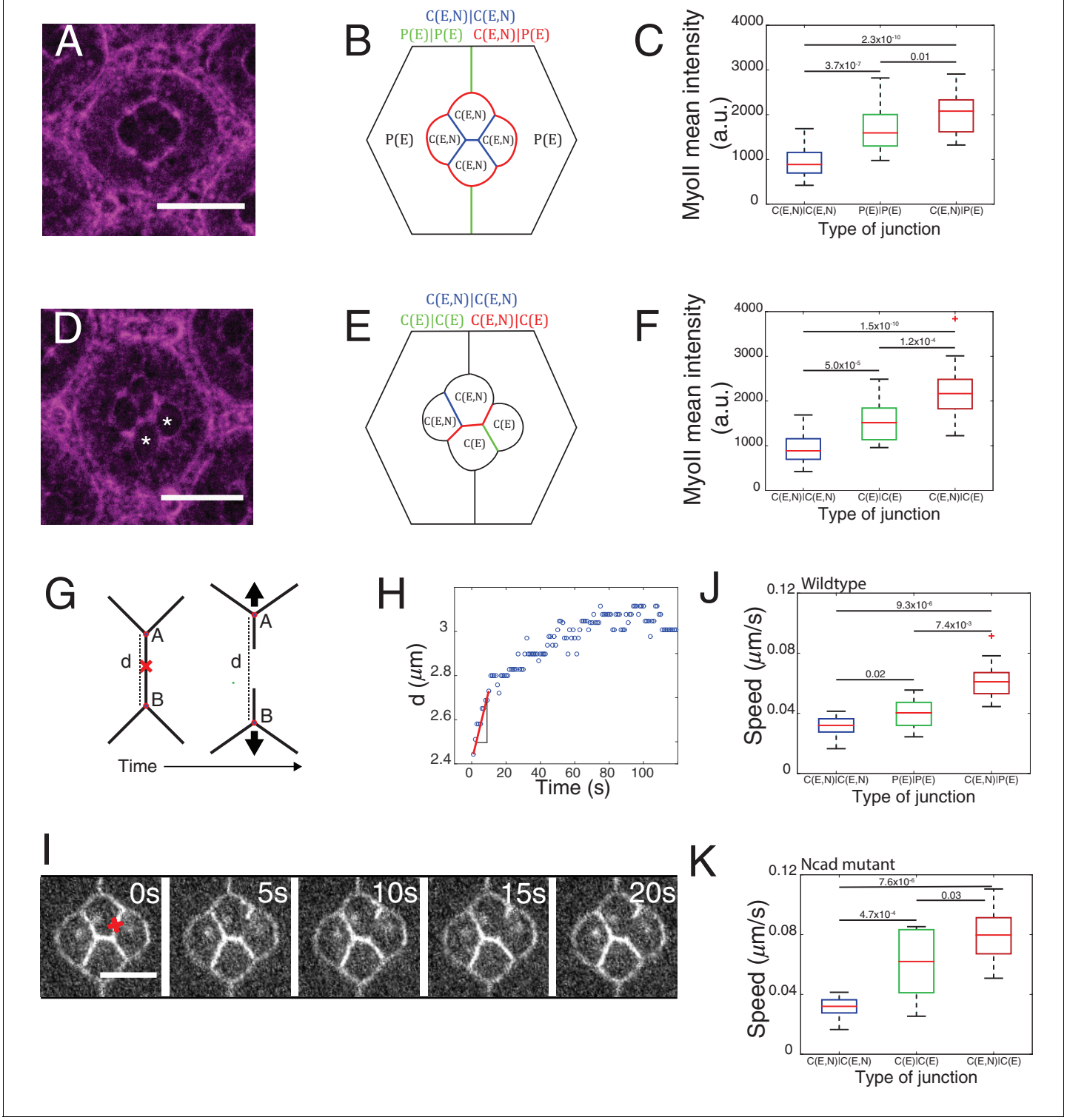

Figure 2. Differential MyoII levels and interfacial tensions at various cell contacts. (**A**) Wildtype ommatidium with Zip::YFP represented by (**B**) a schematic that highlights three different types of contacts at cell interfaces that express Ecad or Ncad or both E and Ncad. C(E,N)|C(E,N) contact (blue) shared by two cone cells, P(E)|P(E) contact (green) shared by two primary pigment cells and C(E,N)|P(E) contact (red) shared by a cone and a primary pigment cell. Scale bar, 10 μm. (**C**) Quantification of MyoII intensity in C(E,N)|C(E,N) (n = 30), P(E)|P(E) (n = 22) and C(E,N)|P(E) (n = 36) contacts. P-values are shown above the black horizontal lines (non-parametric Mann-Whitney U test on pairs and Bonferroni correction). (**D**) A *Ncad*^{M19} mosaic ommatidium with Zip::YFP. *Ncad*^{M19} cells are marked by white asterisks. Scale bar, 10 μm. (**E**) A schematic represents the corresponding *Ncad*^{M19}

Figure 2 continued on next page

Figure 2 continued

mosaic mutants highlighting C(E,N)|C(E,N) (blue), C(E)|C(E) (green) and C(E,N)|C(E) contacts (red). (**F**) Quantification of MyoII intensity in C(E,N)|C(E,N) (n = 30), C(E)|C(E) (n = 22) and C(E,N)|C(E) (n = 36) contacts. P-values are shown above the black horizontal lines. (**G**)-(**K**) Laser nanoablation experiments to estimate interfacial tension. (**G**) Schematic of a contact before (left) and after (right) ablation. Red cross represents the point of the ablation. Vertex A and B recoil changing distance 'd' after ablation. (**H**) Opening curve plots the distance' d' over time with a linear fit for initial time points to get the initial recoil speed. (**I**) Snapshot of an ablation at C(E,N)|C(E,N) contact in wildtype ommatidium, red cross indicates the ablation point. (**J**) Quantification of initial recoil speed of C(E,N)|C(E,N) (n = 14), P(E)|P(E) (n = 18) and C(E,N)|P(E) (n = 19) contacts in wildtype ommatidia. P-values are shown above the black horizontal lines. (**K**) Quantification of initial recoil speed in C(E,N)|C(E,N) (n = 14), C(E)|C(E) (n = 18) and C(E,N)|C(E) (n = 17) contacts in *Ncad*^{M19} mosaic mutants. Scale bar, 5 μm. P-values are shown above the black horizontal lines.

DOI: 10.7554/eLife.22796.005

The following source data and figure supplements are available for figure 2:

Source data 1. Dataset for ***Figure 2C,F,J and K***.

DOI: 10.7554/eLife.22796.006

Figure supplement 1. Junction length, cadherins and MyoII levels at different contacts.

DOI: 10.7554/eLife.22796.007

Figure supplement 1—source data 1. Dataset for ***Figure 2—figure supplement 1C,G and H***.

DOI: 10.7554/eLife.22796.008

Figure supplement 2. *Ncad*^{M19} mosaic ommatidium interfacial tension measurements and F-actin distribution.

DOI: 10.7554/eLife.22796.009

Figure supplement 2—source data 1. Dataset for ***Figure 2—figure supplement 2B and C***.

DOI: 10.7554/eLife.22796.010

In an attempt to determine the relationship between MyoII-dependent contractility and tensile forces at cell contacts, we performed laser nano-dissection experiments (***Rauzi et al., 2008***). The initial recoil speed after the cell contact ablation served as a proxy for interfacial tension (***Figure 2G–I***, ***Figure 2—figure supplement 2D***, ***Videos 1*** and ***2***). We found that tension at C(E,N)|C(E) contacts was the highest while tension at C(E,N)|C(E,N) contacts was the lowest (***Figure 2J,K***). These values correlate with the levels of MyoII (compare ***Figure 2C and J*** or ***Figure 2F and K***) and are consistent with the hypothesis that MyoII is a major determinant of interfacial tension.

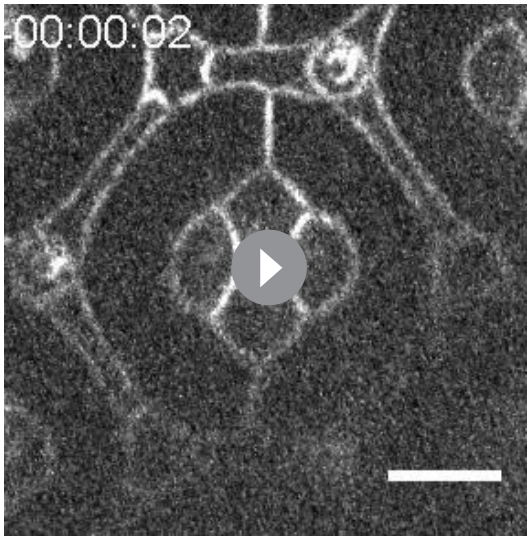

Video 1. Laser nano-ablation of C(E,N)|C(E,N) contact in wildtype ommatidium. Ablation at 00:00:00. Frame rate is 1 s/frame. Labelling: β-cat::GFP. Scale bar, 5 μm.

DOI: 10.7554/eLife.22796.011

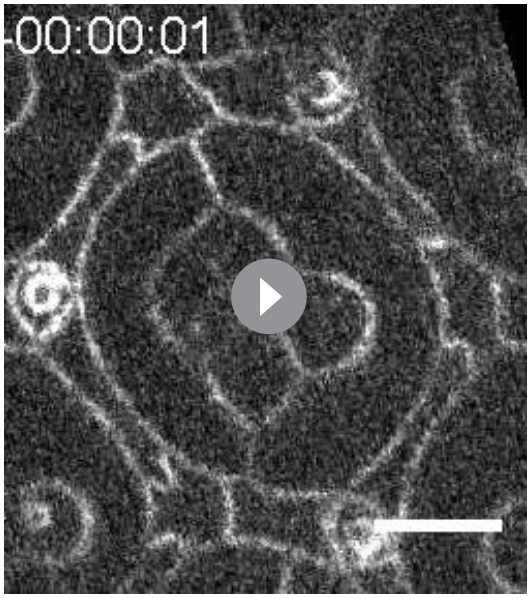

Video 2. Laser nano-ablation of C(E,N)|C(E) contact in *Ncad*^{M19} mosaic ommatidium with polar (Pl) and posterior (P) cone cells(see ***Figure 5A*** for cone cell axes of polarity) lacking *Ncad*. Ablation at 00:00:00. Frame rate is 250 ms/frame. Labelling: Ecad::GFP. Scale bar, 5 μm.

DOI: 10.7554/eLife.22796.012

Bound and unbound N-cadherin differentially impact on Myosin–II junctional localization

To determine whether and how Ncad might control cell shape through MyoII regulation, we focused on the links between Ncad and MyoII localization. We observed high level of Ncad at homotypic contacts (C(E,N)|C(E,N)) which also exhibit the lowest concentration of MyoII, by 1.8 fold lower than the P(E)|P(E) cell contacts. This suggests that homophilic Ncad at homotypic contact reduces MyoII levels (***Figure 2A,C***), in agreement with the idea that cadherin lowers interfacial tension at cell contacts (***Maître and Heisenberg, 2013***). At heterotypic contacts (C(E,N)|P(E)), where Ncad cannot form transhomophilic bond, Ncad was found at very low level (***Figure 1C***, ***Figure 1—figure supplement 1A***) and MyoII at a higher level than at any other contact (***Figure 2A,C***). This suggests that unbound Ncad at heterotypic contact signals to MyoII and induces its accumulation. To confirm this hypothesis, we took advantage of the fact that the primary pigment cells do not express Ncad and asked if we could modify MyoII level at different cell contacts by Ncad misexpression.

Ncad misexpression in one of the primary pigment cell affected the shape of cone cells in contact with it (***Figure 3A,B***). Homophilic Ncad was detected at the C(E,N)|P(E,N+) contacts (***Figure 3—figure supplement 1A and A'***, *yellow arrowhead*) and MyoII levels at these modified contacts (C(E,N)|P(E,N+), ***Figure 3A,B***, *yellow arrowhead*) were significantly reduced compared to wildtype C|P contacts (C(E,N)|P(E), ***Figure 3A,B***, *green arrowhead*, ***Supplementary file 1*** - table 1). This confirms our hypothesis that homophilic Ncad reduces MyoII level (***Figure 3C***). In addition, higher level of MyoII was detected at contacts between primary pigment cells with one of them misexpressing Ncad (P(E)|P(E,N+)) (***Figure 3A,D*** *red arrowhead*) than at contacts between wildtype primary pigment cells expressing only Ecad (P(E)|P(E)) (***Figure 3A,B,D***, ***Supplementary file 1*** -table 1).

To test whether such property of Ncad is specific to the retinal epithelium or more general, we performed clonal misexpression of Ncad in the larval wing pouch which cells express only Ecad. We noticed higher level of MyoII at the boundary of clones compared to MyoII inside the clones or to the surrounding wildtype tissue (***Figure 3—figure supplement 1B,C***, *cyan arrowheads*). This indicates that MyoII regulation by Ncad is not specific to the retina.

At C(E,N)|P(E) contacts, Ncad is asymmetrically localized as it is expressed only in one of the two apposed cells. We thus wondered whether MyoII could also be asymmetrically localized. To address this, we measured the intensity profile of MyoII perpendicular to C(E,N)|P(E) contacts, using Ecad intensity as a marker for the contact position. Localization of Ecad::GFP, and thus the contact position, can be determined with a precision better than the diffraction limit given the high signal/noise ratio (5–22 nm) (***Figure 3—figure supplement 2***, *See Materials and methods*). We found that MyoII maximum intensity was systematically shifted towards the cell that expressed both Ecad and Ncad (***Figure 3—figure supplement 2A,B***). Importantly, the distance between MyoII and Ecad intensity peaks (***Figure 3—figure supplement 2C***) was found larger than the imprecision in peaks' localization (***Figure 3—figure supplement 2D***, *See Material and methods*). This significant and systematic shift indicates that MyoII is enriched in the cortex of an Ecad- and Ncad-expressing cell when it is apposed to an Ecad-expressing cell (***Figure 3E–G***). Using Starry night (Stan), a membrane marker that has a higher signal/noise ratio than Ecad at C(E,N)|C(E,N) contacts (***Figure 3—figure supplement 2E***), we confirmed the asymmetry of MyoII at C(E,N)|P(E) contacts (***Figure 3—figure supplement 2F,G***). In contrast, we observed a symmetric localization of MyoII at C(E,N)|C(E,N) contacts (***Figure 3—figure supplement 2F,H***).

This increase in MyoII level is cell contact autonomous: we observed higher MyoII intensity at C(E,N)|P(E) contacts, irrespective of the other contacts of the cell (for instance, C(E,N)|C(E,N)). This increase is striking in $Ncad^{M19}$ mosaic ommatidia in which a single Ecad- and Ncad-expressing cell is surrounded by Ecad-expressing cells: we noticed an intense ring of MyoII at the cortex (***Figure 3—figure supplement 3A,B,C***, *compare cells marked by white and green arrowheads*, ***Figure 3—figure supplement 3C***). To further confirm the above observation, Ncad was again misexpressed in primary pigment cells to check if it could induce MyoII asymmetry at the modified P(E)|P(E,N+) contacts. An asymmetric localization of MyoII in cells that express both Ecad and Ncad was observed at the P(E)|P(E,N+) contacts (***Figure 3H–J***).

To further explore how Ncad at heterotypic contacts could induce MyoII contractility, we expressed only the extracellular part of Ncad in one primary pigment cell (***Figure 4A***, *white +*). Such truncated Ncad can form adhesion bonds but cannot interact with the actomyosin network

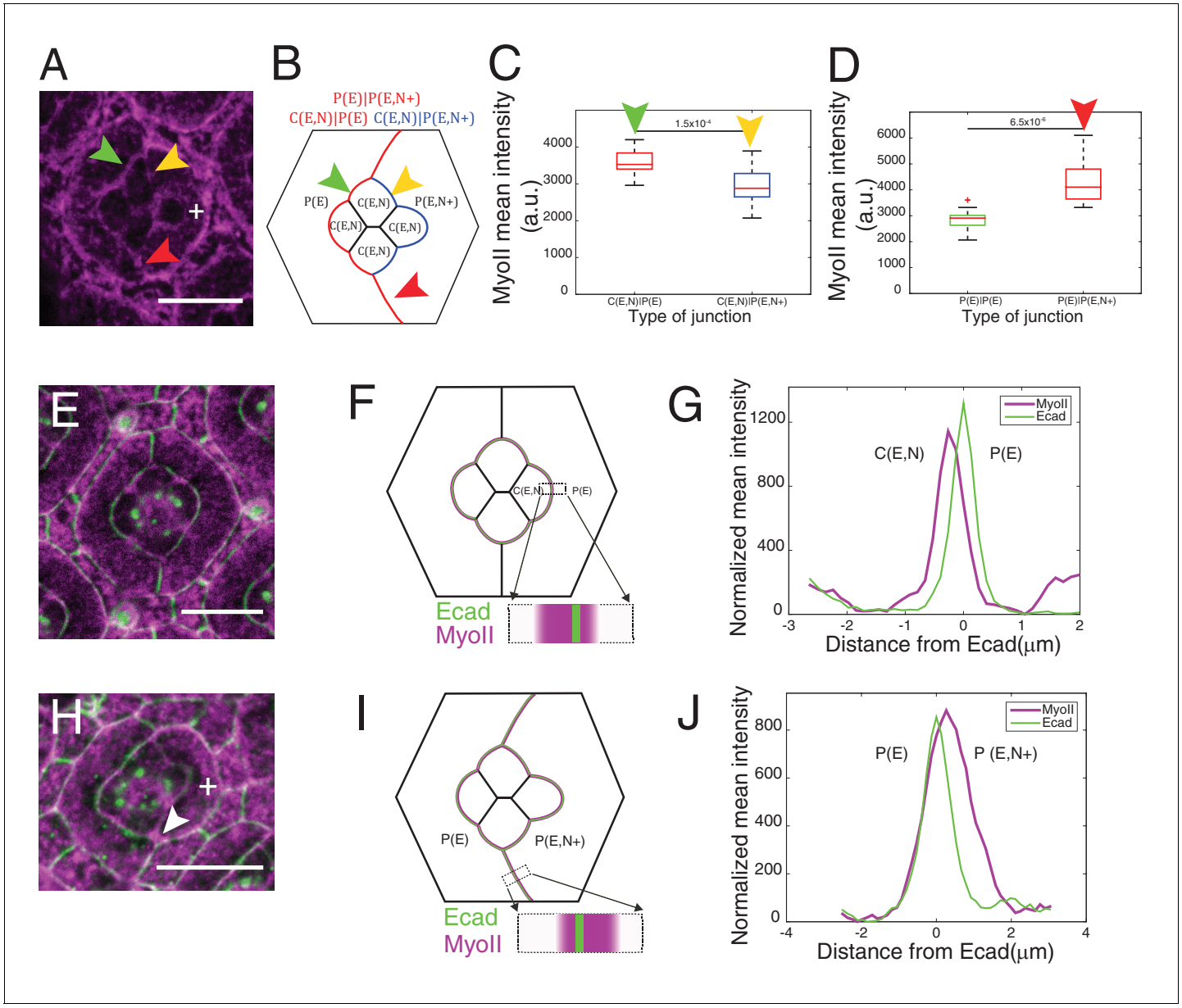

Figure 3. Misexpression of Ncad in primary pigment cells and MyoII accumulation and MyoII asymmetry at cell contacts. (**A**) An ommatidium with Ncad misexpressed in one of the primary pigment cells (white +) with Zip::YFP in magenta. Green arrowhead indicates the C(E,N)|P(E) contact. Yellow and red arrowheads indicate the modified C(E,N)|P(E,N+) and P(E)|P(E,N+) contacts respectively. (**B**) A schematic of Ncad misexpression ommatidium with the modified C(E,N)|P(E,N+) (blue), wildtype C(E,N)|P(E) and modified P(E)|P(E,N+) (red) contacts. (**C**) Quantification of MyoII intensity in C(E,N)|P(E) (n = 20) and C(E,N)|P(E,N+) (n = 20) contacts. P-value is shown above the black horizontal line. (**D**) Quantification of MyoII intensity in P(E)|P(E) (n = 16) and P(E)|P(E,N+) (n = 16) contacts. P-value is shown above the black horizontal line. (**E**) Wildtype ommatidium with Ecad::GFP (green) and Sqh::Ch (magenta). (**F**) Schematic with a zoom-in of a C(E,N)|P(E) contact shared by cone cell and primary pigment cell representing the asymmetric distribution of MyoII. (**G**) Average linescan of Sqh::Ch (magenta) intensity with respect to Ecad::GFP intensity (green) normal to interfaces (n = 10 interfaces). (**H**) An ommatidium with Ncad misexpressed in one of the primary pigment cell (white +) with Sqh::Ch (magenta). White arrowhead indicates the modified P(E)|P(E,N+) contact. (**I**) Schematics with a zoom-in of a modified P(E)|P(E,N+) contact shared by primary pigment cell and Ncad misexpressed primary pigment cell representing the asymmetric distribution of MyoII. (**J**) Average linescan of Sqh::Ch intensity (magenta) with respect to Ecad::GFP intensity (green) (n = 13 interfaces). Scale bar 10 μm.

DOI: 10.7554/eLife.22796.013

The following source data and figure supplements are available for figure 3:

Source data 1. Dataset for ***Figure 3C,D,G and H***.

DOI: 10.7554/eLife.22796.014

Figure supplement 1. Misexpression of Ncad in primary pigment cell in retinas and larval wing pouch.

Figure 3 continued on next page

Figure 3 continued

DOI: 10.7554/eLife.22796.015

Figure supplement 2. Asymmetry of MyoII localization at different contacts.

DOI: 10.7554/eLife.22796.016

Figure supplement 2—source data 1. Dataset for ***Figure 3—figure supplement 2D,F,G and J***.

DOI: 10.7554/eLife.22796.017

Figure supplement 3. MyoII levels of a single wildtype cone cell in $Ncad^{M19}$ mosaic ommatidium.

DOI: 10.7554/eLife.22796.018

Figure supplement 3—source data 1. Dataset for ***Figure 3—figure supplement 3C***.

DOI: 10.7554/eLife.22796.019

(***Figure 4A***, *white arrowhead*). We observed a change in contact shape and MyoII levels at the interface between the wildtype cone cell and primary pigment cell that misexpressed extracellular Ncad (***Figure 4B–D***, *compare blue and red arrowheads*, ***Supplementary file 1*** -table 1), which confirms a role for homophilic Ncad bonds in the downregulation of MyoII contractility. However, MyoII levels at the contact between primary pigment cells, which included one cell that misexpressed extracellular Ncad showed no change in MyoII, when compared to full-length Ncad (***Figure 4B,C,E***, *green arrowhead*, ***Supplementary file 1*** -table 1). This result suggested that cytoplasmic part of Ncad is required for the accumulation of MyoII at the C(E,N)|P(E) contacts.

The above data suggest that while homophilic Ncad reduces MyoII contractility at homotypic contacts, unbound Ncad is able to activate MyoII, and locally enhance contractility at heterotypic contacts through its cytoplasmic part.

Both local tension and cell-scale contractility determine ommatidia shape

To understand how tensions at cell contacts determine ommatidia shape, we sought to build a simple mechanical model integrating both local tension and cell-scale contractility. Following earlier works, we thus designed a 2D model based on the minimization of a tension-based energy function (***Käfer et al., 2007***; ***Hilgenfeldt et al., 2008***; ***Farhadifar et al., 2007***). Although retina is obviously a 3D system, we treat the plane of adherens junctions, where both adhesion and MyoII molecules are recruited, as a 2D system. Since retinal cells have a complex shape and are variant in the z-direction, the relevance of the model is therefore limited to the junctional plane. Such an energy-based model assumes that the system settles to a configuration of minimum potential energy, which is likely to be the case in vivo since the developmental process is very slow and quasi-static. We then assume that individual contacts have a local tension γ_{loc}. As shown by our experiments, γ_{loc} is likely to be determined by the concentration of MyoII and cadherins engaged at the contact. The contribution of γ_{loc} at each contact to the total energy of the system is simply $\gamma_{loc}l$, where l is the contact length. In addition, and as shown by others (***Käfer et al., 2007***; ***Hilgenfeldt et al., 2008***; ***Farhadifar et al., 2007***), the contractile cortical network and the 3D cell volume constraint are likely to impose a 2D geometry constraint at the cell level. We encapsulate this in a perimeter elasticity term, in which deviations Δp of the cell perimeter p from a preferred cell perimeter p_0 yield an energy penalty $\frac{K}{2}\frac{(p-p_0)^2}{p_0}$. The elastic constant K, which we assume is the same for all cells, determines how big this penalty is. In two-dimension, the mechanical energy of the ommatidium thus writes:

$$E = \sum_{\text{contact } ij} \gamma_{locij} l_{ij} + \sum_{\text{cells } i} \frac{K}{2} \frac{(p_i - p_{0i})^2}{p_{0i}}$$

While cell area can vary experimentally, in a range which is likely to be determined by volume constraint and cell elasticity, in the model we chose to fix the area using a Lagrange multiplier. This choice is driven by simplicity arguments. Unlike perimeter elasticity, area elasticity is not crucial to select a shape or configuration, but mostly set the cell size (***Hilgenfeldt et al., 2008***). Interfacial tension at a cell junction is, by definition, the derivative of the energy function with respect to junction length, and writes:

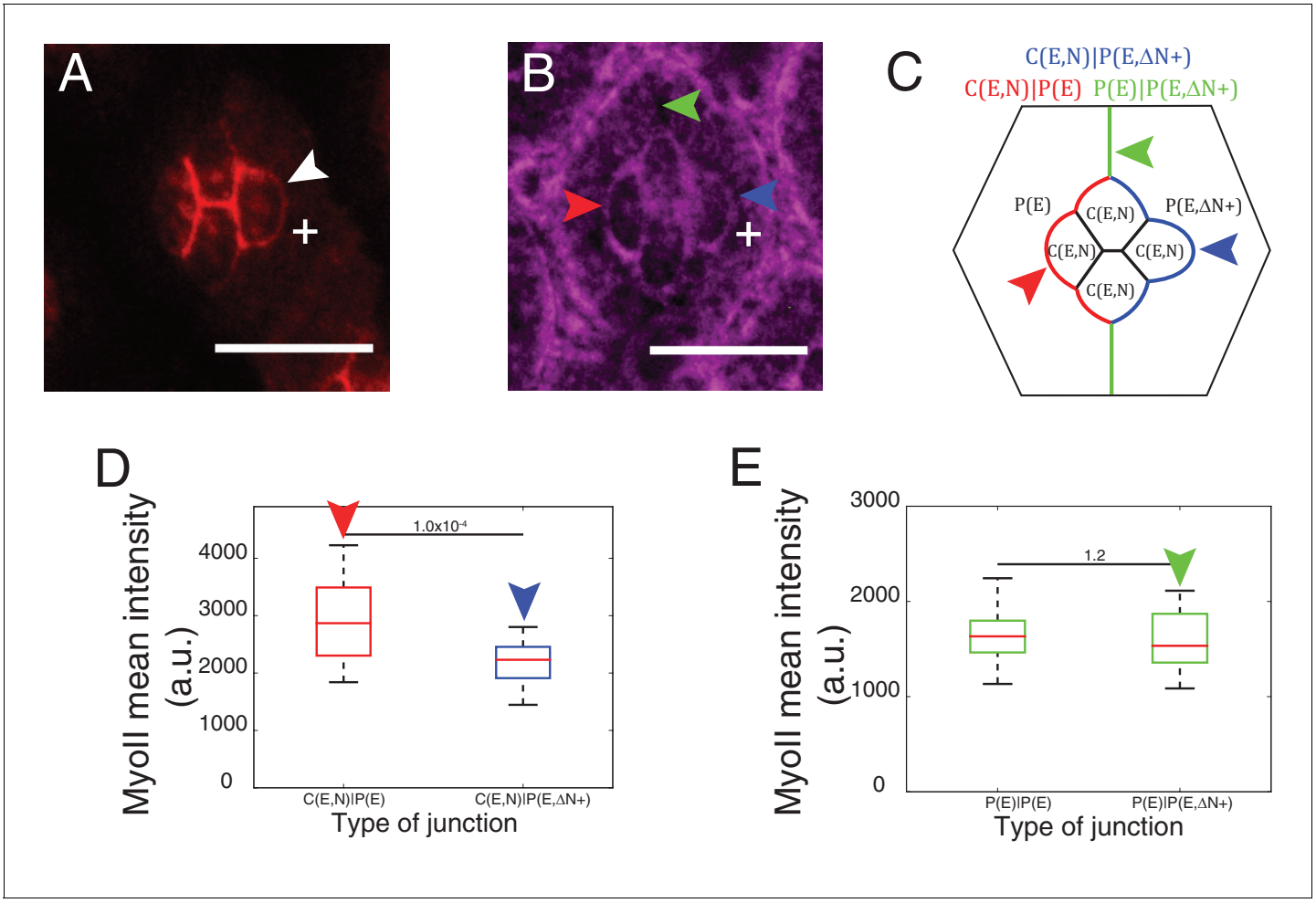

Figure 4. Cytoplasmic part of Ncad is required for MyoII accumulation in heterotypic contacts. (**A–B**) An ommatidium misexpressing extracellular part of Ncad in one of the primary pigment cells (white +) with Ncad (**A**) and Zip::YFP (**B**). White arrowhead indicates the C(E,N)|P(E,ΔN+) cell contact with homophilic Ncad in (**A**), red arrowhead indicates C(E,N)|P(E,ΔN+) wildtype cell contact, blue arrowhead indicates modified C(E,N)|P(E) cell contact and green arrowhead indicates the unchanged P(E)|P(E,ΔN+) cell contact. (**C**) Schematic of ommatidium misexpressing extracellular part of Ncad shows the modified cell contacts, C(E,N)|P(E) contact (blue), wildtype C(E,N)|P(E) contact (red) and unaffected P(E)|P(E,ΔN+) contact (green). (**D**) Quantification of MyoII intensity in C(E,N)|P(E) (n = 28) and C(E,N)|P(E,ΔN+) (n = 28). P-value is shown above the black horizontal line. (**E**) Quantification of MyoII intensity in wildtype P(E)|P(E) (n = 19) and unaffected P(E)|P(E,ΔN+) contact (n = 19). Scale bar, 10 μm. P-value is shown above the black horizontal line.

DOI: 10.7554/eLife.22796.020

The following source data is available for figure 4:

Source data 1. Dataset for ***Figure 4D and E***.

DOI: 10.7554/eLife.22796.021

$$\gamma_{ij} = \gamma_{locij} + K\frac{\Delta p_i}{p_{0i}} + K\frac{\Delta p_j}{p_{0j}} \quad (1)$$

Interfacial tension γ is thus the sum of the local term, γ_{loc}, and of a cell-scale elastic term, $\gamma_{el} = K\frac{\Delta p_i}{p_{0i}} + K\frac{\Delta p_j}{p_{0j}}$. Note that ablation experiments reveal the global interfacial tension γ.

The parameters of the model are the target perimeters, the local tensions, and *K*. We sought to determine as many parameters as possible from experiments. We reasoned that in the absence of forces applied by surrounding cells, cells should acquire their preferred (target) perimeter (***Figure 5—figure supplement 1A***). We thus performed circular ablations, separating a cell from all its neighboring cells to measure the target perimeter. After ablation, cells relaxed towards a circular shape in the plane of adherens junctions (***Video 3***). Note that the perimeter after relaxation was

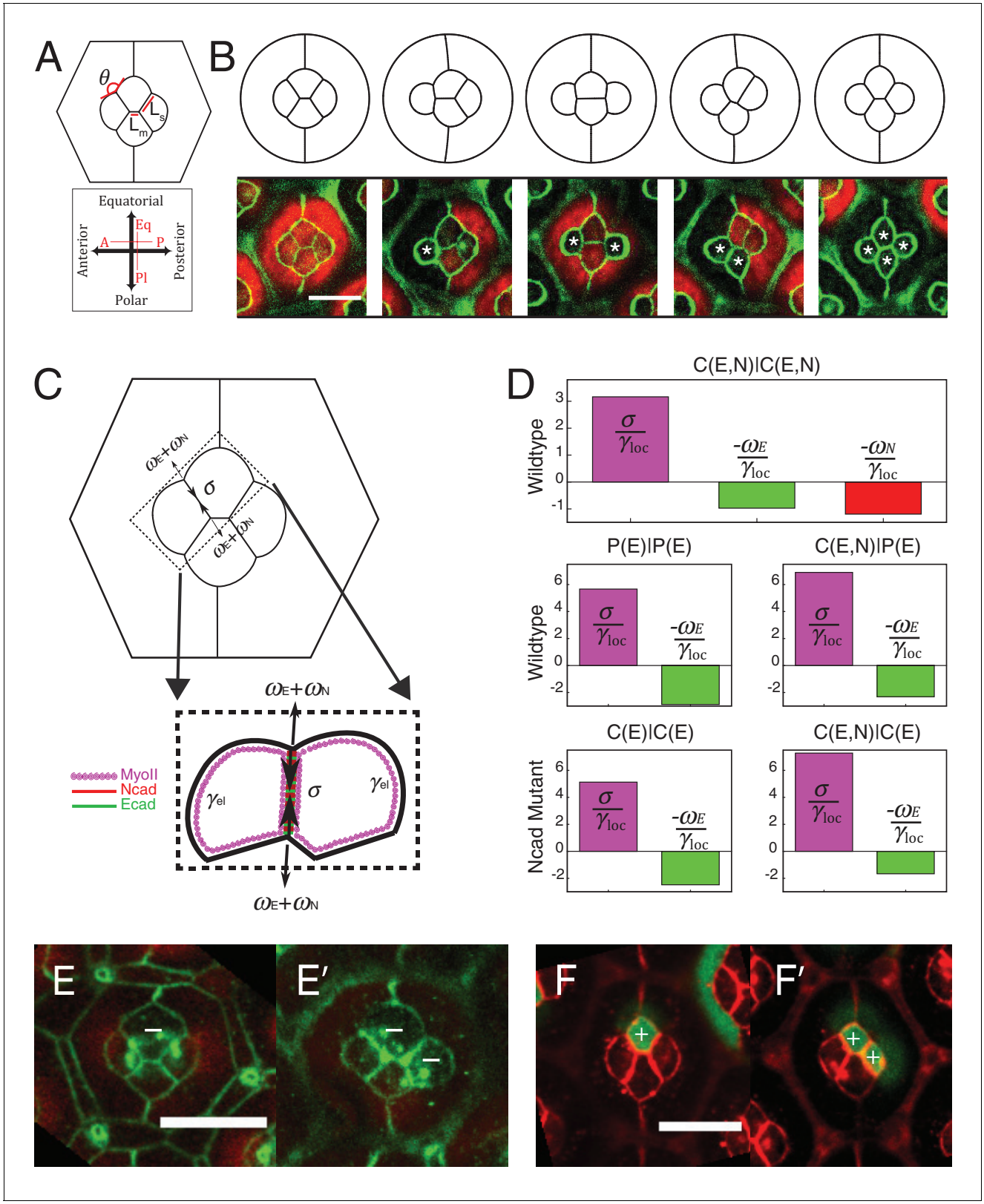

Figure 5. Simulations of cone cell shapes and contribution of cadherins and MyoII to cell shapes. (**A**) Schematics of two axes of polarity, A-P and Eq-Pl, of cone cells (bottom) and fit parameters measured in experiments and simulations, contact angle between cone cell and primary pigment cell (θ), ratio of contact length shared by A/P and Eq/Pl cell (*Ls*) to contact length shared by Eq and Pl cells (*Lm*) (top). (**B**) Comparison of experimental images (lower panel) to the simulations (upper panel), $Ncad^{M19}$ cells are marked by white asterisks. (**C**) Schematic of force balance resulting from adhesion of Ecad

Figure 5 continued on next page

Figure 5 continued

(ω_E, green) and Ncad (ω_N, red), MyoII dependent cortical tension at the cell contact (σ) and cortex elasticity due to actomyosin at the cell perimeter (γ_{el}) (both in magenta). (**D**) Relative contribution of MyoII dependent cortical tension (σ), Ecad adhesion (w_E) and Ncad adhesion (w_N) to the local tension term γ_{loc} for all contact types in wildtype and $Ncad^{M19}$ mosaic mutants. (**E–E'**) Image of the ommatidium with (**E**) Eq and (**E'**) Eq and PI cone cells Sqh^{Ax3} mutant (white -). β-catenin staining in green. (**F–F'**) Image of the ommatidium with (**F**) Eq and (**F'**) Eq and PI cone cells expressing constitutively active form of Sqh, $Sqh^{T20ES20E}$ (white +), β-catenin staining in red. Scale bar, 10 μm.

DOI: 10.7554/eLife.22796.022

The following source data and figure supplements are available for figure 5:

Figure supplement 1. Perimeter elasticity and determination of elastic constant (*K*).

DOI: 10.7554/eLife.22796.023

Figure supplement 1—source data 1. Dataset for ***Figure 5—figure supplement 1C***

DOI: 10.7554/eLife.22796.024

Figure supplement 2. Elastic and local tension contribution to interfacial tension and comparison of simulation to experiment.

DOI: 10.7554/eLife.22796.025

Figure supplement 2—source data 1. Dataset for ***Figure 5—figure supplement 2C and D***.

DOI: 10.7554/eLife.22796.026

Figure supplement 3. Ecad intensity measurements and correlation of interfacial tension to molecular distributions.

DOI: 10.7554/eLife.22796.027

Figure supplement 3—source data 1. Dataset for ***Figure 5—figure supplement 3B and F***.

DOI: 10.7554/eLife.22796.028

Figure supplement 4. MyoII perturbations and simulations.

DOI: 10.7554/eLife.22796.029

Figure supplement 4—source data 1. Dataset for ***Figure 5—figure supplement 4A,B and E***.

DOI: 10.7554/eLife.22796.030

found to be typically 8% smaller (8.4 ± 1.2, n = 7) than prior to ablation (***Figure 5—figure supplement 1B,C***). In addition, laser ablation experiments in ***Figure 2*** provided us with relative estimates of the interfacial tensions (γ) for the different contact types (C(E,N)|C(E,N), P(E)|P(E) and C(E,N)|P(E)). Note that all tensions (including *K*, which has the dimension of γ) were normalized by the interfacial tension measured for C(E,N)|C(E,N) contacts, and therefore are given in units of C(E,N)|C(E,N)=1. Using that $\gamma_{loc} \approx \gamma - 2K\frac{\Delta p}{p_o}$ and having determined $\frac{\Delta p}{p_o}$, K is the only free parameter remaining in the model. To determine its value, we minimized the energy function using the Surface Evolver software starting from an unrealistic configuration (***Figure 5—figure supplement 2A***), until the equilibrium configuration was reached. We then fitted the resulting ommatidia shapes to experimental shapes using *K* as a fit parameter. To fit simulations to experimental geometries, we chose two geometrical descriptors: the angle formed by adjacent C|P contacts and the length ratio between two contacts (polar-equatorial (*Lm*) over polar-posterior (*Ls*) contacts) (***Figure 5A***). We simulated the wildtype and four different $Ncad^{M19}$ mosaic ommatidia, and applied a weighted least squares method to fit them altogether (***Figure 5—figure supplement 2B***). The best fit corresponds to K = 4.2 (in units of $\gamma_{C(E,N)|C(E,N)}$=1). The cell patterns obtained in silico for this value are in very good agreement with the cell patterns observed in vivo, for wildtype ommatidia and for $Ncad^{M19}$ mosaic ommatidia with different numbers and combinations of wildtype and $Ncad^{M19}$ cone cells (***Figure 5B***, ***Figure 5—figure supplement 2C,D***). Interestingly, our estimate of *K* also indicates that elastic tension contributes to 1/3 to 1/2 of the total interfacial tension, depending on the cell contacts considered (***Figure 5—figure supplement 2E***).

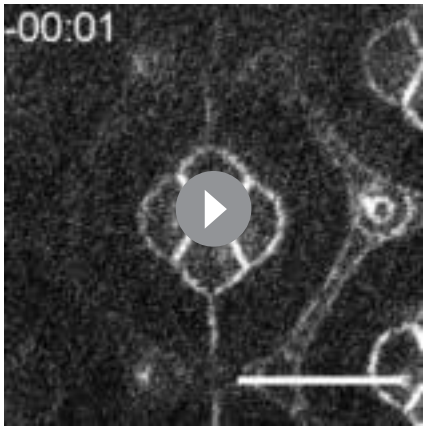

Video 3. Laser nano-ablation of target perimeter measurement ($\Delta p/po$). Ablation at 00:00. Frame rate is 250 ms/frame. Labelling: β-cat::GFP. Scale bar, 5 μm.

DOI: 10.7554/eLife.22796.031

The balance of cortical tension and adhesion determines local tension

The rationale of the model presented above is to predict ommatidia shapes from tensions at the cell contacts measured by ablations, irrespective of MyoII or cadherin levels. Yet, local tension is likely to result from the balance between MyoII-dependent cortical tension and cadherin-based adhesion (***Lecuit and Lenne, 2007***), and we were interested in weighing their respective (direct) contributions. To do so, we measured concentrations of cadherin and MyoII molecules in different configurations for which we knew the local tension.

We assumed that adhesion molecules and motor molecules have an additive and antagonistic contribution to local tension (***Maître et al., 2012***). Hence, MyoII cortical tension σ is balanced by cadherin based adhesion ω, so that $\gamma_{loc} = \sigma - \omega$ (***Figure 5C***). At C(E,N)|C(E,N) contacts, both Ecad and Ncad contribute to the adhesion term, so that $\omega = \omega_E + \omega_N$, while at C(E,N)|P(E) and P(E)|P(E) contacts, only Ecad contributes to adhesion, and $\omega = \omega_E$. For the sake of simplicity, we assumed that adhesion and MyoII-dependent cortical tension were proportional to the concentrations of cadherins and MyoII, respectively. It should be noted that whether MyoII molecules are recruited through an Ncad feedback or any other pathway is not relevant to how they contribute to local tension. Hence the feedback between MyoII and Ncad is not considered to estimate the respective contribution of cadherin and MyoII molecules to tension. From there, we could use the molecular concentrations (***Figure 2C,F***, ***Figure 5—figure supplement 3A,B and E,F***) and local tensions γ_{loc} obtained from ablation experiments combined to numerical modelling (***Figure 2J,K*** and ***Figure 5—figure supplement 2E***) to infer the contributions of Ecad, Ncad and MyoII to the local tension of the different contact types (See Materials and methods). We found that MyoII has a very significant contribution to local tension, which is about two to five times higher than that of Ncad or Ecad depending on the contact type (***Figure 5D***). This data, in agreement with in vitro experiments on cell doublets (***Maître et al., 2012***), emphasizes the quantitative role of MyoII on cell shapes in vivo. It also indicates that control of cell shape by adhesion is mostly indirect, through the regulation of MyoII level by unbound Ncad. This is again exemplified by the higher contribution of MyoII to local tension in C(E,N)|P(E) and C(E,N)|C(E) contacts than in P(E)|P(E) and C(E)|C(E) contacts (***Figure 5D***, *middle and bottom panels*).

To confirm the importance of MyoII on cone cell shapes, we manipulated MyoII activity in cone cells. We first decreased MyoII contractility using Myosin-II light chain loss of function (Sqh^{Ax3}) mutant (***Figure 5E,E'***), and observed a massive increase in cell apical area in the mutant cells and change in cell contact length (***Figure 5—figure supplement 4A Supplementary file 1*** - table 2). Conversely, misexpression of constitutively active form of MyoII ($Sqh^{T20E.S21E}$) leads to a reduction of cell apical area (***Figure 5F,F'***) and change in cell contact length (***Figure 5—figure supplement 4B***). These changes in apical area suggest that shape changes resulting from MyoII loss of function or misexpression are dominated by cell-scale (apical MyoII) rather than cell contact-scale contribution of MyoII. This is exemplified by our simulations, in which a simple change of the (fixed) area yields a qualitatively good prediction of cone cell shapes in different mutant configurations (***Figure 5—figure supplement 4***, *See Materials and methods*). A more quantitative assessment on these experiments would most likely require additional terms of area elasticity. Note that to exemplify experimentally the contribution of MyoII to local tension, one would ideally want to selectively downregulate or upregulate MyoII at cell contacts only, which is technically very challenging.

Myosin-II localization mediated by N-cadherin regulates cell arrangement

Lastly, to test the relevance of our data for tissue morphogenesis, we analyzed ommatidia morphogenesis in wildtype and $Ncad^{M19}$ mosaic retinas, 21 hr after pupal formation (APF) for 5 and 9 hr, respectively (***Figure 6A,B*** and ***Videos 4*** and ***5***). Wildtype cone cells undergo stereotypic neighbor exchanges (***Figure 6A***). Anterior and posterior cells lose A-P contact, while equatorial and polar cells intercalate and form a new Eq-Pl contact (A-P to Eq-Pl contact transition) (***Figure 5A***). However, when imaging the $Ncad^{M19}$ mosaic mutants, we observed defects of this A-P to Eq-Pl transition. 98,2% of analyzed ommatidia where *Ncad* was mutated in either the equatorial or polar cell failed to transit (***Figure 6B***, *red arrowheads*, ***Figure 6C***, n = 114). 100% of analyzed ommatidia where *Ncad* was mutated in both equatorial and polar cells failed to transit (***Figure 6D***, n = 16). We reasoned that this transition might be prevented due to the increase in tension at the transverse cell contacts

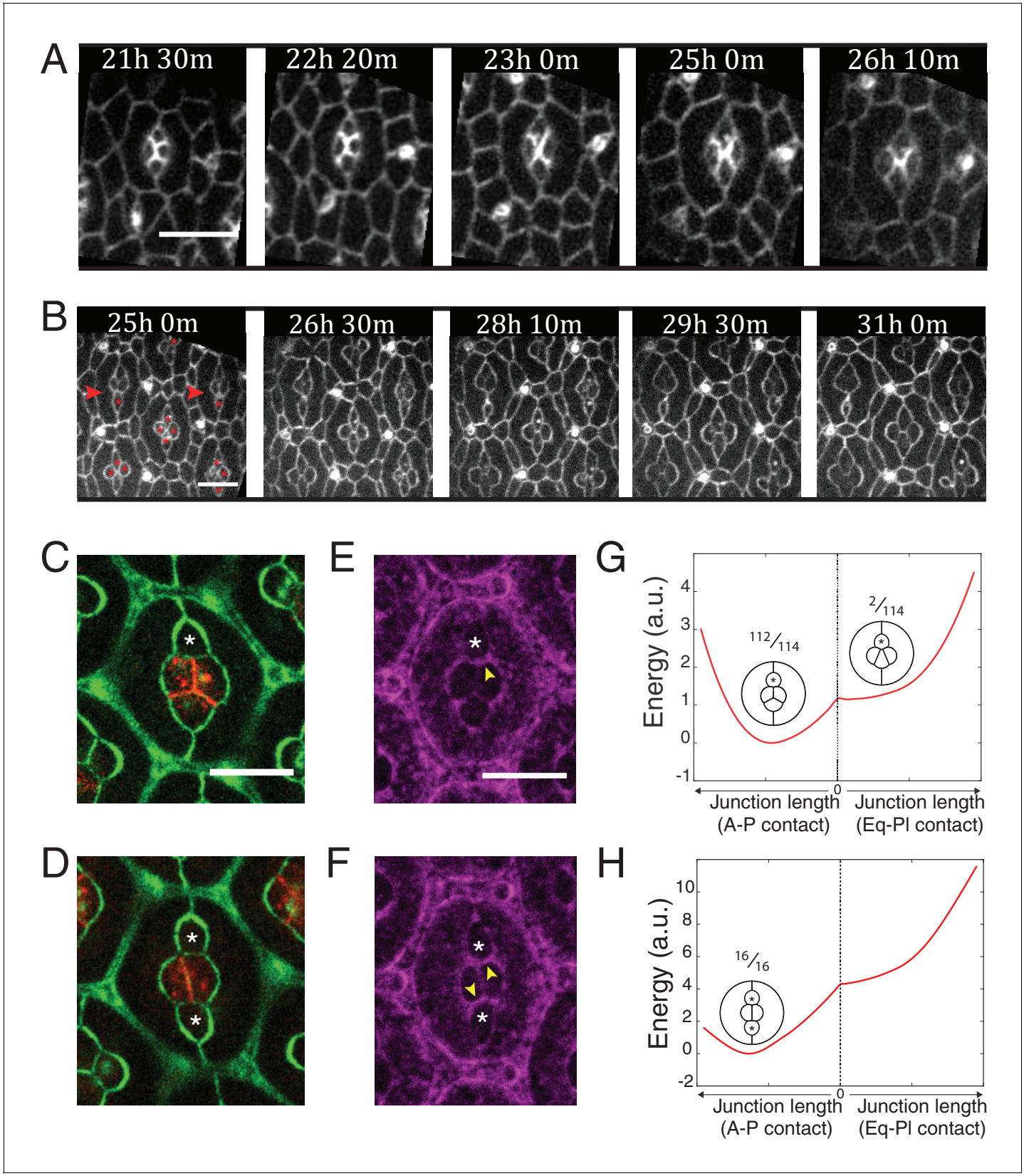

Figure 6. Ncad mediated MyoII contractility impacts on cone cell arrangements. (**A**) Snapshots of a movie at different APF from wildtype retina labelled with β-cat::GFP. Scale bar, 5 µm. (**B**) Snapshots of a movie at different APF from *Ncad*^{M19} mosaic mutant with Ecad::GFP and *Ncad*^{M19} cells (red asterisks). Mosaic ommatidia that failed to undergo normal cell rearrangement are indicated by red arrowheads. Scale bar, 5 µm. (**C**), (**E**) Equatorial

Figure 6 continued on next page

Figure 6 continued

Ncad^{M19} cone cell (white asterisk) in mosaic mutant with Ecad::GFP (green) and Ncad (red) in (**C**) and Zip::YFP (magenta) in (**E**) (both (**C**) and (**E**) total n = 112). (**D**), (**F**) Image of equatorial and polar *Ncad*^{M19} cone cells (white asterisks) with Ecad::GFP (green) and Ncad (red) in (**D**) and Zip::YFP (magenta) in (**F**) (both (**D**) and (**F**) total n = 16). (**G**) Energy profile of ommatidia with an equatorial *Ncad*^{M19} cone cell as a function of the central contact length (left direction: vertical contact length, right direction: horizontal contact length). Diagrams show corresponding simulations, with occurrence numbers observed experimentally. (**H**) Energy profile of ommatidia with equatorial and polar *Ncad*^{M19} cone cells as a function of the central contact length (left direction: vertical contact length, right direction: horizontal contact length). Diagrams show corresponding simulations, with occurrence numbers observed experimentally.

DOI: 10.7554/eLife.22796.032

where C(E,N)|C(E,N) contacts are transformed into C(E,N)|C(E) contacts, and indeed observed increased levels of MyoII in these contacts (***Figure 6E,F***). To further test this hypothesis, we estimated the energy of the system as a function of the central junction length in both vertical and horizontal configurations (***Figure 6G,H***). Note that this required to fix that length during the minimization process. We found that the model predicts an energy minimum in the vertical configuration in both cases (when either 1 or 2 of the polar and equatorial cells are *Ncad* mutants), consistent with our experimental observations. Thus, cell mechanical properties, indirectly controlled by Ncad expression, not only impact on cell shapes but also on cell arrangement.

Discussion

We showed that the adhesion provided by Ecad and Ncad homophilic bonds have a moderate direct contribution to interfacial tension as compared to MyoII dependent contractile forces. Our in vivo findings are consistent with in vitro measurements using the shapes of cell doublets to infer the relative contribution of adhesion and cortical tension to interfacial tension (***Maître et al., 2012***). Here we demonstrate that in vivo, the contribution of adhesion to interfacial tension is roughly half of MyoII cortical tension. Our data indicate that the hypotheses of differential contractility (***Harris, 1976***; ***Brodland, 2002***) or differential adhesion (***Steinberg, 1963***) are not mutually exclusive, and the balance of contractility and adhesion determines cell shapes, cell arrangement (***Lecuit and Lenne, 2007***; ***Käfer et al., 2007***; ***Hilgenfeldt et al., 2008***) and cell sorting (***Krieg et al., 2008***). The moderate contribution of adhesion bonds to interfacial tension might explain why cadherin binding affinities are not predictive of cell sorting outcomes in vivo and in vitro (***Shi et al., 2008***; ***Leckband and Sivasankar, 2012***).

Our work unravels a cell-scale (autonomous) and a junction-scale (non-autonomous) control of cell shape through actomyosin contractility. Following previous models of epithelial mechanics (***Käfer et al., 2007***; ***Hilgenfeldt et al., 2008***), we confirm that actomyosin contractility generates a cell-scale elastic tension at the cell periphery, which restricts cell deformation. This elastic tension is likely to be dependent on the stiffness of the actomyosin network bound to the membrane (***Salbreux et al., 2012***). Our data constrain the model and reduce the number of free parameters down to one, an effective elastic constant. Our model shows that the cell-scale elasticity is crucial to stabilizing the four-cone cell arrangement and it is possible that cell elasticity also ensures correct global patterning of the retina. Analysis of our measurements of mechanical properties and quantification of molecular distribution demonstrate that MyoII contractility also contributes locally to tension at cell contacts (cortical tension) to shape cone cell arrangement. This local contribution of MyoII to tension was not considered in previous works (***Käfer et al., 2007***; ***Hilgenfeldt et al., 2008***).

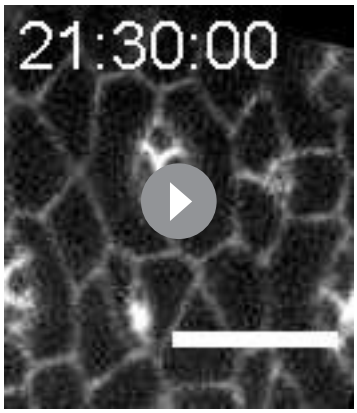

Video 4. A-P to Eq-Pl transition in wildtype retina. Movies starting from 21:30:00 APF. Frame rate is 10 min/frame. Labelling: β-cat::GFP. Scale bar, 5 μm.

DOI: 10.7554/eLife.22796.033

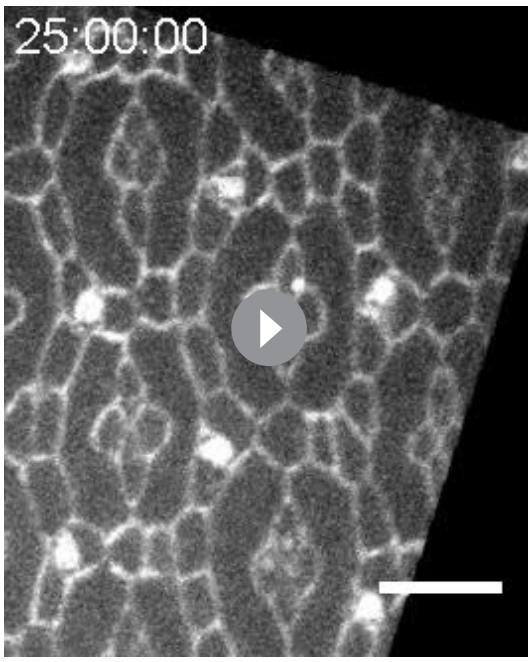

Video 5. Defects in cell rearrangements in *Ncad*^{M19} mosaic mutants. Movies starting from 25:00:00 APF. Frame rate is 10 min/frame. Labelling: Ecad::GFP. Scale bar, 5 μm.
DOI: 10.7554/eLife.22796.034

The cell-scale elasticity and junction-scale cortical tension contributions are on the same order of magnitude (***Figure 5—figure supplement 2E***) and are both crucial to predicting cell shape.

MyoII distribution and thus contractility is strongly dependent on cadherins. While the role of Ecad on contractility during tissue morphogenesis is well documented (***Lecuit and Yap, 2015***), the role of Ncad is poorly known. We identified a dual role of Ncad on cell shapes and cell arrangement. Junctional N-cadherin bonds yield contact expansion between Ncad-expressing cells. However, this effect is moderate and cannot alone account for the shapes of cells in the ommatidia. Through the determination of MyoII distributions at cell contacts, we uncovered another mechanism mediated by Ncad at heterotypic cell contacts, where a low level of Ncad is detected at junctional plane (unbound). Heterotypic contacts between cells expressing Ecad and Ncad and cells expressing Ecad only exhibit increased local contractility as compared to homotypic contacts. This difference in contractility cannot be explained only by differences in adhesion contributed by both Ecad and Ncad. This is a junction-autonomous property, as in an Ecad- and Ncad-expressing cell (C), we observed increased contractility at heterotypic contacts irrespective of the other contacts of the cell (heterotypic and/or homotypic). Our data suggest that unbound Ncad has the ability to redirect MyoII at heterotypic contacts via its signaling intracellular region. Interestingly, this does not seem to be specific to the retina and might be a more general mechanism, as suggested by our observations in the larval wing disc. N-cadherin was found to polarize MyoII contractility directly through it cytoplasmic partners such as β-catenin (***Ouyang et al., 2013***) or indirectly through its interplay with Ecad (***Scarpa et al., 2015***), presumably through an indirect mechanism. Cadherin-mediated adhesion is tightly coupled to actomyosin through small GTPase including Rho and antagonistic Rac (***Takeichi et al., 1997***; ***Ratheesh et al., 2013***). Homophilic N-cadherin dimerization activates Rho (***Comunale et al., 2007***; ***Charrasse et al., 2002***; ***Marrs et al., 2009***; ***Taulet et al., 2009***; ***Puvirajesinghe et al., 2016***) and Rac (***Matsuda et al., 2006***). Also, actin organisation has been shown to be able to affect MyoII (***Reymann et al., 2012***). We did not detect any significant variation in Rho activities among different contacts of the ommatidia using a biosensor which detects active Rho1 (***Munjal et al., 2015***)(data not shown). Further experiments will be required to resolve the mechanism by which unbound Ncad could activate MyoII.

High MyoII contractility induced by cell contact molecules at tissue boundary has a significant impact on tissue separation (***Dahmann et al., 2011***; ***Major and Irvine, 2006***; ***Fagotto, 2014***). In *Drosophila*, supracellular actomyosin structures are found at boundaries in wing imaginal discs (***Major and Irvine, 2006***; ***Landsberg et al., 2009***; ***Monier et al., 2010***; ***Umetsu et al., 2014***; ***Bielmeier et al., 2016***) and embryos (***Monier et al., 2010***; ***Röper, 2013***; ***Laplante and Nilson, 2011***). We show here that the four cone cells in ommatidia form a boundary with primary pigment cells through increased MyoII contractility at the C(E,N)|P(E) heterotypic contacts. This MyoII cable is reminiscent of that triggered by Crumbs anisotropy at the border of placodes in the *Drosophila* (***Röper, 2012***). Cells inside the placodes have higher levels of Crumbs than cells outside placodes. In the peripheral placode cells, Crumbs homophilic interactions, which are thought to negatively regulate MyoII, lead to the selective accumulation of the Myosin cable at the boundary depleted of Crumbs. One could envision that Ecad anisotropy could lead to the accumulation of MyoII at the cell contacts having a high level of Ecad. We ruled out this possibility here as we found conditions where

MyoII and Ecad anisotropy do not correlate (***Figure 2—figure supplement 1G***). In the retina, we showed that accumulation of MyoII is junction-autonomous and determined by the expression of adhesive molecules in the apposed cells.

At the heterotypic contacts, MyoII is asymmetrically distributed: it is mainly localized at the cortex of the Ecad and Ncad expressing cells. A recent study on the localization of polarity proteins on either side of cell interfaces made a similar observation (***Aigouy and Le Bivic, 2016***). From a mechanical point of view, the asymmetry of MyoII is an interesting observation as it suggests that tension can be set and modified asymmetrically. As a consequence, shrinkage or extension of a junction might be driven unilaterally from one of the two apposed cells. So far mechanical models of epithelia, including ours, do not take asymmetry into account, a property which would be interesting to explore further in the future. The adhesion molecules that are engaged in trans-bonds at cell contacts are symmetric in the apposed membranes. Thus, they cannot be the direct cause of this asymmetry. Instead, our data suggest that asymmetrically distributed unbound Ncad could signal to MyoII and cause its asymmetry. While asymmetric localization is an essential feature of planar polarity components (***Goodrich and Strutt, 2011***), it is largely unexplored for other junction constituents. It will be important to determine whether cytoskeletal components and regulators and members of adhesion complexes, also show asymmetric localization.

High MyoII contractility at contacts between two cell types might represent a general mechanism, which could be important for lineage sorting and elimination of misspecified cells (***Bielmeier et al., 2016***). Given the importance of E- to N-cadherin switch in epithelial-mesenchyme transition (***Wheelock et al., 2008***), our findings may also have implications in other developmental processes.

Materials and methods

Drosophila stocks and genotypes

To visualize Myosin-II in wildtype retinas, we used Zip::YFP(CPTI-100036) and *Sqh^{AX3} /FM7; sqh-Sqh ::GFP* flies (***Karess et al., 1991***). To quantify the levels and asymmetry of Myosin-II at contacts in both *Ncad^{M19}* mutant and misexpression background, we used Zip::YFP (RRID:DGGR_115082) and Sqh-Sqh::Cherry (***Martin et al., 2009***) as probes respectively. *FRT40A, Ncad^{M19}* mutants and UAS-Ncad flies were gifts from Tadashi Uemura (***Iwai et al., 1997***). UAS-NcadΔcyto flies was a gift from C.H. Lee (***Yonemura et al., 2010***). UAS-Sqh^{T20ES20E} flies (RRID:BDSC_64411) was a gift from R. Karess (***Jordan and Karess, 1997***). *Sqh^{Ax3} FRT19A/FM7* flies (RRID:BDSC_25712) are from Bloomington *Drosophila* stock centre. In laser ablation experiments, Ecad::GFP (RRID:BDSC_60584) (***Huang et al., 2009***) and β-catenin::GFP (***Huang et al., 2011***) knock-in flies used for visualizing the AJs were gifts from Y. Hong. Ncad::mKate2 flies are generated in house using the CRISPR/Cas9 technique (***Port et al., 2014***). Ncad::GFP flies are from the service of inDROSO. See belows for details of both Ncad knockin flies.

Genotypes used in experiments were as followed:

Figure 1A: *Ncad::mKate2, Ecad::GFP*
Figure 1C: *Ncad::GFP*
Figure 1D: *Ecad::GFP*
Figure 1E: *Zip::YFP/ +*
Figure 1F: *eyFLP; Ecad::GFP, FRT40A, GMR-Gal4 myr-RFP/ FRT40A, Ncad^{M19}*
Figure 1G: *eyFLP; Zip::YFP, FRT40A, GMR-Gal4 myr-RFP/ FRT40A, Ncad^{M19}*
Figure 1- figure supplement 1A: *Ncad::GFP*
Figure 1- figure supplement 1B: *Sqh^{Ax3}; sqh-Sqh::GFP/ sqh-Sqh::GFP*
Figure 1- figure supplement 1C: *Zip::YFP/ +*
Figure 1- figure supplement 1D: *Sqh^{Ax3}; sqh-Sqh::GFP/ sqh-Sqh::GFP*
Figure 2A-C: *Zip::YFP/ +*
Figure 2D-F: *eyFLP; Zip::YFP, FRT40A, GMR-Gal4 myr-RFP/ FRT40A, Ncad^{M19}*
Figure 2I-J: *β-catenin::GFP*
Figure 2K: *eyFLP; Ecad::GFP, FRT40A, GMR-Gal4 myr-RFP/ FRT40A, Ncad^{M19}*
Figure 2- figure supplement 1A-C: *Sqh^{Ax3}; sqh-Sqh::GFP/ sqh-Sqh::GFP*
Figure 2- figure supplement 1E: *eyFLP; Zip::YFP, FRT40A, GMR-Gal4 myr-RFP/ FRT40A Ncad^{M19}*

Figure 2- figure supplement 1F: *eyFLP; Ecad::GFP, FRT40A, GMR-Gal4 myr-RFP/ FRT40A, Ncad^{M19}*

Figure 2- figure supplement 2A-C: *eyFLP; Zip::YFP, FRT40A, GMR-Gal4 myr-RFP/ FRT40A, Ncad^{M19}*

Figure 2- figure supplement 2D: *eyFLP; Ecad::GFP, FRT40A, GMR-Gal4 myr-RFP/ FRT40A, Ncad^{M19}*

Figure 3A-D: *hsFLP; Zip::YFP/ UAS-Ncad; ActGal4, UAS-RFP/ +*

Figure 3E-G: *Sqh^{Ax3}; Ecad::GFP; sqh-Sqh::mCherry*

Figure 3H-J: *hsFLP; UAS-Ncad/ ActGal4 UAS-GFP, sqh-Sqh:mCherry/ +*

Figure 3- figure supplement 1A-A': *hsFLP; Ecad::GFP/ UAS-Ncad; ActGal4, UAS-RFP/ +*

Figure 3- figure supplement 1B-C: *hsFLP; UAS-Ncad/ActGal4, UAS-GFP/; Sqh::Ch/+*

Figure 3- figure supplement 2A-D: *Sqh^{Ax3}; Ecad::GFP; sqh-Sqh::mCherry*

Figure 3- figure supplement 2E-H: *w*

Figure 3- figure supplement 3A-C: *eyFLP; Zip::YFP, FRT40A, GMR-Gal4 myr-RFP/ FRT40A, Ncad^{M19}*

Figure 4A-E: h*sFLP; UAS-NcadΔcyto/ Zip::YFP; Act-Gal4 UAS-RFP/ +*

Figure 5B: eyFLP; *Ecad::GFP, FRT40A, GMR-Gal4 myr-RFP/ FRT40A, Ncad^{M19}*

Figure 5E-E': *Ubi-mRFP.nls, FRT19A/ FRT19A, Sqh^{Ax3};; eyFLP/ +*

Figure 5F-F': *hsFLP; UAS-Sqh^{T20ES20E}/+; ActGal4, UAS-RFP/ +*

Figure 5- figure supplement 3A-B: Ecad::GFP

Figure 5- figure supplement 3E-F: eyFLP; Ecad::GFP, FRT40A, GMR-Gal4 myr-RFP/ FRT40A, Ncad^{M19}

Figure 5- figure supplement 4C': Ubi-mRFP.nls, FRT19A/ FRT19A, Sqh^{Ax3};; eyFLP/ +

Figure 5- figure supplement 4D': hsFLP; UAS-Sqh^{T20ES20E}/+; ActGal4, UAS-RFP/ +

Figure 6A: β-catenin::GFP

Figure 6B-D: eyFLP; Ecad::GFP, FRT40A, GMR-Gal4 myr-RFP/ FRT40A, Ncad^{M19}

Figure 6E-F: eyFLP; Zip::YFP, FRT40A, GMR-Gal4 myr-RFP/ FRT40A, Ncad^{M19}

Movie 1, 3, 4: β-catenin::GFP

Movie 2, 5: eyFLP; Ecad::GFP, FRT40A, GMR-Gal4 myr-RFP/ FRT40A, Ncad^{M19}

Genetics and immunochemistry

FLP/FRT system with eyFLP was used to create mosaic mutant tissues. Gal4-UAS system with hsFLP was used to induce targeted gene expression. 10 min heat-shock was performed 72 hr after egg deposition. Pupae were staged by collecting white prepupae and incubating at 25°C for the indicated times. Retinas were fixed in 4% of paraformaldehyde (PFA) in PBS for 20 mins, washed three times with PBS, permeabilised with PBT (PBS + 0.3% Triton x100), blocked with PBS + 10% NGS (Cat#50197Z, Life technology, CA, USA), immunostained with the indicated primary antibodies in PBS + 10% NGS at 4°C overnight and secondary antibodies for 2 hr at room temperature.

Primary antibodies used rat anti N-cadherin (DSHB Cat# DN-Ex 8 RRID:AB_528121) 1:20, rat anti E-cadherin (DSHB Cat# DCAD2 RRID:AB_528120) 1:20, mouse anti-β-catenin (DSHB Cat# N2 7A1 ARMADILLO RRID:AB_528089), 1:10 and mouse anti-stan #74 (DSHB Cat# Flamingo #74 RRID:AB_2619583), 1:10 (Developmental Studies Hybridoma Bank [DSHB]) and rabbit anti-Phospho-Myosin light Chain-II (Ser19) Antibody, 1:100 (RRID:AB_330248, #3671, Cell Signalling Technology, MA, USA). Secondary antibodies used were goat anti-mouse Alexa 488, goat anti-rabbit Alexa 555 and goat anti-rat/mouse Alexa 633 (1/500) (ThermoFischer Scientific, MA, USA). Fluorescence images were acquired with a Zeiss LSM780 confocal microscope with ×63, 1.4 N.A oil immersion objective. Images typically have 5–6 stacks, 0.5 µm apart.

Time-lapse imaging of living pupal retinas

Pupae at indicated time after pupal formation were dissected and mounted on glass slides as described previously (***Corrigall et al., 2007***). Prepared samples in a temperature control chamber at 25°C were imaged using a Nikon spinning-disc Eclipse Ti inverted microscope with ×100, 1.4 N.A oil immersion objective. MetaMorph software was used and images were acquired every 10 min for 12 hr. Every image has ~10 stacks, 1 µm apart and stacks featuring the apical junctions were registered

using Fiji. Wildtype retinas live imaging was performed with β-cat::GFP flies and $Ncad^{M19}$ mosaic mutant live imaging was with Ecad::GFP flies.

Laser ablation experiment and analysis

Laser ablation experiments were performed as previously described (**Rauzi et al., 2008**). Experiments were performed in $Ncad^{M19}$ mosaic mutants labelled with Ecad::GFP, $Ncad^{M19}$ mutant cells were differentiated from wildtype cells by RFP signal. Ablations in wildtype were performed on flies labelled with β-catenin. For C(E,N)|P(E) ablation experiments, contacts shared by equatorial or polar with primary pigments cells were used.

The recorded images of ablation were analysed in ImageJ by measuring the opening distance between vertices of the ablated junction. This opening distance was plotted over time and linear fit over the first 10 points was used to the recoil speed, which is used as an estimate of interfacial tension.

Quantification of MyoII intensity

PFA-fixed retinas with Zip::YFP or Sqh::Ch to mark MyoII were imaged with Zeiss LSM780 confocal microscope and images were quantified by Fiji. Fluorescence signal at C(E,N)|P(E) contact can be clearly marked by ROI (generally of Linewidth 4 (0.439 µm) of the segmented 'selection' tool). Once the Line width is chosen for C(E,N)|P(E) contact same is used for the P(E)|P(E) and C(E,N)|C(E,N). To localize the P(E)|P(E) and C(E,N)|C(E,N)contacts, marked RFP signal was used (***Figure 2—figure supplement 2A**, right panels*). Background was measured from the lowest frame of the image (~2.5 µm below from the adherens junction). Remaining stacks were summed on Z project (images were taken with 4–5 Z slices of 0.5 µm). Then, with chosen ROI junctional Myosin-II intensity at various contact type i. e. C(E,N)|C(E,N), C(E,N)|P(E), P(E)|P(E), C(E)|C(E) and C(E,N)|C(E), excluding the vertices, were measured. Mean intensity was measured using 'measure' tool of Fiji and background was subtracted from each.

Quantification of asymmetric localization of MyoII

To determine MyoII localization with respect to cell contacts, we imaged retinas with Zip::YFP or Sqh::Ch to mark MyoII and Ecad::GFP to mark Ecad as a proxy for contact position. The images were acquired with a Zeiss LSM780 confocal microscope and quantified using Fiji. Intensity plot profiles ('Plot profile tool') for MyoII and Ecad were drawn from line segments of about 5 µm (generally of Linewidth 8 (1.05µm) of the segmented 'selection' tool) intersecting cell contacts orthogonally and at their middle. Mean intensities values were plotted for MyoII and Ecad. We used Gaussian fits to determine the position of intensity peaks and the signal to noise ratio of individual intensity line traces to estimate the precision in localization (**Bobroff, 1986**). We used multicolour Tetraspek microspheres 200 nm diameter (Invitrogen/Life Technologies, CA, USA) to measure the chromatic shift between red and green channels, which was found to be 50 and 70 nm in x, y directions, respectively.

Angle θ measurement and ratio *Lm/Ls* measurement

The 'Angle' tool in Fiji was used to measure the angle θ. The brightest pixel at the contact point was used as the angle vertex. Angles are measured for different types of cell contacts between cone cells and primary pigment cell, in wildtype as well as in $Ncad^{M19}$ mosaic conditions. The lengths are measured using the straight line 'Selection' tool of Fiji.

Statistics

All the statistical analyzis was done in Matlab. We used the non-parametric Mann-Whitney U test on pairs and systematically applied a Bonferroni correction for multiple comparisons. Note that P-values shown in graphs include the Bonferroni correction (p>0.5, N.S). Summary for all the statistical value is in ***Supplementary file 1*** – table 3.

Simulations

Simulations were performed with Surface Evolver version 2.7 (**Brakke, 1992**). Mesh grooming was implemented during minimization by refinement, and various refinement lengths have been tested

to ensure that the system had really reached energy minima. The perimeter elasticity term in the energy function (**Equation 1**) was programmed by method instance, which can be defined in the datafile. Tension was specifically set for each contact depending on its type (See parameter measurements and model simulations section).

Parameters measurements and model simulations

Simulations of ommatidia rely on the minimization of the energy function using Surface Evolver. Surface Evolver is a freely available software (**Brakke, 1992**) designed for the study of objects maintained by surface energy (in our 2D case, line energy) and other customizable forms of energy (in our case, perimeter elasticity). Surface Evolver evolves the given surface towards its minimal energy by a gradient descent method. Area of each cell is fixed in the model, even though the apical area can change experimentally. This choice is driven by simplicity arguments. Indeed, area variations could be accounted for with an area elasticity term (in the form $K_A(A-A_0)^2$, where K_A is the area elastic constant, and A and A_0 are the actual and preferred area, respectively). Yet, and unlike perimeter elasticity, area elasticity is not crucial to select a shape or configuration (**Hilgenfeldt et al., 2008**) but mostly to set cell area. Hence, we chose to fix the area so that it matches the experimentally measured one, which spared us from having additional free parameters (K_A and A_0). In MyoII perturbation experiments, in which cell area is significantly modified, we changed the fixed area to that measured in experiments.

The simulation parameters are γ_{loc}, which depends on the cell contact type, the elastic constant K, which we assume constant for all cells, and the preferred perimeters p_0. Using our circular ablation experiments to determine preferred perimeters, our measurements of γ for the different contact types, and the fact that $\gamma_{loc} \approx \gamma - 2K\frac{\Delta p}{p_0}$, K is the only free parameter remaining. We ran simulations with K ranging from 0.1 to 6 and fitted the resulting shapes to wildtype and Ncad mosaic ommatidia. The geometrical descriptors that we used for the fit are i) the contact angle θ between cone cells and primary pigment cells, and ii) the ratio *Ls*/*Lm*. *Ls* is the length of the junction shared by the posterior/anterior cone cell and the polar/equatorial cell, and *Lm* is the length of the junction shared by equatorial and polar cells (**Figure 5A**). To actually perform the fit, we calculated the sum of residuals for the measured angles and ratios in five configurations (one wildtype +4 different $Ncad^{M19}$ mosaic configurations), hence 2 x 5 = 10 residuals. We used a weighted least square method to take into account that the descriptors (an angle and a length ratio) are different quantities. Note that to simulate Ncad mosaic ommatidia, we only changed the parameter γ_{loc} according to the contact type. For example, if the anterior cone cell lacks Ncad, then its contacts shared with equatorial and polar cone cells become C(E,N)|C(E) and its contact shared with the primary pigment cell becomes C(E)|P(E). Tensions were set according to the ablation experiments performed for each contact type.

Estimation of the contribution of adhesion and cortical tension to γ_{loc}

Local tension γ_{loc} results from the balance between MyoII contractility σ and cadherin-based adhesion ω_N, and we were interested in weighing their respective (direct) contributions. In order to do so, we assumed that adhesion molecules and motor molecules have an additive and antagonistic role. Hence we have $\gamma_{loc} = \sigma - \omega$. $\omega = \omega_E + \omega_N$ if both Ecad and Ncad are present at the contact, and $\omega = \omega_E$ if only Ecad is present. We assumed that σ is proportional to MyoII intensity ($\sigma = \alpha C_M$) and ω proportional to Cadherin intensity ($\omega_E = \beta C_E$ for Ecad and $\omega_N = \delta C_N$ for Ncad). Tension measurements combined to intensity measurements provide an equation for each contact type (C(E,N|C(E,N), C(EN)|P(E), P(E)|P(E), C(E,N)|C(E) and C(E)|C(E)), so that we have 5 equations for 3 unknowns (α, β, and δ). We use a least square fit method to find the best solution to this overdetermined system, thus estimate (α, β, δ) and consequently determine the relative contributions of MyoII (σ), Ecad (ω_E) and Ncad (ω_N) to γ_{loc} for the different contact types (**Figure 5D**).

Simulations of MyoII mutants and MyoII overexpression

MyoII manipulation experiments changed the apical areas of the cone cells and length of the cell contacts (**Figure 5—figure supplement 4A,B**). Myosin-II light chain (Sqh^{Ax3}) mutant cone cells showed larger apical surface area than their wildtype counterparts. Cone cells misexpressing the constitutively active Myosin-II light chain (UAS-$Sqh^{T20ES21E}$) showed smaller apical surface area than their wildtype counterparts. To simulate the shape of these perturbed cells, we measured the area

(*A*) of these cells to fix it in the simulations and the target perimeter by $p_0 = 2\sqrt{A\pi}$. The in silico patterns obtained for this simple change in area and target perimeter are in good agreement with the in vivo cell patterns (***Figure 5—figure supplement 4C,C', D,D', E***).

Cell contact length measurement in ommatidium with two *Ncad*^{M19} cone cells

PFA-fixed retinas with Ecad::GFP and RFP to differentiate wildtype from *Ncad*^{M19} mutant cells were used to measure the junction length of C(E,N)|C(E,N), C(E)|C(E), C(E,N)|C(E) cell contacts in ommatidia with two adjacent cone cells *Ncad*^{M19} mutants. Lengths were measured using 'line tool' of Fiji. Different types of lengths measured in an ommatidum is normalized to its C(E,N)|C(E,N) length.

Quantification of Ecad intensity

PFA-fixed retinas with Ecad::GFP and RFP to differentiate wildtype from *Ncad*^{M19} mutant cells. Images were obtained with Zeiss LSM780 confocal microscopy and Fiji was used for quantification. Background subtraction was not used since the background was nearly zero. Stacks were summed on 'Z project'. Linewidth 4 (0.659µm) of the segmented 'selection' tool was used to measure the mean intensity of junctional Ecad according to the contact type.

Quantification of MyoII intensity in *Ncad*^{M19} mosaic ommatidia with only one wildtype Ecad and Ncad expressing cone cell

PFA-fixed retinas with Zip::YFP to mark MyoII and RFP to differentiate wildtype from *Ncad*^{M19} cells were imaged with Zeiss LSM780 confocal microscope and images were quantified by Fiji. Stacks were summed on 'Z project' for all the images. Background was measured from the center (apical region) of any cone cell. Linewidth 4 of the segmented 'selection' tool was used to measure mean intensity around wildtype cell and around *Ncad*^{M1} mutant cell. Background was subtracted from wildtype and mutant mean intensities for each image. After background subtraction, intensities were compared (wildtype n = 41, mutant n = 41).

Quantification of F-Actin intensity

PFA-fixed retinas with Zip::YFP to mark MyoII, RFP to differentiate wildtype from *Ncad*^{M19} mutant cells and phalloidin staining for F-actin. Images were obtained with Zeiss LSM780 confocal microscopy and Fiji was used for quantification. Stacks were summed on 'Z project'. Linewidth 7 (0.615µm) of the segmented 'selection' tool was used to measure the mean intensity of junctional F-Actin according to the contact type (junctional Zip::YFP was used for the reference).

Quantification of Ncad intensity

PFA-fixed retinas with Ncad::GFP were obtained with Zeiss LSM780 confocal microscopy and Fiji was used for quantification. Line width 5 (0.659µm) of the segmented 'selection' tool was used to measure the mean intensity. For each measurement at the C(E,N)|C(E,N) and C(E,N)|P(E) contacts, background is measured adjacent to the contact and subtracted from the signal at junctions.

Analysis of localization error in Ecad or MyoII peaks

The localization precision ΔX of Ecad or MyoII peaks was evaluated using (***Bobroff, 1986***) $\Delta X \sim \frac{1.8}{SNR}\sqrt{\Gamma\delta x}$, where Γ is the standard deviation of the Gaussian fit of the intensity profiles, *SNR* is the signal to noise ratio, and δx is the pixel size. Typical values were Γ_{Ecad}~250 nm, Γ_{MyoII}~300 nm, SNR_{Ecad}~34 and SNR_{MyoII}~10 and δx=131 nm. The analysis of multiple intensity profiles (n=10) led to ΔX_{Ecad} = 5–22 nm and ΔX_{MyoII} = 18–77 nm.

Generation of CRISPR/Cas9 mediated Ncad::eGFP flies

Ncad::eGFP flies were designed and generated by *inDROSO* functional genomics (France). eGFP was inserted just before the stop codon of Ncad with a flexible linker GVG and the resulting flies was validated by sequencing. Homozygous flies are viable and occasionally exhibit islets of black cells.

Generation of CRISPR/Cas9 mediated Ncad:mKate2 flies

Plasmid construction

Cloning was performed with the Gibson assembly Mix (New England Biolabs, Ipswich, MA, USA). PCR products were produced with the Phusion Hot Start II HF DNA Polymerase (ThermoFischer Scientific, MA, USA). All inserts were verified by sequencing. Primers used for plasmid construction are listed in ***Supplementary file 1*** - table 4. Primers gRNA-NCadFw and gRNA-NCadRev were used to obtain the Ncad-gRNA from pACMAN BAC DN.CAD CH321-57H14. pCFD3 plasmid containing the U6:3 promoter (from Addgene no. 49410; ***Port et al., 2014***) was used to clone annealed complementary Ncad oligo-nucleotides into the BbsI digested backbone using standards procedures to produce the following 5'-to-3' configuration: U6 promoter-gRNA-Ncad-gRNA core sequence. The construct was inserted in the attP2 site on chromosome three to generate transgenic flies (BestGene Inc., Chino Hills, CA, USA).

Ncad::mKate2 donor plasmid production

The donor plasmid was designed to introduce a mKate2-coding sequence before the stop codon of Ncad. The exogenous sequence is flanked by homology arms of 2.31 kb (5' homology) and 1.46 kb (3' homology). The 5' homology arm contains a synonymous mutation that removes the protospacer-adjacent motif (PAM) sequence for g-RNA-NCAD to prevent mutagenesis after the integration of donor-derived sequences. The 5' and 3' homology arms were PCR amplified from genomic DNA from the clone pACMAN BAC DN.CAD CH321-57H14 using primers Ncad5'. For, Ncad5'.Rev, Ncad3'-For, Ncad3'-Rev. The mKate2 coding sequence was amplified from a mKate2-containing plasmid (***Shcherbo et al., 2009***) using the primers mKate2For and mKate2Rev. The sequences of all the primers can be found in ***Supplementary file 1***- table 4. All fragments were assembled by Gibson assembly Mix into pBluescript SK(+) (Stratagene, La Jolla, CA, USA) that was digested with XhoI and NotI.

Embryo injections

Embryos from crosses between transgenic nos-cas9 (BL 54591) virgin females and U6:3-gRNA-NCAD-expressing males were injected using standard procedures. Plasmid DNA for homologous recombination-mediated integration of mKate2 into the NCAD locus was injected at a concentration of 300 ng/µl into the nos-cas9/+;U6:3-gRNA-NCAD/+ embryos. After injection of plasmids, embryos were transferred on their coversplips to a plastic box containing wet paper towel at 25°C until they hatched as larvae. Larvae were collected with forceps and transferred to a food vial with fresh yeast, followed by culture at 25°C.

Drosophila genetics and screen

Approximately 2% of the injected Nos-cas9/+; gRNA-NCAD/+ larvae survived the injection and were crossed to a *w; Sp/CyO* balancer strain. In the next generation (F1), the males were conserved at 18°C and five females were pooled for genomic extraction and PCR screen. The quality of the DNA extraction was tested with the TIO-F and TIO-R primers. The presence of mKate2 insertion in the genome was detected by PCR using the m-Kate2-Fw and m-Kate2-Rv primers. When an amplification was obtained for mKate2, 30 F1 males were crossed individually with *w; Sp/CyO* females. When the F2 generation is well developed, the F1 male was sacrified to extract the genomic DNA and screen for the presence of mKate2. Then, the progeny of positive male was amplified and stored. To confirm that the sequences remain in-frame after the CRISPR integration, the DNA sequence surrounding the fusion was amplified by PCR using primers NCAD-F2 and mKate2R2 (***Supplementary file 1*** - table 4) and checked by sequencing. The resulting Ncad::mKate2 flies are homozygous viable.

Acknowledgements

We are grateful to Y Hong, R Karess, CH Lee, T Lecuit, AC Martin, D Pinheiro, N Tapon, T Uemura and Bloomington *Drosophila* Stock Centre for generously providing fly stocks. We thank K Brakke, for surface evolver guidance and suggestions. We thank C Chardès for development and assistance with the ablation setup. R Flores-Flores on chromatic aberration testing and JM Philippe for

excellent assistance on molecular biology. We thank members of the Lenne and Lecuit groups and B Aigouy for stimulating and useful discussion during the course of this project. We thank B Aigouy, F Graner, M Labouesse, R Levayer, P Mangeol, Q Mao, P Recouvreux, C Toret for critical comments on the manuscript. We thank L Spinelli for advices on statistical analysis. This work was supported by an FRM Equipe Grant FRM DEQ20130326509 and Agence Nationale de la Recherche ANR-Blanc Grant, Morfor ANR-11-BSV5-0008 (to P-FL). P S was supported by PhD grant from the Labex INFORM (ANR-11-LABX-0054) and of the A*MIDEX project (ANR-11-IDEX-0001–02), funded by the 'Investissements d'Avenir French Government program'. We acknowledge France-BioImaging infrastructure supported by the French National Research Agency (ANR–10–INSB-04-01, «Investments for the future»).

Additional information

Funding

Funder	Grant reference number	Author
Fondation pour la Recherche Médicale	FRM DEQ20130326509	Eunice HoYee Chan Raphaël Clément Edith Laugier Pierre-François Lenne
Agence Nationale de la Recherche	ANR-11-BSV5-0008	Eunice HoYee Chan Pierre-François Lenne
Agence Nationale de la Recherche	ANR-11-IDEX-0001–02	Pruthvi Chavadimane Shivakumar Pierre-François Lenne

The funders had no role in study design, data collection and interpretation, or the decision to submit the work for publication.

Author contributions

EHoYC, Conceptualization, Data curation, Designed and performed all the genetic experiments, IF staining, confocal microscopy, and live-imaging experiments, Formal analysis, Supervision, Validation, Investigation, Visualization, Methodology, Writing—original draft, Project administration, Writing—review and editing, Commented on manuscript; PCS, Conceptualization, Data curation, Performed laser-ablation experiments and quantified all the images and data, Formal analysis, Designed the physical model, Performed the simulations and calculations, Validation, Investigation, Visualization, Methodology, Writing—original draft, Project administration, Writing—review and editing, Commented on manuscript; RC, Conceptualization, Formal analysis, Designed the physical model, Supervision, Validation, Visualization, Methodology, Writing—original draft, Writing—review and editing, Commented on manuscript; EL, Resources, Methodology, Designed and generated the CRISPR/Cas9 Ncad::mKate2 knockin line; P-FL, Conceptualization, Resources, Formal analysis, Designed the physical model, Supervision, Funding acquisition, Validation, Investigation, Visualization, Methodology, Writing—original draft, Project administration, Writing—review and editing, Commented on manuscript

Author ORCIDs

Eunice HoYee Chan, http://orcid.org/0000-0003-3162-3609
Pierre-François Lenne, http://orcid.org/0000-0003-1066-7506

Additional files

Supplementary files

• Supplementary file 1. Table 1: MyoII levels in different experiments at different contact types. Table 2: Junction length, MyoII level, Ecad level and Ncad level in different experiments at different contact types. Table 3: Statistical value for all quantifications. Table 4: Oligos used in generating CRISPR/Cas9 mediated knock-in Ncad::mKate2 flies.
DOI: 10.7554/eLife.22796.035

References

Aigouy B, Le Bivic A. 2016. The PCP pathway regulates Baz planar distribution in epithelial cells. *Scientific Reports* **6**:33420. doi: 10.1038/srep33420, PMID: 27624969

Bard L, Boscher C, Lambert M, Mège RM, Choquet D, Thoumine O. 2008. A molecular clutch between the actin flow and N-cadherin adhesions drives growth cone migration. *Journal of Neuroscience* **28**:5879–5890. doi: 10.1523/JNEUROSCI.5331-07.2008, PMID: 18524892

Baum B, Georgiou M. 2011. Dynamics of adherens junctions in epithelial establishment, maintenance, and remodeling. *The Journal of Cell Biology* **192**:907–917. doi: 10.1083/jcb.201009141, PMID: 21422226

Bertet C, Sulak L, Lecuit T. 2004. Myosin-dependent junction remodelling controls planar cell intercalation and Axis elongation. *Nature* **429**:667–671. doi: 10.1038/nature02590, PMID: 15190355

Bielmeier C, Alt S, Weichselberger V, La Fortezza M, Harz H, Jülicher F, Salbreux G, Classen AK. 2016. Interface contractility between differently fated cells drives cell elimination and cyst formation. *Current Biology* **26**:563–574. doi: 10.1016/j.cub.2015.12.063, PMID: 26853359

Blankenship JT, Backovic ST, Sanny JS, Weitz O, Zallen JA. 2006. Multicellular rosette formation links planar cell polarity to tissue morphogenesis. *Developmental Cell* **11**:459–470. doi: 10.1016/j.devcel.2006.09.007, PMID: 17011486

Bobroff N. 1986. Position measurement with a resolution and noise-limited instrument. *Review of Scientific Instruments* **57**:1152–1157. doi: 10.1063/1.1138619

Brakke KA. 1992. The surface evolver. *Experimental Mathematics* **1**:141–165. doi: 10.1080/10586458.1992.10504253

Brodland GW. 2002. The differential interfacial tension hypothesis (DITH): a comprehensive theory for the self-rearrangement of embryonic cells and tissues. *Journal of Biomechanical Engineering* **124**:188–197. doi: 10.1115/1.1449491, PMID: 12002128

Cagan RL, Ready DF. 1989. The emergence of order in the Drosophila pupal retina. *Developmental Biology* **136**:346–362. doi: 10.1016/0012-1606(89)90261-3, PMID: 2511048

Charrasse S, Meriane M, Comunale F, Blangy A, Gauthier-Rouvière C. 2002. N-cadherin-dependent cell-cell contact regulates rho GTPases and beta-catenin localization in mouse C2C12 myoblasts. *The Journal of Cell Biology* **158**:953–965. doi: 10.1083/jcb.200202034, PMID: 12213839

Chazeau A, Garcia M, Czöndör K, Perrais D, Tessier B, Giannone G, Thoumine O. 2015. Mechanical coupling between transsynaptic N-cadherin adhesions and actin flow stabilizes dendritic spines. *Molecular Biology of the Cell* **26**:859–873. doi: 10.1091/mbc.E14-06-1086, PMID: 25568337

Chopra A, Tabdanov E, Patel H, Janmey PA, Kresh JY. 2011. Cardiac myocyte remodeling mediated by N-cadherin-dependent mechanosensing. *AJP: Heart and Circulatory Physiology* **300**:H1252–H1266. doi: 10.1152/ajpheart.00515.2010, PMID: 21257918

Comunale F, Causeret M, Favard C, Cau J, Taulet N, Charrasse S, Gauthier-Rouvière C. 2007. Rac1 and RhoA GTPases have antagonistic functions during N-cadherin-dependent cell-cell contact formation in C2C12 myoblasts. *Biology of the Cell* **99**:503–517. doi: 10.1042/BC20070011, PMID: 17459003

Corrigall D, Walther RF, Rodriguez L, Fichelson P, Pichaud F. 2007. Hedgehog signaling is a principal inducer of Myosin-II-driven cell ingression in Drosophila epithelia. *Developmental Cell* **13**:730–742. doi: 10.1016/j.devcel.2007.09.015, PMID: 17981140

Dahmann C, Oates AC, Brand M. 2011. Boundary formation and maintenance in tissue development. *Nature Reviews Genetics* **12**:43–55. doi: 10.1038/nrg2902, PMID: 21164524

Deng H, Wang W, Yu J, Zheng Y, Qing Y, Pan D. 2015. Spectrin regulates Hippo signaling by modulating cortical actomyosin activity. *eLife* **4**:e06567. doi: 10.7554/eLife.06567, PMID: 25826608

Derycke LD, Bracke ME. 2004. N-cadherin in the spotlight of cell-cell adhesion, differentiation, embryogenesis, invasion and signalling. *The International Journal of Developmental Biology* **48**:463–476. doi: 10.1387/ijdb.041793ld, PMID: 15349821

Fagotto F. 2014. The cellular basis of tissue separation. *Development* **141**:3303–3318. doi: 10.1242/dev.090332, PMID: 25139853

Farhadifar R, Röper JC, Aigouy B, Eaton S, Jülicher F. 2007. The influence of cell mechanics, cell-cell interactions, and proliferation on epithelial packing. *Current Biology* **17**:2095–2104. doi: 10.1016/j.cub.2007.11.049, PMID: 18082406

Founounou N, Loyer N, Le Borgne R. 2013. Septins regulate the contractility of the actomyosin ring to enable adherens junction remodeling during cytokinesis of epithelial cells. *Developmental Cell* **24**:242–255. doi: 10.1016/j.devcel.2013.01.008, PMID: 23410939

Garcia M, Leduc C, Lagardère M, Argento A, Sibarita JB, Thoumine O. 2015. Two-tiered coupling between flowing actin and immobilized N-cadherin/catenin complexes in neuronal growth cones. *PNAS* **112**:6997–7002. doi: 10.1073/pnas.1423455112, PMID: 26038554

Goodrich LV, Strutt D. 2011. Principles of planar polarity in animal development. *Development* **138**:1877–1892. doi: 10.1242/dev.054080, PMID: 21521735

Guillot C, Lecuit T. 2013. Adhesion disengagement uncouples intrinsic and extrinsic forces to drive cytokinesis in epithelial tissues. *Developmental Cell* **24**:227–241. doi: 10.1016/j.devcel.2013.01.010, PMID: 23410938

Harris AK. 1976. Is cell sorting caused by differences in the work of intercellular adhesion? A critique of the steinberg hypothesis. *Journal of Theoretical Biology* **61**:267–285. doi: 10.1016/0022-5193(76)90019-9, PMID: 985668

Harris TJ. 2012. Adherens junction assembly and function in the Drosophila embryo. *International Review of Cell and Molecular Biology* **293**:45–83. doi: 10.1016/B978-0-12-394304-0.00007-5, PMID: 22251558

Hayashi T, Carthew RW. 2004. Surface mechanics mediate pattern formation in the developing retina. *Nature* **431**:647–652. doi: 10.1038/nature02952, PMID: 15470418

Heisenberg CP, Bellaïche Y. 2013. Forces in tissue morphogenesis and patterning. *Cell* **153**:948–962. doi: 10.1016/j.cell.2013.05.008, PMID: 23706734

Herszterg S, Leibfried A, Bosveld F, Martin C, Bellaiche Y. 2013. Interplay between the dividing cell and its neighbors regulates adherens junction formation during cytokinesis in epithelial tissue. *Developmental Cell* **24**:256–270. doi: 10.1016/j.devcel.2012.11.019, PMID: 23410940

Hilgenfeldt S, Erisken S, Carthew RW. 2008. Physical modeling of cell geometric order in an epithelial tissue. *PNAS* **105**:907–911. doi: 10.1073/pnas.0711077105, PMID: 18192402

Hirano S, Takeichi M. 2012. Cadherins in brain morphogenesis and wiring. *Physiological Reviews* **92**:597–634. doi: 10.1152/physrev.00014.2011, PMID: 22535893

Huang J, Huang L, Chen YJ, Austin E, Devor CE, Roegiers F, Hong Y. 2011. Differential regulation of adherens junction dynamics during apical-basal polarization. *Journal of Cell Science* **124**:4001–4013. doi: 10.1242/jcs.086694, PMID: 22159415

Huang J, Zhou W, Dong W, Watson AM, Hong Y. 2009. From the Cover: directed, efficient, and versatile modifications of the Drosophila genome by genomic engineering. *PNAS* **106**:8284–8289. doi: 10.1073/pnas.0900641106, PMID: 19429710

Iwai Y, Usui T, Hirano S, Steward R, Takeichi M, Uemura T. 1997. Axon patterning requires DN-cadherin, a novel neuronal adhesion receptor, in the Drosophila embryonic CNS. *Neuron* **19**:77–89. doi: 10.1016/S0896-6273(00)80349-9, PMID: 9247265

Jordan P, Karess R. 1997. Myosin light chain-activating phosphorylation sites are required for oogenesis in Drosophila. *The Journal of Cell Biology* **139**:1805–1819. doi: 10.1083/jcb.139.7.1805, PMID: 9412474

Karess RE, Chang XJ, Edwards KA, Kulkarni S, Aguilera I, Kiehart DP. 1991. The regulatory light chain of nonmuscle myosin is encoded by spaghetti-squash, a gene required for cytokinesis in Drosophila. *Cell* **65**:1177–1189. doi: 10.1016/0092-8674(91)90013-O, PMID: 1905980

Käfer J, Hayashi T, Marée AF, Carthew RW, Graner F. 2007. Cell adhesion and cortex contractility determine cell patterning in the Drosophila retina. *PNAS* **104**:18549–18554. doi: 10.1073/pnas.0704235104, PMID: 18003929

Krieg M, Arboleda-Estudillo Y, Puech PH, Käfer J, Graner F, Müller DJ, Heisenberg CP. 2008. Tensile forces govern germ-layer organization in zebrafish. *Nature Cell Biology* **10**:429–436. doi: 10.1038/ncb1705, PMID: 18364700

Kumar A, Gupta T, Berzsenyi S, Giangrande A. 2015. N-cadherin negatively regulates collective Drosophila glial migration through actin cytoskeleton remodeling. *Journal of Cell Science* **128**:900–912. doi: 10.1242/jcs.157974, PMID: 25593128

Ladoux B, Anon E, Lambert M, Rabodzey A, Hersen P, Buguin A, Silberzan P, Mège RM. 2010. Strength dependence of cadherin-mediated adhesions. *Biophysical Journal* **98**:534–542. doi: 10.1016/j.bpj.2009.10.044, PMID: 20159149

Landsberg KP, Farhadifar R, Ranft J, Umetsu D, Widmann TJ, Bittig T, Said A, Jülicher F, Dahmann C. 2009. Increased cell bond tension governs cell sorting at the Drosophila anteroposterior compartment boundary. *Current Biology* **19**:1950–1955. doi: 10.1016/j.cub.2009.10.021, PMID: 19879142

Laplante C, Nilson LA. 2011. Asymmetric distribution of echinoid defines the epidermal leading edge during Drosophila dorsal closure. *The Journal of Cell Biology* **192**:335–348. doi: 10.1083/jcb.201009022, PMID: 21263031

Leckband D, Sivasankar S. 2012. Cadherin recognition and adhesion. *Current Opinion in Cell Biology* **24**:620–627. doi: 10.1016/j.ceb.2012.05.014, PMID: 22770731

Lecuit T, Lenne PF. 2007. Cell surface mechanics and the control of cell shape, tissue patterns and morphogenesis. *Nature Reviews Molecular Cell Biology* **8**:633–644. doi: 10.1038/nrm2222, PMID: 17643125

Lecuit T, Yap AS. 2015. E-cadherin junctions as active mechanical integrators in tissue dynamics. *Nature Cell Biology* **17**:533–539. doi: 10.1038/ncb3136, PMID: 25925582

Lee CH, Herman T, Clandinin TR, Lee R, Zipursky SL. 2001. N-cadherin regulates target specificity in the Drosophila visual system. *Neuron* **30**:437–450. doi: 10.1016/S0896-6273(01)00291-4, PMID: 11395005

Luccardini C, Hennekinne L, Viou L, Yanagida M, Murakami F, Kessaris N, Ma X, Adelstein RS, Mège RM, Métin C. 2013. N-cadherin sustains motility and polarity of future cortical interneurons during tangential migration. *Journal of Neuroscience* **33**:18149–18160. doi: 10.1523/JNEUROSCI.0593-13.2013, PMID: 24227724

Maître JL, Heisenberg CP. 2013. Three functions of cadherins in cell adhesion. *Current Biology* **23**:R626–R633. doi: 10.1016/j.cub.2013.06.019, PMID: 23885883

Maître JL, Berthoumieux H, Krens SF, Salbreux G, Jülicher F, Paluch E, Heisenberg CP. 2012. Adhesion functions in cell sorting by mechanically coupling the cortices of adhering cells. *Science* **338**:253–256. doi: 10.1126/science.1225399, PMID: 22923438

Major RJ, Irvine KD. 2006. Localization and requirement for Myosin II at the dorsal-ventral compartment boundary of the Drosophila wing. *Developmental Dynamics* **235**:3051–3058. doi: 10.1002/dvdy.20966, PMID: 17013876

Marinari E, Mehonic A, Curran S, Gale J, Duke T, Baum B. 2012. Live-cell delamination counterbalances epithelial growth to limit tissue overcrowding. *Nature* **484**:542–545. doi: 10.1038/nature10984, PMID: 22504180

Marrs GS, Theisen CS, Brusés JL. 2009. N-cadherin modulates voltage activated calcium influx via RhoA, p120-catenin, and myosin-actin interaction. *Molecular and Cellular Neuroscience* **40**:390–400. doi: 10.1016/j.mcn.2008.12.007, PMID: 19162191

Martin AC, Kaschube M, Wieschaus EF. 2009. Pulsed contractions of an actin-myosin network drive apical constriction. *Nature* **457**:495–499. doi: 10.1038/nature07522, PMID: 19029882

Matsuda T, Fujio Y, Nariai T, Ito T, Yamane M, Takatani T, Takahashi K, Azuma J. 2006. N-cadherin signals through Rac1 determine the localization of connexin 43 in cardiac myocytes. *Journal of Molecular and Cellular Cardiology* **40**:495–502. doi: 10.1016/j.yjmcc.2005.12.010, PMID: 16515795

Monier B, Pélissier-Monier A, Brand AH, Sanson B. 2010. An actomyosin-based barrier inhibits cell mixing at compartmental boundaries in Drosophila embryos. *Nature Cell Biology* **12**:60–65. doi: 10.1038/ncb2005, PMID: 19966783

Munjal A, Philippe JM, Munro E, Lecuit T. 2015. A self-organized biomechanical network drives shape changes during tissue morphogenesis. *Nature* **524**:351–355. doi: 10.1038/nature14603, PMID: 26214737

Nandadasa S, Tao Q, Menon NR, Heasman J, Wylie C. 2009. N- and E-cadherins in xenopus are specifically required in the neural and non-neural ectoderm, Respectively, for F-actin assembly and morphogenetic movements. *Development* **136**:1327–1338. doi: 10.1242/dev.031203, PMID: 19279134

Okamura K, Tanaka H, Yagita Y, Saeki Y, Taguchi A, Hiraoka Y, Zeng LH, Colman DR, Miki N. 2004. Cadherin activity is required for activity-induced spine remodeling. *The Journal of Cell Biology* **167**:961–972. doi: 10.1083/jcb.200406030, PMID: 15569714

Ouyang M, Lu S, Kim T, Chen CE, Seong J, Leckband DE, Wang F, Reynolds AB, Schwartz MA, Wang Y. 2013. N-cadherin regulates spatially polarized signals through d istinct p120ctn and β-catenin-dependent signalling pathways. *Nature Communications* **4**:1589. doi: 10.1038/ncomms2560, PMID: 23481397

Port F, Chen HM, Lee T, Bullock SL. 2014. Optimized CRISPR/Cas tools for efficient germline and somatic genome engineering in Drosophila. *PNAS* **111**:E2967–E2976. doi: 10.1073/pnas.1405500111, PMID: 25002478

Priya R, Yap AS, Gomez GA. 2013. E-cadherin supports steady-state rho signaling at the epithelial zonula adherens. *Differentiation* **86**:133–140. doi: 10.1016/j.diff.2013.01.002, PMID: 23643492

Puvirajesinghe TM, Bertucci F, Jain A, Scerbo P, Belotti E, Audebert S, Sebbagh M, Lopez M, Brech A, Finetti P, Charafe-Jauffret E, Chaffanet M, Castellano R, Restouin A, Marchetto S, Collette Y, Gonçalvès A, Macara I, Birnbaum D, Kodjabachian L, et al. 2016. Identification of p62/SQSTM1 as a component of non-canonical wnt VANGL2-JNK signalling in breast Cancer. *Nature Communications* **7**:10318. doi: 10.1038/ncomms10318, PMID: 26754771

Ratheesh A, Priya R, Yap AS. 2013. Coordinating rho and rac: the regulation of rho GTPase signaling and cadherin junctions. *Progress in Molecular Biology and Translational Science* **116**:49–68. doi: 10.1016/B978-0-12-394311-8.00003-0, PMID: 23481190

Rauzi M, Verant P, Lecuit T, Lenne PF. 2008. Nature and anisotropy of cortical forces orienting Drosophila tissue morphogenesis. *Nature Cell Biology* **10**:1401–1410. doi: 10.1038/ncb1798, PMID: 18978783

Reymann AC, Boujemaa-Paterski R, Martiel JL, Guérin C, Cao W, Chin HF, De La Cruz EM, Théry M, Blanchoin L. 2012. Actin network architecture can determine myosin motor activity. *Science* **336**:1310–1314. doi: 10.1126/science.1221708, PMID: 22679097

Röper K. 2012. Anisotropy of Crumbs and aPKC drives myosin cable assembly during tube formation. *Developmental Cell* **23**:939–953. doi: 10.1016/j.devcel.2012.09.013, PMID: 23153493

Röper K. 2013. Supracellular actomyosin assemblies during development. *Bioarchitecture* **3**:45–49. doi: 10.4161/bioa.25339, PMID: 23760352

Röper K. 2015. Integration of cell-cell adhesion and contractile actomyosin activity during morphogenesis. *Current Topics in Developmental Biology* **112**:103–127. doi: 10.1016/bs.ctdb.2014.11.017, PMID: 25733139

Salbreux G, Charras G, Paluch E. 2012. Actin cortex mechanics and cellular morphogenesis. *Trends in Cell Biology* **22**:536–545. doi: 10.1016/j.tcb.2012.07.001, PMID: 22871642

Scarpa E, Szabó A, Bibonne A, Theveneau E, Parsons M, Mayor R. 2015. Cadherin switch during EMT in Neural Crest cells leads to contact inhibition of Locomotion via Repolarization of Forces. *Developmental Cell* **34**:421–434. doi: 10.1016/j.devcel.2015.06.012, PMID: 26235046

Shcherbo D, Murphy CS, Ermakova GV, Solovieva EA, Chepurnykh TV, Shcheglov AS, Verkhusha VV, Pletnev VZ, Hazelwood KL, Roche PM, Lukyanov S, Zaraisky AG, Davidson MW, Chudakov DM. 2009. Far-red fluorescent tags for protein imaging in living tissues. *Biochemical Journal* **418**:567–574. doi: 10.1042/BJ20081949, PMID: 19143658

Shi Q, Chien YH, Leckband D. 2008. Biophysical properties of cadherin bonds do not predict cell sorting. *Journal of Biological Chemistry* **283**:28454–28463. doi: 10.1074/jbc.M802563200, PMID: 18552401

Shih W, Yamada S. 2012. N-cadherin as a key regulator of collective cell migration in a 3D environment. *Cell Adhesion & Migration* **6**:513–517. doi: 10.4161/cam.21766, PMID: 23076138

Steinberg MS. 1963. Reconstruction of tissues by dissociated cells. some morphogenetic tissue movements and the sorting out of embryonic cells may have a common explanation. *Science* **141**:401–408. doi: 10.1126/science.141.3579.401, PMID: 13983728

Takeichi M, Matsunami H, Inoue T, Kimura Y, Suzuki S, Tanaka T. 1997. Roles of cadherins in patterning of the developing brain. *Developmental Neuroscience* **19**:86–87. doi: 10.1159/000111189, PMID: 9078437

Taulet N, Comunale F, Favard C, Charrasse S, Bodin S, Gauthier-Rouvière C. 2009. N-cadherin/p120 catenin association at cell-cell contacts occurs in cholesterol-rich membrane domains and is required for RhoA activation and myogenesis. *Journal of Biological Chemistry* **284**:23137–23145. doi: 10.1074/jbc.M109.017665, PMID: 19546217

Tepass U, Harris KP. 2007. Adherens junctions in Drosophila retinal morphogenesis. *Trends in Cell Biology* **17**: 26–35. doi: 10.1016/j.tcb.2006.11.006, PMID: 17134901

Umetsu D, Aigouy B, Aliee M, Sui L, Eaton S, Jülicher F, Dahmann C. 2014. Local increases in mechanical tension shape compartment boundaries by biasing cell intercalations. *Current Biology* **24**:1798–1805. doi: 10.1016/j.cub.2014.06.052, PMID: 25065753

Warner SJ, Longmore GD. 2009. Distinct functions for Rho1 in maintaining adherens junctions and apical tension in remodeling epithelia. *The Journal of Cell Biology* **185**:1111–1125. doi: 10.1083/jcb.200901029, PMID: 19506041

Wheelock MJ, Shintani Y, Maeda M, Fukumoto Y, Johnson KR. 2008. Cadherin switching. *Journal of Cell Science* **121**:727–735. doi: 10.1242/jcs.000455, PMID: 18322269

Winklbauer R. 2015. Cell adhesion strength from cortical tension - an integration of concepts. *Journal of Cell Science* **128**:3687–3693. doi: 10.1242/jcs.174623, PMID: 26471994

Yashiro H, Loza AJ, Skeath JB, Longmore GD. 2014. Rho1 regulates adherens junction remodeling by promoting recycling endosome formation through activation of myosin II. *Molecular Biology of the Cell* **25**:2956–2969. doi: 10.1091/mbc.E14-04-0894, PMID: 25079692

Yonemura S, Wada Y, Watanabe T, Nagafuchi A, Shibata M. 2010. alpha-Catenin as a tension transducer that induces adherens junction development. *Nature Cell Biology* **12**:533–542. doi: 10.1038/ncb2055, PMID: 20453849

Supplementary Figures

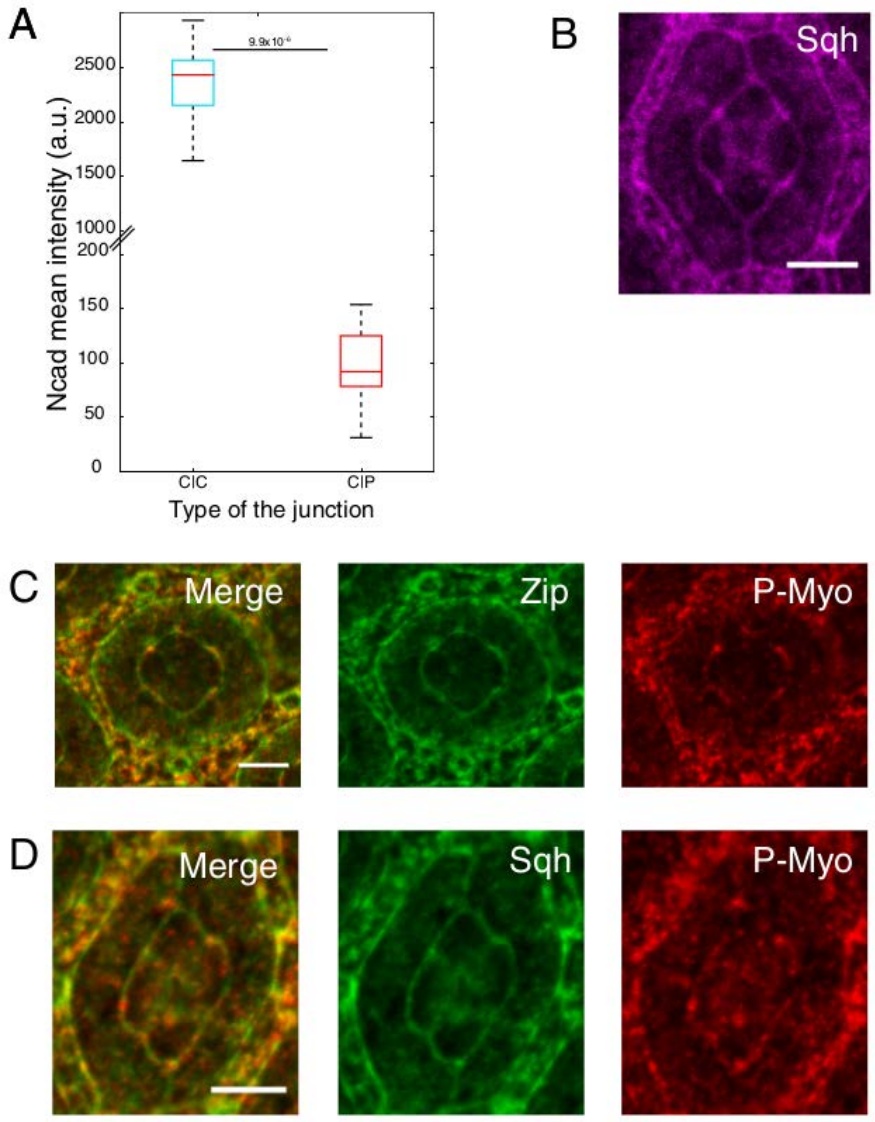

Figure 1 - figure supplement 1: Ncad and MyoII levels using different reporters (Myosin light chain II and Phospho-myosin light chain II).
(**A**) Quantification of Ncad::GFP intensity in C|C (n=12) and C|P (n=20) contacts at 41hrs APF. (**B**) An ommatidium with Zip::YFP (green) co-stained with P-MyoII antibodies (red). (**C**) An ommatidium with Sqh::GFP (green) in *Sqh* mutant background co-stained with P-MyoII antibodies (red). Scale bar, 5µm.

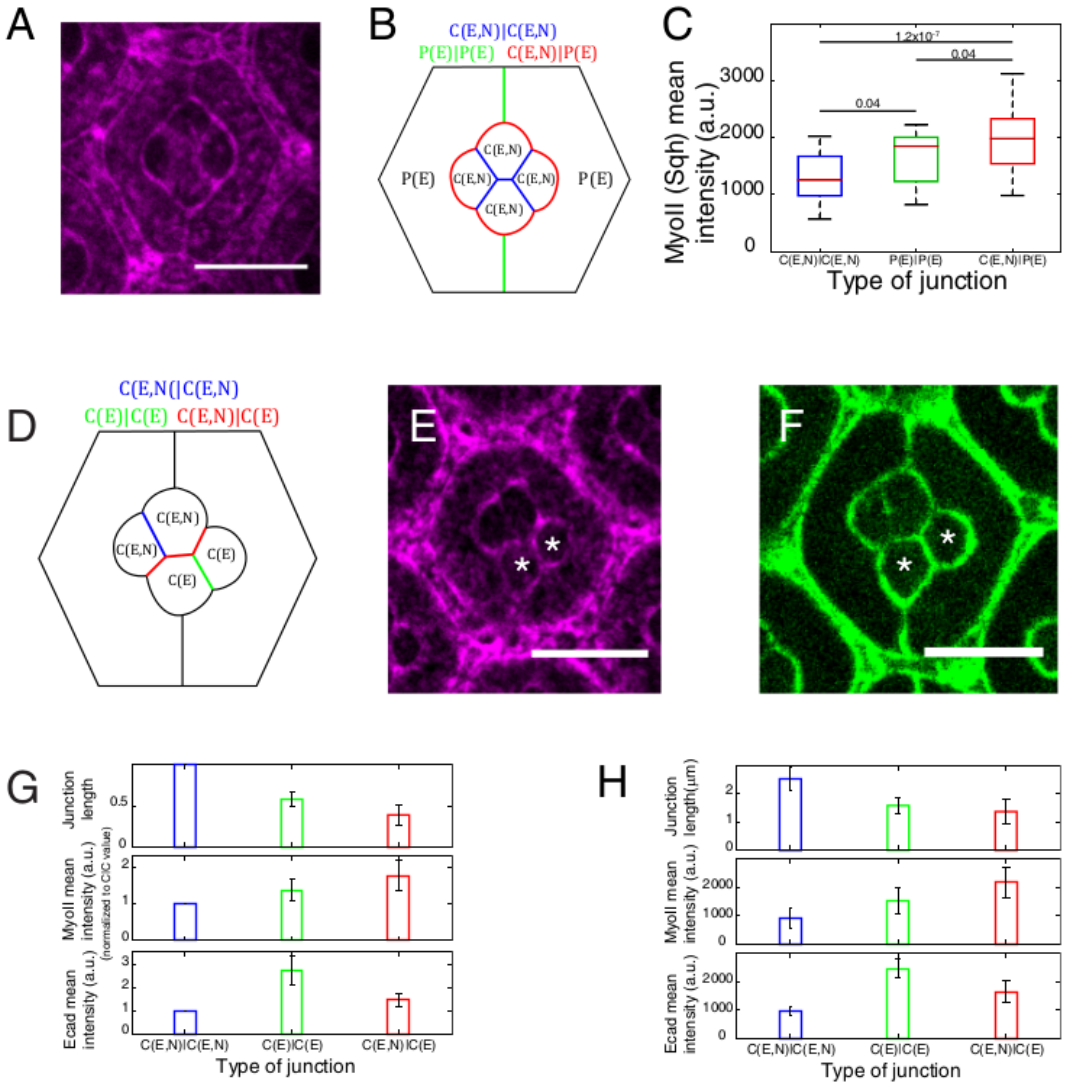

Figure 2 - figure supplement 1: Junction length, cadherins and MyoII levels at different contacts

(**A**) An ommatidium with Sqh::GFP in *Sqh* mutant background at 41hrs APF represented by (**B**) a schematic that highlights 3 different types of contacts at cell interfaces that express Ecad or Ncad or both Ecad and Ncad. C(E,N)|C(E,N) (blue), P(E)|P(E) (green) and C(E,N)|P(E) (red) contacts. Scale bar, 10μm. (**C**) Quantification of MyoII intensity in C(E,N)|C(E,N) (n=33), P(E)|P(E) (n=21) and C(E,N)|P(E) (n=50) contacts of ommatidia in (**A**). (**D**) A schematic of an ommatidium with 3 types of cell contacts in *Ncad*^{M19} mosaic mutants highlighting C(E,N)|C(E,N) contact (blue), C(E)|C(E) contact (green) and C(E,N)|C(E) contact (red) (**E**)-(**F**) Image of MyoII (**E**) and Ecad (**F**) of *Ncad*^{M19} mosaic ommatidium in (**D**). *Ncad*^{M19} cells marked by white asterisks. (**G**) Normalized cell contact length (C|C (n=15), C(E)|C(E) (n=15) , C(E,N)|C(E) (n=29)) , MyoII mean intensity (C(E,N)|C(E,N) (n=10), C(E)|C(E) (n=10) , C(E,N)|C(E) (n=20)) and Ecad mean intensity C(E,N)|C(E,N) (n=15), C(E)|C(E) (n=15) , C(E,N)|C(E) (n=29)) of the *Ncad*^{M19} mosaic ommatidia in (**D**). (**H**) Cell contact length C(E,N)|C(E,N) (n=38), C(E)|C(E) (n=36) , C(E,N)|C(E) (n=26)) MyoII mean intensity (same as Figure 2F) and Ecad mean intensity in *Ncad*^{M19} mosaic ommatidia (same as Figure 5, figure supplement 3F).

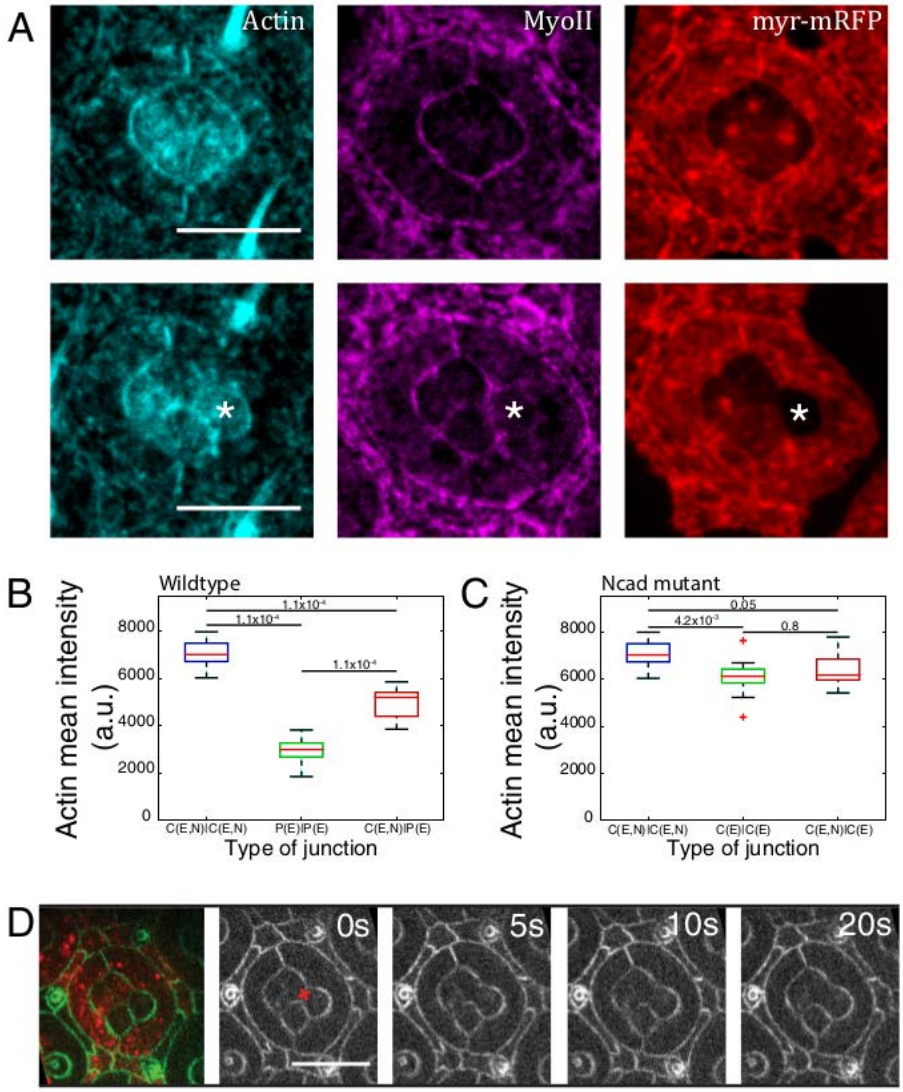

Figure 2 - figure supplement 2: ***Ncad*^{M19} mosaic ommatidium interfacial tension measurements and F-actin distribution.**

(**A**) Wildtype (upper panels) and *Ncad*^{M19} mosaic ommatidia (lower panels) with phalloidin staining for F-actin in cyan, Zip::YFP in magenta and wildtype cells are marked in myr-RFP (red) for locating the cell contacts. (**B**) Quantification of F-actin intensity in wildtype C|C (n= 12), P(E)|P(E) (n= 12) and C(E,N)|P(E) (n= 12) contacts. (**C**) Quantification of F-actin intensity in *Ncad*^{M19} mosaic ommatidia C(E,N)|C(E,N) (n= 12), C(E)|C(E) (n= 15) and C(E,N)|C(E) (n= 15) contacts. Scale bar, 10µm. (**D**) Image of a *Ncad*^{M19} mosaic ommatidium with Ecad::GFP (green) and wildtype cells in red, followed by snapshot of an ablation at a C(E,N)|C(E) contact (red cross). Scale bar, 10µm.

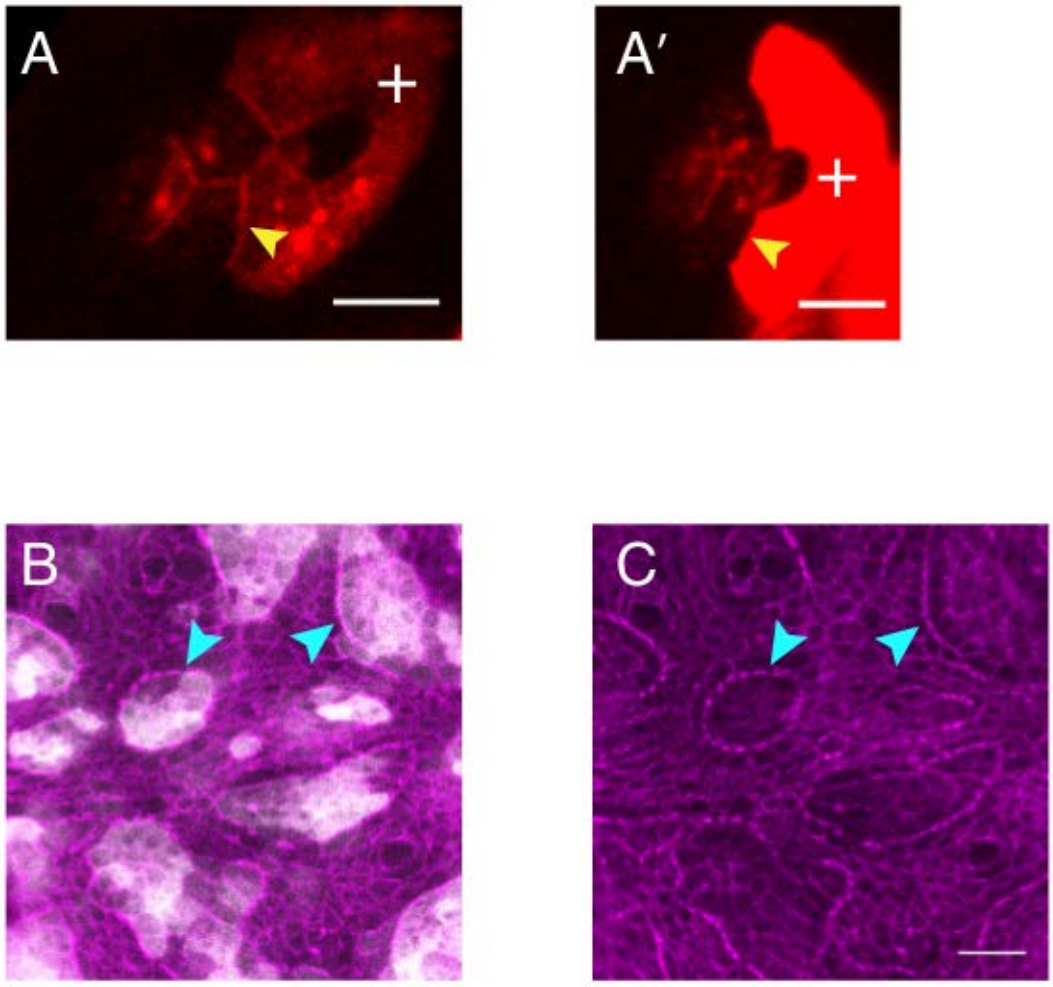

Figure 3 - figure supplement 1

Misexpression of Ncad in primary pigment cell in retinas and larval wing pouch

(**A**)-(**A'**) Examples of ommatidium misexpressing Ncad in one of the primary pigment cells (white **+**) with antibody staining for Ncad in red. Yellow arrowhead indicates the C(E,N)|P(E,N+) cell contact with homophilic Ncad. Scale bar, 5μm. (**B**)-(**C**) Larval wing pouch with Sqh::Ch (magenta) in (**C**) and misexpression of Ncad clones (grey in (**B**). Accumulation of MyoII at clonal boundaries indicated by cyan arrowheads. Scale bar, 10μm.

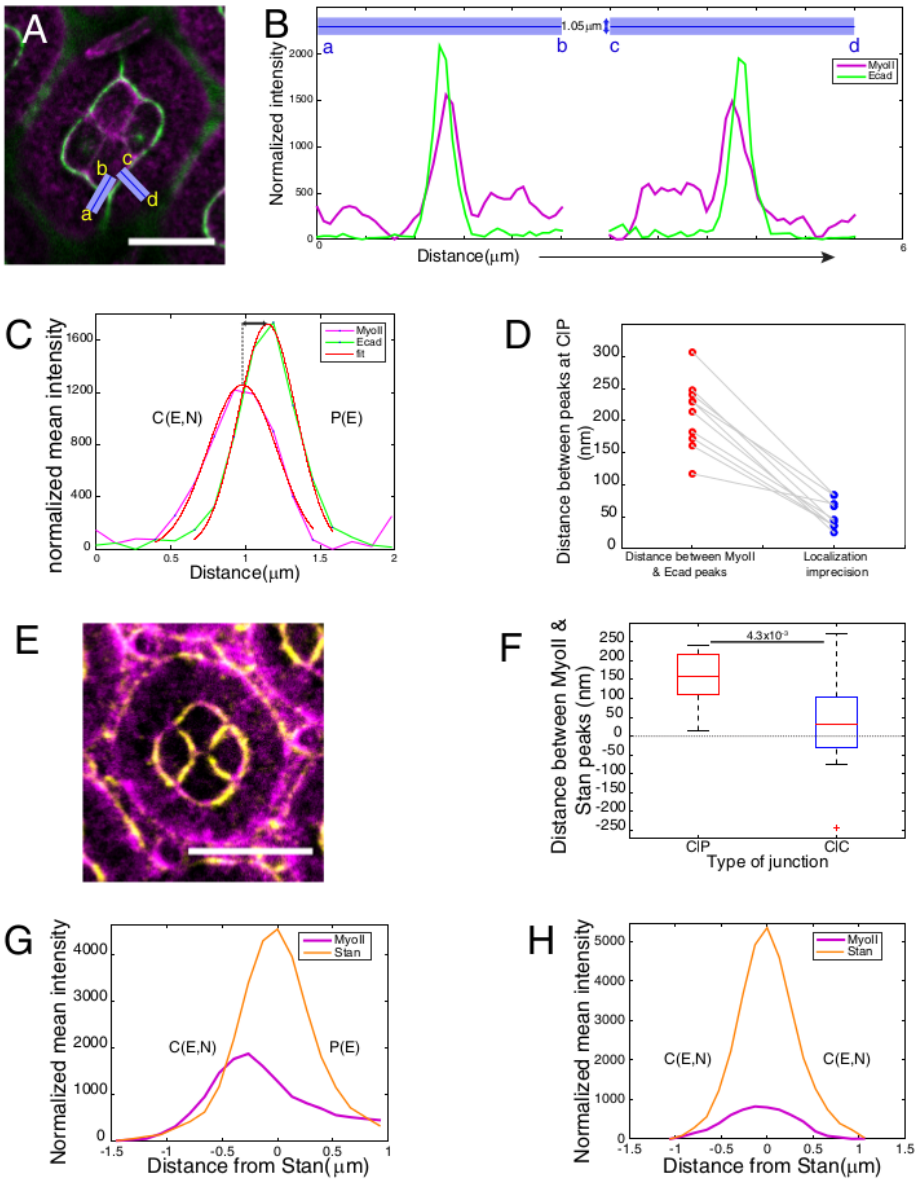

Figure 3 - figure supplement 2: Asymmetry of MyoII localization at different contacts

(**A**)-(**B**) Individual linescan of Sqh::Ch (magenta) and Ecad::GFP (green) from the purple lines (linewidth 1.05mm) drawn orthogonal to cell contacts from cone cell to primary pigment cell in a wildtype ommatidium in (**A**). (**C**) Individual linescan orthogonal to a C(E,N)|P(E) contact. Peak positions were determined by fitting intensity profiles with Gaussian. (**D**) Distance between Ecad and MyoII peak positions at C(E,N)|P(E) contacts and the respective imprecision in localization of the two peaks. (**E**) Wildtype ommatidium with Zip::YFP in magenta and antibody staining for Starry night (Stan) (yellow). (**F**) Distance between Ecad and MyoII peak positions at C(E,N)|P(E) and C(E,N)|C(E,N) contacts obtained from individual linescan (n=15 different contacts for each contact type) (**G**) Average linescan of Zip::YFP (magenta) with respect to Stan (orange) at C(E,N)|P(E) contact (n=15 contacts). (**H**) Average linescan of Zip::YFP (magenta) with respect to Stan (orange) at C(E,N)|C(E,N) (n=15 contacts). Scale bar 10μm.

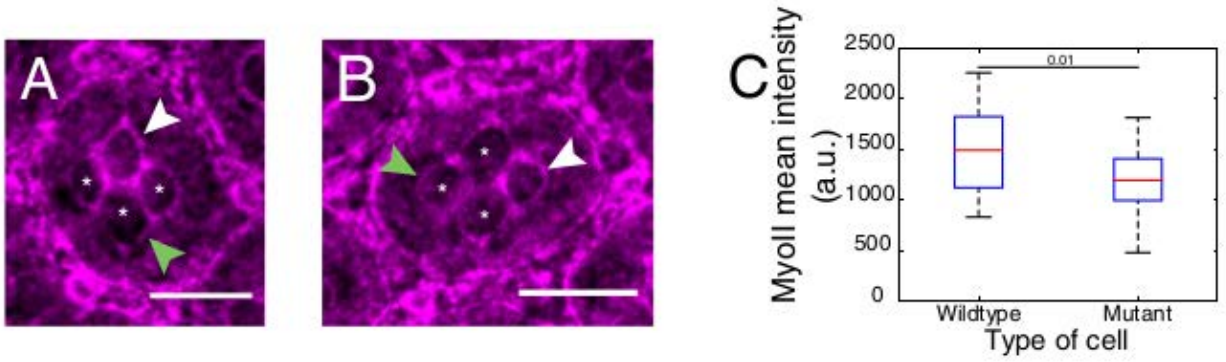

Figure 3 - figure supplement 3: MyoII levels of a single wildtype cone cell in *Ncad*^{M19} mosaic ommatidium.
(**A**) MyoII (Zip::YFP) (in magenta) in wildtype equatorial cone cell expressing both Ecad and Ncad (indicated by white arrowhead) surrounded by *Ncad*^{M19} cone cells. (**B**) MyoII in wildtype posterior expressing both Ecad and Ncad (indicated by white arrowhead) surrounded by *Ncad*^{M19} cone cells. (**C**) Quantification of MyoII intensity in contour of 1(E,N)|2(E) contacts of wildtype cone cell (n=41, white arrowhead in images (**A**), (**B**) and in contour of 1(E)|2(E) *Ncad*^{M19} cone cells (n=41, green arrowhead in images (**A**), (**B**)).

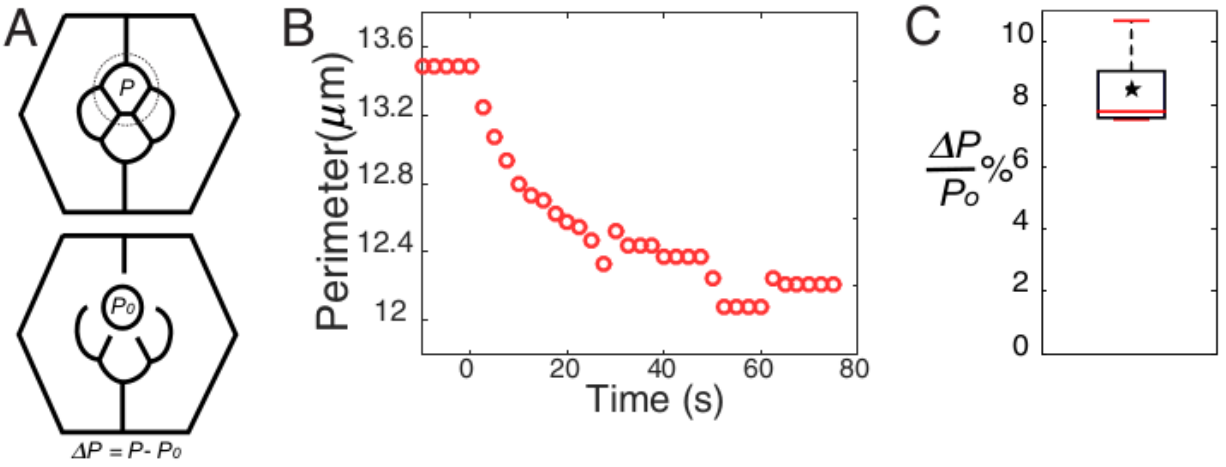

Figure 5 - figure supplement 1: Perimeter elasticity and determination of elastic constant (*K*).
(**A**) Schematic of a circle ablation experiment. Dotted circle marks the ablation position with *P*, perimeter before ablation and *P0*, perimeter after ablation with Δ*P*= *P*-*P0*. (**B**) Plot of a perimeter change over the time from an experiment. (**C**) Boxplot showing percentage change of perimeter (n=7).

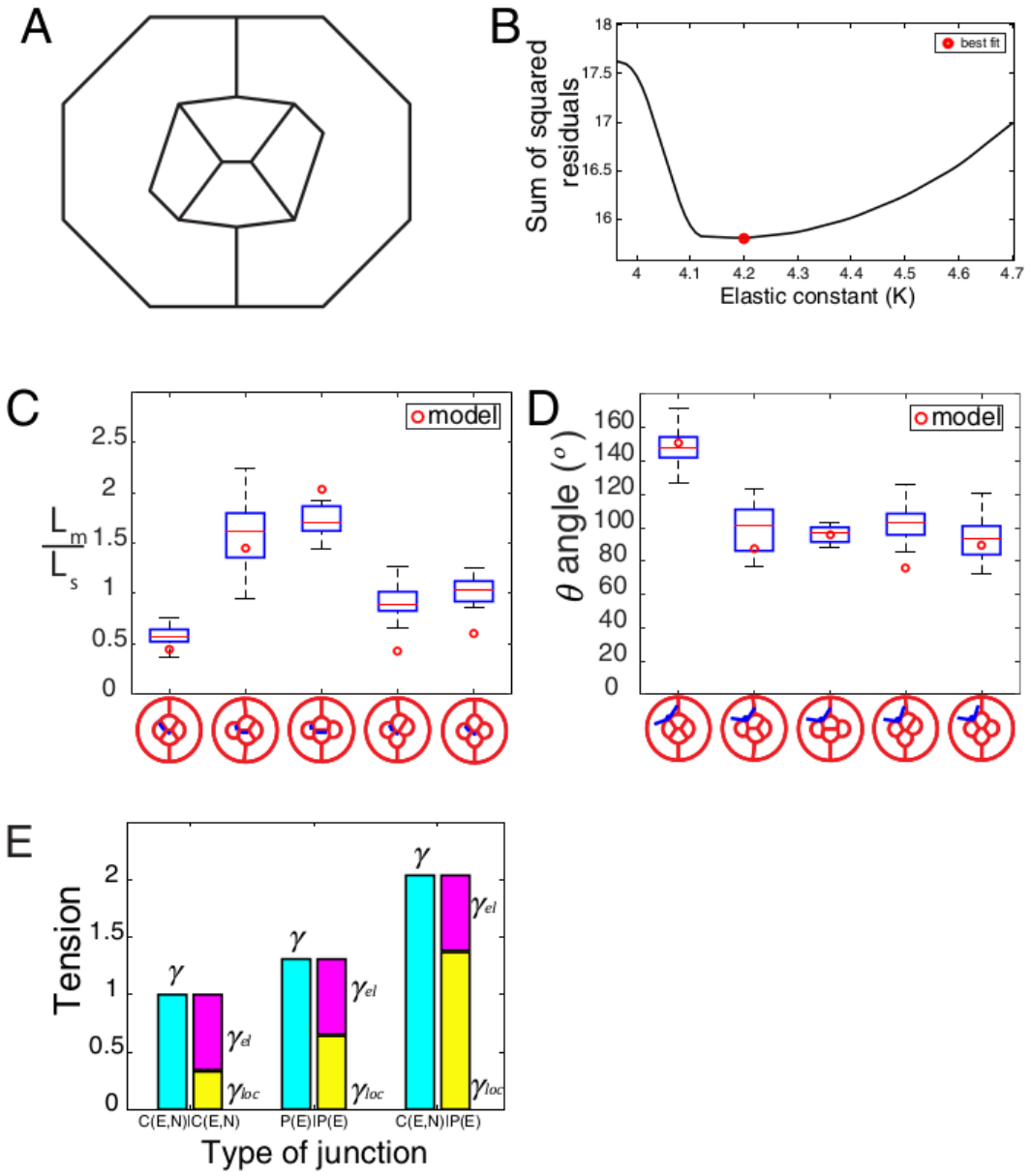

Figure5 - figure supplement 2: Elastic & local tension contribution to interfacial tension and comparison of simulation to experiment.

(**A**) Initial configuration used in Surface Evolver before the minimization of the energy function. (**B**) Plot of the sum of squared residuals as a function of K. The best fit is obtained for K=4.2 (red circle). (**C**) Graph of fit-parameter *Lm/Ls* (n1= 43, n2= 9, n3= 8, n4= 28, n5= 15) for experimental images in wildtype and $Ncad^{M19}$ mosaic configurations, and comparison to the respective simulation value. (**D**) Graph of fit-parameter angle (θ) (n1= 210, n2= 9, n3= 8, n4= 28, n5= 64) for experimental images in wildtype and $Ncad^{M19}$ mosaic configurations, and comparison to the respective simulation value. (**E**) Tensions γ, γ_{el}, γ_{loc} for the three different types of wildtype contacts.

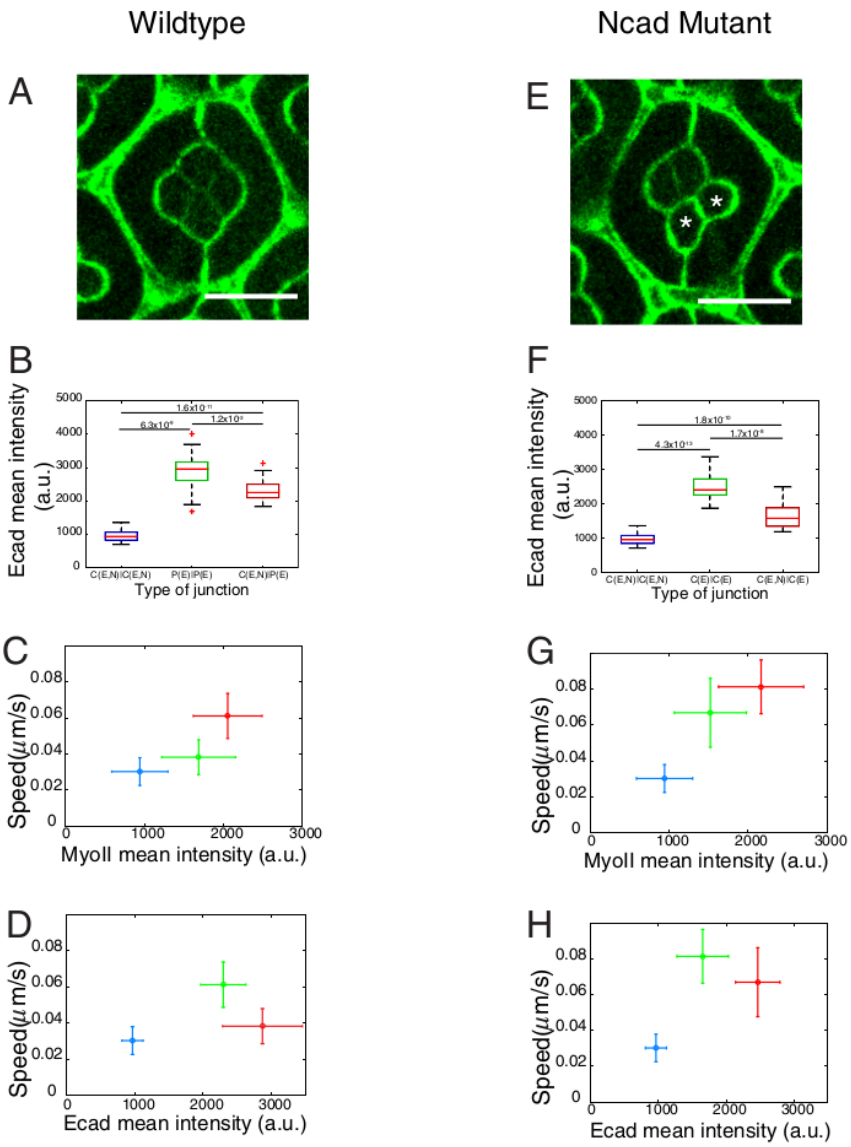

Figure 5 - figure supplement 3: Ecad intensity measurements and correlation of interfacial tension to molecular distributions.

(**A**) Wildtype ommatidium with Ecad::GFP. (**B**) Quantification of Ecad intensity in wildtype ommatidia with C(E,N)|C(E,N) (n=38), P(E)|P(E) (n=18) and C(E,N)|P(E) (n=28) contacts. (**C**)-(**D**) Correlation of interfacial tension to the mean intensity of MyoII (**C**) and Ecad (**D**) at three different cell contacts in wildtype ommatidia. Correlation of interfacial tension to MyoII mean intensity at three different cell contacts in (**E**) A *Ncad*^{M19} mosaic mutant ommatidium with Ecad::GFP. *Ncad*^{M19} marked by white asterisks. (**F**) Quantification of Ecad intensity in C|C (n=38), C(E)|C(E) (n=36) and C(E,N)|C(E) (n=26) contacts. (**G**)-(**H**) Correlation of interfacial tension to the mean intensity of MyoII (**G**) and Ecad (**H**) at three different cell contacts in wildtype ommatidia. Scale bar, 10μm.

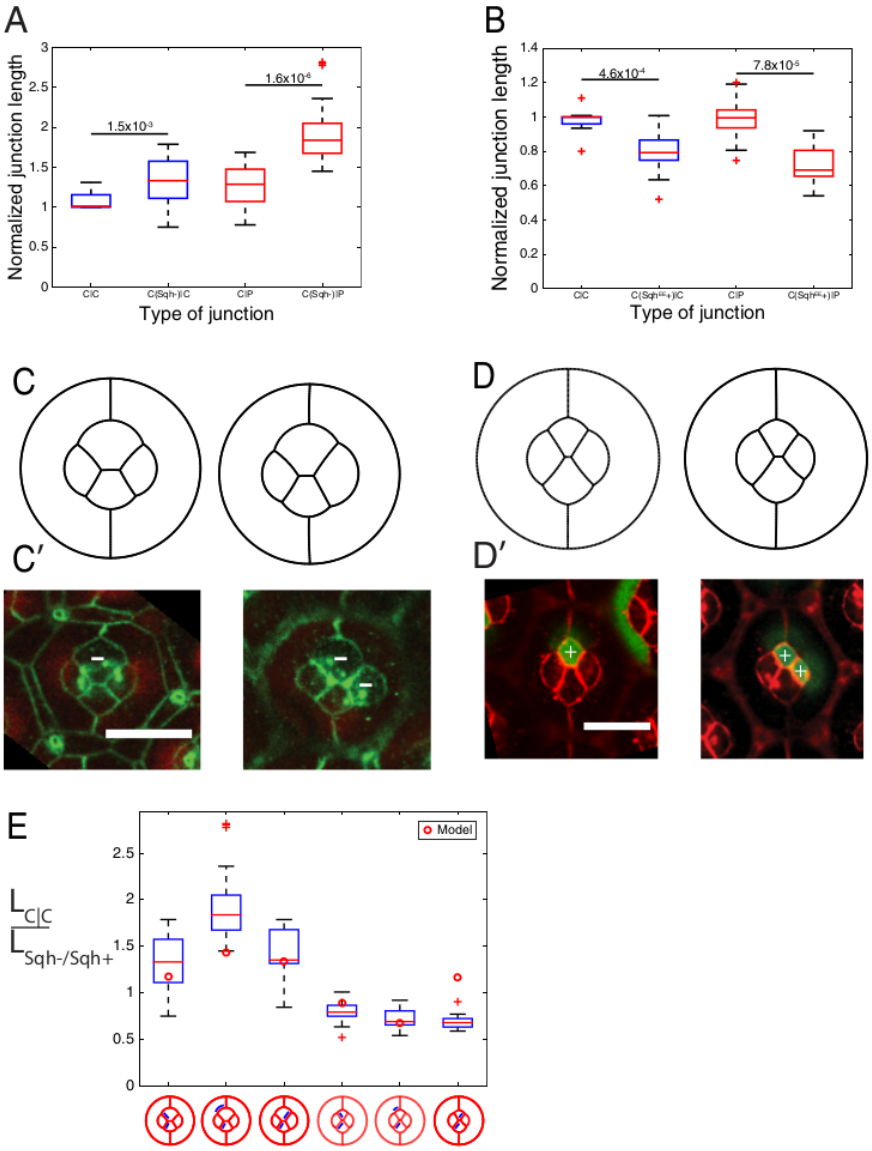

Figure 5 - figure supplement 4: MyoII perturbations and simulations.
(**A**) Comparison of junction length of wildtype C|P contact, modified contacts containing one *Sqh*^{Ax3} mutant cell (C(Sqh-)|C or C(Sqh-)|P) to wildtype C|C contacts in experiments. (**B**) Comparison of junction length between wildtype C|P contacts(C|C or C|P) ,and modified contacts misexpressed active Sqh(Sqh^{EE}) in one cell (C(Sqh^{EE}+)|C or C(Sqh^{EE}+)|P) to wildtype C|C contacts in experiments. (**C**)-(**C′**) Comparison of simulations (**C**) to the experimental images (**C′**) of *Sqh*^{Ax3} mutant (white **-**), b-catenin staining in green. (**D**)-(**D′**) Comparison of simulations (**D**) to the experimental images (**D′**) of Sqh^{EE} misexpression (white **+**), β-catenin staining in red. Scale bar, 10μm. (**E**) Ratio of contact length in C|C to different modified contacts with *Sqh*^{Ax3} or *Sqh*^{EE} cells.

Supplementary Materials and Methods

Parameters measurements and model simulations

Simulations of ommatidia rely on the minimization of the energy function using Surface Evolver. Surface Evolver is a freely available software [82] designed for the study of objects maintained by surface energy (in our 2D case, line energy) and other customizable forms of energy (in our case, perimeter elasticity). Surface Evolver evolves the given surface towards its minimal energy by a gradient descent method. The area of each cell is fixed in the model, even though apical area can change experimentally. This choice is driven by simplicity arguments. Indeed, area variations could be accounted for with an area elasticity term (in the form k_a*(A-A0)^2). Yet, and unlike perimeter elasticity, area elasticity is not crucial to select a shape or configuration [21] but mostly sets cell area. Hence we chose to fix the area so that it matches the experimentally measured one, which spared us from having additional free parameters (k_a and A0). In MyoII perturbation experiments, in which cell area is significantly modified, we changed the fixed area to that measured in experiments.

The simulations parameters are γ_{loc}, which depends on the cell contact type, the elastic constant K, which we assume constant for all cells, and the preferred perimeters P_0. Using our circular ablation experiments to determine preferred perimeters, our measurements of (γ) for the different contact types, and the fact that $\gamma_{loc} \approx \gamma - 2K\frac{\Delta P}{P_{0i}}$, K is the only free parameter remaining. We ran simulations with K ranging from 0.1 to 6 and fitted the resulting shapes to wildtype and Ncad mosaic ommatidia. The geometrical descriptors that we used for the fit are i) the contact angle θ between cone cells and primary pigment cells, and ii) the ratio Ls/Lm. Ls is the length of the junction shared by the posterior/anterior cone cell and the polar/equatorial cell, and Lm the length of the junction shared by equatorial and polar cells (Figure 5A). To actually perform the fit we calculated the sum of residuals for the measured angles and ratios in 5 configurations (1 wildtype + 4 different $Ncad^{M19}$ mosaic configurations), hence 2x5=10 residuals. We used a weighted least square method to take into account that the descriptors (an angle and a length ratio) are different quantities. Note that to simulate Ncad mosaic ommatidia, we only changed the parameter γ_{loc} according to the contact type. For example, if the anterior cone cell lacks Ncad, then its contacts shared with equatorial and polar cone cells become C(E,N)|C(E) and its contact shared with the

primary pigment cell becomes C(E)|P(E). Tensions were set according to ablation experiments performed for each contact type.

Estimation of the contribution of adhesion and cortical tension to γ_{loc}

Local tension γ_{loc} results from the balance between MyoII contractility σ and cadherin-based adhesion ω_N, and we were interested in weighing their respective (direct) contributions. In order to do so, we assumed, adhesion molecules and motor molecules have an additive and antagonistic role. Hence we have $\gamma_{loc} = \sigma - \omega$. $\omega = \omega_E + \omega_N$ if both Ecad and Ncad are present at the contact, and $\omega = \omega_E$ if only Ecad is present. We assumed that σ is proportional to MyoII intensity ($\sigma = \alpha C_M$) and ω proportional to Cadherin intensity ($\omega_E = \beta C_E$ for Ecad and $\omega_N = \delta C_N$ for Ncad). Each contact type (C(E,N|C(E,N), C(EN)|P(E), P(E)|P(E), C(E,N)|C(E) and C(E)|C(E)) provides an equation, so that we have 5 equations for 3 unknowns (α, β, and δ). We use a least square fit method to find the best solution to this overdetermined system, thus estimate (α, β, δ) and consequently determine the relative contributions of MyoII(σ), Ecad(ω_E) and Ncad(ω_N) to γ_{loc} for the different contact types (*Figure 5D*).

Simulations of MyoII mutants and MyoII overexpression

MyoII manipulation experiments changed the apical areas of the cone cells and length of the cell contacts (*Figure 3- figure supplement 4A,B)*. Myosin light chain (Sqh^{Ax3}) mutant cone cells showed larger apical surface area than their wildtype counterparts. Cone cells misexpressing the constitutively active Myosin light chain (UAS-$Sqh^{T20ES21E}$) showed smaller apical surface area than their wildtype counterparts. To simulate the shape of these perturbed cells, we measured the area (A) of these cells to fix it in the simulations and the target perimeter by $P_0 = 2\sqrt{A\pi}$. The *in silico* patterns obtained for this simple change in area and target perimeter are in good agreement with the *in vivo* cell patterns (*Figure 3- figure supplement 4 C, C', D, D', E*).

Cell contact length measurement in ommatidium with two $Ncad^{M19}$ cone cells

PFA-fixed retinas with Ecad::GFP and RFP to differentiate wildtype from $Ncad^{M19}$ mutant cells were used to measure the junction length of C(E,N)|C(E,N), C(E)|C(E) , C(E,N)|C(E) cell

contacts in ommatidia with two adjacent cone cells *Ncad*^{M19} mutants. Lengths were measured using 'line tool' of Fiji. Different types of lengths measured in an ommatidum is normalized to its C(E,N)|C(E,N) length.

Quantification of Ecad intensity

PFA-fixed retinas with Ecad::GFP and RFP to differentiate wildtype from *Ncad*^{M19} mutant cells. Images were obtained with Zeiss LSM780 confocal microscopy and Fiji was used for quantification. Background subtraction was not used since the background was nearly zero. Stacks were summed on 'Z project'. Linewidth 4 (0.659µm) of the segmented 'selection' tool was used to measure the mean intensity of junctional Ecad according to the contact type.

Quantification of MyoII intensity in *Ncad*^{M19} mosaic ommatidia with only one wildtype Ecad and Ncad expressing cone cell

PFA-fixed retinas with Zip::YFP to mark MyoII and RFP to differentiate wildtype from *Ncad*^{M19} cells were imaged with Zeiss LSM780 confocal microscope and images were quantified by Fiji. Stacks were summed on 'Z project' for all the images. Background was measured from the center (apical region) of any cone cell. Linewidth 4 of the segmented 'selection' tool was used to measure mean intensity around wildtype cell and around *Ncad*^{M1} mutant cell. Background was subtracted from wildtype and mutant mean intensities for each image. After background subtraction, intensities were compared (wildtype n= 41, mutant n=41).

Quantification of F-Actin intensity

PFA-fixed retinas with Zip::YFP to mark MyoII, RFP to differentiate wildtype from *Ncad*^{M19} mutant cells and phalloidin staining for Actin. Images were obtained with Zeiss LSM780 confocal microscopy and Fiji was used for quantification. Stacks were summed on 'Z project'. Linewidth 7 (0.615µm) of the segmented 'selection' tool was used to measure the mean intensity of junctional F-Actin according to the contact type (junctional Zip::YFP was used for the reference).

Quantification of Ncad intensity

PFA-fixed retinas with Ncad::GFP were obtained with Zeiss LSM780 confocal microscopy and Fiji was used for quantification. Line width 5 (0.659µm) of the segmented 'selection' tool was used to measure the mean intensity. For each measurement at the C(E,N)|C(E,N) and C(E,N)|P(E) contacts, background is measured adjacent to the contact and subtracted from the signal at junctions.

Analysis of localization error in Ecad or MyoII peaks

The localization precision (ΔX) of Ecad or MyoII is given by [81]:

Where Γ is the standard deviation of the Gaussian fit of the intensity profiles, SNR is the signal to noise ratio, and dx is the pixel size. We used the following values:

$$\Delta X \sim \frac{1.8}{SNR}\sqrt{\Gamma\ \delta x}$$

$\Gamma_{Ecad} \sim 250$ nm and $\Gamma_{MyoII} \sim 300$ nm

$SNR_{Ecad} \sim 34$ and $SNR_{MyoII} \sim 10$

dx = 131nm

Finally we found that:

DX_{Ecad} = 5- 22nm

DX_{MyoII} = 18- 77nm (n=10)

Generation of CRISPR/Cas9 mediated NCAD:mKate2 flies

Plasmid Construction. Cloning was performed with the Gibson assembly Mix (New England Biolabs). PCR products were produced with the Phusion Hot Start II HF DNA Polymerase (Thermo Scientific). All inserts were verified by sequencing. Primers used for plasmid construction are listed in Table S1. Primers gRNA-NCadFw and gRNA-NCadRev were used to obtain the Ncad-gRNA from pACMAN BAC DN.CAD CH321-57H14. pCFD3 plasmid containing the U6:3 promoter (from Addgene no. 49410;; [79]) was used to clone annealed complementary NCAD oligo-nucleotides into the BbsI digested backbone using standards procedures to produce the following 5'-to-3' configuration : U6 promoter-gRNA-Ncad-gRNA core sequence. The construct was inserted in the attP2 site on chromosome 3 to generate transgenic flies (BestGene Inc., Chino Hills, CA).

Ncad::mKate2 Donor Plasmid Production. The donor plasmid was designed to introduce a mKate2-coding sequence before the stop codon of NCAD. The exogenous sequence is flanked by homology arms of 2.31 kb (5' homology) and 1.46 kb (3' homology). The 5' homology arm contains a synonymous mutation that removes the protospacer-adjacent motif (PAM) sequence for g-RNA-NCAD to prevent mutagenesis after the integration of donor-derived sequences. The 5' and 3' homology arms were PCR amplified from genomic DNA from the clone pACMAN BAC DN.CAD CH321-57H14 using primers Ncad5'. For, Ncad5'.Rev, Ncad3'-For, Ncad3'-Rev. The mKate2 coding sequence was amplified from a mKate2-containing plasmid [83] using the primers mKate2For and mKate2Rev. The sequences of all the primers can be found in Table S1. All fragments were assembled by Gibson assembly into pBluescript SK(+) (Stratagene) that was digested with XhoI and NotI.

Embryo Injections. Embryos from crosses between transgenic nos-cas9 (BL 54591) virgin females and U6:3-gRNA-NCAD-expressing males were injected using standard procedures. Plasmid DNA for homologous recombination-mediated integration of mKate2 into the NCAD locus was injected at a concentration of 300 ng/µl into the nos-cas9/+;U6:3-gRNA-NCAD/+ embryos. After injection of plasmids, embryos were transferred on their coversplips to a plastic box containing wet paper towel at 25 °C until they hatched as larvae. Larvae were collected with forceps and transferred to a food vial with fresh yeast, followed by culture at 25 °C.

***Drosophila* Genetics and Screen**

Approximately 2% of the injected Nos-cas9/+; gRNA-NCAD/+ larvae survived the injection and were crossed to a w; Sp/CyO balancer strain. In the next generation (F1), the males were conserved at 18 °C and 5 females were pooled for genomic extraction and PCR screen. The quality of the DNA extraction was tested with the TIO-F and TIO-R primers. The presence of mKate2 insertion in the genome was detected by PCR using the m-Kate2-Fw and m-Kate2-Rv primers. When an amplification was obtained for mKate2, 30 F1 males were crossed

individually with w; Sp/CyO females. When the F2 generation is well developed, the F1 male was sacrified to extract the genomic DNA and screen for the presence of mKATE2. Then, the progeny of positive male was amplified and stored. To confirm that the sequences remain in-frame after the CRISP-R integration, the DNA sequence surrounding the fusion was amplified by PCR using primers NCAD-F2 and mKate2R2 (Table S1) and checked by sequencing. The resulting Ncad::mKate2 flies are homozygous viable.

Supplementary File 1

Table 1: MyoII levels in different experiments at different contact types

Experiment	Type, mean±SD, n	Type, mean±SD, n	Type, mean±SD, n
MyoII levels (**zipper**) in **wildtype** ommatidium	C(E,N)|C(E,N) 943±356 30	P(E)|P(E) 1687±467 22	C(E,N)|P(E) 2054±434 36
MyoII levels (**Zipper**) in **Ncad mutant** conditions	C(E,N)|C(E,N) 943±356 30	C(E)|C(E) 1523±457 22	C(E,N)|C(E) 2166±538 36
MyoII levels (**Sqh**) in **wildtype** ommatidium	C(E,N)|C(E,N) 1943±404 33	P(E)|P(E) 2269±465 21	C(E,N)|P(E) 2619±498 50
MyoII levels (**P-myo**) in **wildtype** ommatidium	C(E,N)|C(E,N) 861±181 24	P(E)|P(E) 1018±229 19	C(E,N)|P(E) 1249±295 29
MyoII levels **Mis-expression** of	C(E,N)|P(E, N+) 2959±465	----------	C(E,N)|P(E) 35956±354

Ncad in Primary pigment cell	20		20
MyoII levels **Mis-expression** of **Ncad** in Primary pigment cell	---------- ---	P(E)|P(E) 2871±364 16	P(E)|P(E,N+) 4248±762 16
MyoII levels **Mis-expression** of **NcadΔcyto** in Primary pigment cell	C(E,N)|P(E,ΔN+) 2174±374 28	----------	C(E,N)|P(E) 2926±681 28
MyoII levels **Mis-expression** of **NcadΔcyto** in Primary pigment cell	---------- ---	P(E)|P(E) 1644±331 16 P(E)|P(E,ΔN+) 1601±315 19	---------- --

Table 2 : Junction length, MyoII level, Ecad level and Ncad level in different experiments at different contact types

Experiment	Junction length	MyoII level	Ecad level	Ncad level
Wildtype ommatidia (single experiment)	In µm C(E,N)|C(E,N) 2.5±0.4 n=38 P(E)|P(E) 3.1 ±0.3 n=18 C(E,N)|P(E) 4.3±1.9 n=28 (Normalized to C(E,N)|C(E,N)=1) 1 : 1.2 : 1.7	C(E,N)|C(E,N) 942±355 n=30 P(E)|P(E) 1686±467 n=22 C(E,N)|P(E) 2054±434 n=36 (Normalized to C(E,N)|C(E,N)=1) 1 : 1.8 : 2.2	C(E,N)|C(E,N) 965±155 n=38 P(E)|P(E) 2868±583 n=36 C(E,N)|P(E) 2294±330 n=26 (Normalized to C(E,N)|C(E,N)=1) 1 : 3.0 : 2.4	C(E,N)|C(E,N) 2382±369 n=12 C(E,N)|P(E) 77±52 n=20 (Normalized to C(E,N)|C(E,N)=1) 1 : 0 : 0.03

Ncad mutant ommatidia (single experiment)	In µm C(E,N)|C(E,N) 2.5±0.4 n=38 C(E)|C(E) 1.58±0.3 n=36 C(E,N)|C(E) 1.4±0.4 n=26 (Normalized to C(E,N)|C(E,N)=1) 1 : 0.6 : 0.5	C(E,N)|C(E,N) 942±355 n=30 C(E)|C(E) 1523±456 n=22 C(E,N)|C(E) 2165±537 n=36 (Normalized to C(E,N)|C(E,N) =1) 1 : 1.6 : 2.3	C(E,N)|C(E,N) 965±155 n=38 C(E)|C(E) 2467±327 n=36 C(E,N)|C(E) 1654±379 n=26 (Normalized to C(E,N)|C(E,N)=1) 1 : 2.6 : 1.7	---------- -
MyoII	(Normalized to		(Normalized to	(Normalized to

overexpression (Sqh^{EE}+) (Collected over many experiment)	C|C=1) C(Sqh^{EE}+)|C 0.8±0.1 n=14 C(Sqh^{EE}+)|P 0.7±0.1 n=14	----------	C|C=1) C(Sqh^{EE}+)|C 1.06±0.3 n=14 C(Sqh^{EE}+)|P 2.6±0.9 n=14	C|C=1) C(Sqh^{EE}+)|C 1±0.1 n=14
MyoII Mutant (Sqh -) (Collected over many experiments)	(Normalized to C|C=1) C(Sqh-)|C 1.3±0.3 n=20 C(Sqh-)|P	---------- ---	(Normalized to C|C=1) C(Sqh-)|C 1.7±0.7 n=10 C(Sqh-)|P	(Normalized to C|C=1) C(Sqh-)|C 1.1±0.2 n=11

	1.9±0.4 n=20		1.9±0.6 n=10	

Table 3 : Statistics

Figure	Test	Methods	N values	Replicates	P values
2C	Mann-Whitney test with Bonferroni correction (P≥0.5, N.S)	Box plot with median, 25th percentile and 75th percentile If present, In '+' are outliers	N1=30, n2=22, n3=36 cell contacts in a retina	3 independent experiments (2C is an independent experiment).	C(E,N)|C(E,N), P(E)|P(E) 3.5x10^{-6} P(E)|P(E), C(E,N)|P(E) 0.01 C(E,N)|P(E), C(E,N)|C(E,N) 3.5x10^{-10}
2F	Mann-Whitney	Box plot with	n1=30, n2=22,	3 independent experiments	C(E,N)|C(E,N), C(E)|C(E)

	test with Bonferroni correction (P≥0.5, N.S)	median, 25th percentile and 75th percentile In '+' are outliers	n3=36 cell contacts in a retina	(2F is an independent experiment).	5.0x10^{-5} C(E)|C(E), C(E,N)|C(E) 1.2x10^{-4} C(E,N)|P(E), C(E,N)|C(E,N) 1.5x10^{-10}
2J	Mann-Whitney test with Bonferroni correction (P≥0.5, N.S)	Box plot with median, 25th percentile and 75th percentile In '+' are outliers	N1=14, n2=18, n3=19 for each type of contact, 4-5 ablation experiment in a retina	Experiments in 4-5 retinas (2J is not an independent experiment)	C(E,N)|C(E,N), P(E)|P(E) 0.02 P(E)|P(E), C(E,N)|P(E) 9.3x10^{-6} C(E,N)|P(E), C(E,N)|C(E,N) 4.2x10^{-6}

2K	Mann-Whitney test with Bonferroni correction (P≥0.5, N.S)	Box plot with Median, 25th percentile and 75th percentile In '+' are outliers	n=13 for each type of contact, 2-3 ablation experiment in a retina	Experiments in 4-5 retinas (2K is not an independent experiment)	C(E,N)|C(E,N), C(E)|C(E) $4.7x10^{-4}$ C(E)|C(E), C(E,N)|C(E) 0.04 C(E,N)|P(E), C(E,N)|C(E,N $7.6x10^{-6}$
3C	Mann-Whitney test with Bonferroni correction (P≥0.5, N.S)	Box plot with Median, 25th percentile and 75th percentile In '+' are outliers	n1 = 20, n2 = 20 cell contacts in a retina	2 independent experiments (3C is an independent experiment)	C(E,N)|P(E), C(E,N)|P(E,N+) $1.5x10^{-4}$
3D	Mann-	Box plot	n1 = 16,	2 independent	P(E)|P(E),

	Whitney test with Bonferroni correction (P≥0.5, N.S)	with Median, 25th percentile and 75th percentile	n2 = 16 cell contacts in a retina	experiments (3D is an independent experiment)	P(E)|P(E,N+) $6.5x10^{-6}$
3G	Not applicable (NA)	NA	n=10	2 independent experiments (3G is an independent experiment)	NA
3J	NA	NA	n=13	3 independent experiments (3J is an independent experiment)	NA
4D	Mann-Whitney test with Bonferroni correction	Box plot with Median, 25th percentile and 75th percentile	n1 = 28, n2 = 28 cell contacts in a retina	4D is combination of 2 experiments	C(E,N)|P(E), C(E,N)|P(E,ΔN+) $1x10^{-4}$

	(P≥0.5, N.S)	In '+' are outliers			
4E	Mann-Whitney test with Bonferroni correction (P≥0.5, N.S)	Box plot with Median, 25th percentile and 75th percentile In '+' are outliers	n1 = 19, n2 = 19 cell contacts in a retina	4E is combination of 2 experiments	P(E)|P(E), P(E)|P(E,ΔN+) 1.2
Fig. 1 Suppl. Fig. 1 A	Mann-Whitney test with Bonferroni correction (P≥0.5, N.S)	Box plot with Median, 25th percentile and 75th percentile In '+' are outliers	n1 = 12, n2 = 20 cell contacts in a retina	1S1A is an independent experiment	C(E,N)|C(E,N), C(E,N)|P(E) $6.6x10^{-6}$
Fig. 2 Suppl. Fig. 1 D	NA	Mean, SD	Length (n=15 ommatidia) Ecad (n=15 ommatida)	n>5 independent experiments	NA

			MyoII (n= 10 ommatidia)		
Fig. 2 Suppl. Fig. 1 C	Mann-Whitney test with Bonferroni correction (P≥0.5, N.S)	Box plot with Median, 25th percentile and 75th percentile In '+' are outliers	n1 = 33, n2 = 21, n3= 50 cell contacts in a retina	1S1C is an independent experiment	C(E,N)|C(E,N), P(E)|P(E) 0.04 P(E)|P(E), C(E,N)|P(E) 0.04 C(E,N)|P(E), C(E,N)|C(E,N) $3.5x10^{-10}$
Fig. 2 Suppl. Fig. 1 G	NA	Mean, SD	Length and Ecad (n1 = 38, n2 = 36, n3 = 26) MyoII (n1=30, n2=22,	Length and Ecad measurement from an independent experiment. MyoII measurement	NA

			n3=36)	from an independent experiment (same as 2F)	
Fig. 2 Suppl. Fig. 1 H	Mann-Whitney test with Bonferroni correction (P≥0.5, N.S)	Box plot with Median, 25th percentile and 75th percentile In '+' outliers	n1 = 17, n2 = 12, n3= 20 cell contacts in a retina	1S1H is an independent experiment	C(E,N)|C(E,N), P(E)|P(E) 0.06 P(E)|P(E), C(E,N)|P(E) 0.02 C(E,N)|P(E), C(E,N)|C(E,N) 1.2x10^{-5}
Fig. 2 Suppl. Fig. 2 B	Mann-Whitney test with Bonferroni correction (P≥0.5, N.S)	Box plot with Median, 25th percentile and 75th percentile In '+' are	n1 = 12, n2 = 12, n3= 12 cell contacts in a retina	3 independent experiments (2S2B is an independent experiment)	C(E,N)|C(E,N), P(E)|P(E) 1.1x10^{-4} P(E)|P(E), C(E,N)|P(E) 1.1x10^{-4} C(E,N)|P(E),

		outliers			C(E,N)|C(E,N) $1.1x10^{-4}$
Fig. 2 Suppl. Fig. 2 C	Mann-Whitney test with Bonferroni correction (P≥0.5, N.S)	Box plot with Median, 25th percentile and 75th percentile In '+' are outliers	n1 = 12, n2 = 15, n3= 15 cell contacts in a retina	3 independent experiments (2S2C is an independent experiment)	C(E,N)|C(E,N), C(E)|C(E) $4.2x10^{-3}$ C(E)|C(E), C(E,N)|C(E), 0.84 C(E,N)|P(E), C(E,N)|C(E,N) 0.05
Fig. 3 Suppl. Fig. 2 D	NA	NA	n=10	Same data set as in 3G	NA
Fig. 3 Suppl. Fig. 2 F	Mann-Whitney test with Bonferroni	Box plot with Median, 25th percentile	n1=15, n2=15	From 3S2G and 3S2H	C|C , C|P $4.3x10^{-3}$

	correction (P≥0.5, N.S)	and 75th percentile In '+' are outliers			
Fig. 3 Suppl. Fig. 2 G	NA	NA	n=15	2 independent experiments (3S2G is an independent experiment)	NA
Fig. 3 Suppl. Fig. 2 H	NA	NA	n=15	3S2H is an independent experiment	NA
Fig. 3 Suppl. Fig. 3 C	Mann-Whitney test with Bonferroni correction (P≥0.5, N.S)	Box plot with Median, 25th percentile and 75th percentile In '+' are outliers	n1 = 41, n2 = 41 cell contacts in n>5 retina	n>5 independent experiments	0.01

Fig. 5 Suppl. Fig. 1 C	NA	Box plot with Median, 25th percentile and 75th percentile In '+' are outlies	n=7	Experiments in 7 retinas	NA
Fig. 5 Suppl. Fig. 2 C	NA	Box plot with Median, 25th percentile and 75th percentile In '+' are outliers	n1= 43, n2=9, n3=8, n4=28, n5=15 in n>5 mosaic retinas. n=1 simulation for each type	n>5 independent experiments	NA
Fig. 5 Suppl. Fig. 2 D	NA	Box plot with Median, 25th percentile and 75th percentile	n1= 43, n2=9, n3=8, n4=28, n5=15 in n>5 mosaic retinas. n=1	n>5 independent experiments	NA

			simulation for each type		
Fig. 5 Suppl. Fig. 3 B	Mann-Whitney test with Bonferroni correction (P≥0.5, N.S)	Box plot with Median, 25th percentile and 75th percentile In '+' are outliers	n1 = 38, n2 = 18, n3 = 28 cell contacts in a retina	4 independent experiments (5S3B is an independent experiment)	C(E,N)|C(E,N), P(E)|P(E) $6.3x10^{-9}$ P(E)|P(E), C(E,N)|P(E) $1.2x10^{-3}$ C(E,N)|P(E), C(E,N)|C(E,N) $1.6x10^{-11}$
Fig. 5 Suppl. Fig. 3 F	Mann-Whitney test with Bonferroni correction (P≥0.5, N.S)	Box plot with Median, 25th percentile and 75th percentile	n1 = 38, n2 = 36, n3 = 26 cell contacts in a retina	4 independent experiments (5S3F is an independent experiment)	C(E,N)|C(E,N), C(E)|C(E) $4.3x10^{-13}$ C(E)|C(E), C(E,N)|C(E) $1.7x10^{-8}$

					C(E,N)|P(E), C(E,N)|C(E,N) $1.7x10^{-8}$
Fig. 5 Suppl. Fig. 4 A	Mann-Whitney test with Bonferroni correction (P≥0.5, N.S)	Box plot with Median, 25th percentile and 75th percentile In '+' are outliers	n1=10, n2=10, n3=10, n4=10 cell contacts from different retinas	n>5 independent experiments	C(E,N)|C(E,N), C(E,N, Sqh-)|C(E,N) $1.5x10^{-3}$ C(E,N)|P(E), C(E,N, Sqh-)|P(E) $1.6x10^{-6}$
Fig. 5 Suppl. Fig. 4 B	Mann-Whitney test with Bonferroni correction (P≥0.5, N.S)	Box plot with Median, 25th percentile and 75th percentile In '+' are outliers	n1=7, n2=7, n3=7, n4=7 cell contacts from different retinas	n>5 independent experiments	C(E,N)|C(E,N), C(E,N, Sqh+)|C(E,N) $4.6x10^{-4}$ C(E,N)|P(E), C(E,N, Sqh+)|P(E) $7.8x10^{-5}$
Fig. 5	Mann-	Box plot	n1= 10,	n>5	NA

Suppl. Fig. 4 E	Whitney test with Bonferroni correction (P≥0.5, N.S)	with Median, 25th percentile and 75th percentile In '+' are outliers	n2=10, n3=10, n4=7, n5=7, n6=10 in n>5 MyoII perturbed retinas. n=1 simulation for each type	independent experiments	

Table 4. Oligonucleotides used in this study

Primers used for cloning (5'-3')

Ncad5'-For

TACGACTCACTATAGGGCGAATTGGGTACCGGGCCCCCCCTCGAGGTCGCCCTGGCGC

Ncad5'-Rev

CCTGAGCTAGCCAATTCTAGTTCGGTATTGTGGGGATTGGGCGCtTCGGGTCCATACATGTTGG

Ncad3'-For

GCATGGACGAGCTGTACAAGTAAGCATGCGCTGGTGGAGCGAGCA

Ncad3'-Rev

TCACTAAAGGGAACAAAAGCTGGAGCTCCACCGCGGTGGCGGCCGCGCGACCACTGTCGATCGAC

mKate2-For

GAATTGGCTAGCTCAGGAGGTGGAGGCAGTATGGTGAGCGAGCTGATTAAGGAG

mKate2-Rev

GCTCGCTCCACCAGCGCATGCTCATCTGTGCCCCAGTTTGCTAGG

gRNA-NCadFw

GTCGGGCCAACATGTATGGACCCG

gRNA-NCadRev

AAACCGGGTCCATACATGTTGGCC

Primers used for the screen of the injected flies

m-Kate2-Fw

GGCAGTATGGTGAGCGAGCTGATTAAGGAGAACATG

m-Kate2-Rv

CTCATCTGTGCCCCAGTTTGCTAGGGAGG

TIO-F

CTCGCGATTCCAACACCTCAGCTGGAG

TIO-R

GCTGAGTCTCCTTCATGTGGGCAG

Ncad-F2

GCTCGGGCAGCACCTGTGTCAACG

mKate2R2

GTGGTGGTTGTTCACGGTGCCCTCCATG

3.2 Exploring different mechanisms explaining the T1 transitions in the retina

As explained in Section 1.2.2, the most consistent and stereotypic behavior of cone cells is the T1-like cell neighbor exchange. During the initial stage, around 21hrs APF, anterior and posterior cone cells are in contact. They form a four-way-vertex and equatorial and polar cone cells come in contact [Figure 3.1a]. Unlike in *Drosophila* embryo where T1 transition occurs on the time scale of minutes, here it occurs on the time scale of hours. Preliminary results show that there is no involvement of MyoII, at least through an anisotropic distribution, unlike its involvement in other T1 transitions. MyoII localization seems symmetric and there is no increase in MyoII level in the shrinking junction. When either equatorial or polar cells, or both equatorial and polar cells are Ncad mutants, cone cells fail to undergo T1 transition. We observed higher MyoII levels at the transverse junctions of those mutants [Figure 3.1b], which might have prevented them from undergoing neighbor exchange, as higher MyoII leads to increase in the cell contact tension. We want to understand, why do wildtype cone cells undergo transition?

3.2.1 Tissue level anisotropy in stress driving the T1 process?

During tissue morphogenesis, tissues can be shaped by anisotropic stresses arising either within them or due to external forces like forces such as the forces exerted on tissues by extracellular matrix or by surrounding tissue (Bonnet et al., 2012; Etournay et al., 2015). We reasoned that cone cell neighbor exchange could be resulting from the higher stress in anterior-posterior direction than the equatorial-polar direction. In order to test this we performed tissue scale ablation experiments by making cuts in horizontal (along anterior-posterior) and vertical (along equatorial-polar) directions around 24 hrs APF (when they form a four-way-vertex). The horizontal cuts resulted in a larger opening with higher initial velocities, compared to vertical cuts [Figure 3.2a]. This suggests that there is anisotropy in stress, with higher stress along the equatorial-polar direction, thus not in the direction of

transition [Figure 3.2b, c]. Cone cells are undergoing transition in spite of the tissue level force against them.

Upon careful observation we found that these T1 transitions were not synchronized. They are not undergoing neighbor exchange one after the other or in a wave like manner (as in photoreceptor cluster formation after morphogenetic furrow, which occurs in the earlier stage of retinal morphogenesis). The Figure 3.2d shows ommatidia with different stages of transition. These results suggest that cone cell neighbor exchange is a property of each individual ommatidium with little or no interaction taking place with the neighboring ommatidia.

3.2.2 Decrease in the tension of the cell contacts between primary pigment cells leading to transition?

In soap bubble like simulations, low junction tension or no tension for the contacts of two primary pigment cells favors the contact between polar and equatorial cells (Käfer et al., 2007). We hypothesized that these junctions could be relaxing over time leading to the T1 transition. Hence we performed junction scale ablation experiments at different time points: 22 hrs APF, 24 hrs APF, 28 hrs APF [Figure 3.3a]. If the hypothesis was right we should have observed that the initial velocities must be lowering with time. The results did not follow this trend [Figure 3.3b, c].

3.2.3 Apical actomyosin in primary pigments pulling the cone cells?

Actomyosin contractility can locally change to aid in the extension of a junction (Collinet et al., 2015). We performed ablation experiments to test if the apical actomyosin in primary pigment cells are pulling the anterior and posterior cone cells that is leading them to the transition [Figure 3.4a]. At different time points, cuts were made at the apical surface of the primary pigment cells as shown in the Figure 3.4b. The cuts should have opened faster and

wider with time to help in transition but the experiments did not show this trend [Figure 3.4 c, d].

All the three experiments outlined above proved to be against the idea of cone cell T1 transition. These results suggest that a process within cone cells might be responsible for the T1 transition. The four cone cells lacking Ncad undergo transition, suggesting that the differential regulation of Ncad, i.e. the downregulation of MyoII at the homotypic contacts and the upregulation of MyoII at heterotypic contacts, might not be actively involved in cone cell T1 transition.

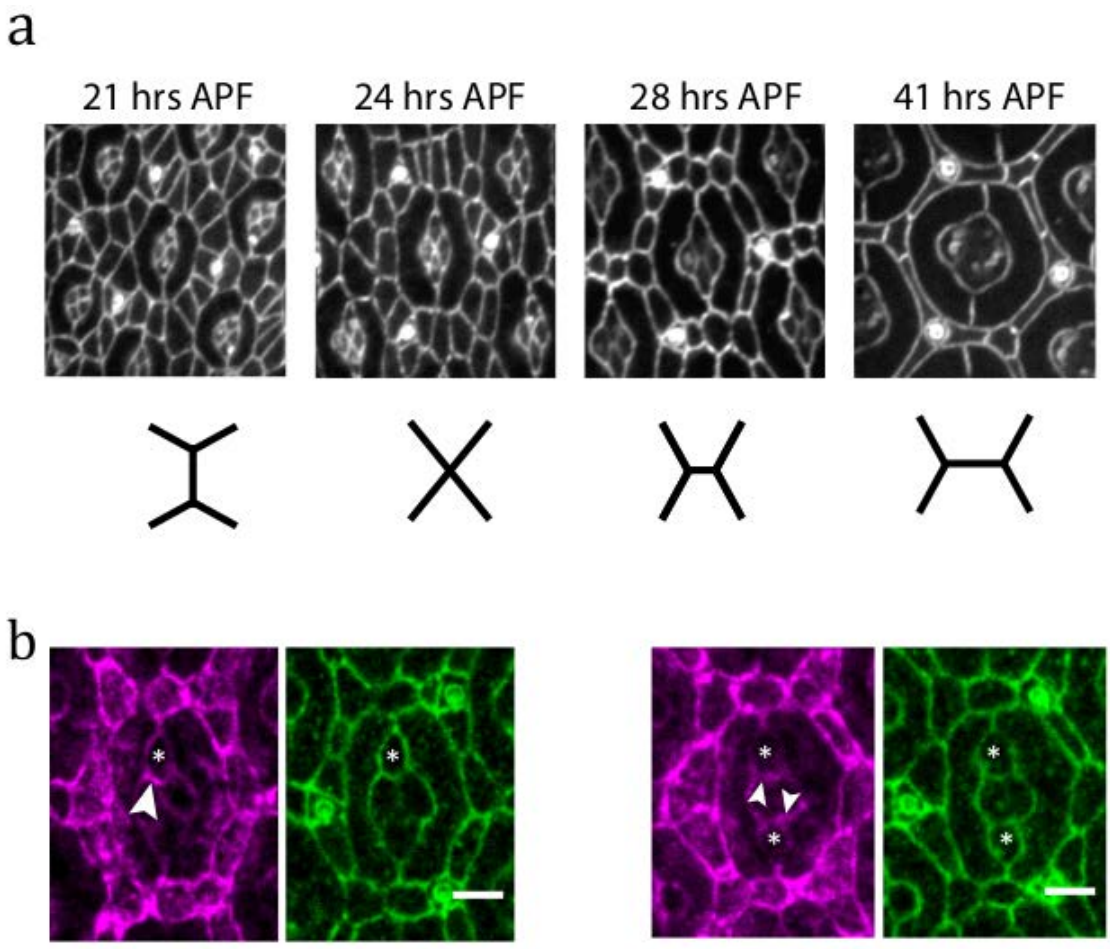

Figure 3.1: T1-like transition among cone cells

a) Images of an ommatidium at different stages (APF) during retinal epithelium with cone cells undergoing neighbor exchange. b) Images of Ncad mutant (mutant cells are marked by white asterisks) ommatidia with MyoII (in magenta) and Ecad (in green) showing failure in neighbor exchange at 26 hours APF (white arrows indicate the higher MyoII level).

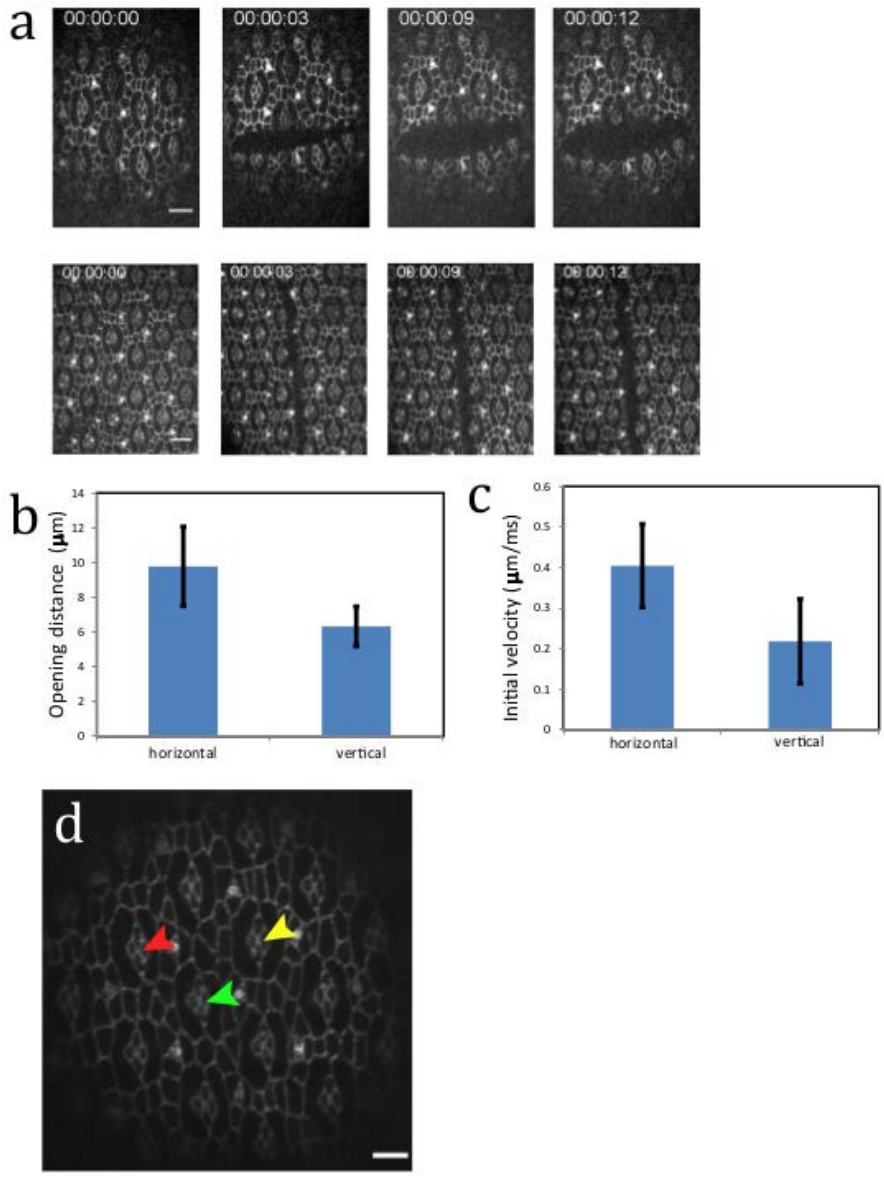

Figure 3.2: Tissue scale laser ablation

a) Snapshots of a movie at different time points of horizontal (anterior-posterior) cut (top panel) and vertical (equatorial-polar direction) cut (down panel) time in seconds Scale bar, 5µm. b) Quantification of length of maximum opening distance. c) Quantification of initial velocity of the opening (in b, c: n = 8 (horizontal), 6 (vertical), mean±s. d.). d) Image of a retina with cone cells in different transition configurations (green arrow points at vertical configuration), (yellow arrow points at four-way vertex) and (red arrow points at horizontal configuration).

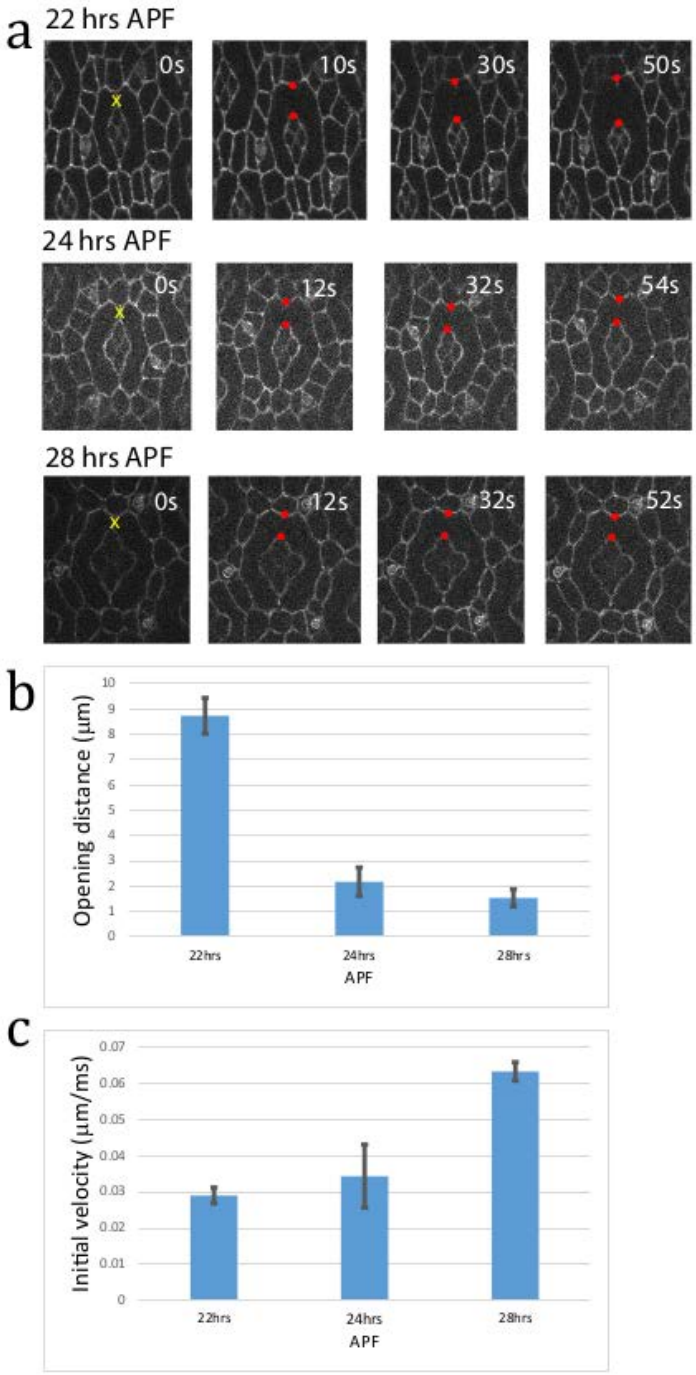

Figure 3.3: Primary pigment cell interface cuts

a) Snapshots of a movies at different time points (in seconds) of primary pigment cell junction cut at three different stages (yellow cross indicates the ablation point and red dots vertices position after the cut). b) Quantification of length of maximum opening distance. c) Quantification of initial velocity of the opening (in b, c: n = 4 (22 hrs APF), 4 (24 hrs APF) and 4 (28 hrs APF), mean±s. d.).

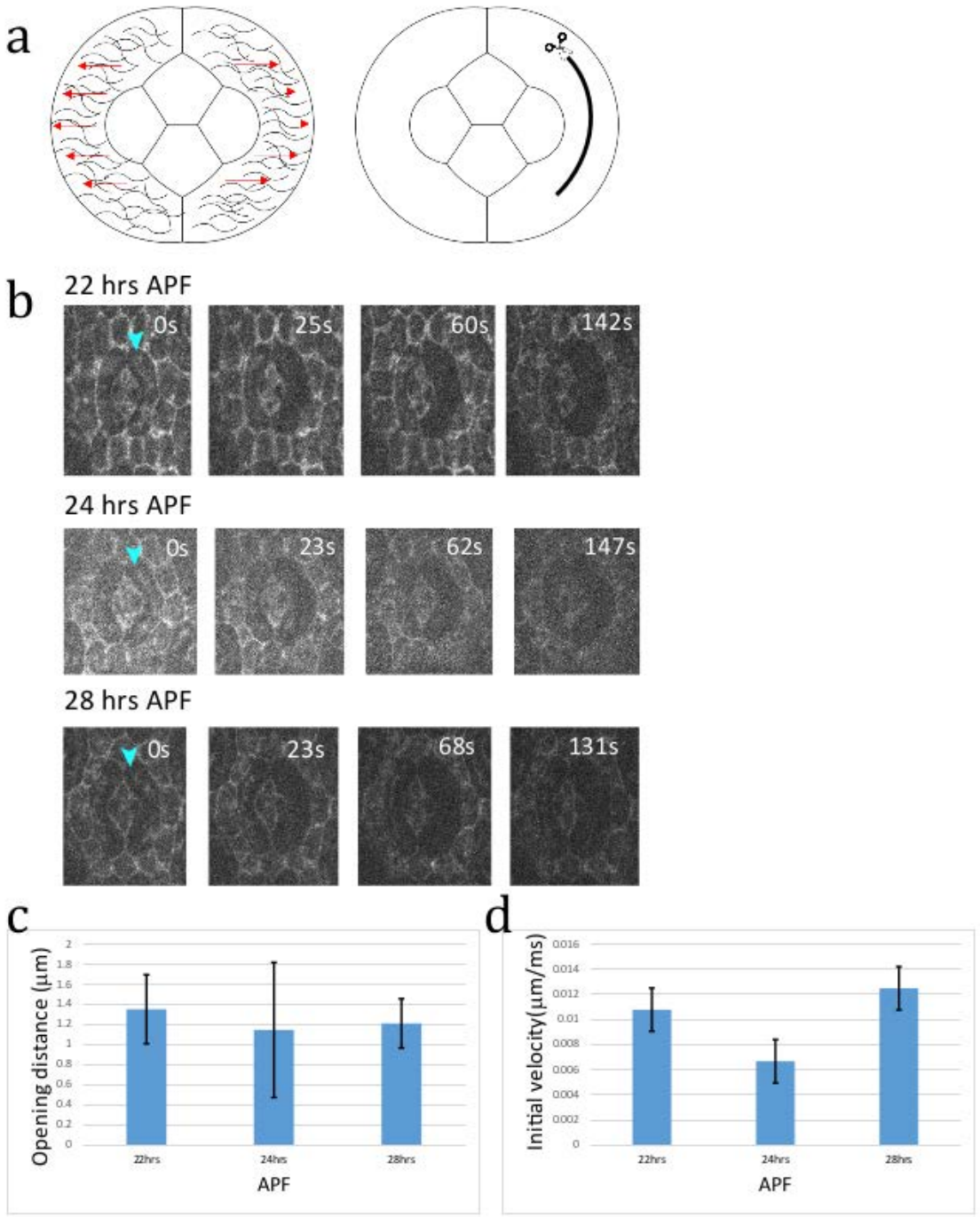

Figure 3.4: Ablation of apical actomyosin mesh in primary pigment cell

a) Schematics of apical actomyosin network in the primary pigment cells pulling the anterior and posterior cone cells over and position of the ablation. b) Snapshots of a movies at different time points (in seconds) of primary pigment apical cut at three different stages (cyan arrows pointing at the primary pigment cells prior to the ablation). c) Quantification of length of maximum opening distance. d) Quantification of initial velocity of the opening (in c, d n = 3 (22 hrs APF), 3 (24 hrs APF) and 3 (28 hrs APF), mean±s. d.).

3.3 Experiments on Ecad overexpression to study its relation to MyoII

In ommatidium, cone cells express Ecad and Ncad, whereas other surrounding cells express only Ecad and no Ncad. There is a higher level of MyoII at the interfaces of Ecad expressing and both Ecad and Ncad expressing cells [Figure 3.5b]. This is not restricted to the ommatidium alone, as we observed higher MyoII level around mis-expressed Ncad clones in wing disc [Figure 3.5a]. There are many other instances in experiments where MyoII forms a boundary. During *Drosophila* salivary gland formation MyoII boundary is formed at the interfaces between placode cells expressing high Crumbs, and surrounding cells expressing low Crumbs (Röper, 2012). In *Drosophila* wing disc, MyoII is present at the interface of differently fated cells. Here, MyoII boundary is formed around clones of aberrant cells in the wildtype tissue, or around clones of wildtype cells in the aberrant tissue (Bielmeier et al., 2016).

Considering all these studies together, one can view MyoII around cone cells as a boundary formed around cells expressing Ncad, separating them from cells expressing Ecad [Figure 3.5c]. Ecad is known to behave in a concentration dependent manner; when cells expressing different levels of Ecad are mixed together they sort out according to the Ecad levels *in vitro*; in *Drosophila* egg chamber the oocyte that expresses Ecad preferentially attaches itself to the follicle cells that have higher levels of Ecad (Friedlander et al., 1989; Godt & Tepass, 1998; Steinberg & Takeichi, 1994). We asked the question, do cells expressing Ecad create a boundary of MyoII when they face cells expressing higher level of Ecad? The previous experiments of overexpression of Ecad clones in wing disc has shown tissue separation and the clones were nearly circular (Dahmann & Basler, 2000). The smoothness of the boundaries is thought to be due to high actomyosin contractility. This suggested that there could be a role of MyoII in generating smoother clones.

We overexpressed Ecad in clones in the wing disc, and looked at MyoII expression (Sqh::Ch). We did not see any change in the MyoII intensity [Figure 3.6a, b]. We confirmed that Ecad is overexpressed in the clones by immunostaining for Ecad [Figure 3.6c, d]. However looking at the shape of clones as previously observed by others (Dahmann & Basler, 2000), clones

had smooth boundaries [Figure 3.6f] in contrast to clones with same level of Ecad as in surrounding cells [Figure 3.6e] Hence we looked at actin, to check if actin is involved in the smoother shape of the clones. We did immunostaining for phalloidin using Alexa 488 (see methods and materials in this chapter). Here again, there was no apparent change in the actin intensity at the boundary of the clones compared to tissue inside or outside the clones [Figure 3.6g, h].

Methods: Genetics and immunochemistry

FLP/FRT system was used to create mosaic mutant tissues. Gal4-UAS system with hsFLP was used to induce targeted gene expression. Flies were maintained at 25°C and time allowed for egg laying was 0±3 hours. A 10 min heat-shock was performed at 72±3 hours after egg laying. Wing discs were dissected from 96±3 hours larvae. They were fixed in 4% of paraformaldehyde (PFA) in PBS for 20 mins, washed 3 times with PBS, permeabilised with PBT (PBS + 0.3% Triton x100), blocked with PBS + 10% NGS (Life technology Cat#50197Z), immunostained with the indicated primary antibodies in PBS + 10% NGS at 4°C overnight and secondary antibodies for 2 hours at room temperature.

The primary antibody used rat anti E-cadherin in 1:10, with secondary antibody goat anti-rat/mouse Alexa 633 in 1:500. Fluorescence images were acquired with a Zeiss LSM780 confocal microscope with ×63, 1.4N.A oil immersion objective. Images typically have 5-6 stacks, 0.25μm apart.

Actin staining (Phalloidin 647): The antibody for Phalloidin staining in 1:400 and kept at room temperature for one and a half hours, washed in PBST three times and dissected for imaging.

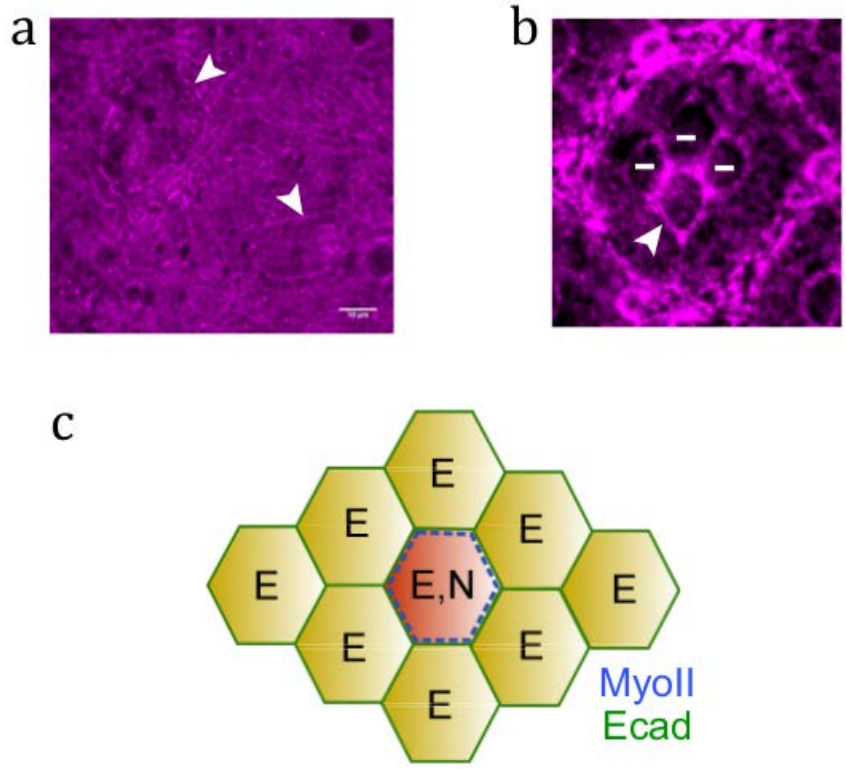

Figure 3.5: MyoII boundary around Ncad cells

a) MyoII in Ncad mis-expressing clones. b) MyoII at the boundary of single wildtype cone cell with three Ncad mutant cell (MyoII in magenta, white arrows point at the MyoII boundary, Ncad mutant cells are marked by white asterisks). c) Cartoon depicting a single cell expressing E & Ncad (red) among Ecad cells (yellow) forming a boundary of MyoII (blue).

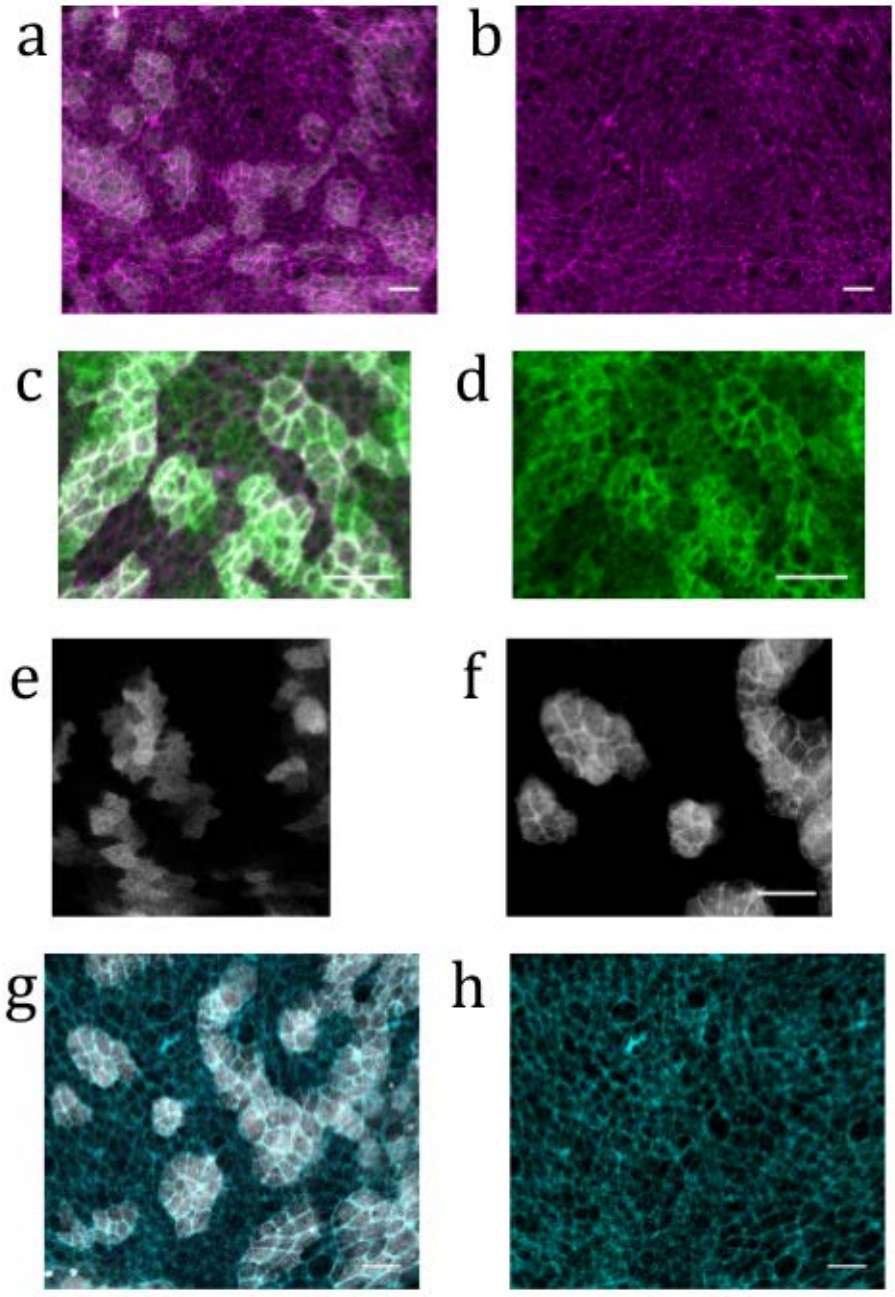

Figure 3.6: Ecad overexpression in wing disc

a, b) Ecad expressing clones (in grey) and Sqh::ch (in magenta). c, d) Immunostaining for Ecad (in green) and clones of Ecad overexpressing cell (in grey). e) Shape of clones in normal wing disc and f) Shape of clones with high level of Ecad than wildtype tissue. g, h) Staining for actin (in cyan) and Ecad overexpressing clones (in grey). Scale bar, 10μm.

Chapter 4: Discussions and perspective

We show that there is a gradation in MyoII levels at the cell contact of *Drosophila* pupal retina at 41 hrs APF. This gradation depends on the cadherins expressed in the cells, and results in a gradation in the interfacial tension. The MyoII level at a cell contact can be tuned by simply removing Ncad from the cell or by introducing Ncad to the cell. The asymmetric expression of Ncad in a cell leads to upregulation of MyoII at its cell contact, and this MyoII is asymmetrically localized. Our studies suggest that the cytoplasmic part of the Ncad is involved in the upregulation of MyoII at cell contacts. Mutations in Ncad lead to drastic changes in the shape of cone cells. We know that this is due to MyoII that is indirectly controlled by Ncad. Our results show that Ncad adhesion and Ecad adhesion by themselves have little effect on the cone cell shapes. The local concentration of MyoII at the cell contact determines the cell shape irrespective of its origin (whether is recruited through Ncad or by any other pathways).

Our experiments show that T1-like transition among cone cells is a local phenomenon. Cone cells in each ommatidium undergo neighbor exchange with little or no interaction with its neighbors.

Our studies on Ecad in *Drosophila* wing disc show that Ecad does not seem to signal to MyoII like Ncad does. Ecad by its adhesion, without invoking MyoII, is able to change the shape of the clones.

4.1 Differential regulation of MyoII by Ncad

In our study we show that Ncad differentially impacts on MyoII depending on whether there is adhesion or not. We showed that Ncad engaged in homophilic adhesion, downregulates MyoII, and these homotypic contacts have the lowest level of MyoII, with lower interfacial tension. Whereas at heterotypic contacts, where there is no adhesion by Ncad, MyoII is

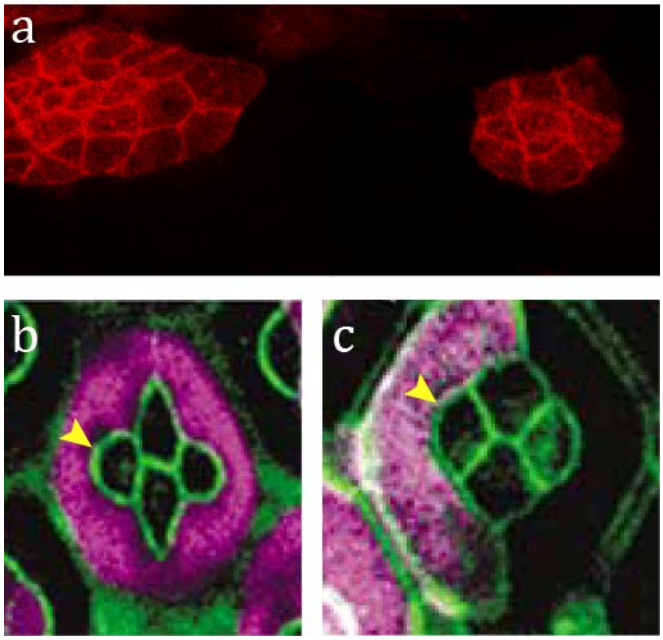

Figure 4.1: Ecad overexpression

a) Smooth boundary of clones (in red) with cells overexpressing Ecad (cell contacts of Ecad overexpressing cells in red, Ecad::GFP). b) Primary pigment cells mis-expressing Ncad in an ommatidium (in magenta). c) One of the primary pigment cells overexpressing Ecad *(image: Modified from Hayashi & Carthew, 2004)* (yellow arrows point at the change in cone cell shape in (b) and no change in shape in (c)).

upregulated and these contacts have higher levels of MyoII with higher interfacial tension. This MyoII concentration can be tuned by changing heterotypic contacts to homotypic contacts. By regulating the expression of Ncad, cells are able to achieve different types of cell contacts, and thereby shapes, thus "killing two birds with one stone". The details of MyoII regulation by Ncad remains unknown and is an open question.

Clones mis-expressing Ncad in *Drosophila* wing imaginal disc have MyoII at the boundary and smooth interfaces [Figure 4.2a], suggesting that the phenomenon of Ncad differentially regulating MyoII is not restricted only to *Drosophila* pupal eye. Clones with cells overexpressing Ecad in wing disc do not have higher MyoII at the boundary, but have a comparatively smooth surface [Figure 4.1a, Figure 4.2b]. Also in *Drosophila* pupal eye, mis-

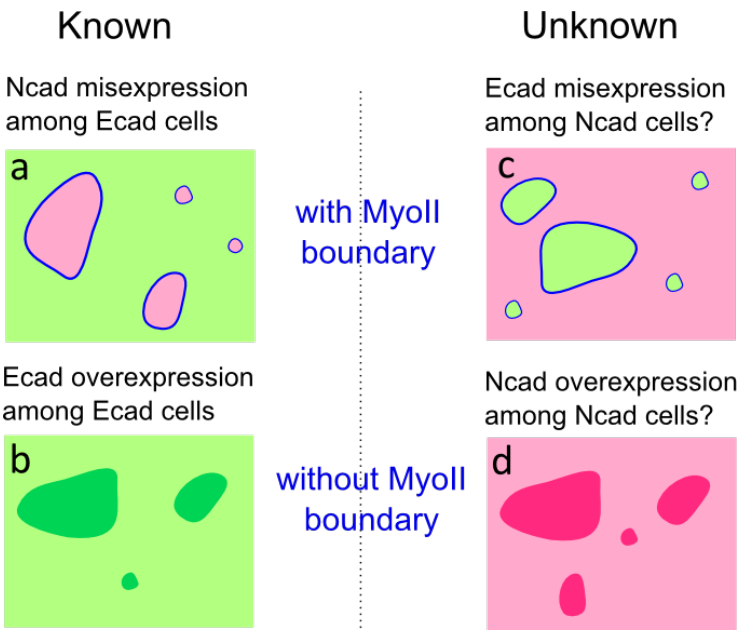

Figure 4.2: Cartoon of cadherins and clone shape

a) Ncad mis-expressing clones in a wing disc with smooth boundary having a higher level of MyoII at the interface of clone and wildtype tissue. b) Ecad overexpressing clones in a wing disc with smooth boundary, having no change in MyoII level at the interface of clone and wildtype tissue. c) Cartoon showing hypothetical experiment of Ecad expression among Ncad cells to check if there is a higher level of MyoII at the interface. d) Cartoon showing a hypothetical experiment for Ncad overexpression among Ncad cells to check if there is no change in the level of MyoII at the interface.

expressing Ncad in primary pigment cell changes the shape of cone cells [Figure 4.1b], but overexpressing Ecad in primary pigment cell does not [Figure 4.1c] (Hayashi & Carthew, 2004).

These experiments show that Ncad and Ecad might not behave in the same way. At least Ecad does not affect MyoII in a dose dependent manner, but we do not know if Ecad clones among uniformly expressed Ncad cells create MyoII boundary [Figure 4.2c]; such an experiment will clearly answer if Ncad and Ecad interact with MyoII in the same way. It is interesting to

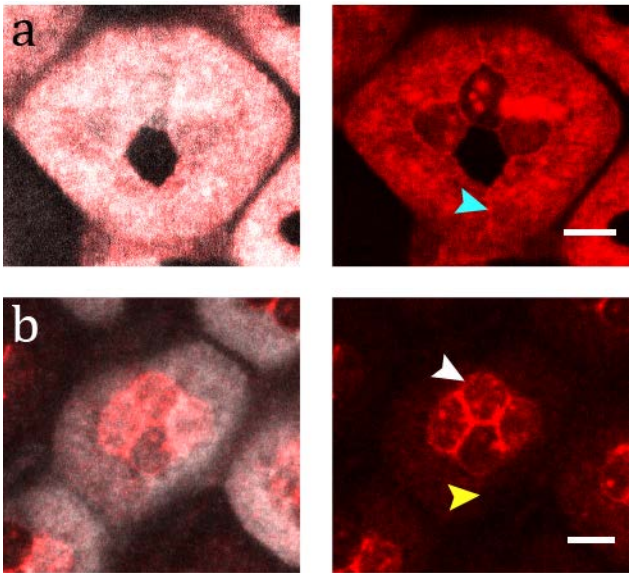

Figure 4.3: Ncad adhesion needs anchoring to actomyosin in at least one cell

a) Ncad mis-expression (in grey) and Ncad (in red) at the interfaces of primary pigment cells (cyan arrow). b) Truncated Ncad (Ncad-Δcyto) mis-expression (in grey) and absence of Ncad (in red) at the interfaces of primary pigment cells (yellow arrow).

investigate this further as Ecad to Ncad switch has implications in cancer metastasis.

In the study by Warner and Longmore (Warner & Longmore, 2009), Rho1-RNAi disrupts adherens junctions (AJs) (Ecad, β-cat and α-cat) between pigment cells, but AJs between primary pigment cells and cone cells, and AJs of cone cells are not affected. They have shown that Rho1 maintains AJs by regulating endocytosis of Ecad. This suggests that Rho1 is not involved in Ncad endocytosis. Rho1 is the effector of Rok and Rok regulates MyoII. In their experiments, depleting MyoII does not affect the AJs of pigment cells, but only their apical area. This led them to conclude that in an already formed AJ, maintenance of AJs by Ecad endocytosis and maintenance of cell's apical tension by MyoII through Rok are different pathways of Rho. This is a bit puzzling, as AJs between the primary pigment cell and cone cell are not affected even though only Ecad adhesion is present at those AJs. It could be possible that Ncad at these contacts maintain AJs through MyoII. Our experiments show depleting

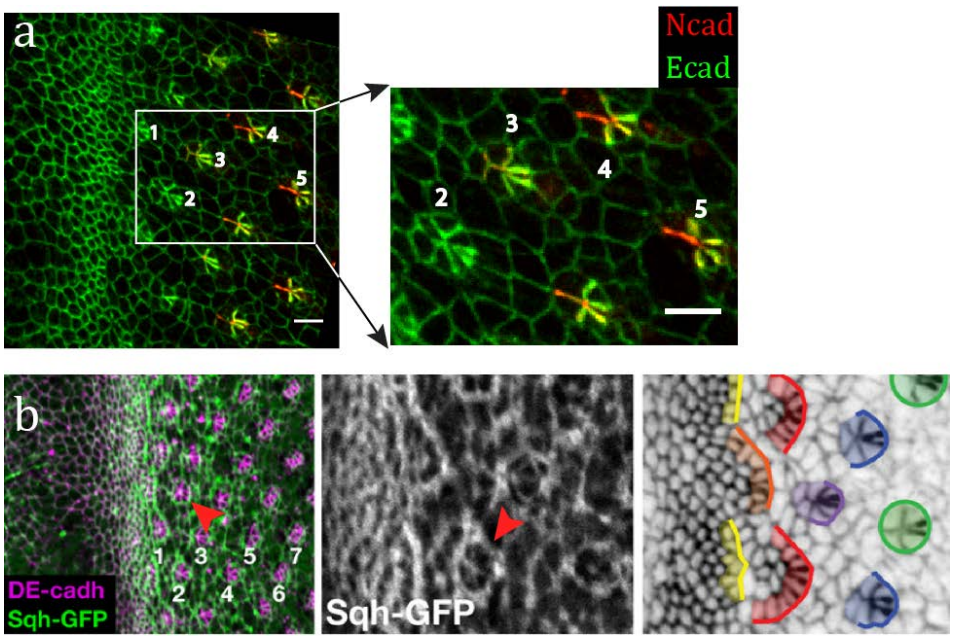

Figure 4.4: Ncad and MyoII in photoreceptor clusters

a) Photoreceptor cluster formation in eye disc with Ecad::ch (in green) and Ncad::GFP (in red) (photoreceptor clusters are numbered as in *Escudero, Bischoff, & Freeman, 2007*). A zoomed-in image shows different clusters with different levels of Ncad. b) The pattern of MyoII expression in eye disc and specific patterns around the photoreceptor clusters (red arrows highlight the higher level of MyoII around the newly forming photoreceptor clusters) (*image: Modified from Escudero, Bischoff, & Freeman, 2007)*.

MyoII in neighboring cone cells does not affect Ncad or Ecad at their contact, we only observe a change in the apical area of the cells.

When Ncad is mis-expressed in both the primary pigment cells, Ncad forms homophilic adhesion and can be observed at the interface between primary pigment cells [Figure 4.3a, cyan arrow]. Expressing Ncad-Δcyto in both the primary pigment cells do not form Ncad adhesion at the cell contact even though they have an extracellular domain [Figure 4.3b, yellow arrow]. Whereas, at the contacts between a primary pigment cell and a cone cell, with primary pigment cell expressing Ncad-Δcyto, there is Ncad adhesion [Figure 4.3b, white arrow], suggesting that Ncad needs anchoring in at least one of the cells for proper adhesion. As discussed earlier, when MyoII is disrupted in both cone cells, it does not affect Ncad. This suggests Ncad regulates MyoII contractility but the converse is not true, MyoII does not

influence Ncad adhesion. Cadherin adhesions are known to be stabilized by actin (Cavey et al., 2008), disrupting actin might have an impact on Ncad adhesion. But a more careful analysis would be required to reach a conclusion.

During retinal morphogenesis, at the third instar larval stage, cells arrange into clusters at the posterior side of the eye disc as the morphogenetic furrow moves anteriorly. These clusters progressively mature, adding more and more cells called photoreceptors. These photoreceptors have distinct expression of Ecad and Ncad at their contacts which are essential for the rotation of the cluster (Mirkovic & Mlodzik, 2006). We also looked at the expression of Ecad and Ncad at these contacts with a tagged version of Ncad (Ncad::GFP, Ecad::Ch). Ncad is present in all the contacts but at different levels [Figure 4.4a].

The photoreceptor clusters have MyoII at the boundary in the shape of an arc, and as they mature the arc becomes circular (Escudero, Bischoff, & Freeman, 2007) [Figure 4.4b]. Ncad and MyoII expression in these clusters resembles the expression pattern of Ncad and MyoII in cone cells. It would be interesting to check if the same mechanism of differential regulation occurs in photoreceptor cells.

Olfactory epithelium (OE), which is present in the nasal cavity of mammals, is comprised of olfactory cells (OCs) and supporting cells (SCs). OCs express Ncad, Nectin-2 and SCs express Ecad, Ncad, Nectin-2 and Nectin-3 (Katsunuma et al., 2016). In mouse embryo, during the morphogenesis of OE, the localization pattern of Ecad remains the same, but the localization pattern of Ncad changes. Katsunuma et al. argue that heterophilic interactions of Nectin-2 and Nectin-3 bring cadherins to heterotypic cell junctions and the differential cadherin distribution between cell contacts assist the cell intercalation to create mosaic pattern in OE. It is possible that the differential regulation of MyoII via Ncad is playing a role in OC arrangement because in αN-catenin (the crosslinker of actomyosin to Ncad) knockout mice, OCs form Ncad adhesion but fail to undergo cell arrangement [Figure 4.5].

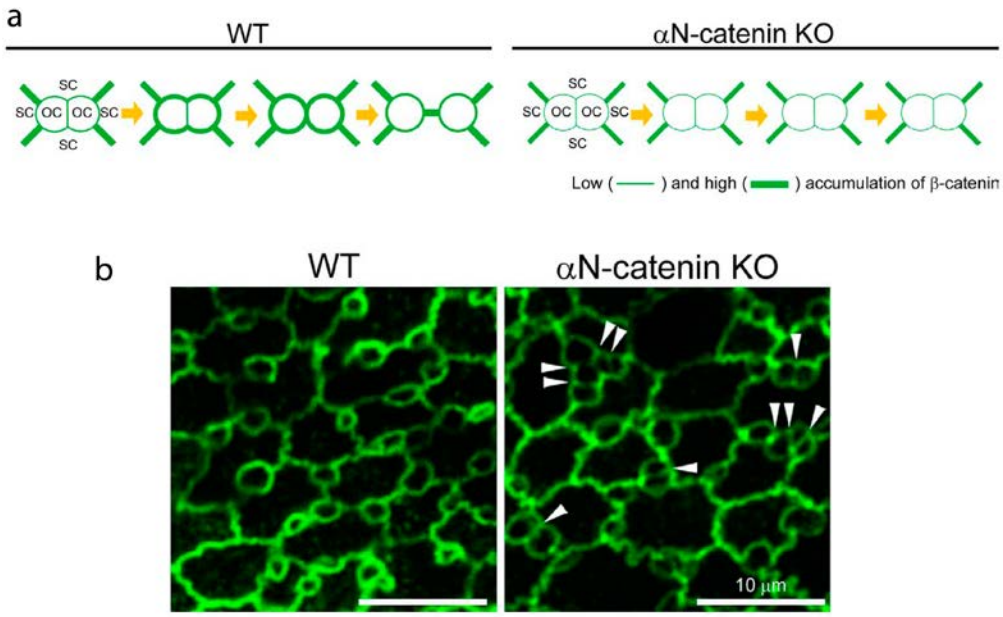

Figure 4.5: Cell rearrangements in olfactory epithelium

a) Schematics of cell rearrangements and β-catenin levels in wildtype (WT) and αN-catenin knockout (KO) mice during development of olfactory epithelium (OE). b) Images of cellular patterns of OE at P0 (postnatal day) in WT and αN-catenin KO mice (white arrows point at the OCs that failed to undergo cell arrangement). (*Image: adapted from Katsunuma et al., 2016)*.

4.2 Experimental inputs from laser ablation

The ablation experiments were performed at 41hrs APF when all the cells have reached their final shape and size. The concentration measurements of Ecad and MyoII were also done at 41hrs APF. The cells in ommatidia vary in shape and size during the retinal morphogenesis. Similar measurements can be done at earlier time points, say, 28hrs APF to understand the cell mechanics during the change from one cell shape to another. Comparison of the parameters at 28hrs APF and 41hrs APF, to understand how cell scale parameter and junction parameter change over time during morphogenesis, might help in understanding T1 like transition among cone cells.

4.3 Model

Our work—like previous studies (Farhadifar et al., 2007; Käfer et al., 2007)—further demonstrated the importance of elastic properties in defining cell shapes. It highlighted the fact that MyoII contribution to line tension is not enough to explain the observed shape, in addition, MyoII regulated cell scale property is necessary. With line tension alone, the system behaves like soap bubbles. The presence of elastic tension arising from perimeter elasticity makes cells mechanically different from soap bubbles. What differentiates our model from other models is that we have used experimental inputs and minimized the number of free parameters to one.

The limitations of our model are its assumptions and simplifications, which are as follows. We have measured the cell scale parameter ($\Delta P/P_0$) for only anterior and posterior cone cells and assumed it to be the same for polar, equatorial cone cells, as well as for Ncad mutant cells. Since this parameter depends on MyoII contractility, and we observe different MyoII level at different contacts, this might lead to different $\Delta P/P_0$ for different cells. We assumed that change in MyoII levels affects only the local tension, this can be tested by doing similar experiments on different mutant cells, which will improve the comparison between experiments and simulations.

For simplicity, we have omitted the area elasticity term as it gives information on the size of the cell, rather than the shape. However, MyoII perturbations show that the size of the cells varies as compared to the wildtype cone cells. The model can be further improved with more experimental input, with the downside being that there will be more free parameters. Even though the differential regulation of MyoII by Ncad is the 'take home message' of our work, the model does not include the feedback between Ncad and MyoII.

To validate the importance of MyoII on cone cell shapes, we manipulated MyoII activity by decreasing and increasing MyoII contractility in cone cells. This resulted in a change in the overall size of the cone cell (as the perturbations change the activity of both apical MyoII and junctional MyoII). The importance of junctional MyoII contribution to local tension and cell shapes can only be observed by manipulating MyoII on the scale of a single junction. In the

future, optogenetic techniques could be used to perturb the MyoII in a single cell contact, currently optogenetic tools are employed on the scale of a few cells, or in a single MDCK cell in cell culture (Valon et al., 2017); optogenetics is used to blockade the cell contractility at the level of a few cells in *Drosophila* embryo (Guglielmi & De Renzis, 2017).

The different shapes of cone cells were simulated using the principle of energy minimization, with the assumption that the system is in quasi-static equilibrium. In wing disc epithelium, it has been shown that cells go from disordered to hexagonal ordered arrangement (Classen et al., 2005). Farhadifar et al. suggested that the balance of adhesion and contractility defines the arrangement. The higher adhesive cells make softer tissue with more or less than six neighbors and higher contractile cells make stiffer tissue with six neighbors (Farhadifar et al., 2007). Since we are interested in retinal development, as discussed earlier, measuring the parameters at an earlier stage and simulating the early stage ommatidium might shed light on the mechanics involved in morphogenesis.

List of Figures

Supplementary Figures (article)

List of Tables

References

Aldaz, S., Escudero, L. M., & Freeman, M. (2013). Dual role of myosin II during Drosophila imaginal disc metamorphosis. *Nature Communications*, *4*, 1761. https://doi.org/10.1038/ncomms2763

Bambardekar, K., Clément, R., Blanc, O., Chardès, C., & Lenne, P.-F. (2015). Direct laser manipulation reveals the mechanics of cell contacts in vivo. *Proceedings of the National Academy of Sciences*, *112*(5), 1416–1421. https://doi.org/10.1073/pnas.1418732112

Baumgartner, W., Hinterdorfer, P., Ness, W., Raab, A., Vestweber, D., Schindler, H., & Drenckhahn, D. (2000). Cadherin interaction probed by atomic force microscopy. *Proceedings of the National Academy of Sciences*, *97*(8), 4005–4010. https://doi.org/10.1073/pnas.070052697

Beauzamy, L., Nakayama, N., & Boudaoud, A. (2014). Flowers under pressure: Ins and outs of turgor regulation in development. *Annals of Botany*, *114*(7), 1517–1533. https://doi.org/10.1093/aob/mcu187

Bershadsky, A. (2004). Magic touch: How does cell-cell adhesion trigger actin assembly? *Trends in Cell Biology*, *14*(11), 589–593. https://doi.org/10.1016/j.tcb.2004.09.009

Bertet, C., Sulak, L., & Lecuit, T. (2004). Myosin-dependent junction remodelling controls planar cell intercalation and axis elongation. *Nature*, *429*. https://doi.org/10.1038/nature02581.1.

Besson, S., & Dumais, J. (2011). Universal rule for the symmetric division of plant cells. *Proceedings of the National Academy of Sciences*, *108*(15), 6294–6299. https://doi.org/10.1073/pnas.1011866108

Betapudi, V. (2014). Life without double-headed non-muscle myosin II motor proteins. *Frontiers in Chemistry*, *2*(July), 1–13. https://doi.org/10.3389/fchem.2014.00045

Bielmeier, C., Alt, S., Weichselberger, V., La Fortezza, M., Harz, H., Jülicher, F., … Classen, A. K. (2016). Interface Contractility between Differently Fated Cells Drives Cell Elimination

and Cyst Formation. *Current Biology*, *26*(5), 563–574. https://doi.org/10.1016/j.cub.2015.12.063

Boal, D. (2012). *Mechanics of the cell* (2nd ed.).

Bonnet, I., Marcq, P., Bosveld, F., Fetler, L., Bellaiche, Y., & Graner, F. (2012). Mechanical state, material properties and continuous description of an epithelial tissue. *Journal of The Royal Society Interface*, *9*(75), 2614–2623. https://doi.org/10.1098/rsif.2012.0263

Borghi, N., Sorokina, M., Shcherbakova, O. G., Weis, W. I., Pruitt, B. L., Nelson, W. J., & Dunn, A. R. (2012). E-cadherin is under constitutive actomyosin-generated tension that is increased at cell-cell contacts upon externally applied stretch. *Proceedings of the National Academy of Sciences*, *109*(31), 12568–12573. https://doi.org/10.1073/pnas.1204390109

Bosveld, F., & Nodal, T. (2012). Mechanical Control of Morphogenesis. *Science*, *336*(May), 724–727. https://doi.org/10.1126/science.1221071

Brakke, K. A. (1992). The Surface Evolver.

Bray, D., & White, J. G. (1988). Cortical flow in animal cells. *Science*, *239*(4842), 883 LP-888. Retrieved from http://science.sciencemag.org/content/239/4842/883.abstract

Broadbent, I. D., & Pettitt, J. (2002). The C. elegans hmr-1 gene can encode a neuronal classic cadherin involved in the regulation of axon fasciculation. *Current Biology*, *12*(1), 59–63. https://doi.org/10.1016/S0960-9822(01)00624-8

Brodu, V., & Casanova, J. (2006). The RhoGAP crossveinless-c links trachealess and EGFR signaling to cell shape remodeling in Drosophila tracheal invagination. *Genes & Development* , *20*(13), 1817–1828. https://doi.org/10.1101/gad.375706

Cai, D., Chen, S. C., Prasad, M., He, L., Wang, X., Choesmel-Cadamuro, V., … Montell, D. J. (2014). Mechanical feedback through E-cadherin promotes direction sensing during collective cell migration. *Cell*, *157*(5), 1146–1159. https://doi.org/10.1016/j.cell.2014.03.045

Campàs, O., Mammoto, T., Hasso, S., Sperling, R. A., O'Connell, D., Bischof, A. G., … Ingber, D. E. (2013). Quantifying cell-generated mechanical forces within living embryonic tissues. *Nature Methods*, *11*(2), 183–189. https://doi.org/10.1038/nmeth.2761

Cavey, M., & Lecuit, T. (2008). Imaging Cellular and Molecular Dynamics in Live Embryos Using Fluorescent Proteins. In C. Dahmann (Ed.), *Drosophila: Methods and Protocols* (pp. 219–238). Totowa, NJ: Humana Press. https://doi.org/10.1007/978-1-59745-583-1_13

Cavey, M., Rauzi, M., Lenne, P.-F., & Lecuit, T. (2008). A two-tiered mechanism for stabilization and immobilization of E-cadherin. *Nature*, *453*(7196), 751–756. https://doi.org/10.1038/nature06953

Chan, E. H. Y., Shivakumar, P. C., Clément, R., Laugier, E., & Lenne, P.-F. (2017). Patterned cortical tension mediated by N-cadherin controls cell geometric order in the drosophila eye. *eLife*, *6*. https://doi.org/10.7554/eLife.22796

Chen, C. S., Mrksich, M., Huang, S., Whitesides, G. M., & Ingber, D. E. (1997). Geometric Control of Cell Life and Death. *Science*, *276*(5317), 1425 LP-1428. Retrieved from http://science.sciencemag.org/content/276/5317/1425.abstract

Chu, Y. S., Eder, O., Thomas, W. A., Simcha, I., Pincet, F., Ben-Ze'ev, A., … Dufour, S. (2006). Prototypical type I E-cadherin and type II cadherin-7 mediate very distinct adhesiveness through their extracellular domains. *Journal of Biological Chemistry*, *281*(5), 2901–2910. https://doi.org/10.1074/jbc.M506185200

Clark, A. G., Dierkes, K., & Paluch, E. K. (2013). Monitoring actin cortex thickness in live cells. *Biophysical Journal*, *105*(3), 570–580. https://doi.org/10.1016/j.bpj.2013.05.057

Classen, A. K., Anderson, K. I., Marois, E., & Eaton, S. (2005). Hexagonal packing of Drosophila wing epithelial cells by the planar cell polarity pathway. *Developmental Cell*, *9*(6), 805–817. https://doi.org/10.1016/j.devcel.2005.10.016

Collinet, C., Rauzi, M., Lenne, P.-F., & Lecuit, T. (2015). Local and tissue-scale forces drive oriented junction growth during tissue extension. *Nature Cell Biology*, *17*(10), 1247–1258. https://doi.org/10.1038/ncb3226

Dahmann, C., & Basler, K. (2000). Opposing Transcriptional Outputs of Hedgehog Signaling and Engrailed Control Compartmental Cell Sorting at the Drosophila A/P Boundary. *Cell*, *100*(4), 411–422. https://doi.org/10.1016/S0092-8674(00)80677-7

Davis, M. A., Ireton, R. C., & Reynolds, A. B. (2003). A core function for p120-catenin in cadherin turnover. *Journal of Cell Biology*, *163*(3), 525–534. https://doi.org/10.1083/jcb.200307111

de Vries, W. N., Evsikov, A., Haac, B., Fancher, K., & Holbrook, A. (2004). Maternal β-catenin and E-cadherin in mouse development. *Development*, *131*(18), 4435–4445. https://doi.org/10.1242/dev.01316

Derycke, L. D. M., & Bracke, M. E. (2004). N-cadherin in the spotlight of cell-cell adhesion, differentiation, invasion and signalling. *International Journal of Developmental Biology*, *48*(5–6), 463–476. https://doi.org/10.1387/ijdb.041793ld

Discher, D. E. (2005). Tissue Cells Feel and Respond to the Stiffness of Their Substrate. *Science*, *310*(5751), 1139–1143. https://doi.org/10.1126/science.1116995

Dufour, S., Beauvais-Jouneau, A., Delouvée, A., & Thiery, J. P. (1999). Differential function of N-cadherin and cadherin-7 in the control of embryonic cell motility. *Journal of Cell Biology*, *146*(2), 501–516. https://doi.org/10.1083/jcb.146.2.501

Engl, W., Arasi, B., Yap, L. L., Thiery, J. P., & Viasnoff, V. (2014). Actin dynamics modulate mechanosensitive immobilization of E-cadherin at adherens junctions. *Nature Cell Biology*, *16*(6), 587–594. https://doi.org/10.1038/ncb2973

Escudero, L. M., Bischoff, M., & Freeman, M. (2007). Myosin II Regulates Complex Cellular Arrangement and Epithelial Architecture in Drosophila. *Developmental Cell*, *13*(5), 717–729. https://doi.org/10.1016/j.devcel.2007.09.002

Etournay, R., Popović, M., Merkel, M., Nandi, A., Blasse, C., Aigouy, B., … Eaton, S. (2015). Interplay of cell dynamics and epithelial tension during morphogenesis of the Drosophila pupal wing. *eLife*, *4*(JUNE2015), 1–51. https://doi.org/10.7554/eLife.07090

Farhadifar, R., Röper, J. C., Aigouy, B., Eaton, S., & Jülicher, F. (2007). The Influence of Cell Mechanics, Cell-Cell Interactions, and Proliferation on Epithelial Packing. *Current Biology*. https://doi.org/10.1016/j.cub.2007.11.049

Fernandez-Gonzalez, R., Simoes, S. de M., Röper, J. C., Eaton, S., & Zallen, J. A. (2009). Myosin II Dynamics Are Regulated by Tension in Intercalating Cells. *Developmental Cell*, *17*(5), 736–743. https://doi.org/10.1016/j.devcel.2009.09.003

Fernández-Sánchez, M. E., Barbier, S., Whitehead, J., Béalle, G., Michel, A., Latorre-Ossa, H., … Farge, E. (2015). Mechanical induction of the tumorigenic β-catenin pathway by tumour growth pressure. *Nature*, *523*(7558), 92–95. https://doi.org/10.1038/nature14329

Fletcher, A. G., Osterfield, M., Baker, R. E., & Shvartsman, S. Y. (2014). Vertex models of epithelial morphogenesis. *Biophysical Journal*, *106*(11). https://doi.org/10.1016/j.bpj.2013.11.4498

Forgacs, G., Foty, R. A., Shafrir, Y., & Steinberg, M. S. (1998). Viscoelastic Properties of Living Embryonic Tissues: a Quantitative Study. *Biophysical Journal*, *74*(5), 2227–2234. https://doi.org/10.1016/S0006-3495(98)77932-9

Friedlander, D. R., Mège, R. M., Cunningham, B. A., & Edelman, G. M. (1989). Cell sorting-out is modulated by both the specificity and amount of different cell adhesion molecules (CAMs) expressed on cell surfaces. *Proceedings of the National Academy of Sciences of the United States of America*, *86*(September), 7043–7047. https://doi.org/10.1073/pnas.86.18.7043

Georges, P. C., & Janmey, P. a. (2005). Cell type-specific response to growth on soft materials. *Journal of Applied Physiology*, *98*(4), 1547–1553. https://doi.org/10.1152/japplphysiol.01121.2004.

Godt, D., & Tepass, U. (1998). Drosophila oocyte localization is mediated by differential cadherin-based adhesion. *Nature*, *395*(6700), 387–391. https://doi.org/10.1038/26493

Guglielmi, G., & De Renzis, S. (2017). *Optogenetic inhibition of apical constriction during*

Drosophila embryonic development. *Methods in Cell Biology* (Vol. 139). Elsevier Ltd. https://doi.org/10.1016/bs.mcb.2016.10.007

Guillot, C., & Lecuit, T. (2013). Adhesion Disengagement Uncouples Intrinsic and Extrinsic Forces to Drive Cytokinesis in Epithelial Tissues. *Developmental Cell*, *24*(3), 227–241. https://doi.org/10.1016/j.devcel.2013.01.010

Harrison, O. J., Bahna, F., Katsamba, P. S., Jin, X., Brasch, J., Vendome, J., … Shapiro, L. (2010). Two-step adhesive binding by classical cadherins. *Nature Structural & Molecular Biology*, *17*(3), 348–357. https://doi.org/10.1038/nsmb.1784

Harrison, O. J., Jin, X., Hong, S., Bahna, F., Ahlsen, G., Brasch, J., … Honig, B. (2011). The extracellular architecture of adherens junctions revealed by crystal structures of type i cadherins. *Structure*, *19*(2), 244–256. https://doi.org/10.1016/j.str.2010.11.016

Hayashi, T., & Carthew, R. W. (2004). Surface mechanics mediate pattern formation in the developing retina. https://doi.org/10.1038/nature02952

Heisenberg, C. P., & Bellaïche, Y. (2013). Forces in tissue morphogenesis and patterning. *Cell*, *153*(5). https://doi.org/10.1016/j.cell.2013.05.008

Herbomel, G., Hatte, G., Roul, J., Padilla-Parra, S., Tassan, J.-P., & Tramier, M. (2017). Actomyosin-generated tension on cadherin is similar between dividing and non-dividing epithelial cells in early Xenopus laevis embryos. *Scientific Reports*, *7*(March), 45058. https://doi.org/10.1038/srep45058

Hilgenfeldt, S., Erisken, S., & Carthew, R. W. (2008). Physical modeling of cell geometric order in an epithelial tissue. *Proceedings of the National Academy of Sciences of the United States of America*, *105*(3), 907–911. https://doi.org/10.1073/pnas.0711077105

Hirano, S., & Takeichi, M. (2012). Cadherins in Brain Morphogenesis and Wiring. *Physiological Reviews*, *92*(2), 597–634. https://doi.org/10.1152/physrev.00014.2011

Hirokawa, N., & Heuser, J. E. (1981). Quick-freeze, deep-etch visualization of the cytoskeleton beneath surface differentiations of intestinal epithelial cells. *The Journal of Cell Biology*, *91*(2 Pt 1), 399–409. https://doi.org/10.1083/jcb.91.2.399

Hutson, M. S. (2003). Forces for Morphogenesis Investigated with Laser Microsurgery and Quantitative Modeling. *Science*, *300*(5616), 145–149. https://doi.org/10.1126/science.1079552

Ishihara, S., & Sugimura, K. (2012). Bayesian inference of force dynamics during morphogenesis. *Journal of Theoretical Biology*, *313*, 201–211. https://doi.org/10.1016/j.jtbi.2012.08.017

Islam, S., Carey, T. E., Wolf, G. T., Wheelock, M. J., & Johnson, K. R. (1996). Expression of N-cadherin by human squamous carcinoma cells induces a scattered fibroblastic phenotype with disrupted cell-cell adhesion. *Journal of Cell Biology*, *135*(6), 1643–1654. https://doi.org/10.1083/jcb.135.6.1643

Jamora, C., & Fuchs, E. (2002). Intercellular adhesion, signalling and the cytoskeleton. *Nature Cell Biology*, *4*(4), E101–E108. https://doi.org/10.1038/ncb0402-e101

Käfer, J., Hayashi, T., Marée, A. F. M., Carthew, R. W., & Graner, F. (2007). Cell adhesion and cortex contractility determine cell patterning in the Drosophila retina. *Proceedings of the National Academy of Sciences of the United States of America*, *104*(47), 18549–18554. https://doi.org/10.1073/pnas.0704235104

Kashima, T., Nakamura, K., Kawaguchi, J., Takanashi, M., Ishida, T., Aburatani, H., … Grigoriadis, A. E. (2003). Overexpression of cadherins suppresses pulmonary metastasis of osteosarcoma in vivo. *International Journal of Cancer*, *104*(2), 147–154. https://doi.org/10.1002/ijc.10931

Katsunuma, S., Honda, H., Shinoda, T., Ishimoto, Y., Miyata, T., Kiyonari, H., … Togashi, H. (2016). Synergistic action of nectins and cadherins generates the mosaic cellular pattern of the olfactory epithelium. *Journal of Cell Biology*, *212*(5), 561–575. https://doi.org/10.1083/jcb.201509020

Keller, R. (2006). Mechanisms of elongation in embryogenesis. *Development*, *133*(12), 2291–2302. https://doi.org/10.1242/dev.02406

Kenney, D. E., & Borisy, G. G. (2009). Thomas Hunt Morgan at the marine biological laboratory: Naturalist and experimentalist. *Genetics*, *181*(3), 841–846.

https://doi.org/10.1534/genetics.109.101659

Kiehart, D. P., Galbraith, C. G., Edwards, K. A., Rickoll, W. L., & Montague, R. A. (2000). Multiple forces contribute to cell sheet morphogenesis for dorsal closure in Drosophila. *Journal of Cell Biology*, *149*(2), 471–490. https://doi.org/10.1083/jcb.149.2.471

Kim, J. B., Islam, S., Kim, Y. J., Prudoff, R. S., Sass, K. M., Wheelock, M. J., & Johnson, K. R. (2000). N-cadherin extracellular repeat 4 mediates epithelial to mesenchymal transition and increased motility. *Journal of Cell Biology*, *151*(6), 1193–1205. https://doi.org/10.1083/jcb.151.6.1193

Kim, J. H., Ren, Y., Ng, W. P., Li, S., Son, S., Kee, Y. S., … Chen, E. H. (2015). Mechanical Tension Drives Cell Membrane Fusion. *Developmental Cell*, *32*(5), 561–573. https://doi.org/10.1016/j.devcel.2015.01.005

Koenderink, G. H., Dogic, Z., Nakamura, F., Bendix, P. M., MacKintosh, F. C., Hartwig, J. H., … Weitz, D. A. (2009). An active biopolymer network controlled by molecular motors. *Proceedings of the National Academy of Sciences*, *106*(36), 15192–15197. https://doi.org/10.1073/pnas.0903974106

Krieg, M., Arboleda-Estudillo, Y., Puech, P.-H., Käfer, J., Graner, F., Müller, D. J., & Heisenberg, C.-P. C.-P. (2008). Tensile forces govern germ-layer organization in zebrafish. *Nature Cell Biology*, *10*(4), 429–36. https://doi.org/10.1038/ncb1705

Landsberg, K. P., Farhadifar, R., Ranft, J., Umetsu, D., Widmann, T. J., Bittig, T., … Dahmann, C. (2009). Increased Cell Bond Tension Governs Cell Sorting at the Drosophila Anteroposterior Compartment Boundary. *Current Biology*, *19*(22), 1950–1955. https://doi.org/10.1016/j.cub.2009.10.021

Le Goff, L., Hallatschek, O., Frey, E., & Amblard, F. (2002). Tracer Studies on F-Actin Fluctuations. *Physical Review Letters*, *89*(25), 258101. https://doi.org/10.1103/PhysRevLett.89.258101

Lecuit, T., & Lenne, P.-F. (2007). Cell surface mechanics and the control of cell shape, tissue patterns and morphogenesis. *Nature Reviews Molecular Cell Biology*, *8*(8), 633–644.

https://doi.org/10.1038/nrm2222

Lecuit, T., Lenne, P.-F., & Munro, E. (2011). Force Generation, Transmission, and Integration during Cell and Tissue Morphogenesis. *Annual Review of Cell and Developmental Biology*, *27*(1), 157–184. https://doi.org/10.1146/annurev-cellbio-100109-104027

Legant, W. R., Miller, J. S., Blakely, B. L., Cohen, D. M., Genin, G. M., & Chen, C. S. (2010). Measurement of mechanical tractions exerted by cells in three-dimensional matrices. *Nature Methods*, *7*(12), 969–971. https://doi.org/10.1038/nmeth.1531

Levayer, R., Dupont, C., & Moreno, E. (2016). Tissue Crowding Induces Caspase-Dependent Competition for Space. *Current Biology*, *26*(5), 670–677. https://doi.org/10.1016/j.cub.2015.12.072

Levayer, R., & Lecuit, T. (2013). Oscillation and Polarity of E-Cadherin Asymmetries Control Actomyosin Flow Patterns during Morphogenesis. *Developmental Cell*, *26*(2). https://doi.org/10.1016/j.devcel.2013.06.020

Levayer, R., Pelissier-Monier, A., & Lecuit, T. (2011). Spatial regulation of Dia and Myosin-II by RhoGEF2 controls initiation of E-cadherin endocytosis during epithelial morphogenesis. *Nature Cell Biology*, *13*(5), 529–540. https://doi.org/10.1038/ncb2224

Maitre, J.-L., Berthoumieux, H., Krens, S. F. G., Salbreux, G., Julicher, F., Paluch, E., & Heisenberg, C.-P. (2012). Adhesion Functions in Cell Sorting by Mechanically Coupling the Cortices of Adhering Cells. *Science*, *338*(6104), 253–256. https://doi.org/10.1126/science.1225399

Maître, J. L., & Heisenberg, C. P. (2011). The role of adhesion energy in controlling cell-cell contacts. *Current Opinion in Cell Biology*. https://doi.org/10.1016/j.ceb.2011.07.004

Major, R. J., & Irvine, K. D. (2006). Localization and requirement for myosin II at the dorsal-ventral compartment boundary of the Drosophila wing. *Developmental Dynamics*. https://doi.org/10.1002/dvdy.20966

Marinari, E., Mehonic, A., Curran, S., Gale, J., Duke, T., & Baum, B. (2012). Live-cell

delamination counterbalances epithelial growth to limit tissue overcrowding. *Nature*, *484*(7395), 542–545. https://doi.org/10.1038/nature10984

Martin, A. C., Kaschube, M., & Wieschaus, E. F. (2009). Pulsed contractions of an actin–myosin network drive apical constriction. *Nature*, *457*(7228), 495–499. https://doi.org/10.1038/nature07522

Mayer, M., Depken, M., Bois, J. S., Jülicher, F., & Grill, S. W. (2010). Anisotropies in cortical tension reveal the physical basis of polarizing cortical flows. *Nature*, *467*(7315), 617–621. https://doi.org/10.1038/nature09376

Mirkovic, I., & Mlodzik, M. (2006). Cooperative activities of Drosophila DE-Cadherin and DN-Cadherin regulate the cell motility process of ommatidial rotation. *Development*, *133*(17), 3283–3293. https://doi.org/10.1242/dev.02468

Monier, B., Gettings, M., Gay, G., Mangeat, T., Schott, S., Guarner, A., & Suzanne, M. (2015). Apico-basal forces exerted by apoptotic cells drive epithelium folding. *Nature*, *518*(7538), 245–248. https://doi.org/10.1038/nature14152

Morgan, T. (1910). SEX LIMITED INHERITANCE IN DROSOPHILA. *Science*, *XXXII*(812), 120–122.

Munjal, A., & Lecuit, T. (2014). Actomyosin networks and tissue morphogenesis. *Development*, *141*(9), 1789–1793. https://doi.org/10.1242/dev.091645

Nagafuchi, A., & Takeichi, M. (1988). Cell binding function of E-cadherin is regulated by the cytoplasmic domain. *The EMBO Journal*, *7*(12), 3679–3684. Retrieved from http://www.ncbi.nlm.nih.gov/pmc/articles/PMC454940/

Nieman, M. T., Prudoff, R. S., Johnson, K. R., & Wheelock, M. J. (1999). N-Cadherin Promotes Motility in Human Breast Cancer Cells Regardless of Their E-Cadherin Expression. *The Journal of Cell Biology*, *147*(3), 631–644. Retrieved from http://www.ncbi.nlm.nih.gov/pmc/articles/PMC2151177/

Niessen, C. M., Leckband, D., & Yap, A. S. (2011). Tissue organization by cadherin adhesion molecules: dynamic molecular and cellular mechanisms of morphogenetic regulation.

Physiological Reviews, *91*(2), 691–731. https://doi.org/10.1152/physrev.00004.2010

Niewiadomska, P., Godt, D., & Tepass, U. (1999). *D* E-Cadherin Is Required for Intercellular Motility during *Drosophila* Oogenesis. *The Journal of Cell Biology*, *144*(3), 533–547. https://doi.org/10.1083/jcb.144.3.533

Oda, H., & Tsukita, S. (1999). Nonchordate classic cadherins have a structurally and functionally unique domain that is absent from chordate classic cadherins. *Developmental Biology*, *216*(1), 406–422. https://doi.org/10.1006/dbio.1999.9494

Padmanabhan, A., Ong, H. T., & Zaidel-Bar, R. (2016). Non-junctional E-Cadherin Clusters Regulate the Actomyosin Cortex in the C. elegans Zygote. *Current Biology*, 1–10. https://doi.org/10.1016/j.cub.2016.10.032

Peláez, N., Gavalda-Miralles, A., Wang, B., Navarro, H. T., Gudjonson, H., Rebay, I., … Carthew, R. W. (2015). Dynamics and heterogeneity of a fate determinant during transition towards cell differentiation. *eLife*, *4*(NOVEMBER2015), 1–23. https://doi.org/10.7554/eLife.08924

Pla, P., Moore, R., Morali, O. G., Grille, S., Martinozzi, S., Delmas, V., & Larue, L. (2001). Cadherins in neural crest cell development and transformation. *Journal of Cellular Physiology*, *189*(2), 121–32. https://doi.org/10.1002/jcp.10008

Pollard, T. D. (2007). Regulation of Actin Filament Assembly by Arp2/3 Complex and Formins. *Annu. Rev. Biophys. Biomol. Struct.* https://doi.org/10.1146/annurev.biophys.35.040405.101936

Pollard, T. D., & Cooper, J. A. (2009). Actin, a Central Player in Cell Shape and Movement. *Science*, *326*(5957), 1208–1212. https://doi.org/10.1126/science.1175862

Rauzi, M., Lenne, P.-F., & Lecuit, T. (2010). Planar polarized actomyosin contractile flows control epithelial junction remodelling. *Nature*, *468*(7327), 1110–1114. https://doi.org/10.1038/nature09566

Rauzi, M., & Lenne, P. F. (2011). *Cortical Forces in Cell Shape Changes and Tissue Morphogenesis*. *Current Topics in Developmental Biology* (Vol. 95).

https://doi.org/10.1016/B978-0-12-385065-2.00004-9

Rauzi, M., Verant, P., Lecuit, T., & Lenne, P.-F. (2008). Nature and anisotropy of cortical forces orienting Drosophila tissue morphogenesis. *Nat Cell Biol*, *10*(12), 1401–1410. Retrieved from http://dx.doi.org/10.1038/ncb1798

Röper, K. (2012). Anisotropy of Crumbs and aPKC Drives Myosin Cable Assembly during Tube Formation. *Developmental Cell*, *23*(5), 939–953. https://doi.org/10.1016/j.devcel.2012.09.013

Rusconi, J. C., Hays, R., & Cagan, R. L. (2000). Programmed cell death and patterning in Drosophila. *Cell Death and Differentiation*, *7*(11), 1063–1070. https://doi.org/10.1038/sj.cdd.4400767

Salbreux, G., Charras, G., & Paluch, E. (2012). Actin cortex mechanics and cellular morphogenesis. *Trends in Cell Biology*. https://doi.org/10.1016/j.tcb.2012.07.001

Sedzinski, J., Biro, M., Oswald, A., Tinevez, J.-Y., Salbreux, G., & Paluch, E. (2011). Polar actomyosin contractility destabilizes the position of the cytokinetic furrow. *Nature*, *476*(7361), 462–466. https://doi.org/10.1038/nature10286

Shan, W., Tanaka, H., Phillips, G. R., Arndt, K., Yoshida, M., Colman, D. R., & Shapiro, L. (2000). Functional cis-Heterodimers of N- and R-Cadherins. *The Journal of Cell Biology*, *148*(3), 579–590. https://doi.org/10.1083/jcb.148.3.579

Shapiro, L., Love, J., & Colman, D. R. (2007). Adhesion Molecules in the Nervous System: Structural Insights into Function and Diversity. *Annual Review of Neuroscience*, *30*(1), 451–474. https://doi.org/10.1146/annurev.neuro.29.051605.113034

Shewan, A. M., Maddugoda, M., Kraemer, A., Stehbens, S. J., Verma, S., Kovacs, E. M., & Yap, A. S. (2005). Myosin 2 Is a Key Rho Kinase Target Necessary for the Local Concentration of E-Cadherin at Cell–Cell Contacts. *Molecular Biology of the Cell*, *16*(10), 4531–4542. https://doi.org/10.1091/mbc.E05-04-0330

Shivakumar, P. C., & Lenne, P.-F. (2016). Laser Ablation to Probe the Epithelial Mechanics in Drosophila. In C. Dahmann (Ed.), *Drosophila: Methods and Protocols* (pp. 241–251).

New York, NY: Springer New York. https://doi.org/10.1007/978-1-4939-6371-3_14

Simões, S., Oh, Y., Wang, M. F. Z., Fernandez-Gonzalez, R., & Tepass, U. (2017). Myosin II promotes the anisotropic loss of the apical domain during Drosophila neuroblast ingression. *Journal of Cell Biology*, *216*(5), 1387–1404. https://doi.org/10.1083/jcb.201608038

Spahn, P., & Reuter, R. (2013). A Vertex Model of Drosophila Ventral Furrow Formation. *PLoS ONE*, *8*(9). https://doi.org/10.1371/journal.pone.0075051

Steinberg, M. S., & Takeichi, M. (1994). Experimental specification of cell sorting, tissue spreading, and specific spatial patterning by quantitative differences in cadherin expression. *Proceedings of the National Academy of Sciences*, *91*(1), 206–209. https://doi.org/10.1073/pnas.91.1.206

Stewart, M. P., Helenius, J., Toyoda, Y., Ramanathan, S. P., Muller, D. J., & Hyman, A. A. (2011). Hydrostatic pressure and the actomyosin cortex drive mitotic cell rounding. *Nature*, *469*(7329), 226–230. https://doi.org/10.1038/nature09642

Suarez, F., Thostrup, P., Colman, D., & Grutter, P. (2013). Dynamics of presynaptic protein recruitment induced by local presentation of artificial adhesive contacts. *Developmental Neurobiology*, *73*(1), 98–106. https://doi.org/10.1002/dneu.22037

Sugimura, K., & Ishihara, S. (2013). The mechanical anisotropy in a tissue promotes ordering in hexagonal cell packing. *Development*, *140*(19), 4091–4101. https://doi.org/10.1242/dev.094060

Sugimura, K., Lenne, P.-F., & Graner, F. (2016). Measuring forces and stresses in situ in living tissues. *Development*, *143*(2), 186–196. https://doi.org/10.1242/dev.119776

Sweeton, D., Parks, S., Costa, M., & Wieschaus, E. (1991). Gastrulation in Drosophila: the formation of the ventral furrow and posterior midgut invaginations. *Development (Cambridge, England)*, *112*(3), 775–89. Retrieved from http://dev.biologists.org/content/112/3/775.abstract

Takeichi, M. (1991). Cadherin cell adhesion receptors as a morphogenetic regulator. *Science*

(New York, N.Y.), *251*(1989), 1451–1455. https://doi.org/10.1126/science.2006419

Tanentzapf, G., Smith, C., McGlade, J., & Tepass, U. (2000). Apical, lateral, and basal polarization cues contribute to the development of the follicular epithelium during Drosophila oogenesis. *Journal of Cell Biology*, *151*(4), 891–904. https://doi.org/10.1083/jcb.151.4.891

Tepass, U., & Harris, K. P. (2007). Adherens junctions in Drosophila retinal morphogenesis. *Trends in Cell Biology*. https://doi.org/10.1016/j.tcb.2006.11.006

Thompson, D. W. (1992). *On Growth and Form*. *Canto*. Cambridge: Cambridge University Press. https://doi.org/DOI: 10.1017/CBO9781107325852

Uehara, R., Goshima, G., Mabuchi, I., Vale, R. D., Spudich, J. A., & Griffis, E. R. (2010). Determinants of myosin II cortical localization during cytokinesis. *Current Biology*, *20*(12), 1080–1085. https://doi.org/10.1016/j.cub.2010.04.058

Valon, L., Marín-Llauradó, A., Wyatt, T., Charras, G., & Trepat, X. (2017). Optogenetic control of cellular forces and mechanotransduction. *Nature Communications*, *8*, 14396. https://doi.org/10.1038/ncomms14396

Volk, T., Cohen, O., & Geiger, B. (1987). Formation of heterotypic adherens-type junctions between L-CAM-containing liver cells and A-CAM-containing lens cells. *Cell*, *50*(6), 987–994. https://doi.org/10.1016/0092-8674(87)90525-3

Volk, T., & Geiger, B. (1986). A-CAM: A 135-kD receptor of intercellular adherens junctions. II. Antibody-mediated modulation of junction formation. *Journal of Cell Biology*, *103*(4), 1451–1464. https://doi.org/10.1083/jcb.103.4.1451

Wang, F., Dumstrei, K., Haag, T., & Hartenstein, V. (2004). The role of DE-cadherin during cellularization, germ layer formation and early neurogenesis in the Drosophila embryo. *Developmental Biology*, *270*(2), 350–363. https://doi.org/10.1016/j.ydbio.2004.03.002

Warner, S. J., & Longmore, G. D. (2009). Distinct functions for Rho1 in maintaining adherens junctions and apical tension in remodeling epithelia. *Journal of Cell Biology*, *185*(6),

1111–1125. https://doi.org/10.1083/jcb.200901029

Weliky, M., & Oster, G. (1990). The mechanical basis of cell rearrangement. I. Epithelial morphogenesis during Fundulus epiboly. *Development (Cambridge, England)*, *109*(2), 373–386.

Yagi, T., & Takeichi, M. (2000). Cadherin superfamily genes: Functions, genomic organization, and neurologic diversity. *Genes and Development*, *14*(10), 1169–1180. https://doi.org/10.1101/gad.14.10.1169

Yamada, S., & Nelson, W. J. (2007). Localized zones of Rho and Rac activities drive initiation and expansion of epithelial cell-cell adhesion. *Journal of Cell Biology*, *178*(3), 517–527. https://doi.org/10.1083/jcb.200701058

Yao, M., Qiu, W., Liu, R., Efremov, A. K., Cong, P., Seddiki, R., … Yan, J. (2014). Force-dependent conformational switch of α-catenin controls vinculin binding. *Nature Communications*, *5*. https://doi.org/10.1038/ncomms5525

Yonekura, S., Xu, L., Ting, C. Y., & Lee, C. H. (2007). Adhesive but not signaling activity of Drosophila N-cadherin is essential for target selection of photoreceptor afferents. *Developmental Biology*, *304*(2), 759–770. https://doi.org/10.1016/j.ydbio.2007.01.030

Zhou, J., Pal, S., Maiti, S., & Davidson, L. A. (2015). Force production and mechanical accommodation during convergent extension. *Development*, *142*(4), 692–701. https://doi.org/10.1242/dev.116533